

*Conjugated Microporous Polymers for
Heterogeneous Visible Light Photocatalysis in
Aqueous Medium*

Dissertation

Beatriz Chiyin Ma



MAX-PLANCK-GESELLSCHAFT

JOHANNES GUTENBERG
UNIVERSITÄT MAINZ



Max-Planck-Institut
für Polymerforschung

Max Planck Institute
for Polymer Research



Conjugated Microporous Polymers for Heterogeneous Visible Light Photocatalysis in Aqueous Medium

Dissertation

Zur Erlangung des Grades

“Doktor der Naturwissenschaften”

im Promotionsfach Chemie

dem Fachbereich Chemie, Pharmazie und Geowissenschaften

der Johannes Gutenberg-Universität Mainz

Beatriz Chiyin Ma

Geboren in Brasília, Brasilien

Mainz, 2016

Dekan:

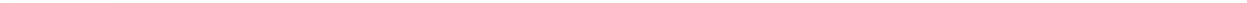
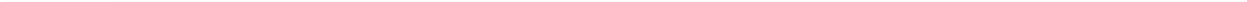
1. Berichterstatter: Prof. Dr. Katharina Landfester

2. Berichterstatter: Prof. Dr. Michael Maskos

Tag der mündlichen Prüfung: 07 Dezember 2016

ABSTRACT

Visible light-driven photochemistry and photocatalysis have found significant broad utility in organic synthesis in recent years. Among the visible light-active photocatalytic systems, conjugated microporous polymers (CMPs) offer a promising alternative in comparison to traditional molecular transition metal photocatalysts due to their visible light activity, heterogeneous nature, high stability, ease of reusability and highly tunable electronic and optical properties. However, there are two main drawbacks which impair the broader application of CMPs: (1) their insoluble nature limits their processability in solvents and (2) the highly hydrophobic backbone reduces their compatibility with aqueous reaction media, which is considered as the cheapest and more sustainable reaction environment. In this work, we aim to address the above-mentioned problems. A number of different structural designs of CMPs are presented and thoroughly investigated as promising new approaches for the use of CMPs as water-compatible visible light-active and heterogeneous photocatalysts in aqueous media. First, a model of dispersed CMP nanoparticles (NPs) is presented as processability modification method. It is demonstrated that the nanostructure morphology can be finely adjusted by molecular structural design between various aromatic building block moieties in the polymer backbone. Second, it is shown that different molecular combinations can largely influence the energy band levels of the CMP NPs and result in great impacts on the photocatalytic performance, especially for enhancement in the generation of *singlet* oxygen, which in the best case, the production rate lies at *ca.* 0.14 mmol g⁻¹ s⁻¹. Third, CMP NPs have shown ability for the photocatalytic regeneration of nicotinamide cofactors under visible light irradiation. At last, another processability improvement method is achieved by dispersing conventional CMPs in water under the use of hydrophilic phase transfer agent during the photocatalytic process. Furthermore, the impact of different geometric settings on the photocatalytic efficiency of CMPs is also investigated. The study of the architectural variation of CMPs demonstrates that one dimensional polymer offers the highest photocatalytic efficiency for H₂ evolution from water with a significant evolution rate of 116 μmol⁻¹ h⁻¹ g⁻¹ achieved with an apparent quantum yield of 4.01% under visible-light irradiation at 420 nm. We believe that this study will pave the way for a broader application field for CMPs as a visible light metal-free photocatalyst.



ZUSAMMENFASSUNG

Photokatalyse mit sichtbarem Licht führte in letzter Zeit zu einem breiten Anwendungsfeld in der organischen Synthesechemie. Neben den weit entwickelten molekularen Photocatalysatoren, die unter sichtbarem Licht aktiv sind, wie z.B. den Übergangsmetallkomplexen oder organischen Farbstoffen, stellen konjugierte mikroporöse Polymere, welche die photoaktive π -konjugierte Hauptkette mit porösen Grenzflächen kombinieren, aufgrund ihrer hohen Stabilität und metallfreien Natur eine vielversprechende Alternative dar. Jedoch existieren zwei nicht übersehbare Schwächen bei CMPs: (i) die Unlöslichkeit beschränkt die Prozessbarkeit der CMPs in Lösung; und (ii) die hohe Hydrophobie des aromatischen Grundgerüsts behindert eine breite Nutzung von CMPs in wässrigen Medien, insbesondere in Wasser, welches als das günstigste und umweltfreundlichste Reaktionsmedium angesehen wird. In dieser Arbeit stellen wir eine Lösung für die oben genannte Probleme dar. Zunächst wird ein Modell zur Herstellung von wasser-dispergierbaren CMPs in Form von Nanopartikeln (NP) mit Hilfe der Miniemulsionspolymerisation hergestellt. Es kann gezeigt werden, dass durch Variation von verschiedenen Monomeren sowohl die Morphologie als auch die Gestalt der CMP-NPs modifiziert werden können. Des Weiteren wird in dem folgenden Projekt durch die sogenannte „Dotierung“ durch einen Elektronenakzeptor, der allmählich in das Elektronendonordhaltige Polymergerüst eingebaut wird, die optischen und energetischen Eigenschaften gezielt variiert werden können. Eine erhöhte photokatalytische Effektivität von den CMP-NPs kann anhand der Produktion von Singuletsauerstoff mit einer maximalen Produktionsrate von *ca.* 0.14 mmol g⁻¹ s⁻¹ demonstriert werden, indem der Akzeptoranteil im Polymer erhöht wird. Als praktische Anwendung in Wasser wird die licht-induzierte Deaktivierung von Bakterien mit Hilfe der CMP-NPs erfolgreich demonstriert. Schließlich wird eine Studie über die erfolgreiche Anwendung von CMPs für photokatalytische H₂-Produktion aus Wasser präsentiert. Hier werden konventionelle CMPs mit Hilfe eines Opferreagenz, das gleichzeitig als Elektronendonator und Phasentransferreagenz fungiert, ins wässrige Reaktionsmedium gebracht. Dabei kann das 1-dimensionale lineare Polymer als die beste CMP-Geometrie identifiziert werden, um die beste H₂-Produktionsrate von 116 $\mu\text{mol/h/g}$ mit einer Quantenausbeute von 4.01% unter Bestrahlung bei 420 nm zu

erzielen. Wir sind überzeugt, dass mit dieser Arbeit der Weg für eine breitere Anwendung von CMPs als metall-freie Photokatalysatoren bereitet ist.

TABLE OF CONTENTS

1	INTRODUCTION AND MOTIVATION	13
2	THEORETICAL BACKGROUND.....	15
2.1	PHOTOCATALYSIS.....	15
2.1.1	A brief history	15
2.1.2	Fundamentals	15
2.2	VISIBLE LIGHT PHOTOCATALYSIS	18
2.2.1	Homogeneous visible light photocatalysis	18
2.2.2	Heterogeneous visible light photocatalysis.....	20
2.2.2.1	Metal based visible light photocatalysts.....	20
2.2.2.2	Non-metal based visible light photocatalysts.....	22
2.3	CONJUGATED POLYMERS.....	22
2.3.1	Conjugated Microporous Polymers.....	24
2.3.1.1	Synthetic reaction routes.....	25
2.3.1.2	Suzuki-Miyaura coupling.....	25
2.3.1.3	Sonogashira coupling	26
2.3.1.4	Applications	28
2.4	COLLOIDAL SYSTEMS	29
2.4.1	Emulsions	30
2.4.1.1	Miniemulsions.....	31
2.4.1.2	Stability.....	32
3	CHARACTERIZATION TECHNIQUES	35
3.1	TRANSMISSION ELECTRON MICROSCOPY	35
3.2	SCANNING ELECTRON MICROSCOPY	35
3.3	ULTRAVIOLET-VISIBLE SPECTROSCOPY AND FLUORESCENCE SPECTROSCOPY.....	36
3.4	FOURIER TRANSFORM INFRARED SPECTROSCOPY	36
3.5	ELECTRON PARAMAGNETIC RESONANCE.....	37
3.6	GAS ADSORPTION SURFACE AREA ANALYSIS ACCORDING TO THE BET-THEORY.....	37
3.7	CYCLIC VOLTAMMETRY	39
4	RESULTS AND DISCUSSION	41

4.1 CONJUGATED MICROPOROUS POLYMER NANOPARTICLES WITH ENHANCED PHOTOCATALYTIC APPLICATIONS IN WATER	41
4.1.1 Motivation	41
4.1.2 Synthesis and characterization of CMP NPs.....	42
4.1.3 Photocatalytic activity of CMP NPs for photodegradation of Rhodamine B.....	54
4.1.4 The ability to generate reactive oxygen species.....	56
4.1.5 Photooxidation of TMPD.....	59
4.1.6 Conclusions and outlook.....	60
4.2 CONJUGATED MICROPOROUS POLYMER NANOPARTICLES AS VISIBLE LIGHT ANTIBACTERIAL PHOTOCATALYSTS VIA MOLECULAR DOPING	61
4.2.1 Motivation	61
4.2.2 Synthesis and characterization of CMP NPs.....	62
4.2.3 Photocatalytic antibacterial properties	73
4.2.4 The role of reactive oxygen species.....	76
4.2.5 Conclusions and outlook.....	80
4.3 VISIBLE LIGHT INDUCED PHOTOCATALYTIC RECYCLING OF NAD ⁺ COFACTOR BY CONJUGATED MICROPOROUS POLYMER NANOPARTICLES	81
4.3.1 Motivation	81
4.3.2 Synthesis and characterization	82
4.3.3 Photocatalytic properties for regeneration of NAD ⁺ cofactor.....	86
4.3.4 Conclusions and outlook.....	90
4.4 MOLECULAR ENGINEERING OF CONJUGATED POLY-BENZOTHIADIAZOLES FOR ENHANCED HYDROGEN PHOTOSYNTHESIS	91
4.4.1 Motivation	91
4.4.2 Synthesis and characterization	92
4.4.3 Photocatalytic properties for hydrogen photosynthesis	110
4.4.4 Conclusions and outlook.....	118
5 EXPERIMENTAL SECTION.....	119
5.1 CONJUGATED MICROPOROUS POLYMER NANOPARTICLES WITH ENHANCED PHOTOCATALYTIC APPLICATIONS IN WATER	119
5.1.1 Materials	119
5.1.2 Synthesis of B-FL ₃ -a, B-BPh ₃ -a and B-BT ₃ -a.....	119
5.1.3 Synthesis of B-FL ₃ -b, B-BPh ₃ -b and B-BT ₃ -b.....	120

5.1.4	Photodegradation of Rhodamine B	120
5.1.5	Photooxidation of TMPD.....	121
5.1.6	Photooxidation of furoic acid into 5-hydroxy-2(5H)-furanone in aqueous solution	121
5.1.7	Characterization.....	121
5.2	CONJUGATED MICROPOROUS POLYMER NANOPARTICLES AS VISIBLE LIGHT ANTIBACTERIAL PHOTOCATALYSTS VIA MOLECULAR DOPING	123
5.2.1	Materials	123
5.2.2	Synthesis of CMP NPs.....	123
5.2.3	Photocatalytic disinfection test.....	124
5.2.4	Photooxidation of α -terpinene	124
5.2.5	Characterization.....	125
5.3	VISIBLE LIGHT INDUCED PHOTOCATALYTIC RECYCLING OF NAD ⁺ COFACTOR BY CONJUGATED MICROPOROUS POLYMER NANOPARTICLES	127
5.3.1	Materials	127
5.3.2	Synthesis of B-BO ₃	127
5.3.3	Photocatalytic test for regeneration of NAD ⁺ cofactor.....	127
5.3.4	Biocompatibility of regenerated-NAD (rNAD).....	127
5.3.5	Characterization.....	128
5.4	MOLECULAR ENGINEERING OF CONJUGATED POLYBENZOTHIADIAZOLES FOR ENHANCED HYDROGEN PRODUCTION BY PHOTOSYNTHESIS.....	131
5.4.1	Materials	131
5.4.2	Synthesis of polybenzothiadiazoles	131
5.4.3	Photocatalytic activity test for hydrogen evolution.....	132
5.4.4	AQY measurement	132
5.4.5	Characterization.....	133
6	SUMMARY AND OUTLOOK.....	135
7	REFERENCES	137
8	LIST OF ACRONYMS.....	151
9	LIST OF FIGURES	155
10	LIST OF SCIENTIFIC CONTRIBUTIONS	163
11	ACKNOWLEDGEMENT	165



1 Introduction and Motivation

The sun as the star of the solar system is an enormous power reservoir which every day supplies the earth with an immense amount of energy.^[1] As the largest and most available renewable energy source, Nature in its wisdom has shown the great ability to use the energy from sunlight to drive chemical processes with photosynthesis as one of its best examples. Inspired by Nature, the earliest reports of the use of photochemistry dates back to Ancient Egypt and India,^[2] these ancient civilizations reported the application of plant extracts on skin with further exposure of the patient under the sunlight for the treatment of skin lesions.

From the ancient times to modern days, tremendous development has been seen in photochemistry with applications in a great variety of scientific fields, i.e.: medicine, optics, environment, electronics and energy. In the latest case, researchers have been devoting considerable efforts in the past decades in the field of photocatalysis, which consists of the initiation or the change in the rate of a chemical reaction in the presence of a photocatalyst under light radiation.^[3] Nowadays, in a world with growing concerns towards sustainable sources of energy and the impacts of industry on the environment, photocatalysis emerged as a promising field since sunlight offers a clean, inexpensive, abundant and sustainable alternative to perform countless chemical reactions.

Among a variety of photocatalytic systems, visible-light photocatalysis has received particular attention from researchers. This consists with the fact that close to 44% of the solar energy lies in the visible range, whereas nearly 3% rest in the UV part.^[4] A number of molecular systems with visible light active properties have been developed in the last years. Among them, inorganic or transition metal based complexes such as $\text{Ru}(\text{bpy})_3\text{Cl}_2$ and *fac*- $\text{Ir}(\text{ppy})_3$, porphyrin derivatives and organic dyes.^[5, 6] However, several drawbacks are associated to these systems, i.e. toxicity of metals, limited availability in nature, high cost and difficulties in purification steps in homogeneous systems.^[7] Therefore, taking into account the disadvantages mentioned above, it is mandatory to seek the development of a new class of photocatalyst with great stability and recyclability. In this regard, a pure organic and heterogeneous system is greatly beneficial.

As an emerging class of organic and heterogeneous materials, conjugated microporous polymers (CMPs) have recently attracted much attention as a metal-free

and visible light active photocatalyst with the combination of unique features like microporosity and π -conjugated backbones.^[8, 9] Recently, CMPs have demonstrated great applicability for heterogeneous photocatalytic reactions under irradiation of visible light.^[8-10]

Despite its promising performance, most of the CMPs are insoluble networks, which limit the range of processing options. Thus, the processability of CMPs has been highlighted as one of the most important targets in the field and especially for its use as heterogeneous photocatalysts to direct organic reactions.^[11-13]

Other than the choice of the catalyst material, another concern related to sustainable approaches to conduct chemical reactions lies on the type of solvent as reaction medium. Indeed, much effort has also been devoted to the use of “green” solvents, in particular water as a cheap and environmental friendly alternative for chemical transformations instead of hazardous halogenated solvents.^[11-14] Given the usually hydrophobic nature of the CMPs, it is highly challenging to employ this class of material in processes conducted in aqueous media. So far, only a few research reports have been described as steps towards the use of CMPs in aqueous media or the synthesis of water compatible CMPs for photocatalytic reactions under visible light.^[12, 13, 15]

Herein, the main objectives of this study rest in thoroughly investigate new approaches for the design of conjugated microporous polymers with the following two desired properties: (1) high solution processability and (2) applications as heterogeneous visible light photocatalysts in aqueous media.

This work is composed in separated chapters in order to facilitate comprehension. In chapter 2, fundamental aspects of photocatalysis, visible light photocatalysis, conjugated polymers and colloidal systems are laid out along with the current state of art of conjugated microporous polymers. Moreover, in chapter 3 the main characterization methods employed in this work are briefly described. The results acquired in this work are presented and thoroughly discussed in chapter 4 and experimental details can be found in chapter 5.

2 Theoretical Background

2.1 Photocatalysis

2.1.1 A brief history

Every day the earth is fuelled by light from the sun. The perception of light is one of the fundamental experiences of a living being and observation of the effects resulting from the interaction of light with matter is probably one of the prime realizations of mankind. From simple remark to active attempts to use the chemical properties derived from the combination with light radiation, early reports mentioned the practice of the so-called heliotherapy around 3000 BC in Ancient Egypt and India,^[2] which consisted in a form of phototherapy for the treatment of skin related disorders.

Although early attempts to use the energy of sunlight started several thousand years ago,^[16] the dawn of photochemistry as a science can be dated back to late nineteenth and early twentieth centuries when fundamental laws were established and first systematic investigations of photochemical reactions were performed by Bodenstein in photolysis and the work of Ciamician and Silber in organic photochemistry.^[17, 18] In a remarkable lecture in 1912, Giacomo Ciamician highlighted the potential of photochemistry for the future of the chemical industry.^[18-20]

The progress of the studies in photochemistry culminated with first appearance of the term *photocatalysis* around 1910.^[21, 22] Pioneering studies by Eibner reported the effect of the combination of light and ZnO on the bleaching of the dye Prussian blue.^[21] At the same time, investigations of the illumination effect on the degradation of oxalic acid in the presence of uranium salts were performed by Bruner & Kozak and Landau.^[21] From these early reports to modern days great progress has been observed in photocatalysis, which encompasses a better understanding of the phenomenon and also involves multidisciplinary fields of knowledge with new possibilities for the development of more sophisticated and efficient photocatalytic platforms for production of fine chemicals, pharmaceuticals and advanced materials.

2.1.2 Fundamentals

The term *catalysis*, introduced by the Swedish chemist Berzelius in 1835, consists of the process of the action of a *catalyst*.^[23] A catalyst is a substance which increases the

rate of a reaction without modifying the overall standard Gibbs energy change in the reaction. In this sense, a catalyst interacts with reagents by lowering the activation energy necessary for the reaction to take place and at the same time the catalyst itself does not undergo any chemical change, which can be recovered to be used in a new reaction cycle.^[3]

In the case of *photocatalysis*, the rate or initiation of a chemical reaction changes in the presence of a catalyst which absorbs energy in the form of light, a *photocatalyst*, which participate in the reaction without being consumed. According to the International Union of Pure and Applied Chemistry (IUPAC) a photocatalyst is defined as a “*catalyst able to produce, upon absorption of light, chemical transformations of the reaction partners. The excited state of the photocatalyst repeatedly interacts with the reaction partners forming reaction intermediates and regenerates itself after each cycle of such interactions*”.^[3]

Around 1817, Grotthuss and Draper formulated what is considered the first law of photochemistry, which stated that only absorbed light can be able to generate a photochemical effect.^[17] In semiconductors the light absorption ability depends on the energy levels of the band structure of the material and is mainly controlled by its band gap. Therefore, photons are absorbed by a photocatalyst only when the energy of the photons is equal or higher than the band gap energy of the semiconductor. The band gap determines the electronic transport properties of the photocatalyst and can be adjusted by band structure modifications.^[4, 24]

In a typical semiconductor photocatalytic system, electrons of the photocatalyst are excited from the valence band to the conduction band by the absorbed photon, an electron energy level transition occurs which leads to the formation of electron-hole pairs. Here, two distinct pathways are formed: the generated electron hole (h^+) which in contact with other molecules can be used for oxidation reactions and the excited electron (e^-) which can participate in reduction reactions (Figure 1).^[4, 21, 24, 25] Therefore, one of the advantages of a photocatalytic system lies in the ability to perform both oxidative and reductive cycles for distinct substrates. As a consequence, a great variety of reactions can be mediated via photoredox processes.

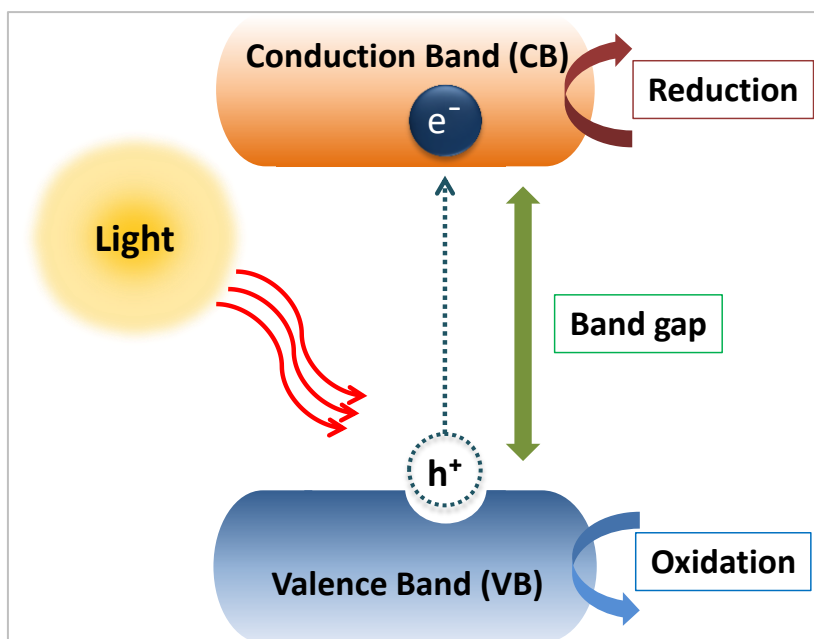


Figure 1. Schematic illustration of the formation of photogenerated electron-hole pairs upon absorption of light.

According to the absorption energy equation:

$$E = \frac{hc}{\lambda}$$

$h = 6.626 \times 10^{-34} \text{ J s}$ (Planck's constant)
 $c = 2.997 \times 10^8 \text{ m s}^{-1}$ (speed of light in vacuum)
 $\lambda = \text{light's wavelength}$

light with shorter wavelength exhibits higher energy values in contrast to light with longer wavelength. As a consequence, ultraviolet (UV) light active photocatalysts have attracted much attention from researchers and extensive work has been done in the past decades in the field of UV light photocatalysis.^[4, 26] Several materials like TiO_2 ,^[27, 28] ZrO_2 ,^[29] ZnO ,^[30] SrTiO_3 ,^[31] and KTaO_3 ^[32] have shown potential to be used in photocatalytic reactions.

Despite its advantages, certain drawbacks are also related to the use of UV light in photochemical reactions, i.e.: special lamps and photoreactors are generally a requirement which elevates costs, the high energy of UV photons can also result in chemical decomposition once weak bonds are present in the reaction and the UV region is not abundant in the solar radiation, comprising only about 4% of the solar spectra (Figure 2). Therefore, the aforementioned drawbacks have increased the interest of researchers towards the field of visible light active photocatalysis.^[18, 19]

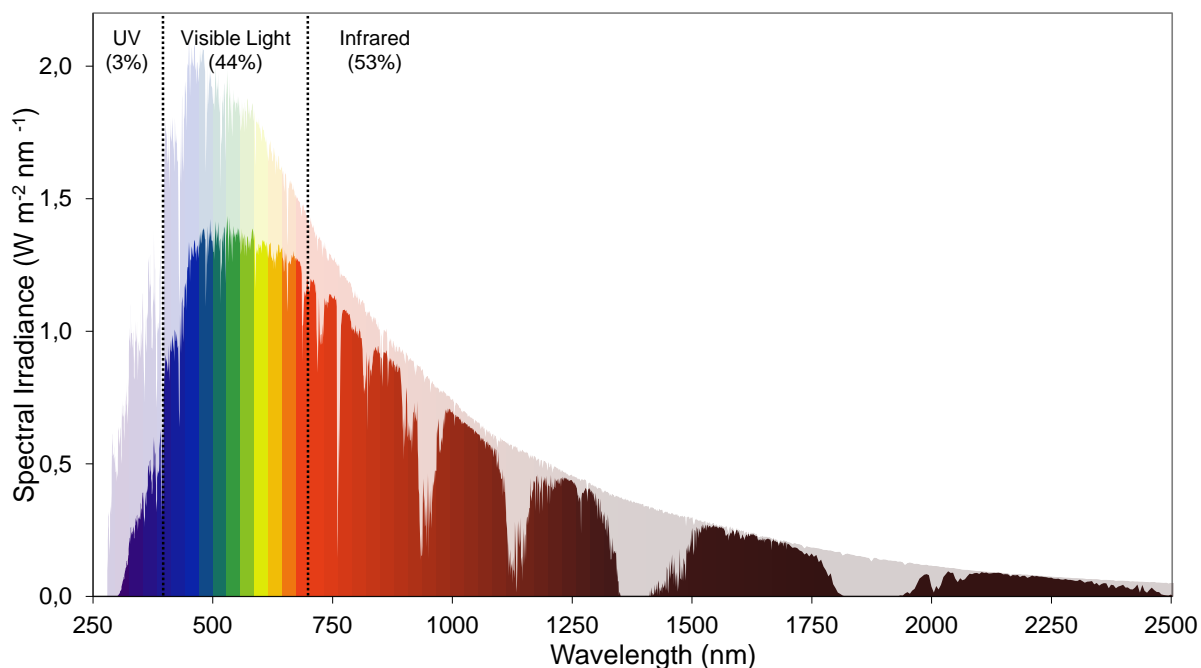


Figure 2. Solar spectrum adapted from ^[33].

2.2 Visible light photocatalysis

Visible light is a particular attractive approach to mediate organic transformations. Nearly 44% of the solar energy lies on the visible range, in contrast to UV irradiation (Figure 2). Moreover, systems that use light in the visible region are environmental friendly, have the advantage of minimizing side reactions and are cost effective, which is more appealing for large-scale production since it does not require special costly settings.^[18, 19]

One of the main challenges in the field of visible light photocatalysis consists in the inability of most organic molecules to absorb light in the visible range.^[18] However, in recent years a dramatic increase in interest has been seen in the field. Transition metal complexes, ^[6, 34, 35] organic dyes, ^[36, 37] carbon nitride, ^[38, 39] modified titania, ^[40] and metal-organic compounds^[41] have been intensively studied as visible light active platforms.

2.2.1 Homogeneous visible light photocatalysis

In homogeneous visible light photocatalysis, photocatalysts and reactants stand in the same phase. Transition metal complexes and organic dyes are some of the most

studied homogeneous photocatalysts with reactions being conducted under visible light in mild conditions.^[26]

A great amount of work has been done with the use of transition metal complexes, mostly with ruthenium and iridium (Figure 3).^[6, 18, 19, 34] These transition metals offer relative ease for ligand alteration and present high redox potentials in the excited state in comparison to other transition metals.^[5] Organometallic ruthenium polypyridine complexes, $\text{Ru}(\text{bpy})_3^{2+}$, are among the most well-studied transition metal based photocatalysts, it presents a broad absorbance in the visible range as a result of a metal-to-ligand charge transfer transition (MLCT) which generates long-lived excited states along with great chemical stability.^[18, 19, 26] Despite the advantages, certain drawbacks related to high costs of rare-earth metals, limited availability in Nature and toxicity of ruthenium and iridium salts are important barriers of these metal based methods.^[5]

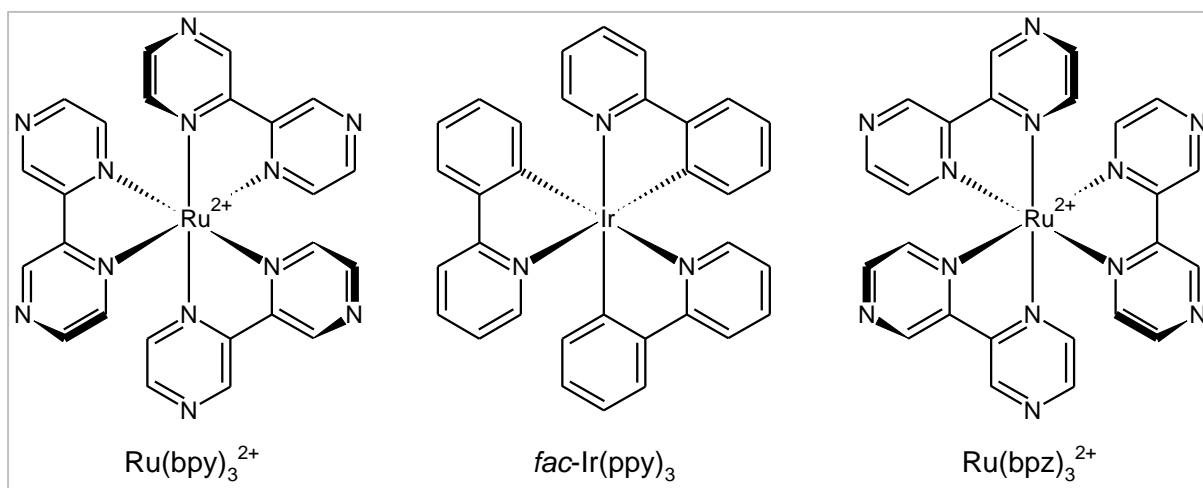


Figure 3. Ruthenium and iridium complexes.

Organic dyes have been subject to intensive research in numerous photochemical reactions.^[36, 42] Rose Bengal, Eosin Y, and Rhodamine B are some examples of organic dyes which have been widely employed in several visible light induced organic transformations with some of the results comparable to the efficiency of $\text{Ru}(\text{bpy})_3^{2+}$ (Figure 4).^[6, 37, 42, 43]

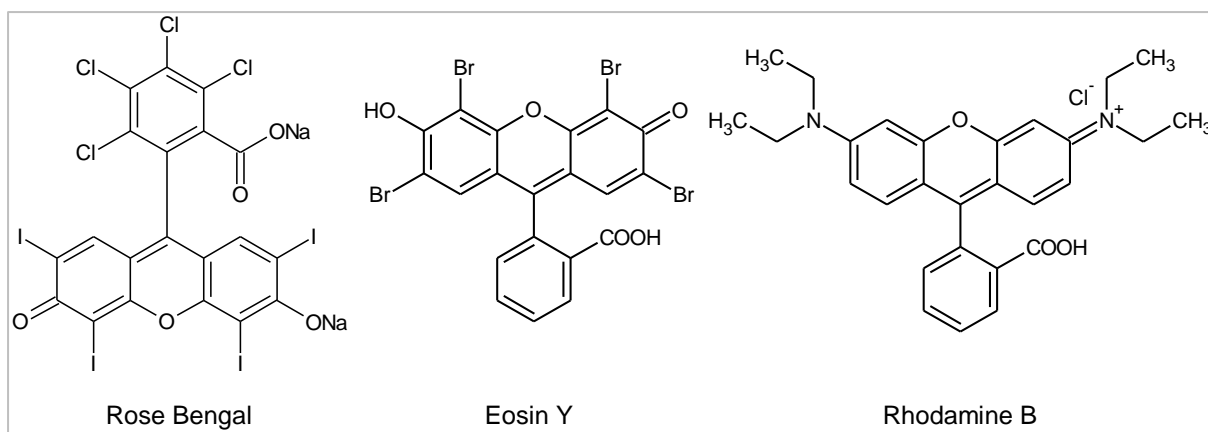


Figure 4. Some of the organic dyes employed in visible light photocatalysis.

Although excellent achievements have been reported, considerable disadvantages related to poor photostability, thermal instability, and difficulties in recovering processes are still major limitations of homogeneous photocatalytic systems.^[44, 45] Therefore, an alternative is strongly needed and for this purpose heterogeneous photocatalysts can offer a promising substitution to the traditional molecular systems.

2.2.2 Heterogeneous visible light photocatalysis

In heterogeneous visible light photocatalysis, the photocatalyst stands in a different phase from that of the reactants, which consists of a major advantage in comparison to homogeneous photocatalysts since separation, recovery and reutilization processes are simpler and cheaper.^[44, 45] Metal based, e.g.: metal sulphides,^[46] metal oxides complexes,^[4, 47] plasmonic-metal nanoparticles,^[48] novel photoelectric materials;^[41] and non-metal based, e.g.: organic semiconductors,^[39] have received great attention as potential heterogeneous photocatalysts under visible light.^[45]

2.2.2.1 Metal based visible light photocatalysts

Among the metal sulphides, CdS based materials have received great attention as efficient visible light active photocatalysts.^[4, 49] Studies have described the use of CdS to catalyse the oxidation of toluene to aldehydes^[4] and benzylamine derivatives to imines.^[45]

Several metal oxide based compounds have been reported bearing visible light active properties, such as complexes with Nb₂O₅,^[50] TiO₂^[47] and ZnO.^[51] Although its

broad band gap, Nb_2O_5 has been studied for visible-light photocatalytic selective oxidation of alcohols.^[50]

The widely known TiO_2 has been actively employed as a highly active photocatalyst.^[47] Although the broad band gap of the material has limited its application in visible-light photocatalysis, several attempts have been studied in modifying TiO_2 with Fe^{3+} , V^{4+} , Cr^{3+} , Sn^{4+} , dye-sensitization, metal and non-metal ion doping in order to extend the photoactivity to the visible range.^[52-54] Dye-sensitized $\text{TiO}_2/\text{TEMPO}$ ^[55] and dye/ ZnO/TEMPO ^[56] have been reported to be able to catalyse oxidation reactions of alcohols to aldehydes. Complexes of TiO_2 with ethylenediaminetetraacetic acid,^[57] *trans*-ferulic acid,^[58] or fullerol^[59] could undergo redox reactions under visible light. Anatase TiO_2 was reported to catalyse the oxidation of benzyl alcohols and derivatives under blue LED irradiation.^[60, 61]

Other oxide-based photocatalysts such as AgO_2 ,^[62] Bi_2MoO_6 ,^[63, 64] and BiVO_4 ^[65] have shown ability for methyl orange photodegradation, photocatalytic degradation of organic pollutants, and water splitting under visible light. In general, on one hand metal oxides hold the advantages of being relatively stable and inexpensive, but on the other hand this type of materials have restricted spectrum of substrates along with a limited range of visible light absorption.

Plasmonic metal nanoparticles have recently emerged with enhanced photocatalytic activity.^[48] In this case, once the plasmonic metal nanoparticle is irradiated by light with wavelength larger than the size of the particle, the charge density of the nanoparticle is redistributed. Once the overall particle charge density oscillation matches with the vibration frequency of the incident light, an effect called localized surface plasmon resonance (LSPR), it can lead to significantly enhanced light absorption.^[66, 67] However, due to poor stability and catalytic performance of single plasmon nanoparticles, this type of material is frequently associated to metal oxides like ZrO_2 ,^[68] Al_2O_3 , SiO_2 ,^[69] CeO_2 ,^[70] and TiO_2 .^[71] Gold plasmonic nanoparticles using CeO_2 ,^[72] rutile TiO_2 ,^[73] or ZrO_2 ,^[74] ZnO ^[75] as supporting platform has been applied to catalyse a variety of oxidation reactions.

Despite the versatility for catalysing organic transformations, the use of metal based visible light photocatalysts is greatly hindered by the limited availability and also for the cost of noble metals.^[26] Therefore, the aforementioned drawbacks have

prompted researchers with the urgent need to develop new non-metal based visible light active photocatalysts.

2.2.2.2 Non-metal based visible light photocatalysts

Polymeric graphitic carbon nitride (g-C₃N₄) has recently gained much attention as a metal-free visible light active photocatalyst.^[76] In special, the mesoporous form (mpg-C₃N₄) with medium range band gap and high structural stability has been employed in a wide range of oxidation reactions, ^[77, 78] C-C bond formation and synthesis of heterocyclic compounds under visible light and O₂.^[79] However, high temperature and high pressure levels consisted of requirements for certain reactions to take place, which can be regarded as drawbacks associated to the use of this material.^[26]

Taking into consideration the disadvantages mentioned above, the development of novel non-metal based visible light active photocatalysts which are active under mild reaction conditions is highly desirable. Very recently, conjugated polymers have received considerable appraisal within the scientific community as quite versatile materials. Extensive tunability of their physical and optical properties, the ease of application and economically viable techniques have motivated researchers to apply these materials in electronic applications^[80] and hold great potential to be used in photochemical reactions.

2.3 Conjugated Polymers

In chemistry, a conjugated system consists of a structure which presents connected π -orbitals with delocalized electrons.^[3] Based on this, conjugated polymers are organic macromolecules whose structure is characterized by a backbone of alternating single and multiple bonds with overlapping π -orbitals, which results in a system of delocalized electrons.^[81]

Early investigations about the electronic, optical and magnetic properties of conjugated polymers dated back to around 1960-1970s with the works from Weiss, Buvet and Jozefowicz on the properties of polypyrrole and polyaniline.^[82] In 1977, the work from Heeger, MacDiarmid and Shirakawa demonstrated that polyacetylene films treated with chlorine, bromine or iodine vapour resulted in a highly conductive “doped” material (Figure 5). This acclaimed work on the discovery and development of

conductive polymers was further recognized by the Nobel Prize award for chemistry in 2000.^[83]

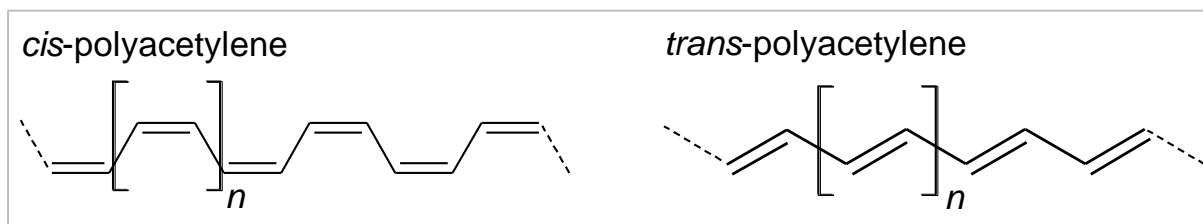


Figure 5. Structure of cis- and trans-polyacetylene.

In comparison to inorganic materials, which are more difficult to adjust the structure and properties at a molecular level, organic conjugated polymers are more accessible to tune their physicochemical properties.^[84] Owing to the π -conjugated backbone with delocalized electrons, the electronic and optical properties combined with the physical and processing versatility make the conjugated polymers especially attractive materials to be applied in the field of optoelectronics, e.g.: organic field-effect transistors (OFETs),^[85, 86] photovoltaic devices and organic solar cells (OSCs),^[87-89] sensors,^[90] optical and organic light emitting devices (OLEDs).^[91-93]

The remarkable light-harvesting and light-amplifying properties of conjugated polymers also prompted researchers in exploring this class of material for further applications in biology, chemistry and material science. In this regard, studies have described the use of water-soluble conjugated polymers as biological and chemical sensors, in fluorescence imaging, in gene and drug delivery systems.^[94, 95]

In the past decade, conjugated polymers have received particular interest in the field of visible light photocatalysis, since their semiconductor properties can be easily tuned by modifications of the band gap and band positions through an appropriate choice of the electron donor and acceptor moieties. Several materials such as polyaniline (PANI),^[96] P3HT,^[97, 98] PEDOT,^[99, 100] and polypyrrole (PPy)^[101] have been investigated as potential visible light active photocatalysts. However, most of the described materials consisted of polymer composites associated Au, TiO₂, ZnO, CdS, g-C₃N₄, and quantum dots (QD).^[101-103] Some studies have given attention to π -conjugated nanoparticles associated to porphyrin derivatives, which resulted in materials with the ability to generate *singlet* oxygen for further oxidative reactions. Composite systems of porphyrin with zirconium-phthalocyanine complexes and QDs were used in the

photodegradation of methyl orange and *singlet* oxygen generation under visible light.^[104, 105]

Lately, pure visible light active conjugated polymer photocatalysts have been developed, including poly(*p*-phenylene),^[106-108] poly(diphenylbutadiyne),^[109] planarized fluorine-type conjugated polymers^[110] and covalent organic frameworks (COFs).^[111, 112]

Polymers based on conjugated linear poly(*p*-phenylene) have shown potential to catalyse photoreduction of water to H₂^[107, 108] and also the reduction of carbonyl compound and olefins under visible light.^[106] Stable nanofibers of poly(diphenylbutadiyne) have shown ability for visible light degradation of pollutants.^[109] Very recently, a new planarized fluorine-type conjugated co-polymer of dibenzo[*b,d*]thiophene sulfone has shown enhanced hydrogen evolution performance in water under visible light (Figure 6).^[110] Hydrazone-based and azine-linked COFs have been employed for photocatalytic hydrogen evolution under visible light irradiation.^[111, 112]

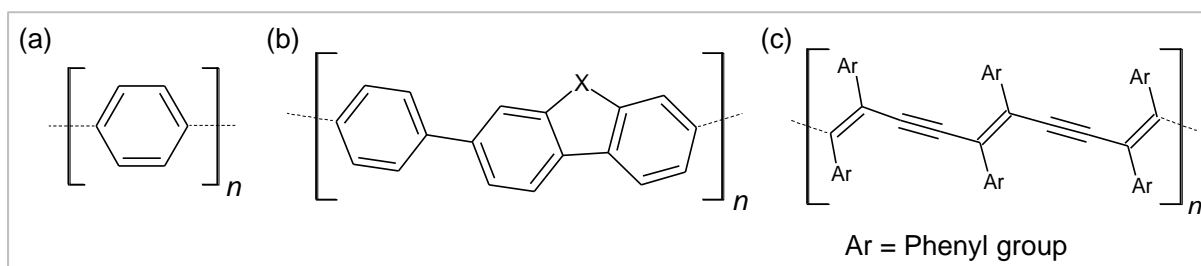


Figure 6. Molecular structures of some conjugated polymer materials investigated in visible light photocatalysis. (a) poly(*p*-phenylene), (b) planarized fluorine-type analogue and (c) poly(diphenylbutadiyne).

Apart from the aforementioned photoactive systems, another promising emerging class of conjugated polymer material has been receiving great attention for its use in heterogeneous photocatalysis under irradiation of visible light, the Conjugated Microporous Polymers (CMPs).

2.3.1 Conjugated Microporous Polymers

Conjugated microporous polymers (CMPs) were first developed by Cooper in 2007 and they consist of a class of amorphous materials which allows the linking of building blocks in a three-dimensional (3D) π -conjugated network.^[113] This structural arrangement features a unique combination of microporosity and π -conjugated backbones, which otherwise is not usually found in other materials, e.g.: porous

materials are typically not π -conjugated and conventional conjugated polymers are not porous.^[114]

The high surface area and microporosity provide an open space for guest molecules while enhancing reactivity and light harvesting properties.^[115] At the same time, one of the main features of CMPs is the diversity of π -units. The versatility in terms of size, geometry and functional groups allows a broad range of building blocks to be exploited for the synthesis of CMPs while tuning the architecture and electronic properties at a molecular level.^[8, 9] Furthermore, an extensive collection of different reaction types is available for the synthesis of this class of material.

2.3.1.1 Synthetic reaction routes

Several chemical reactions can be employed for the synthesis of CMPs, e.g. Friedel-Crafts reaction,^[116] Suzuki-Miyaura cross-coupling reaction,^[117, 118] Sonogashira-Hagihara coupling reaction,^[114] Yamamoto reaction,^[119, 120] oxidative coupling reaction,^[121, 122] phenazine ring fusion reaction,^[9] cyano cyclotrimerization,^[123] and Schiff-base reaction.^[124] In this work, the focus will be addressed to Suzuki-Miyaura and Sonogashira-Hagihara coupling reactions.

2.3.1.2 Suzuki-Miyaura coupling

As one of the most widely exploited transition metal catalysed C-C bond formation reaction, Suzuki-Miyaura cross-coupling was developed by Akira Suzuki and Norio Miyaura at Hokkaido University in 1979.^[125, 126] In this reaction a carbon-carbon single bond is formed by coupling an organoboron compound with an organic halide or sulfonate using palladium as catalyst and a base (Figure 7).^[127]

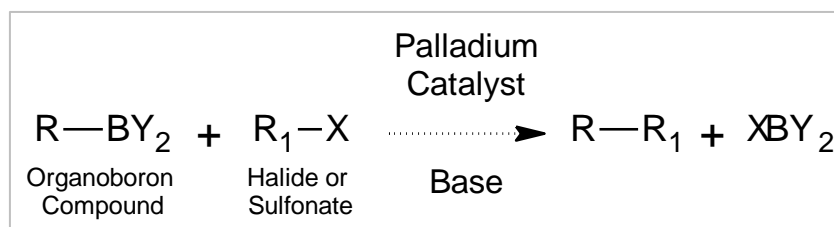


Figure 7. General scheme of the Suzuki-Miyaura cross-coupling reaction.

The mechanism of the Suzuki-Miyaura coupling reaction is generally described as starting with the oxidative addition of the organic halide or sulfonate to the palladium to form organopalladium species. After that, a reaction with the base promotes a ligand

substitution, which subsequently undergoes transmetalation with the organoboron complex originated from the activation of organoboron compound with the base. Finally, a reductive elimination takes place to form the new C-C bond and further regeneration of the palladium catalyst for another catalytic cycle (Figure 8).^[127, 128]

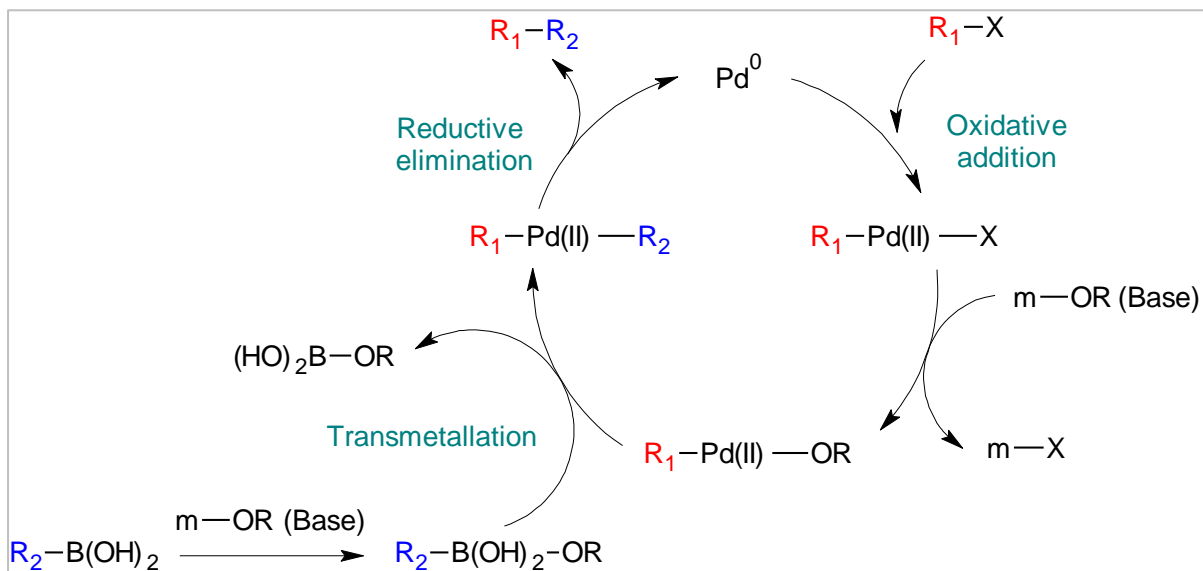


Figure 8. Suzuki-Miyaura cross-coupling reaction mechanism. Adapted from ^[127, 129].

Since its initial reports in 1979, series of developments in the Suzuki-Miyaura coupling have occurred that contributed to the up-scaling and cost-effective use of the reaction, such as: expansion of substrate scope, reaction at lower temperatures and reduction in catalyst loading. Nowadays, the Suzuki-Miyaura coupling is broadly applied in a great variety of fields from fine chemical, pharmaceutical, agrochemical to modern material industries.^[127, 129] The large scope of application of Suzuki-Miyaura coupling can be attributed to several advantages like mild reaction conditions, availability, and lower toxicity of organoboron reagents, stability, and wide range of functional groups compatibility.^[8, 129]

2.3.1.3 Sonogashira coupling

The Sonogashira-Hagihara cross-coupling consists of a reaction for C-C bond formation by coupling a terminal alkyne with aryl or vinyl halide using palladium as catalyst, a copper(I)-salt as co-catalyst and an amine base (Figure 9).^[127] This cross-coupling reaction was first reported by Sonogashira, Tohda and Hagihara in 1975, when they described that reactions of acetylene gas or the terminal alkynes with aryl or alkenyl halides could be performed at mild conditions and improved by using copper(I)-

salts as co-catalysts. In this case, the combination of the palladium catalyst with copper(I)-salts and amine base leads to the formation of alkynylcopper complexes which are important intermediates in the transmetalation process.^[130]

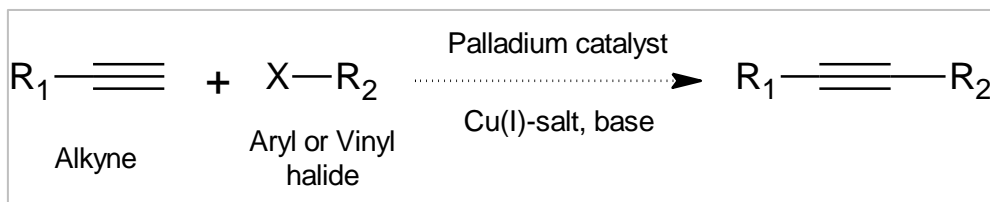


Figure 9. General scheme of the Sonogashira-Hagihara cross-coupling reaction.

The mechanism of the Sonogashira-Hagihara coupling reaction is generally believed to follow two independent catalytic cycles, the “palladium” and the “copper” cycles (Figure 10). While the “palladium” cycle is similar to other C-C coupling reactions, the “copper” cycle is less understood.^[131, 132]

First, the reaction starts with the palladium active species Pd(0)-species which can be stabilized by ligands, Pd(0)L₂, including the base or solvent. Oxidative addition of aryl or vinyl halide to Pd(0)L₂ takes place and the formed palladium complex undergoes transmetalation with the copper acetylide generated in the “copper” cycle. Finally, after *cis/trans*-isomerization a reductive elimination leads to the final formation of the new alkyne and further regeneration of the palladium catalyst. In the “copper” cycle it is suggested that the presence of the base assists the π-alkyne copper complex by making the terminal proton on the alkyne more acidic, which leads to the formation of the copper acetylide complex (Figure 10).^[131]

The Sonogashira-Hagihara coupling comprises the advantages of technical simplicity and functional group compatibility. At the same time, products can be obtained in high yields under mild reaction conditions, being largely employed in a great variety of fields, such as dyes, electronics, sensors, polymers, natural products, guest-host constructs and pharmaceuticals.^[127, 131]

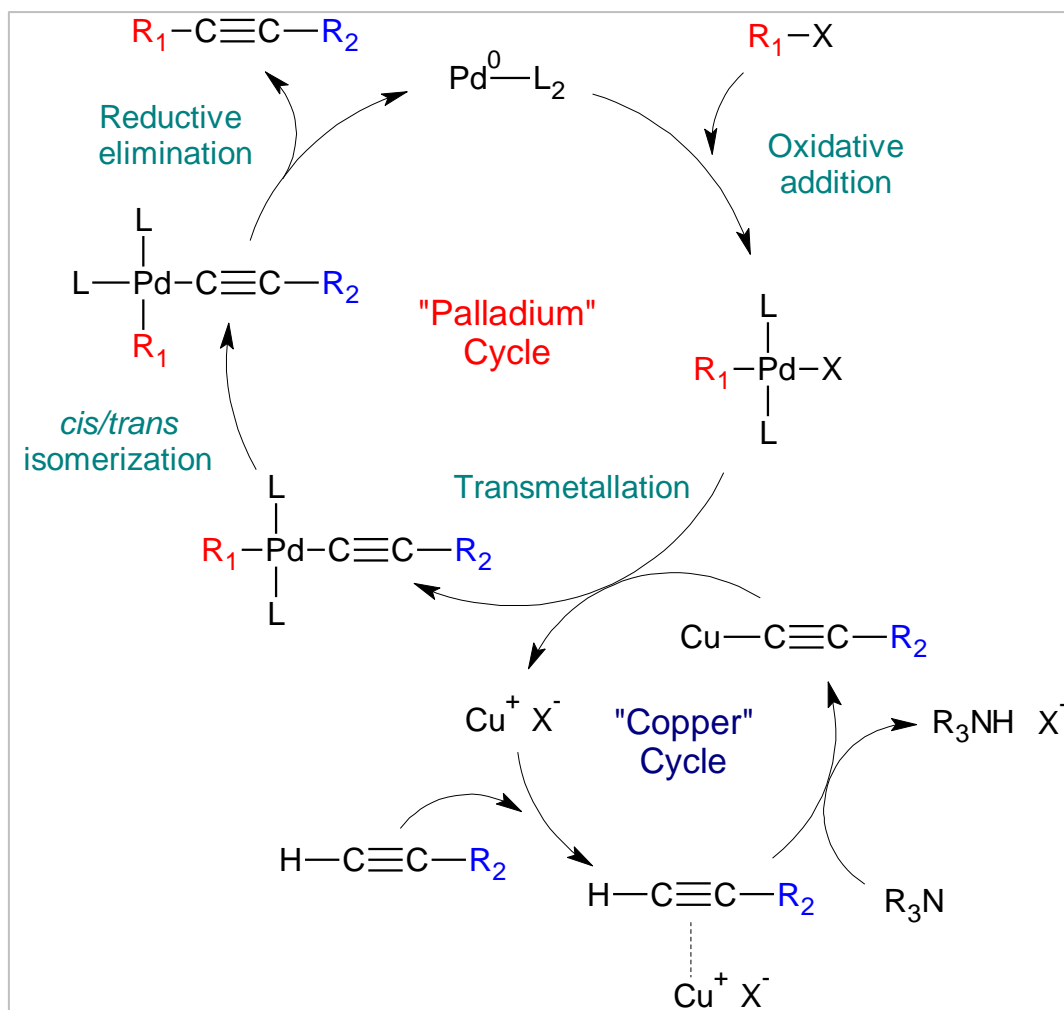


Figure 10. Sonogashira-Hagihara cross-coupling reaction mechanism. Adapted from ^[133].

2.3.1.4 Applications

In the past decade, a tremendous growth in interest has been devoted to Conjugated Microporous Polymers with the development of materials for a broad range of potential applications. CMPs have been widely explored in the field of gas adsorption and storage,^[133, 134] encapsulations of dyes and solvents,^[135, 136] light emission,^[137, 138] chemosensors,^[139, 140] energy storage^[141] and most recently in heterogeneous visible light photocatalysis.^[10, 142]

First examples of the use of CMPs in heterogeneous catalytic systems consisted in association with metalloporphyrin units as active sites, which was able to catalyse the oxidation of sulphides.^[143, 144] Later, metallo-organic and metal-associated CMPs were further developed, a metallophthalocyanine-based CMP have been reported to generate *singlet* oxygen^[145] and CMP associated with Ir, Pt, Pd and Ti with catalytic activity for

reductive amination,^[146] oxidation of methane,^[147] photocatalytic Suzuki coupling,^[148] and asymmetric diethylzinc addition to aldehydes.^[149]

Dye associated CMPs were also investigated for visible light photocatalysis. CMP with rose bengal have shown ability for aza-Henry reactions.^[150] A free base porphyrin linked CMP have been used for Knoevenagel condensation.^[151] A BODIPY linked CMP was able to photocatalyse the oxidation of thioanisole.^[152]

Visible light active photocatalysts based on pure CMPs were first reported around 2012 and 2013. A DMAP-based CMP with pyridine units has demonstrated catalytic activity in the acylation of alcohols.^[153] A benzothiadiazole based CMP showed high performance for *singlet* oxygen generation and oxidation of α -terpinene,^[10] the same reaction was conducted with π -conjugated polyHIPES.^[154] A CMP of benzodifuran moieties has been applied for photocatalytic coupling of primary amines.^[155]

More recently, a series of CMPs from phenylene and pyrene building blocks were used for H₂ evolution under visible light in the presence of sacrificial agents.^[156] Furthermore, apart from the aforementioned chemical transformations, an even broader range of photocatalytic reactions have been demonstrated using pure CMPs as heterogeneous visible light photocatalysts mainly in our research group, such as oxidation of amines,^[157, 158] dehydrogenation of nitrogen heterocycles,^[158] photodegradation of organic pollutants,^[13] reductive dehalogenation reactions,^[159] bromination reaction^[142] and oxidation of sulphides.^[158, 160]

Despite the advantages mentioned above, one of the main drawbacks of CMPs lies on its high hydrophobicity, which restricts the scope of applications due to limited processability options. Therefore, the processability of CMPs is considered as one of the most important targets in the field.^[11, 12] However, few research reports have described the use of CMPs in aqueous media or the synthesis of water compatible CMPs for photocatalytic reactions under visible light. Modifications of pristine CMPs have been employed as strategies to enhance the water compatibility of the polymer networks,^[12, 13] and more recently emulsion techniques.^[148]

2.4 Colloidal systems

A colloid consists of a heterogeneous system of at least two-phases, the dispersed phase finely distributed in the continuous phase. Either or both phases can be a gas, liquid, solid or even supercritical phase. In the case of simple colloids, consisted of two

phases, the system is characterized according to the physical state of both phases. There is a variety of types of colloidal systems and familiar examples can be found in daily life (Table 1). According to the classical definition, the size of colloidal species ranges from 1 to 1000 nm. However, in practical considerations the size can be extended from a few nanometres to several micrometres.^[161, 162]

Table 1. Some types of colloidal systems.

Dispersed Phase	Continuous Phase	Type	Example
Liquid	Gas	Liquid aerosol	Fog, hair sprays
Solid	Gas	Solid aerosol	Industrial smoke
Gas	Liquid	Foam	Whipped cream
Liquid	Liquid	Emulsion	Milk, mayonnaise
Solid	Liquid	Sol	Paints
Gas	Solid	Solid foam	Expanded plastics
Liquid	Solid	Solid emulsion, gel	Jelly, agar
Solid	Solid	Solid suspension	Pearl, stained glass

2.4.1 Emulsions

In polymer science, a great interest has been arisen to the use of emulsion techniques for the preparation, synthesis and application of polymer dispersions. This attention can be largely related to the urge in replacing organic solvents in polymer reactions for safer and environmentally friendlier solvents, like water.^[163]

Emulsions are colloidal systems composed of two immiscible liquids in which one liquid is dispersed in another continuous liquid. The dispersed phase can also be called the inner or internal phase, while the continuous phase is also denominated as the external or outer phase.^[161, 164] The most common emulsions consist of one of the

liquids being aqueous while the counterpart is a liquid that is not soluble in water, customary referred to as oil. In a simple colloid, two kinds of emulsions can be recognized according to the constitution of the continuous phase, the water-in-oil emulsions (W/O) in which water droplets are dispersed in oil as continuous phase, and the oil-in-water (O/W) emulsion when oil droplets are dispersed in water.^[161, 164]

Overall, most emulsions are not thermodynamically stable and usually require an emulsifying agent, in general surfactants, which can help in the formation of the emulsion and stabilize it for longer periods of time. In general, emulsions can be classified into three types according to their stability and droplet size: macroemulsions, microemulsions and in special, miniemulsions.^[163-165]

Macroemulsions are usually thermodynamically unstable systems and do not form spontaneously. An energy input is generally a requirement for the formation of macroemulsions, which can be given by mechanical agitation using devices like homogenizers, stirrers or ultrasonic transducers. Macroemulsions have relatively large droplet sizes of around 1 μm to 100 μm . Phase separation usually occurs within different time periods therefore emulsifiers like surfactants are usually needed for stabilization and to decrease the rate of coalescence of the dispersed droplets (IUPAC).^[164, 166]

Microemulsions are thermodynamically stable systems which form spontaneously therefore high mechanical agitation is generally not needed. The usual composition consists of a dispersion of water, oil and surfactant, sometimes a co-surfactant maybe needed. The droplet sizes ranges from 1 nm to 100 nm and the proportion of surfactant needed is usually significant.^[164, 166]

2.4.1.1 Miniemulsions

Miniemulsions are stable systems which consist of narrowly distributed droplets in a continuous phase. In this case, the droplet size lies usually between 50 nm to 500 nm and is obtained by applying high shear forces, like ultrasonication or high pressure homogenizers.^[163, 165-167]

The miniemulsion process is a versatile technique for the preparation of organic or inorganic nanoparticles. The main advantage lies in the concept that each droplet functions as an individual nanoreactor, where a great variety of polymerization methods can take place. In direct (oil-in-water) or indirect (water-in-oil) miniemulsions,

a combination of water, oil, surfactant and a co-stabilizer which builds up an osmotic pressure secures the stability of the system (Figure 11).^[163, 165, 168]

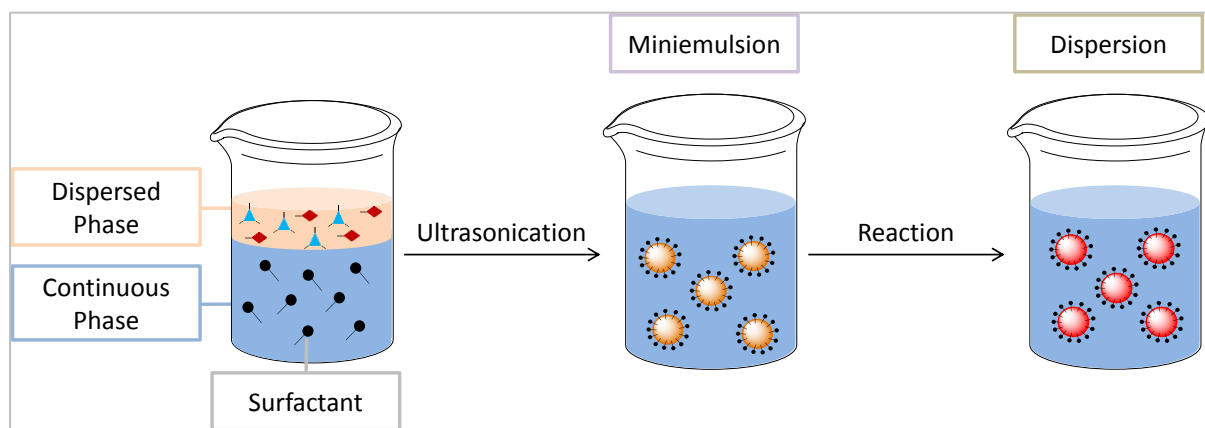


Figure 11. Schematic illustration of the formation of nanoparticles by the miniemulsion process.

2.4.1.2 Stability

The stability of an emulsion is determined by the balance between the repulsive and attractive forces in the system and it should be secured against two mechanisms: Oswald ripening and coalescence.^[162, 163, 165]

In the case of Oswald ripening, the instability happens due to the difference in the Laplace pressure between droplets of different sizes. In this process, larger droplets tend to grow in size as a result of molecular diffusion from the smaller ones (Figure 12b).^[162] Therefore, the process of Oswald ripening is governed by the size, polydispersity and solubility of the dispersed phase in the continuous phase, and it can be prevented by the addition of small amounts of an appropriate agent, called an osmotic pressure agent, which should be highly insoluble in the continuous phase.^[163, 165]

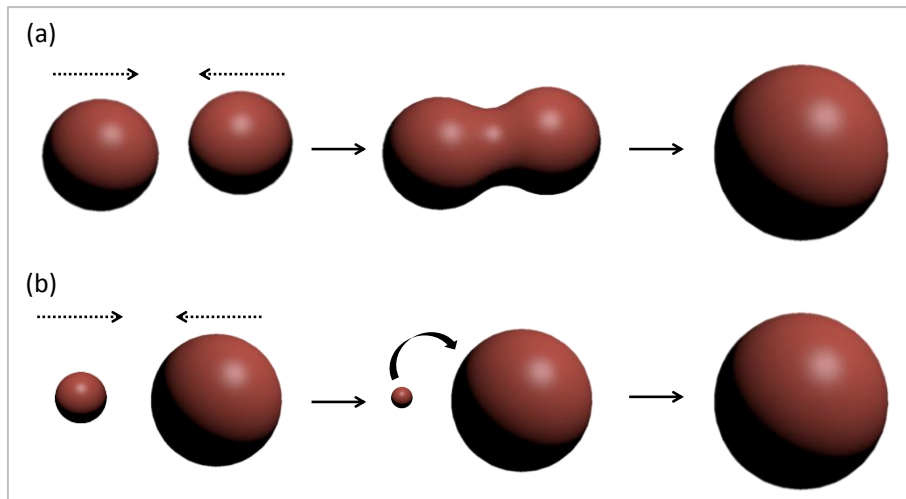


Figure 12. Schematic illustration of (a) coalescence and (b) Oswald ripening.

Coalescence consists in a collision process that leads to the fusion of two or more droplets into a single larger one (Figure 12a).^[161, 162] Contacts between dispersed droplets can occur due to Brownian motion or simple stirring, and the stability of the system depends on the interaction of the droplets when this happens.^[161] In this sense, stabilization of miniemulsion against coalescence can be achieved with the addition of appropriate surfactant, which can provide a steric or an electrostatic shield to the droplets.^[163, 165]

Steric stabilization of emulsions can be achieved by the adsorption of non-ionic surfactant or polymer layer at the surface of dispersed droplets.^[161] In this case, the adsorbed molecules while staying in attachment to the surface of the dispersed phase also present an outward extension with affinity for the continuous phase, which act as a steric hindrance to the droplets in getting to close vicinity in the range of attractive forces. An effective steric stabilization can be achieved for macroemulsions once the droplet surface is completely covered by the adsorbed surfactant or polymer, uncovered regions may cause contact between droplets and subsequent flocculation.^[161, 169] In the case of miniemulsions, the coverage of the nanodroplets can be far below complete.

Electrostatic stabilization is based on coulomb repulsive forces created by the interaction of equally charged surfaces, and in an emulsion system it can be achieved with the use of ionic surfactants or stabilizers.^[169] The combination of electrostatic repulsion with attraction forces like van der Waals forms the basis of the Deryaguin-Landau and Verwey-Overbeek (DLVO) theory for colloid stability.^[161, 169]

According to the DLVO theory, it is possible to calculate the potential energy of interaction between two particles (G_T) by estimating the sum of the potential energy values of repulsion (G_R) and attraction (G_A) at an interparticle distance:

$$G_T = G_R + G_A$$

An illustration of the energy variation of G_T , G_R and G_A is given in Figure 13. The primary minimum (G_{primary}) represents the overall energy in which coagulation occurs. For colloid stability, the energy barrier (G_M) should have a value that is high enough to prevent the particles to undergo irreversible coagulation into the primary minimum, as a consequence of high G_A forces at very short distances. The higher the G_M value, the lower is the probability of coagulation. In certain cases, a secondary minimum ($G_{\text{secondary}}$) energy condition exists at long distances, where the a weak aggregation of particles is usually reversible.^[169, 170]

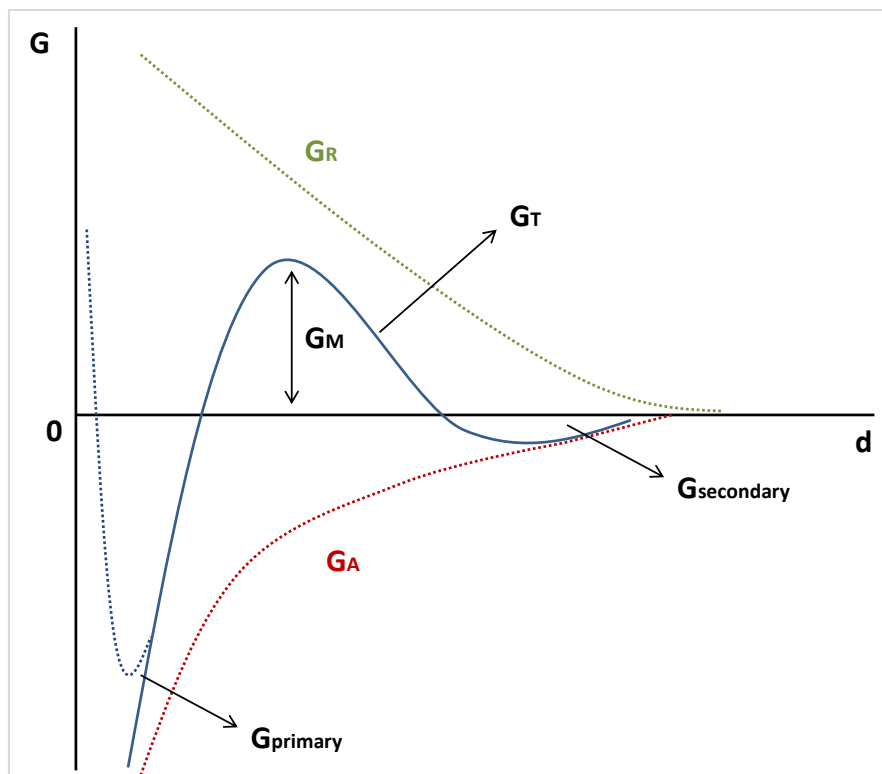


Figure 13. Illustration of the interaction potential between two particles as a function of distance according to the DLVO theory. Adapted from Napper^[170]

3 Characterization Techniques

In the following chapter the characterization techniques employed in this work are briefly described. Experimental details on each technique see Experimental Section 5.

3.1 Transmission Electron Microscopy

The transmission electron microscopy (TEM) consists of a technique which is capable of generating images with resolution close to a few Ångström. This is only possible due to the use of a beam of electrons whose short wavelength allows the formation of high resolution images.^[171]

In a transmission electron microscope, an electron gun connected to a high voltage source, between 200 kV to 400 kV, generates and accelerates electrons forming a focused beam. The electron beam is then transmitted through a very thin sample, interacting with the material while passes through it. From this interaction, several signals like scattered electrons can be generated and detected in different types of transmission electron microscopes with further interpretation and formation of an image.^[171] The TEM imaging is a relevant technique which allows the analysis of the shape and internal organization of nanostructures, and it was further employed for this purpose in this work.

3.2 Scanning Electron Microscopy

The scanning electron microscope makes it possible to observe the surface of organic and inorganic materials from a few nanometres to micrometres scale. In general, in a SEM the electron gun generates and accelerates electrons to an energy range between 0.1 keV to 30 keV, forming a focused beam of electrons which will scan the surface of the sample in a regular pattern.^[172]

Once the electrons interact with the surface of the sample material, several types of signals are generated, such as back-scattered or secondary electrons emitted due to excitation by the electron beam. Those signals are then collected by a detector system which converts the signals in accordance to different intensities and creates a final image.^[172] The scanning electron microscopy (SEM) imaging is an important technique which allowed the analysis of the topography of polymeric and nanostructures further presented in this work.

3.3 Ultraviolet-Visible Spectroscopy and Fluorescence Spectroscopy

The analysis of the interaction of light with matter can be conducted with ultraviolet-visible spectroscopy (UV-vis) and fluorescence spectroscopy. The UV-vis absorption spectroscopy is a technique which allows the measurement of the range of light absorption by a sample material in the ultraviolet and visible regions. In a UV-vis spectrometer, the measuring light is first dispersed into defined wavelengths by a prism or a monochromator, and then a detector measures the relative change of the transmitted light passing through a sample.^[173]

Instead of light absorption, the fluorescence spectroscopy enables the measurement of the scope of emitted radiation by a sample material after being excited by light. In a fluorescence spectrometer, the excitation light is also dispersed by a monochromator. Once light of defined wavelength passes through the sample part of it is absorbed, an electronic excited state is created which can fall back to its original ground electronic state by emitting energy in the form of light, the fluorescence. The intensity of the fluorescence is then collected by a detector usually placed at different angles to the incident light in order to lower the risk of transmitted or reflected incident light being also collected by the detector.^[174]

Further in this work, UV-vis absorption and fluorescence spectroscopy were used to determine the absorption and emission ranges of the designed CMPs and also for the calculation of optical energetic band gaps.

3.4 Fourier Transform Infrared Spectroscopy

The Fourier Transform Infrared Spectroscopy (FTIR) is based on the absorption radiation in the infrared frequency range between 2.5 to 25 μm by vibrations bonds within the molecules of a sample. A molecule is only able to absorb infrared radiation from the same energy frequency of its modes of vibration, which is characteristic for a specific binding. Therefore, when an infrared radiation passes through a sample, part of the incident radiation is absorbed at a specific energy, which corresponds to the frequency of the vibration mode of a particular bond formation within the molecule of the sample material.^[175, 176]

FTIR spectroscopy consists of an important analytical method for the detection of specific functional groups in a molecule and it was used as one of the main characterization techniques for the synthesized compounds in this work.

3.5 Electron Paramagnetic Resonance

Electron Paramagnetic Resonance (EPR) spectroscopy is a method which allows the study of materials with unpaired electrons and it has been applied to the detection and identification of reactive free radicals of higher energy. The basic concept of EPR is rather similar to the nuclear magnetic resonance (NMR), but it is focus on electron spin behaviour rather than the nuclear spin.^[177]

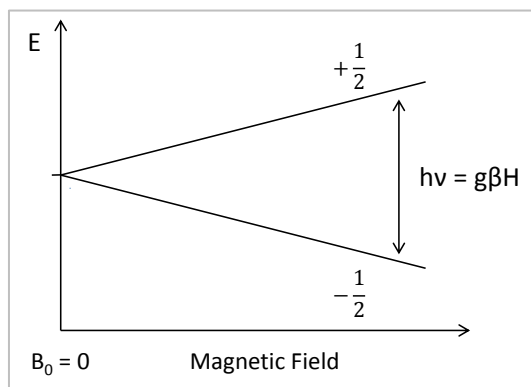


Figure 14. Schematic illustration of the splitting of the energy levels of an electron spin under the influence of an applied magnetic field.

In EPR the sample material is usually placed under strong magnetic field, in which the unpaired electrons are then separated into two groups: one group of spins with parallel orientation with decrease in electron energy and a second group with antiparallel orientation with increase in electron energy (Figure 14). Therefore, when the sample is exposed under electromagnetic radiation of the same frequency to the difference between the electronic levels of the groups, the resonance frequency, the unpaired electrons can move between the energy levels by absorbing or emitting electromagnetic energy, which is detected as an EPR signal.^[177, 178]

Further in this work, the EPR technique was used for the determination of radicals generated during the photocatalytic process. Using specific radical spin trapping technique, different radical intermediates during the reaction were detected and investigated.

3.6 Gas Adsorption Surface Area Analysis according to the BET-Theory

In 1938, Brunauer, Emmett, and Teller (BET) postulated a theory for multilayer adsorption, which serves as the basis for physical gas adsorption technique that provides an analysis of the surface area and pore size characterization of porous materials. This method allows the assessment of a wide range of pore sizes from

micropores (width less than 2 nm), mesopores (width between 2 nm and 50 nm) to macropores (width greater than 50 nm).^[179]

The gas adsorption behaviour is distinct between macropores, mesopores, and micropores. Macropores are wide enough that their adsorption behaviour can be comparable to flat surfaces. In mesopores, the interaction between gas molecules and pore wall as well as the attractive interaction between the molecules themselves play important roles in the adsorption behaviour. In contrast, the adsorption behaviour in micropores is essentially dominated by the interactions between the gas molecules and the pore walls.^[179]

A classification of six adsorption isotherms from IUPAC serves as guidance for the analysis of porous materials.^[180]

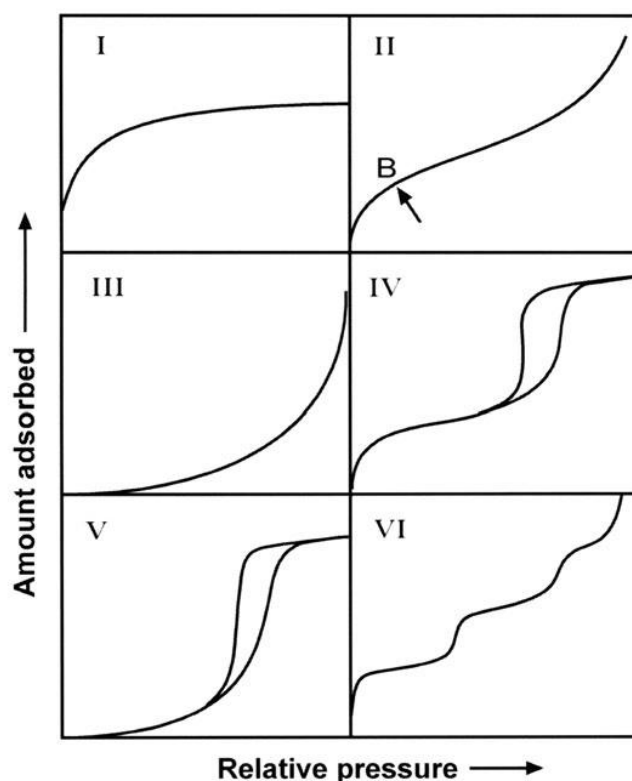


Figure 15. Classification of adsorption isotherms. Adapted from ^[180].

Type I isotherms are often obtained for microporous materials when gas adsorption is restricted to a few molecular layers. Type II consists of non-porous or macroporous materials, an inflection point called point B indicates a step when monolayer coverage is complete and multilayer adsorption starts. Type III shows an increase of the isotherm at higher relative pressures, which is an indication of weak adsorbate-adsorbent interactions. Type IV isotherms are characteristic for mesoporous

materials which shows a hysteresis loop. Type V isotherms also show a hysteresis loop but its initial part is an indication of weak interactions between adsorbent and adsorbate. Type VI isotherms show the gradual formation of multilayer adsorption on a uniform non-porous surface.^[179, 180]

In this work, the BET gas adsorption was used as one of the main characterization techniques for the analysis and comparison of the surface area and pore size distribution of the synthesized porous materials.

3.7 Cyclic Voltammetry

Cyclic voltammetry (CV) is an electrochemical technique which is widely applied for the study of redox processes in electroactive species. The principle of the CV consists in applying a periodic potential that may alternately oxidize and reduce the sample material by withdrawal and addition of electrons.^[181]

A standard CV setup employs an electrochemical cell with three electrodes, which is also referred to as a three-electrode setup (Figure 16): a working electrode, a reference electrode and a counter electrode, all the electrodes are immersed in a solution and connected to a potentiostat. An electrolyte is commonly added to the solution to ensure sufficient conductivity. Commonly used working electrode is made of glassy carbon, gold or platinum. Reference electrode is usually based on aqueous Ag/AgCl or saturated calomel, and a platinum electrode is used as counter electrode.^[181, 182]

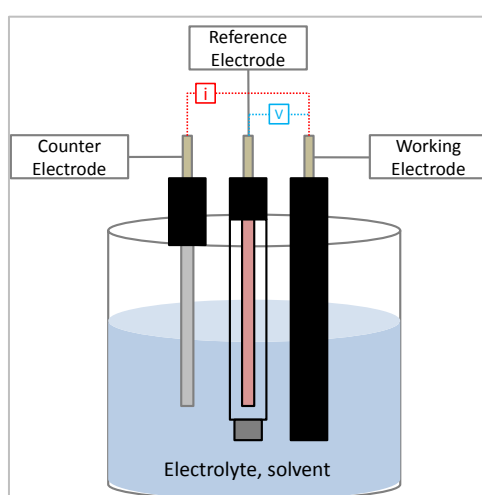


Figure 16. Schematic illustration of a three-electrode configuration of an electrochemical cell for cyclic voltammetry.

In a typical CV measurement, a periodic potential is applied between the working and the reference electrode, while the current between the working and the counter electrode is measured. The counter electrode acts as a compensation element in order to control and maintain the potential between the working and the reference electrodes. The sample material to be analysed undergoes oxidation and reduction at the working electrode, which will then be recorded and plotted in a cyclic voltammogram.^[181, 182]

Further in this work, the CV technique was mainly employed to study the energy band levels of the CMPs and also to determine the valence band (VB) and the conduction band (CB) positions.

4 Results and Discussion

4.1 Conjugated microporous polymer nanoparticles with enhanced photocatalytic applications in water*

In the following chapter, an enhanced processability design of the conjugated microporous polymer nanoparticles (CMP NPs) is presented. The CMPs were synthesized as well-dispersible and highly stable nanoparticles for efficient metal-free visible light photocatalysis. The CMP NPs combine two important features: high porosity and a nanostructured system. By incorporating different electron donor and acceptor moieties the shape of the nanoparticles can be controlled with their morphologies ranging from nanospheres via nanorods to nanorings. High photocatalytic activity, stability and reusability of the materials are also demonstrated in the reductive activation of molecular oxygen and photooxidation of amines under irradiation of a household energy saving light bulb.

4.1.1 Motivation

Recently, researchers have been developing a vast number of visible light-driven systems involving photo-redox processes in order to mimic the nature's process to use visible light energy to promote chemical reactions.^[34, 183-187] Beside the well-developed transition metal-based complexes,^[188, 189] metal-free and organic dyes have also been successfully employed as non-metal photo-redox catalysts in the last two decades.^[43, 190-192] However, a number of disadvantages associated with these homogeneous catalytic systems still affect its long-term usage. For instance, they are either highly expensive, toxic, and with limited availability in nature; or suffer from solvolytic attack in the reaction medium, which can hinder the recycling ability of the catalyst. Therefore, it is beneficial to develop a new class of organic heterogeneous photocatalyst with high stability and reusability.

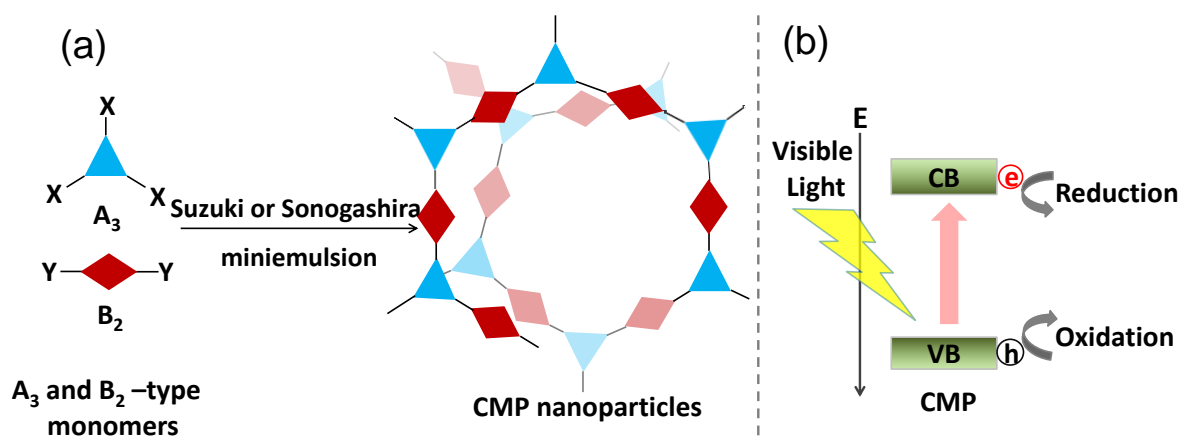
In this chapter, two different heterogeneous photocatalytic model systems, (i) nanometer-sized system and (ii) porous materials are investigated. Nanoparticles (NPs)

* This chapter is based on the publication "Conjugated microporous polymer nanoparticles with enhanced dispersibility and water compatibility for photocatalytic applications" by Beatriz Chiyin Ma, Saman Ghasimi, Katharina Landfester, Filipe Vilela and Kai A. I. Zhang, published in 2015 in the *Journal of Materials Chemistry A*, volume 3, pages 16064–16071. Reprinted with permission with copyright (2015) from The Royal Society of Chemistry.

offer a huge advantage over conventional bulk catalysts due to their high surface-to-volume ratio^[193, 194] and porous materials offer an enlarged active interface during the catalytic process due to their large surface area.^[193] Conjugated microporous polymers (CMPs), which combine photoactive π -electron backbone and microporous properties, have been recently employed as stable heterogeneous photocatalysts for organic synthesis under irradiation of visible light.^[76, 114, 195-198] At the same time, significant studies have demonstrated their ability for *singlet* oxygen generation,^[199] high selective oxidation of organic sulphides,^[200] oxidative C-C bond formation,^[201] oxidative hydroxylation of arylboronic acids,^[202] reductive dehalogenation reaction,^[159] visible light-initiated free radical and cationic polymerization,^[203, 204] and light-induced hydrogen evolution.^[156] A transformation of bulk CMPs into nanostructured systems offers a combination of the aforementioned advantages which allows for a heterogeneous material to behave closer to a homogeneous catalytic system.

4.1.2 Synthesis and characterization of CMP NPs

The design principle and the synthesis of the CMP NPs are illustrated in Scheme 1. The CMP NPs backbone structures were designed to demonstrate the formation of electron-hole pairs under visible light irradiation. After the light-induced charge separation of the electron-hole pair, the valence band (VB) and the conduction band (CB) should function as oxidative and reductive sites of CMP NPs for further redox reactions (Scheme 1b).



Scheme 1. (a) Synthetic route of the CMP NPs via (A₃+B₂)-type Suzuki-Miyaura or Sonogashira-Hagihara cross-coupling polycondensation reactions in an oil-in-water miniemulsion system. (b) Design principle of the CMP NPs for photo-induced reduction and oxidation reactions using the photogenerated electron-hole pair as reductive and oxidative sides.

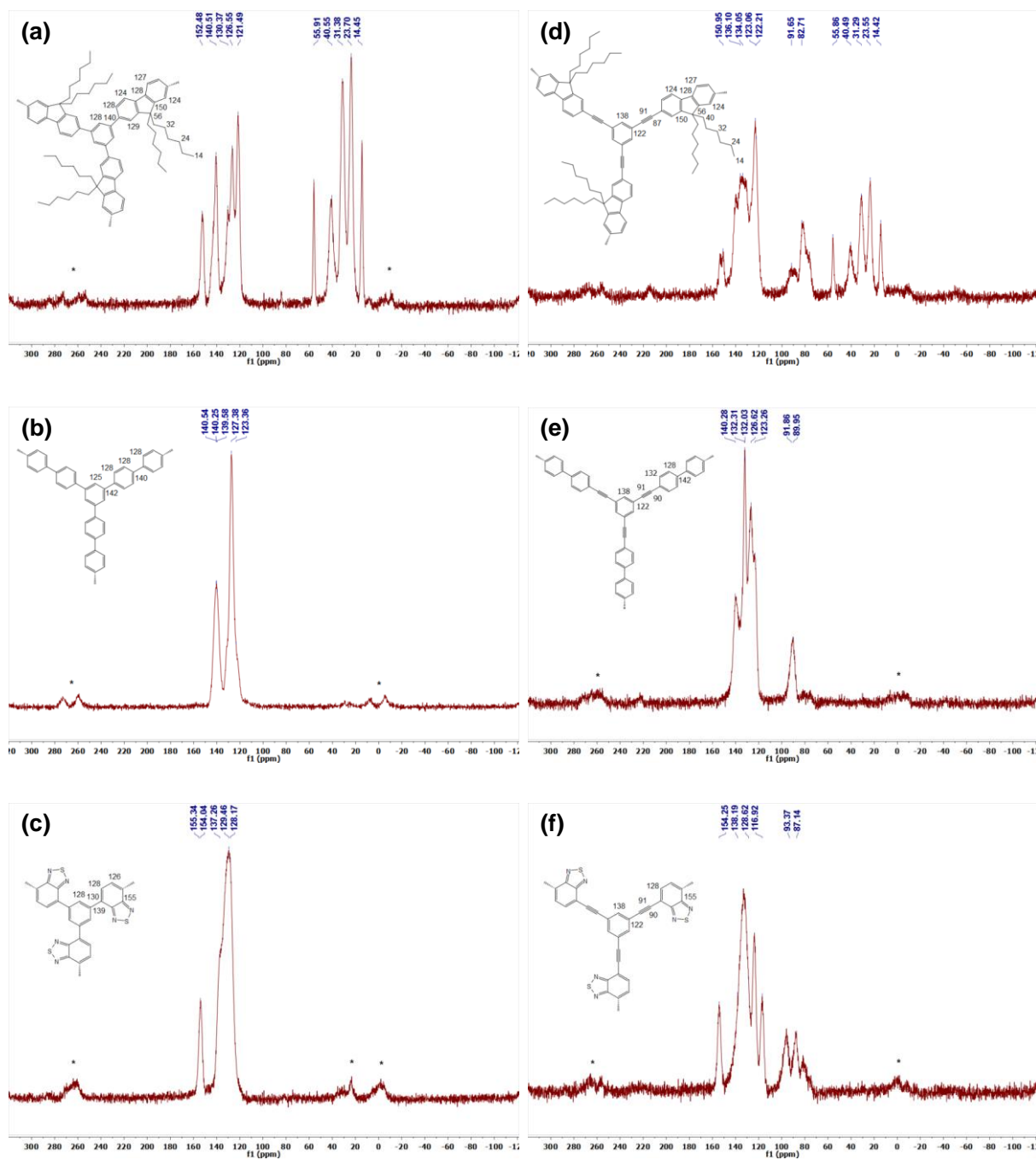


Figure 17. Solid state ^{13}C CP/MAS NMR spectra of (a) B-FL₃-a, (b) B-BPh₃-a, (c) B-BT₃-a, (d) B-FL₃-b, (e) B-BPh₃-b, (f) B-BT₃-b. *Asterisks denote spinning sidebands.

The CMP NPs were obtained via palladium-catalysed Suzuki-Miyaura and Sonogashira-Hagihara cross-coupling polycondensation reaction in an oil-in-water miniemulsion (Scheme 1a).^[148, 205] For each polymerization reaction, the same amount of starting compounds and surfactant were used to achieve similar reaction conditions within the miniemulsion droplets. The detailed reaction conditions along with the

characterization procedure of the polymers are described in the Experimental Section 5.1.

The obtained polymers were characterized by solid state magic angle spinning nuclear magnetic resonance ($^{13}\text{C}/\text{MAS}$ NMR) spectroscopy. All CMP NPs showed typical chemical shifts between 110 and 150 ppm which can be assigned to aromatic rings in the polymer backbone (Figure 17). For B-FL₃-a and B-FL₃-b, alkyl signals of the dihexylfluorene (FL) unit appeared between 14 and 56 ppm. Signals between 85 and 94 ppm of B-FL₃-b, B-BPh₂-b and B-BT₃-b can be assigned to the triple bonds of the polymer backbone. For B-BT₃-a and B-BT₃-b, the benzothiadiazole (BT) unit can be characterized by the signals at about 155 ppm, which are assigned to the adjacent carbon next to nitrogen in the BT unit.

The thermogravimetric analysis (TGA) showed a clear tendency of higher stability of the triple bond-containing CMP NPs B-FL₃-b, B-BPh₃-b and B-BT₃-b (up to 350°C) in comparison to the series without triple bonds (up to 200 °C) (Figure 18). To note, B-FL₃-b and B-BPh₃-b showed a high “left weight”, which could indicate the carbonized content after being heated under nitrogen.

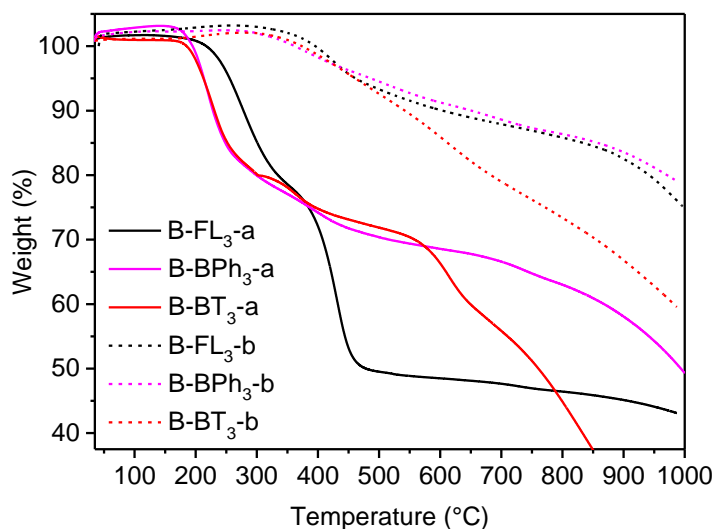


Figure 18. Thermogravimetric analysis of CMP-NPs.

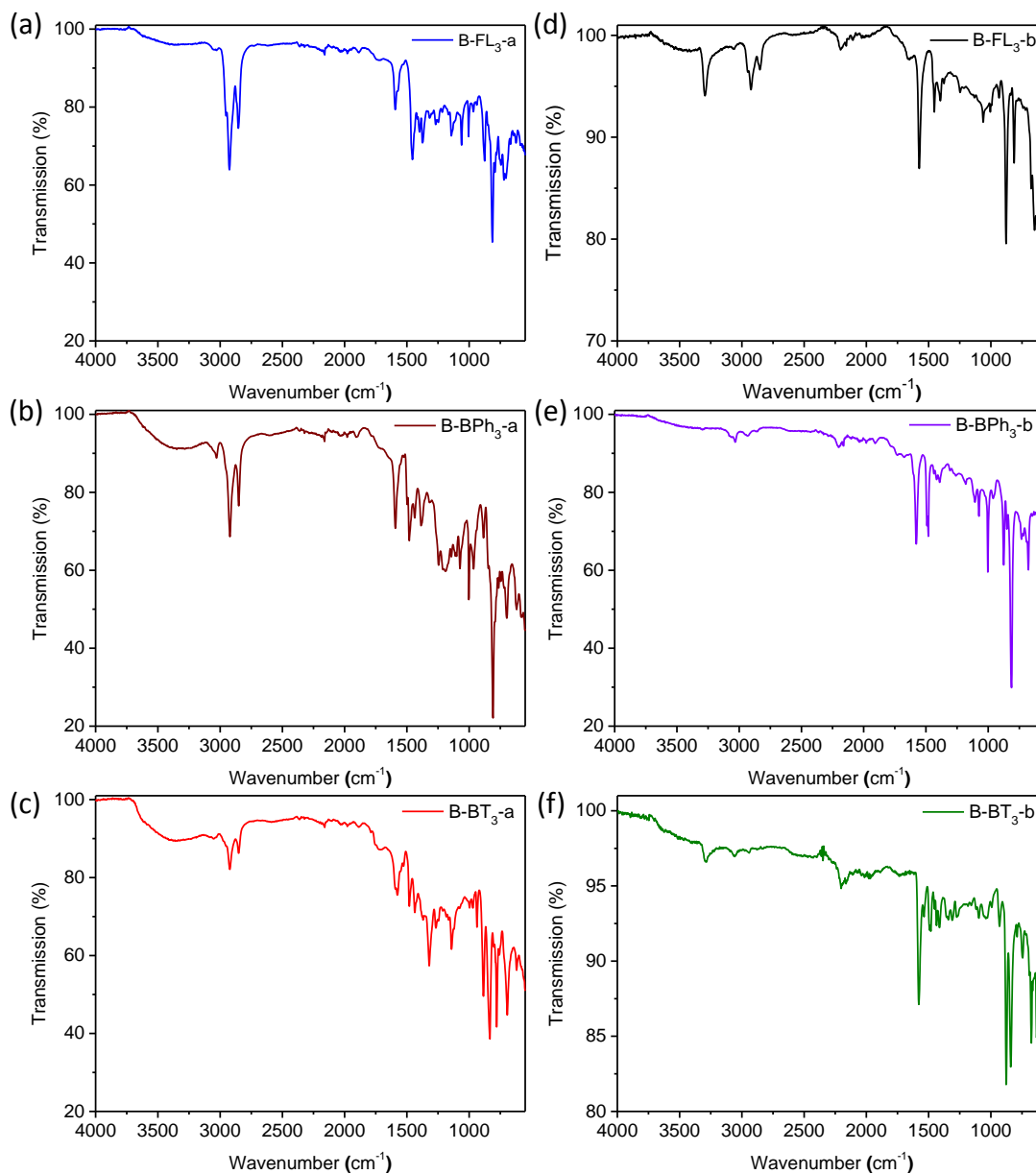


Figure 19. FTIR spectra of (a) B-FL₃-a, (b) B-BPh₃-a, (c) B-BT₃-a, (d) B-FL₃-b, (e) B-BPh₃-b, (f) B-BT₃-b.

Fourier transform infrared spectroscopy (FTIR) analysis of the polymers (Figure 19) showed characteristic vibrational peaks at about 2250-2100 cm^{-1} and 3300 cm^{-1} , which corresponds to the alkyne triple bonds in B-FL₃-b, B-BPh₃-b and B-BT₃-b. Vibrational peaks at about 2850-3000 cm^{-1} are correlated to alkane C-H bonds and a distinctive vibrational peak at about 840 cm^{-1} is assigned to the N-S deformation band of the BT unit on B-BT₃-a and B-BT₃-b (Figure 19c and Figure 19f).

The powder X-ray diffraction (XRD) profile reveals a broad and low intensity pattern around 20° and 24°, which is an indication of amorphous nature (Figure 20).

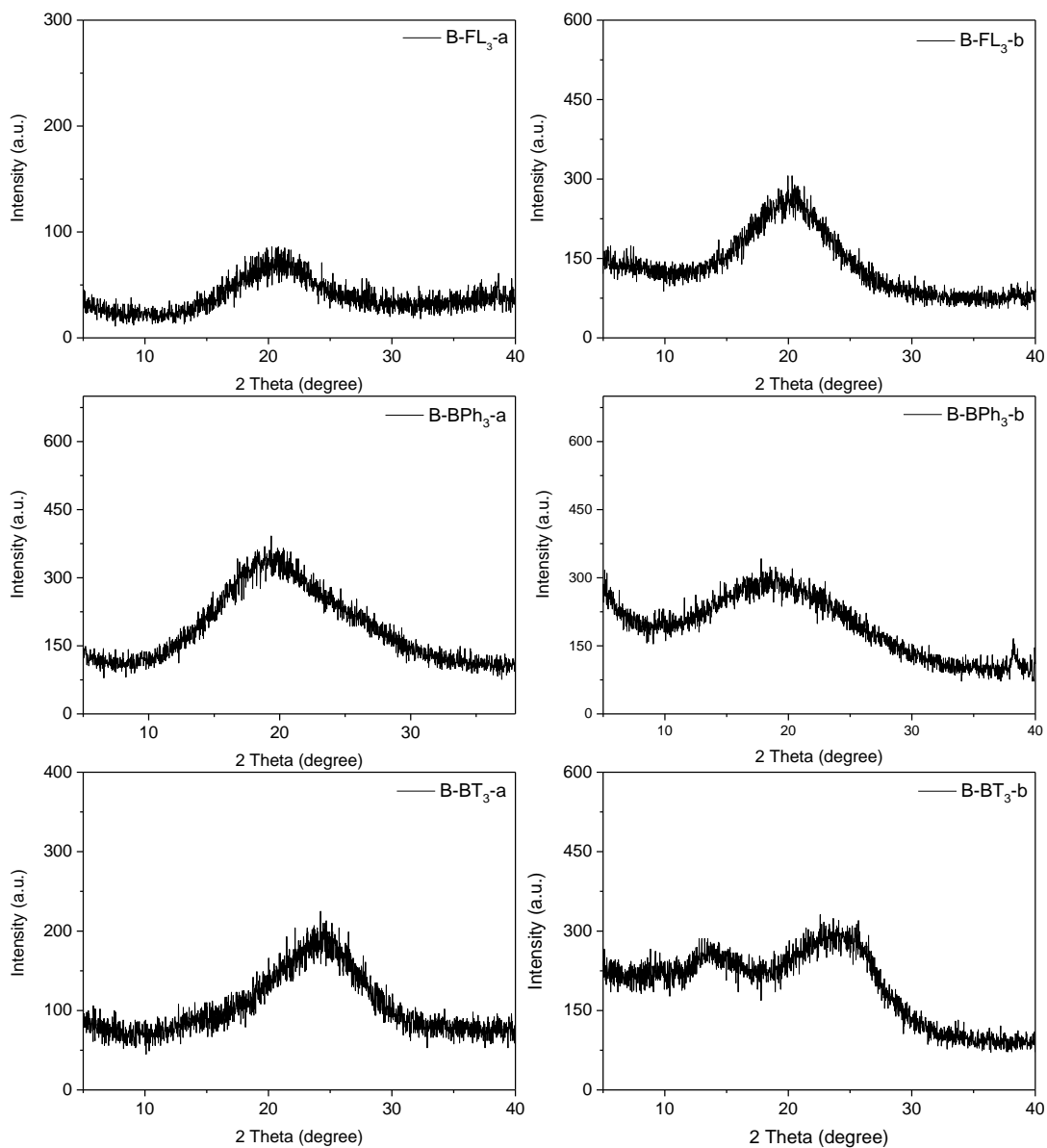


Figure 20. XRD patterns of CMP NPs.

The building-blocks, i.e. the A_3 -type cross-linkers and B_2 -type co-monomers used for the different CMP NPs and their physical properties are listed in Table 2 and the N_2 sorption isotherms and pore size distributions of CMP NPs are displayed in Figure 21 and Figure 22.

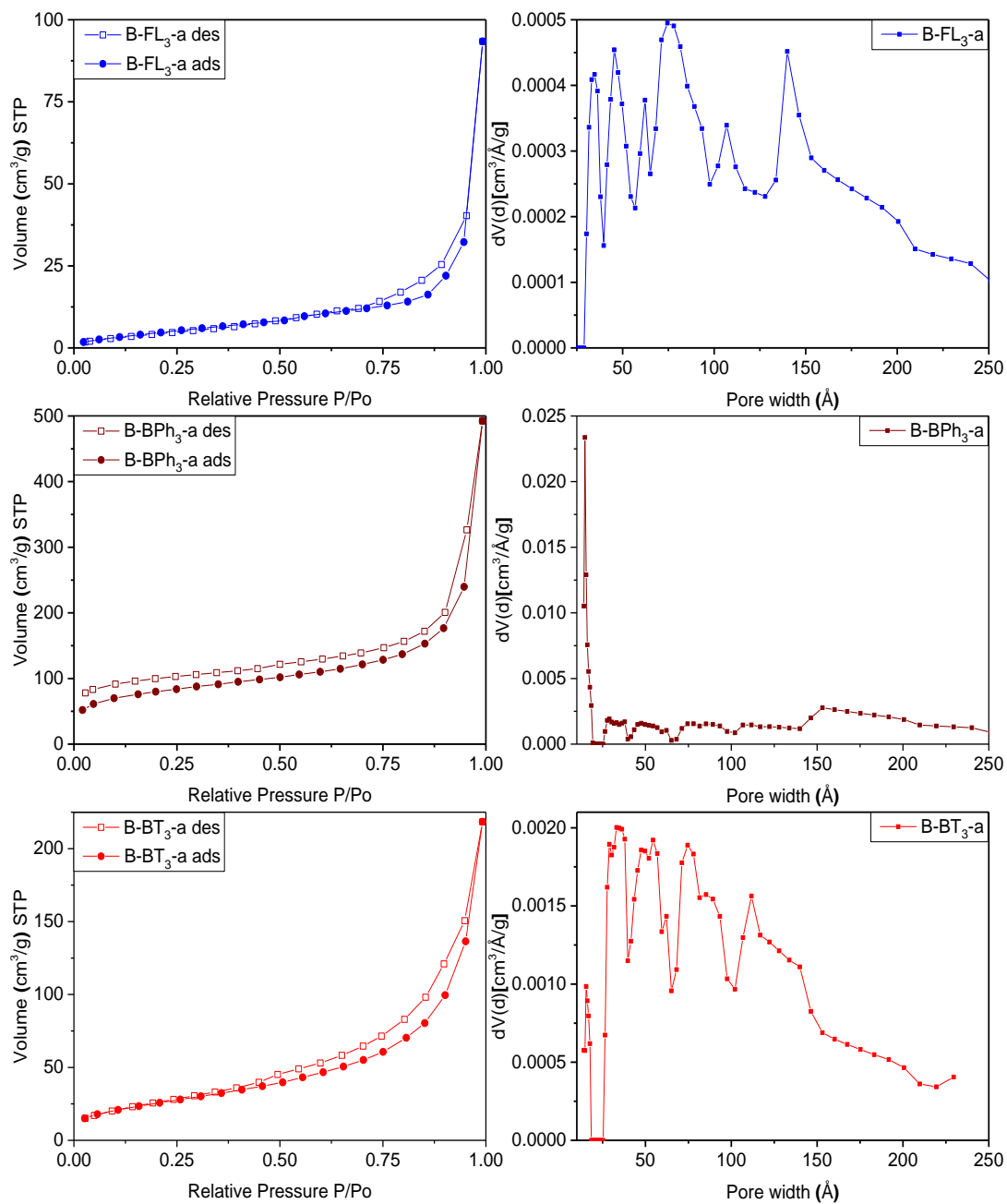


Figure 21. N_2 Sorption Isotherms and Pore Size Distributions of CMP nanoparticles using Suzuki-Miyaura cross-coupling condensation reaction via miniemulsion polymerization.

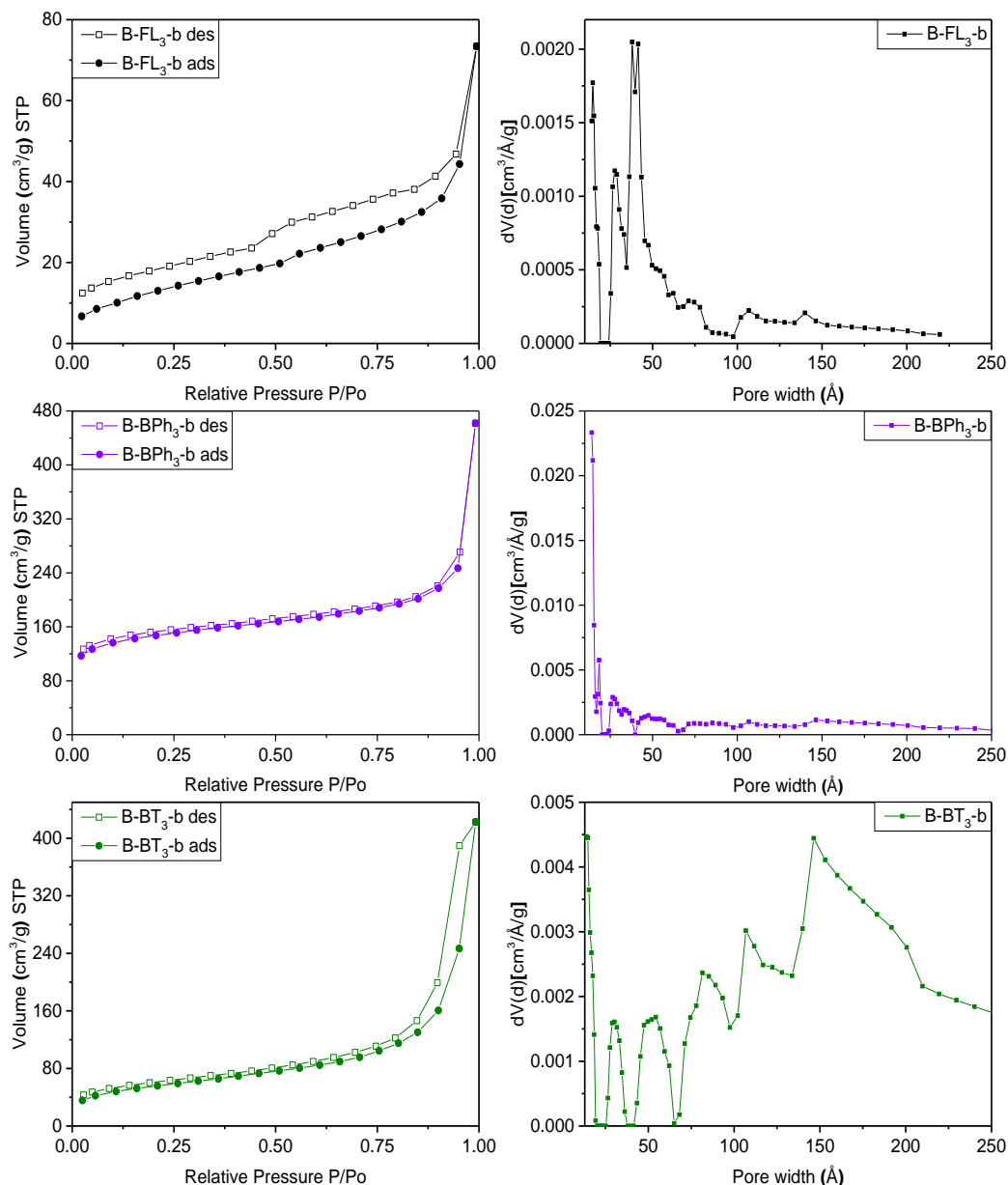


Figure 22. N_2 Sorption isotherms and pore size distributions of CMP nanoparticles using Sonogashira-Hagihara cross-coupling condensation reaction via miniemulsion polymerization.

The FL-containing CMP NPs showed broad pore size distribution with size larger than 2 nm (Figure 21 and Figure 22). This could be caused by the alkyl side chains of the fluorene unit, which blocked the micropores and required larger space inside the porous polymers as reported before.^[159] A previous study of Cooper *et al.* about the formation mechanism of CMPs via Sonogashira coupling showed that the high surface area was mainly obtained at the last phase of the reaction, after the fusion of small

porous fragments.^[207] Here, the lower surface area of the CMP NPs could be partially due to the lack of small fragments inside the droplets during the reaction.

The obtained CMP NPs showed a high stability as dispersion in organic solvents and also in water despite their hydrophobic nature (Figure 23). Zeta potential measurements provided values of -51 ± 11 mV, -47 ± 8 mV, -49 ± 7 mV, -50 ± 9 mV, -49 ± 8 mV and -52 ± 11 mV for B-FL₃-a, B-BPh₃-a, B-BT₃-a, B-FL₃-b, B-BPh₃-b and B-BT₃-b, respectively, which showed a negative surface potential and indicates a good stability of the dispersions. SEM and TEM images of the CMP NPs (Figure 24) show that a variety of nanoparticle shapes was obtained. As expected, the FL-containing B-FL₃-a and B-FL₃-b appeared as round spheres, exhibiting an average size ranging from 60 nm to 100 nm. B-BPh₃-a was obtained as irregular shape particles of ca. 80 nm, whereas B-BPh₃-b appeared as spherical NPs with size ranging between 100 – 150 nm, despite its great rigid polymer backbone structure.

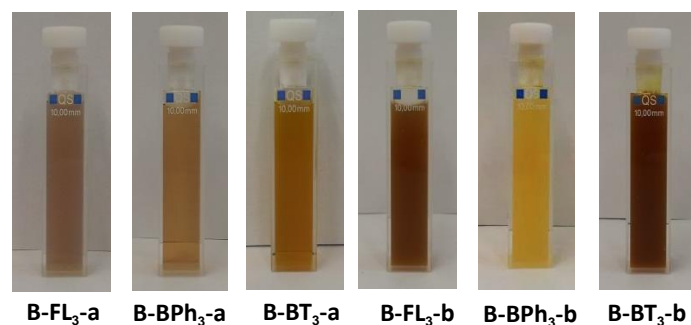


Figure 23. Photographs of the CMP NPs dispersed in water.

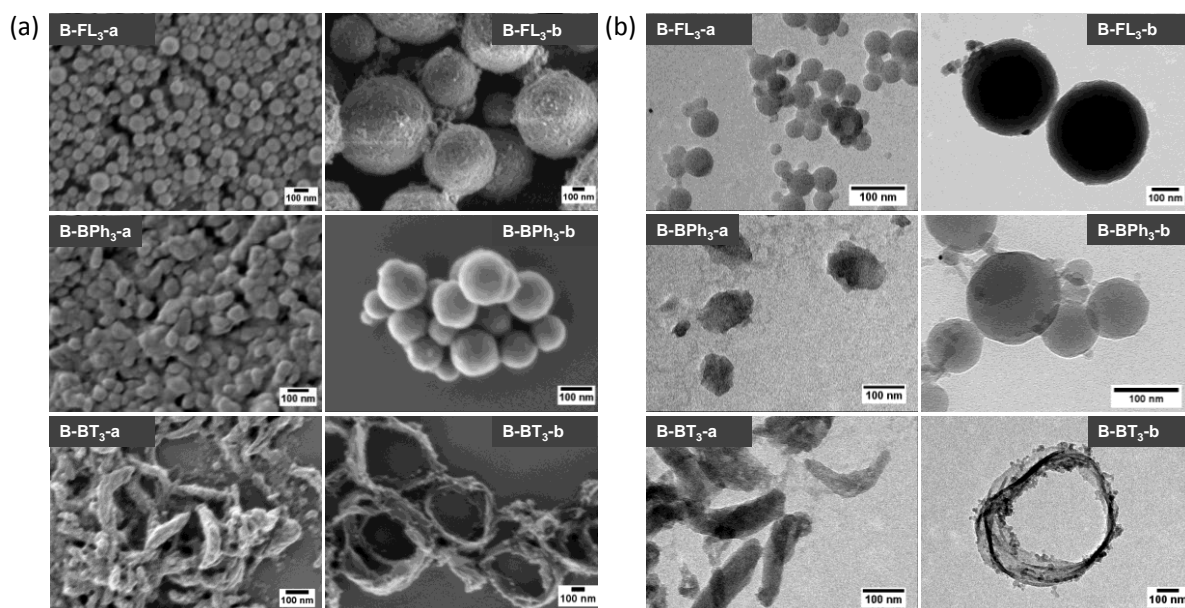


Figure 24. (a) SEM and (b) TEM images of the CMP NPs with different shapes.

The overall trend, similar to the porous properties, consists that the CMP NPs obtained via Sonogashira-coupling are larger in comparison to the ones obtained via Suzuki-coupling. This can be due to a more rigid and extended network structure of the CMP NPs containing triple bonds than the ones without them. Significantly, the BT containing CMP NPs were absolutely non-spherical, B-BT₃-a showed a rod-like shape with a length of ca. 200 nm and a width of ca. 20 nm. Most surprisingly, B-BT₃-b appeared as nanometer-sized rings with a diameter of ca. 200 nm and a width of 20 nm (Figure 24).

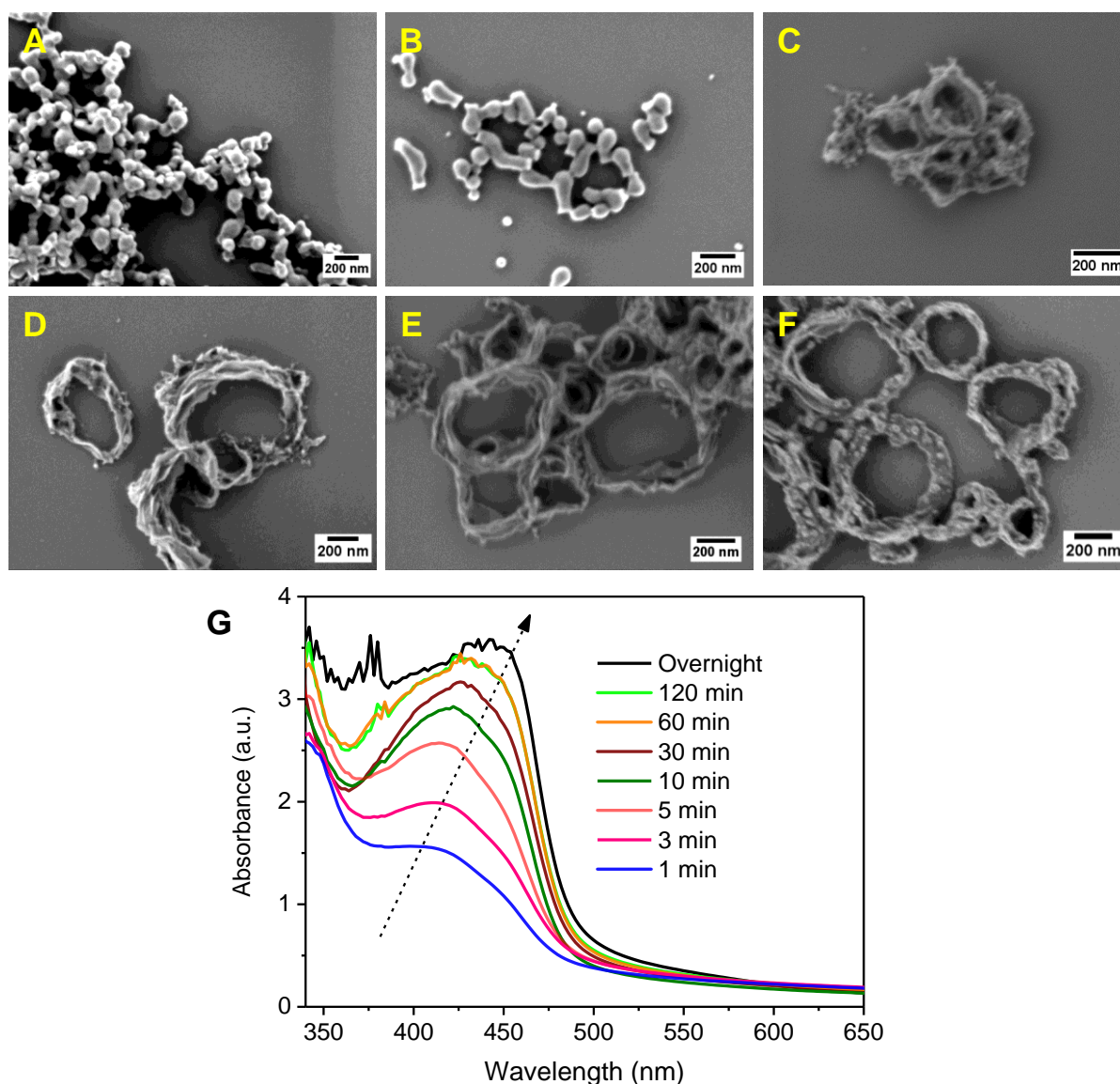


Figure 25. Monitoring experiments of the nanoparticle formation of B-BT₃-b. SEM images of nanoparticles formed in different time intervals after ultrasonication and heating at 80 °C. (a) 1 min, (b) 3 min, (c) 5 min, (d) 10 min, (e) 30 min, (f) 60 min. (G) UV/vis spectra of the NPs formed after defined time intervals.

To investigate the ring formation mechanism of B-BT₃-b, the polymerization process was monitored with defined reaction time intervals. As displayed in Figure 25, the UV/vis spectra of the as-made nanoparticle samples were taken, indicating their development upon the completion of the polymerization process. The graph shows that the main absorption band of B-BT₃-b with a maximum peak at ca. 430 nm appeared directly after the miniemulsion preparation using ultrasonication. Figure 25a – Figure 25f display the SEM images of B-BT₃-b particles after the corresponding reaction time. Directly after the ultrasonication, small particles of ca. 20 nm were already formed (Figure 25). These could be the pre-formed oligomers, which subsequently formed the ring-like particles inside the droplets of the miniemulsion within the first minutes (Figure 25b). After 5 minutes, the ring-shaped particles were clearly formed (Figure 25c), which did not differentiate largely from the ones obtained after 10, 30 or 60 min (Figure 25d – Figure 25f) and the final product after the completion of the polymerization (Figure 24).

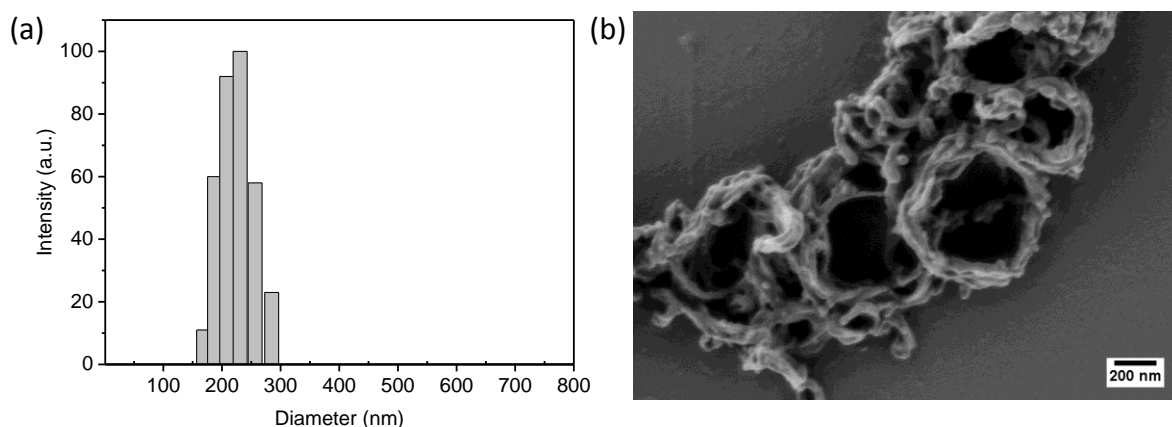


Figure 26. (a) Size distribution of B-BT₃-b measured by dynamic light scattering (DLS) and (b) SEM image of B-BT₃-b, using Lutensol as surfactant.

The monitoring experiment indicates a possible ring formation mechanism of B-BT₃-b. An average droplet size of ca. 250 nm determined by dynamic light scattering (DLS) suggests that the final ring formation of B-BT₃-b might have first taken place at the interface (Figure 26a), followed by an aggregation of the oligomers formed within the first minutes after the ultrasonication. According to the very rigid structure caused by the BT-based polymer backbone, a possible contraction of aggregates might have occurred, which led only to the formation of ring-shaped CMP NPs instead of capsule-

like particles. After changing from an ionic surfactant (sodium n-dodecylsulfate) to a non-ionic one (Lutensol® AT50) in the reaction, a ring-shaped CMP NPs were still formed (Figure 26b). This result suggests that the formation mechanism is not depending on the type of surfactant used. And no strong evidence led to the assumption that the nanorings could likely be collapsed capsules in dried state.

The UV/Vis absorption spectra of the CMP NPs are displayed in Figure 27 and all of them show a broad absorption band. The donor-based CMP NPs, B-FL₃-a and B-FL₃-b, B-BPh₃-a and B-BPh₃-b absorb mainly in the blue light range. After introducing a strong electron acceptor, BT unit into the polymer backbone, a large bathochromic shift up to 100 nm occurred, indicating a narrower band gap of the polymers. According to our recent studies on CMPs with various donor-acceptor combinations, the introduction of strong acceptors lowers mostly the LUMO level and therefore the redox-potential of the polymer, which could favour catalytic reactions initiated by light.^[154, 160] The UV/vis absorption spectra also show that the triple bond-containing B-FL₃-b, B-BPh₃-b, and B-BT₃-b have clearly broader absorption bands than the ones without it. A narrower optical band gap can be derived from the absorption edges (Table 2), the reason behind it can be due to a more ordered structure obtained via efficient π - π stacking during the CMP synthesis, which led to a better conjugation throughout the CMP networks, and therefore, lowering the energy levels.

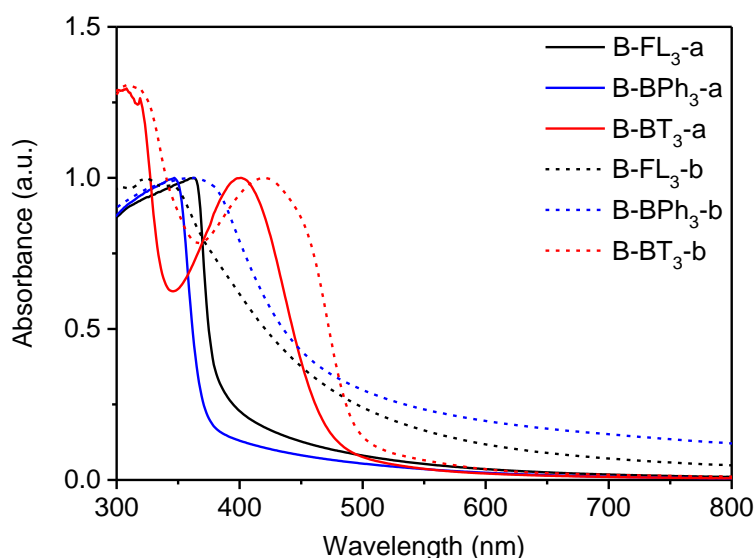


Figure 27. UV/vis absorption spectra of the CMP NPs in water dispersion.

4.1.3 Photocatalytic activity of CMP NPs for photodegradation of Rhodamine B

Taking advantage of the excellent dispersibility of the hydrophobic CMP NPs in water, the photocatalytic activity of the CMP NPs in the reductive activation of molecular oxygen was explored. Here, the photon energy is transferred from the photogenerated electron of the electron-hole pair onto oxygen and the obtained activated oxygen species is then subsequently used for the degradation of a water-soluble organic dye, rhodamine B (RhB) (Figure 28 and Figure 29).

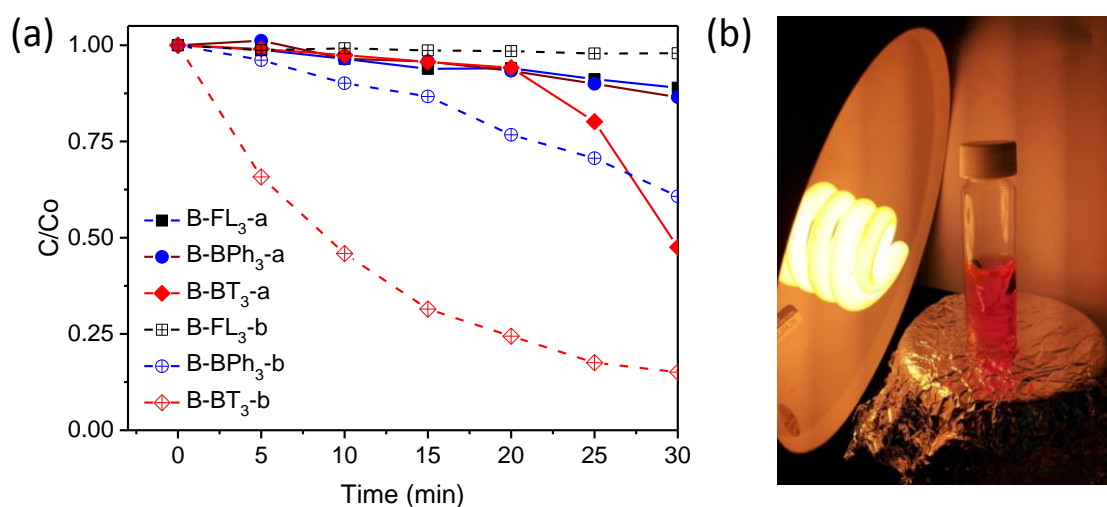


Figure 28. (a) Photocatalytic degradation of RhB in the presence of the CMP NPs in water. C is the concentration of RhB after light irradiation for a certain period and C₀ is the concentration of RhB after reaching adsorption/desorption equilibrium in dark. Concentration of CMP NPs: 1 mg mL⁻¹, concentration of RhB: 10 mg L⁻¹. (b) Photocatalytic set-up using a 23 W household energy saving light bulb.

B-BT₃-b showed the highest photodegradation rate of RhB (Figure 28a and Figure 29). This result is in accordance to the lowest optical band gap from B-BT₃-b, 1.76 eV. After 25 min over 80% of RhB was already degraded, while its counterpart without triple bond, B-BT₃-a (band gap: 1.96 eV) only degraded about 50% of RhB after the same period. Interestingly, B-BPh₃-b showed, despite its larger band gap (2.36 eV), also a slightly higher photocatalytic efficiency in the first minutes in comparison to B-BT₃-a. This could be attributed to its high BET surface area (512 m²g⁻¹), which could offer a large reactive interface during the catalytic process. B-BT₃-a initially showed a low degradation rate of RhB in the first minutes, however after 20 min it showed an accelerated degradation process of RhB, which might indicate a different reaction order in comparison to its triple-bond containing counterpart B-BT₃-b. It is worth mentioning

that a 23 W household energy saving light bulb was used as light source for the experiments (Figure 28b).

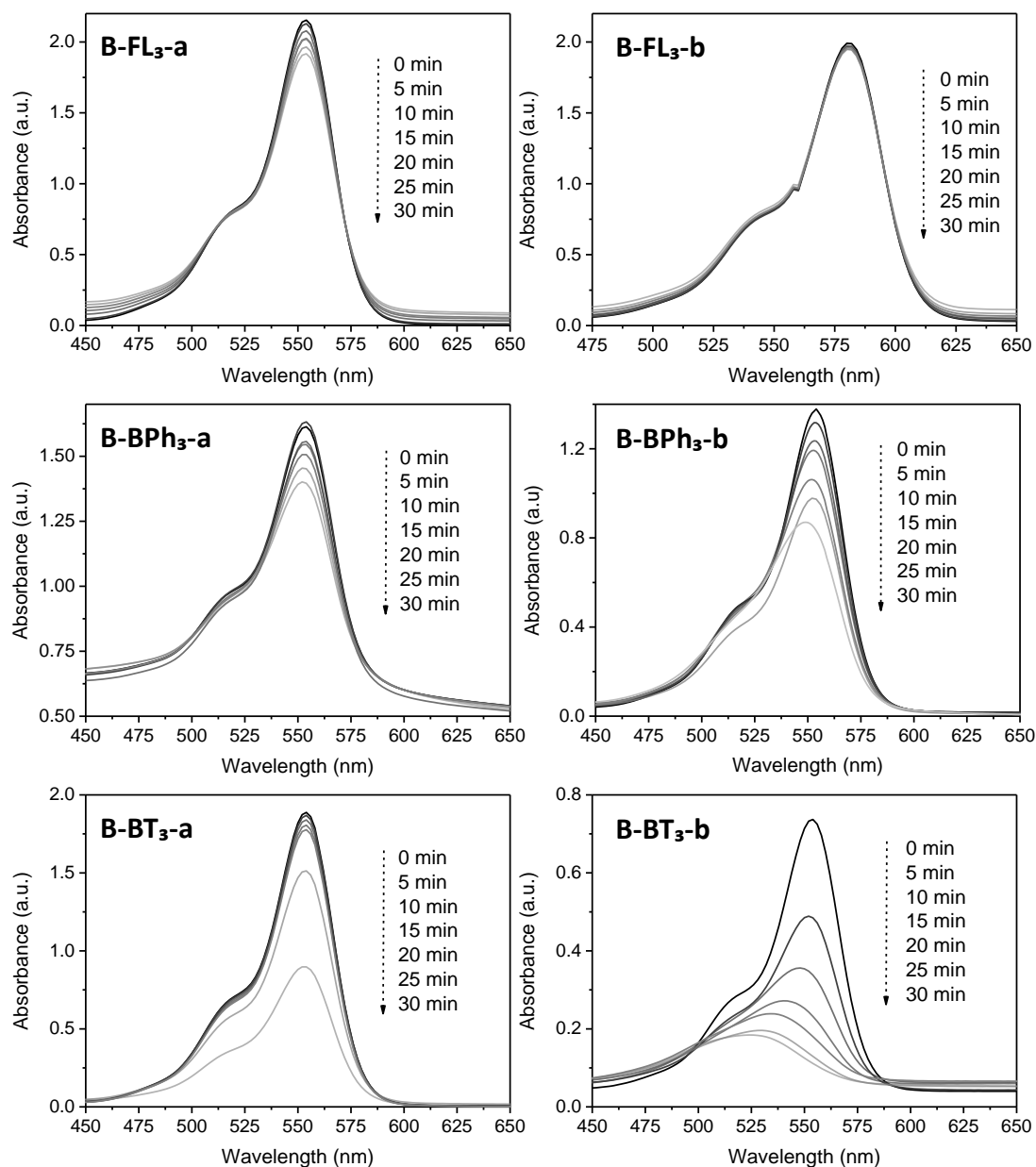


Figure 29. UV-vis spectrum of RhB (10 mg L^{-1}) after different illumination time intervals in the presence of CMP nanoparticles (1 mg mL^{-1}). The black arrow indicates the decrease of RhB absorption (552 nm) as a function of irradiation time.

Other CMP NPs only showed very low photodegradation rates of RhB. At the same time, B-BT₃-b also showed higher photocatalytic efficiency in comparison to its bulk form, which indicates the enhanced photocatalytic activity of B-BT₃-b in the nanostructured form (Figure 30a). The efficiency of the CMP NPs, especially of B-BT₃-b

is comparable to porous carbon nitride (C_3N_4), a state-of-art non-metal based visible light photocatalyst under similar reaction conditions.^[154, 160]

In addition, the CMP NPs showed high stability during the photodegradation reaction. Five extra repeating experiments using B-BT₃-b as photocatalyst were performed. RhB was degraded almost in a quantitative manner after every cycle, indicating the high stability and reusability of the CMP NPs in water. As shown in Figure 30b, the absorption band of B-BT₃-b barely changed after the photodegradation reaction, whilst the UV/vis absorption spectrum of RhB almost disappeared completely. It is important to mention that almost no degradation of RhB occurs under light irradiation without using the CMP NPs as photocatalyst.

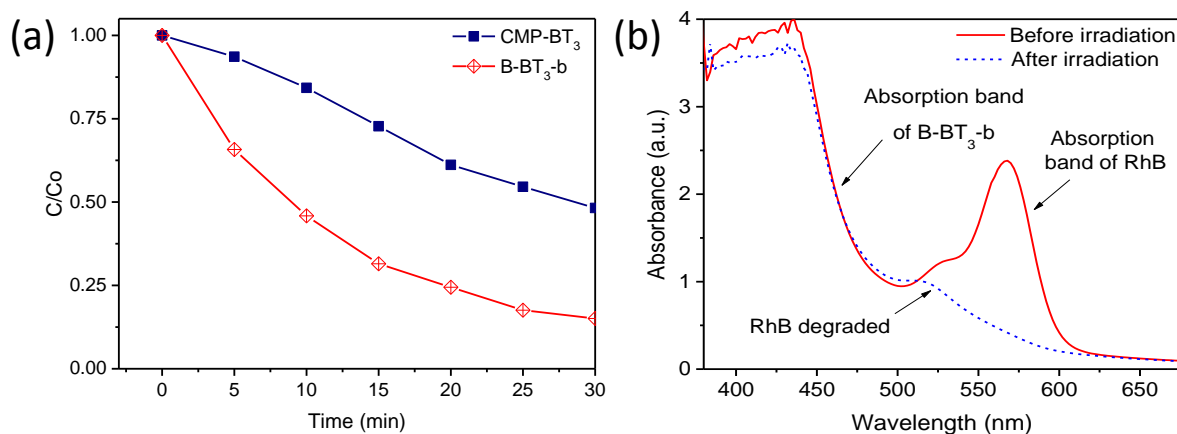


Figure 30. (a) Photocatalytic degradation of RhB in the presence of bulk CMP-BT₃ and B-BT₃-b in water. C is the concentration of RhB after light irradiation for a certain period and C_0 is the concentration of RhB after reaching adsorption/desorption equilibrium in dark. Concentration of CMP-BT₃ and B-BT₃-b: 1 mg mL^{-1} , concentration of RhB: 10 mg L^{-1} . (b) UV/vis spectra of the reaction mixture of the photodegradation of RhB with B-BT₃-b before and after the 5th repeating cycle of the experiment.

4.1.4 The ability to generate reactive oxygen species

In the photodegradation of organic dyes in water, it is well known that reactive species (ROS) such as superoxide ($\cdot O_2^-$), *singlet* oxygen (1O_2), $\cdot OH$ and h^+ play important roles in the photocatalytic process.^[154, 160] In order to better understand whether those species are also involved in the RhB degradation using B-BT₃-b and in which degree, experiments were conducted (Figure 31) using the following radical scavengers: sodium azide (NaN_3) for 1O_2 , benzoquinone (BQ) for $\cdot O_2^-$, isopropanol (IP) for $\cdot OH$ and ammonium oxalate (AO) for h^+ . As shown in Figure 31, the addition of NaN_3 and the

absence of oxygen in the reaction led to an expressive decrease in the photodegradation process of RhB. These results suggest that under visible light irradiation the B-BT₃-b is able to induce the formation of radical oxygen species, which are responsible for the degradation of RhB, with the main role played by ¹O₂.

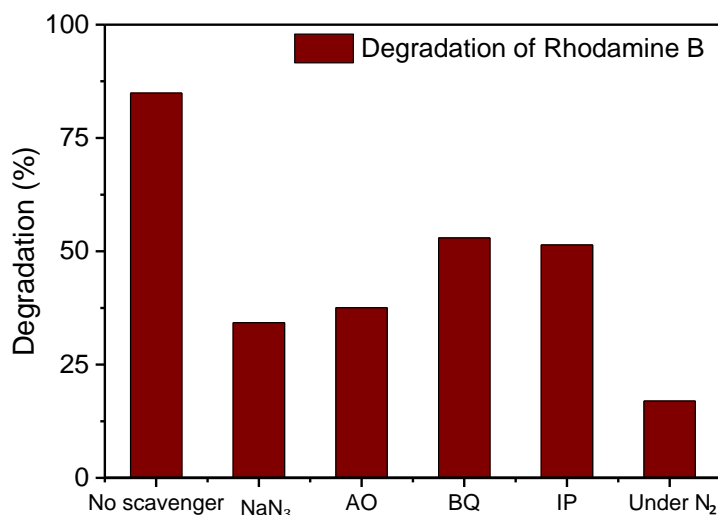
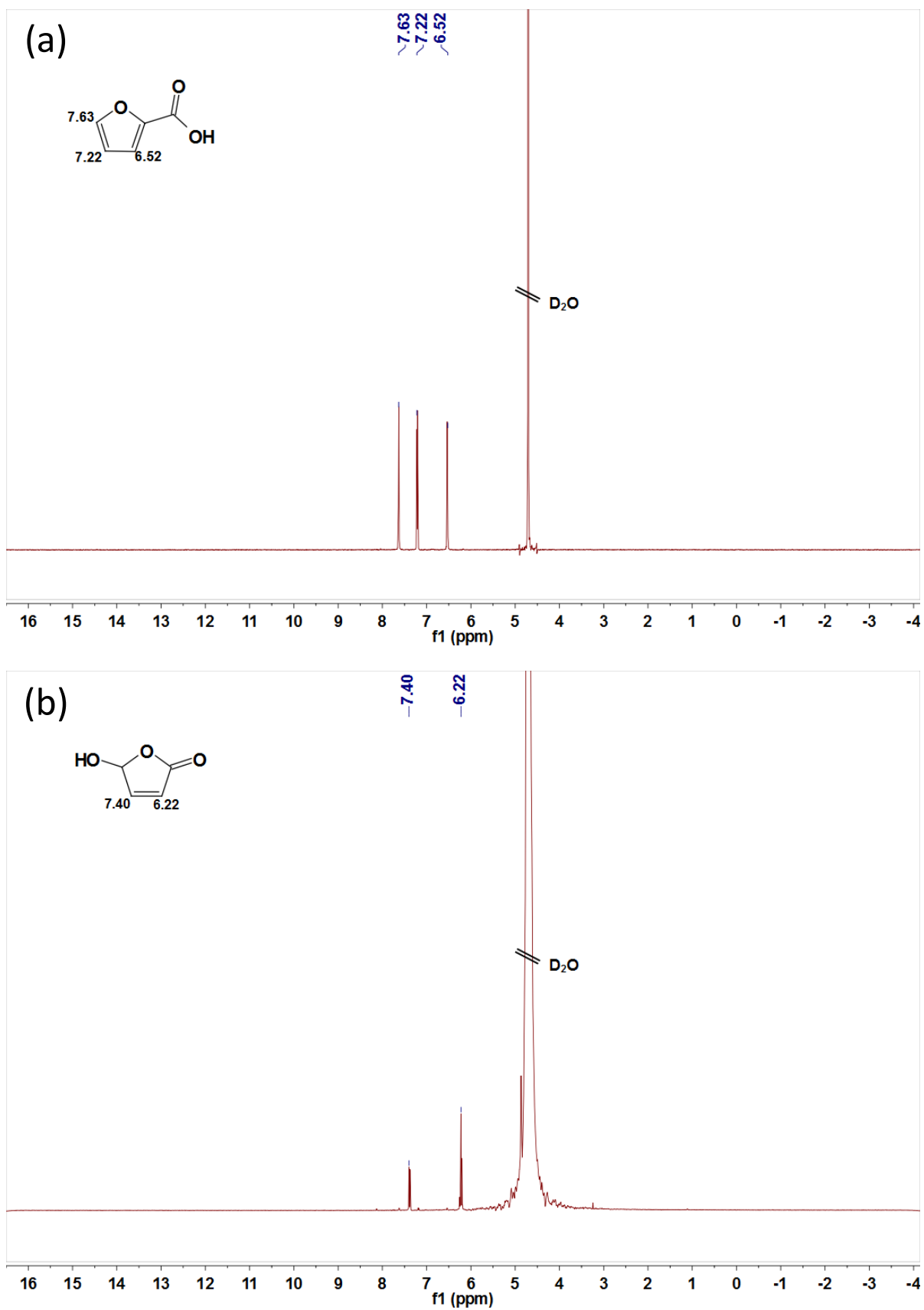


Figure 31. The effect of different scavengers, sodium azide (NaN₃), ammonium oxalate (AO), benzoquinone (BQ), isopropanol (IP) and the absence of oxygen (under N₂) on the degradation of Rhodamine B (RhB) over B-BT₃-b under 30 min of visible light irradiation.

In a previous study, it was shown that the bulk-made CMP similar to B-BT₃-b was able to generate *singlet* oxygen species (¹O₂) under visible light irradiation. Therefore, as an additional control experiment, we further confirmed the role of ¹O₂ in the photocatalytic system by using the well-studied furoic acid as ¹O₂ trap.^[12, 208-210] 5-Hydroxy-2(5H)-furanone was obtained as the oxidized product in a quantitative manner using B-BT₃-b as photocatalyst (Figure 32).

A significant decrease in the photocatalytic reaction was also observed by adding AO as hole scavenger (Figure 31). Since the holes may also contribute to a direct oxidation of RhB in a photocatalytic system^[12, 208-210], the electron transfer between the photogenerated hole inside the CMP NPs and substrate compounds was further evaluated, i. e. the photooxidation reaction.



4.1.5 Photooxidation of TMPD

The transformation of *N,N,N',N'*-tetramethyl-*p*-phenylenediamine (TMPD) into its cationic radical form (TMPD^{•+}) was examined under an oxidative process using the CMP NPs. The oxidized form TMPD^{•+} can be determined by a colour change from colourless to blue, and thus make the intermolecular oxidative electron transfer reaction from TMPD to the CMP NPs visible.^[211]

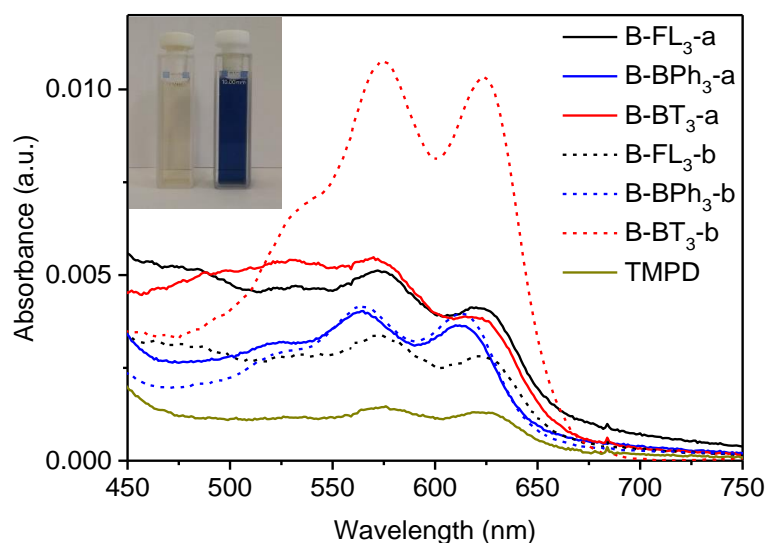


Figure 33. Photooxidation of TMPD using different CMP NPs in acetonitrile. Concentration of CMP NPs: 1 mg mL⁻¹, concentration of TMPD: 32.85 mg mL⁻¹. The insert image shows: (left) pure TMPD solution after light irradiation and (right) TMPD solution mixed with B-BT₃-b after light irradiation.

As displayed in Figure 33, after the same reaction time under light irradiation, the absorption spectra of the dispersion containing B-BT₃-b and TMPD exhibited the highest intensity. B-BT₃-a showed slightly higher photooxidative ability than other CMP NPs, but significantly lower than B-BT₃-b. Similar to the photodegradation experiments of RhB, the absence of any colour changes in the TMPD solution occurred without using the CMP NPs as photoactive oxidizing agent under the same light irradiation condition. It can be observed that B-BT₃-b can generate more and longer-living electron-hole pairs efficiently, which can further catalyse reactions driven either under reductive or oxidative processes.

4.1.6 Conclusions and outlook

As a conclusion from this chapter, a new platform of well-dispersible CMP NPs as a combination of nanostructure and highly porous and heterogeneous photocatalytic system is reported. The variety of shapes of the NPs can be controlled by introducing different electron donor and acceptor as building blocks into the polymer backbone, leading to shape variations ranging from nanospheres, nanorods to nanorings. High photocatalytic activity of the CMP NPs was demonstrated in the reductive activation of molecular oxygen for degradation of rhodamine B and the photooxidation of *N,N,N',N'*-tetramethyl-*p*-phenylenediamine under visible light irradiation. It was shown that the transformation of the CMPs into nanoparticles could enhance the photocatalytic activity due to the higher dispersity and larger active surface content of the material. Additionally, it is important to note that a household energy saving light bulb was used as a light source, which provides an economically low-cost solution for the photocatalytic process in broader application fields.

4.2 Conjugated microporous polymer nanoparticles as visible light antibacterial photocatalysts *via* molecular doping[†]

In the following chapter, the focus is directed to the control of optical and electrochemical properties of a series of conjugated microporous polymer nanoparticles (CMP NPs) by structural design methods. The main aim consists in developing a metal-free and efficient method for inactivation of bacteria in water under visible light exposure. *Via* molecular doping of electron-withdrawing moieties into electron-donating polymer backbones, enhanced antibacterial properties are demonstrated with the inactivation of gram negative *Escherichia coli* K-12 and gram positive *Bacillus subtilis*, mainly by means of photogeneration of *singlet* oxygen as the main photogenerated active species. High stability, reusability and disinfection mechanism of the CMP NPs are also illustrated.

4.2.1 Motivation

The emergence of multi-resistant bacteria against antibiotics is considered as one of the main challenges in modern public health.^[212-216] In recent years, antibacterial photodynamic therapy (PDT) holds great promise as an alternative approach to disinfection of bacteria. In comparison to conventional inactivation methods, PDT presents the advantage of not inducing the selection of resistant strains since its mode of action is based on the generation of reactive oxygen species (ROS) upon light irradiation.^[217, 218]

Recently, a range of inorganic or metalloorganic semiconductor photocatalysts primary based on TiO₂,^[219, 220] porphyrin derivatives, and other metal-based complexes have been developed as suitable materials for disinfection.^[217, 221, 222] Besides these metal-containing active systems, recent studies have reported the development of pure organic and metal-free semiconductors based on water soluble conjugated polymers with visible light induced antibacterial properties.^[223-226] Considerable efforts have been focused on the development of photoactive nanomaterials towards bacterial

[†] This chapter is based on the publication “Enhanced visible light promoted antibacterial efficiency of conjugated microporous polymer nanoparticles *via* molecular doping” by Beatriz Chiyin Ma, Saman Ghasimi, Katharina Landfester and Kai A. I. Zhang, published in 2016 in the *Journal of Materials Chemistry B*, volume 4, pages 5112–5118. Reprinted with permission with copyright (2016) from The Royal Society of Chemistry.

disinfection,^[227] since they offer great advantage due to their surface to volume ratio.^[193] However, only a few examples of the employment of non-metal based nanostructured photoactive systems were reported.^[219] It is therefore of great benefit to further develop a new class of metal-free photoactive systems with broad light absorption range, high efficiency and stability.

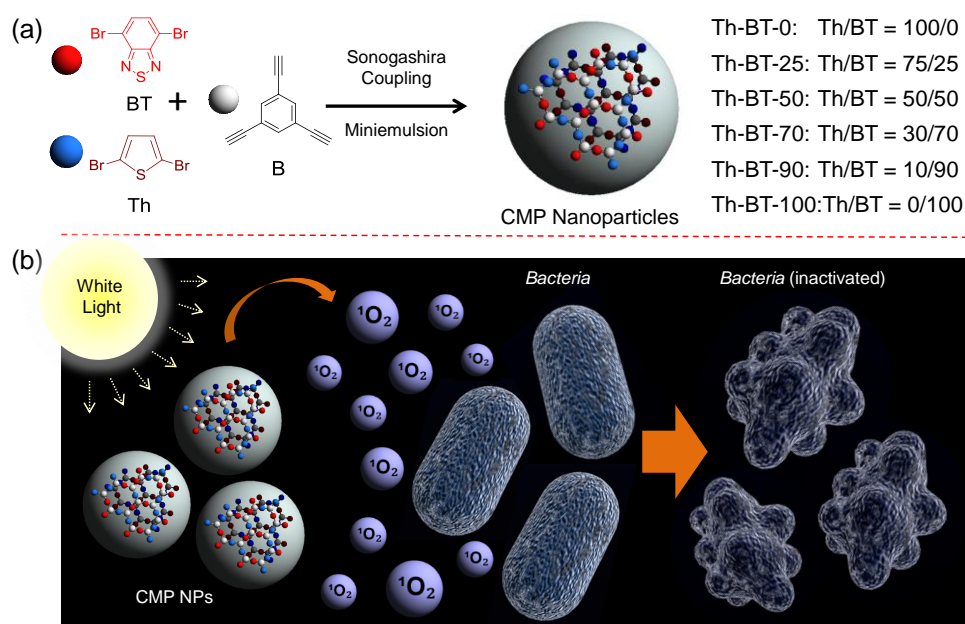
As it was already discussed in chapter 4, conjugated microporous polymers (CMP) have recently emerged as stable heterogeneous photocatalysts for organic synthesis and especially for photo-redox reactions under visible light irradiation.^[133, 150, 155, 197] Previous works and also chapter 4 have shown that conjugated microporous polymers were able to generate active oxygen species such as superoxide ($\bullet\text{O}_2^-$) and *singlet* oxygen ($^1\text{O}_2$) under visible light irradiation.^[7, 10, 12, 157] Especially *singlet* oxygen is well known as the main reactive oxygen species responsible for cell death in antimicrobial photodynamic therapy.^[145, 228, 229]

Besides the material class choice perspective, there are a vast number of useful structural modification methods of semiconductor-based materials in order to enhance the pristine functionalities. Among them, the introduction of foreign impurities into a semiconductor, the so-called doping method has been largely employed as an efficient strategy to manipulate the electronic structure of semiconductors, and thus, to achieve the desired control over the optical, conductive, magnetic or other physical properties for targeted applications.^[220, 230]

In this chapter the use of a series of conjugated microporous polymer nanoparticles (CMP NPs) as a new class of highly efficient metal-free photocatalysts for visible light promoted antibacterial PDT is investigated. Taking the doping method for traditional semiconductors as a role model, a structural design principle via molecular doping of an electron-withdrawing moiety, benzothiadiazole unit (BT), into the backbone of the pure organic polymer network only containing the electron-donating thiophene units is introduced in order to modify the ability for generation of the active oxygen species. Enhanced disinfection effects on *Escherichia coli* K-12 and *Bacillus subtilis* under visible light irradiation are also demonstrated as model systems for gram negative and gram positive bacteria respectively.

4.2.2 Synthesis and characterization of CMP NPs

The conjugated microporous polymer nanoparticles (CMP NPs) were prepared via palladium-catalysed Sonogashira-Hagihara cross-coupling polycondensation reaction in an oil-in-water miniemulsion.^[7, 15] In particular, as illustrated in Scheme 2, the electron-donating thiophene unit-based (Th) polymer network Th-BT-0 was taken as the pristine polymer backbone structure. *Via* successive doping of the electron-withdrawing benzothiadiazole (BT) unit into the polymer backbone, within the miniemulsion droplets, a series of CMP NPs were obtained containing different chemical compositions. The detailed synthesis and characterization of the polymers are described in the Experimental Section 5.2.



Scheme 2. (a) Illustrated structures and synthetic route of the conjugated microporous polymer nanoparticles (CMP NPs) via Sonogashira-Hagihara cross-coupling reaction via miniemulsion polymerization and the ratios of the monomer moieties in the polymer backbones. (b) Schematic representation of the mechanism for the inactivation of bacteria using CMP NPs.

SEM and TEM images of the CMP NPs are shown in Figure 34. A variety of morphologies ranging from nanospheres, nanorods to nanorings was observed. Th-BT-0 and Th-BT-25 were formed as nanospheres with a diameter of *ca.* 180 nm, whereas the Th-BT-50 appeared as “worm-like” nanoparticles with a length of *ca.* 250 nm, which could be a transitional state between nanospheres and ring shaped nanostructures exhibited by Th-BT-70, Th-BT-90 and Th-BT-100. The latest was in accordance to our previous report.^[7] The morphological trend might indicate that the shape variation depends on the addition of the BT unit and the increasing amount of the strong acceptor

unit possibly pushed the structure towards a ring formation due to strong π - π stacking at the interface during the miniemulsion polymerization.^[7] Zeta potential measurements provided values of -54 ± 9 mV, -49 ± 6 mV, -50 ± 7 mV, -47 ± 11 mV, -53 ± 10 mV and -51 ± 11 mV for Th-BT-0, Th-BT-25, Th-BT-50, Th-BT-70, Th-BT-90 and Th-BT-100, respectively, which indicates a good stability of the dispersions.

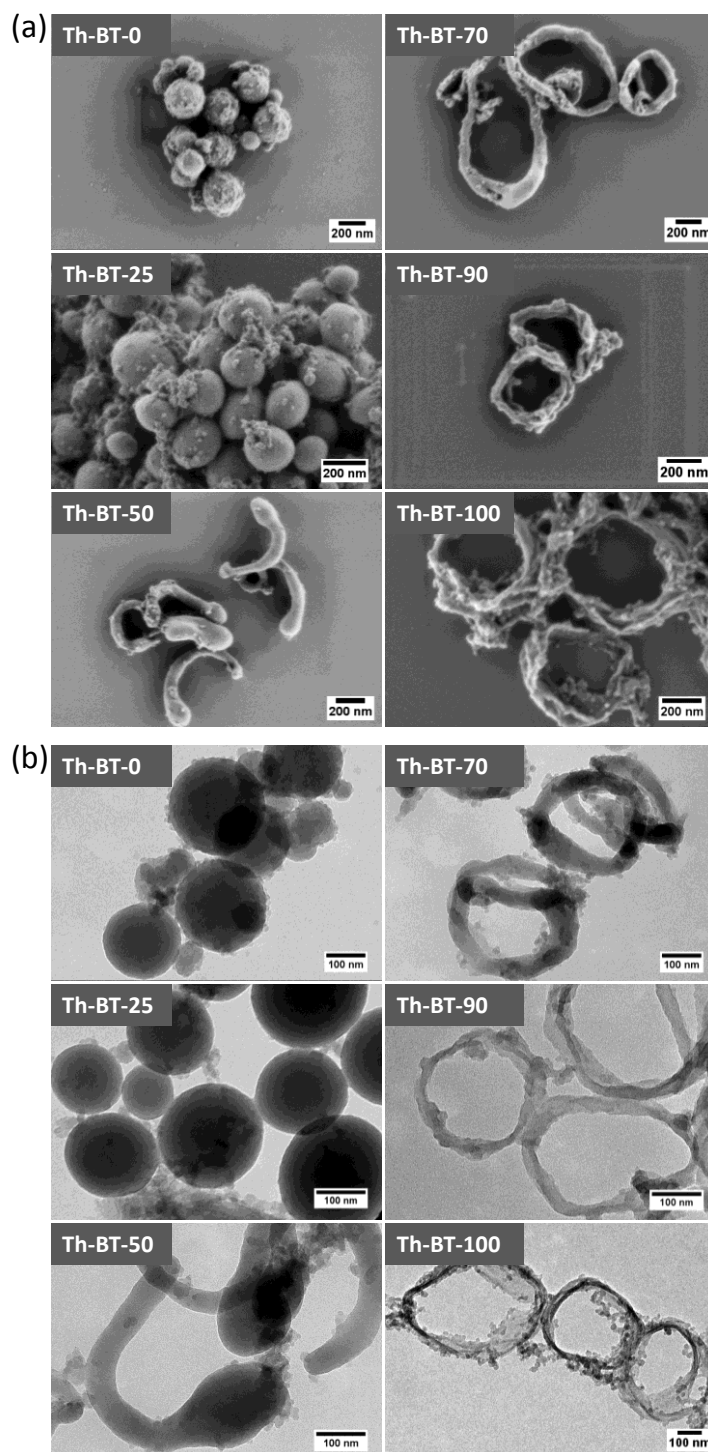


Figure 34. (a) SEM and (b) TEM images of the CMP NPs.

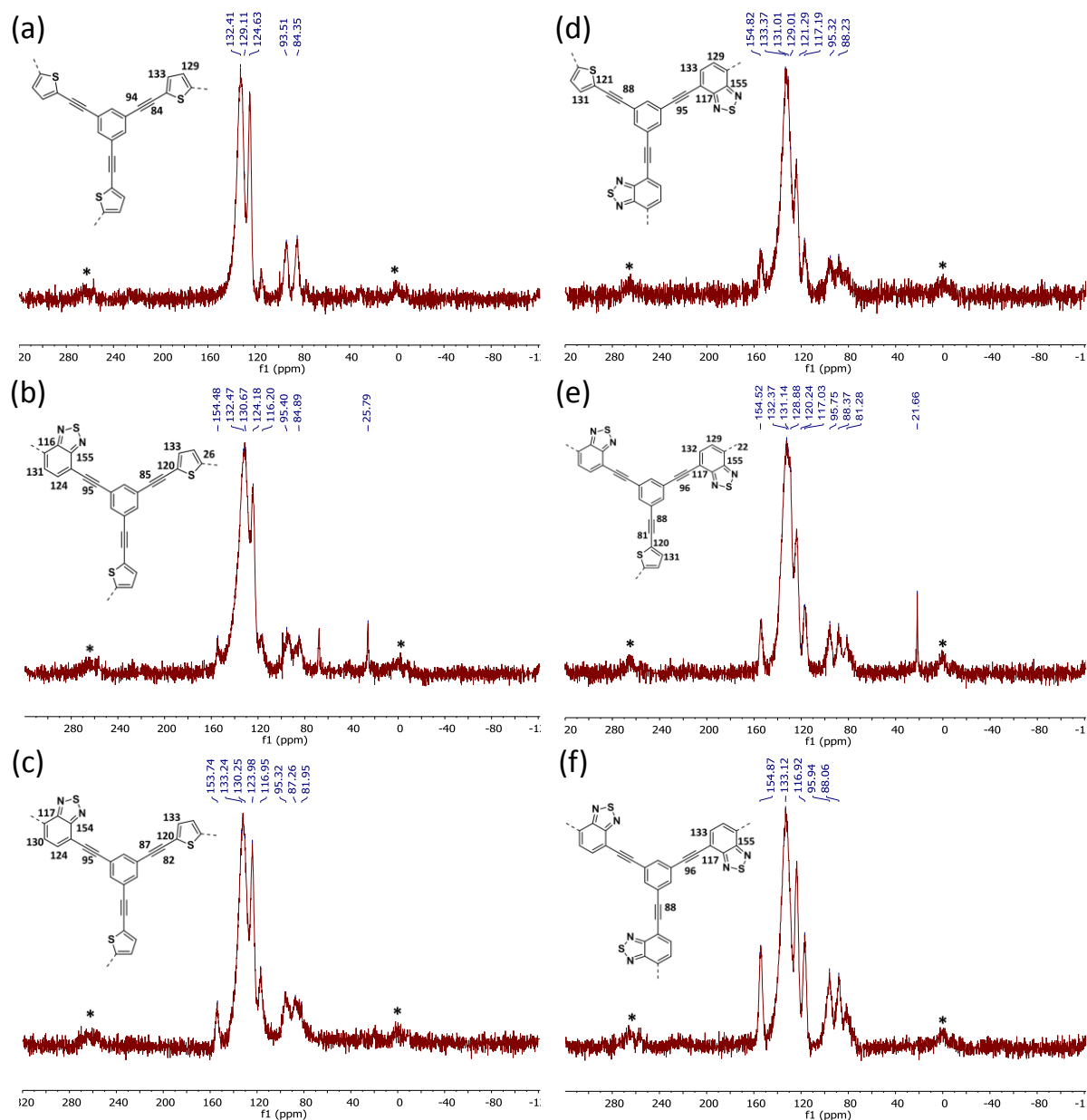


Figure 35. Solid state ^{13}C CP/MAS NMR spectra of (a)Th-BT-0, (b)Th-BT-25, (c)Th-BT-50, (d)Th-BT-70, (e)Th-BT-90 and (f)Th-BT-100. Asterisks denote spinning sidebands.

The CMP NPs were characterized by solid state magic angle spinning nuclear magnetic resonance (^{13}C /MAS NMR) spectroscopy. The spectra showed typical chemical shifts between 120 and 150 ppm for all CMP NPs, which can be assigned to aromatic rings in the polymer backbone (Figure 35). For Th-BT-25, Th-BT-50, Th-BT-70, Th-BT-90 and Th-BT-100 containing benzothiadiazole moieties, a clear increasing signals at about 155 ppm could be observed, which can be assigned to the adjacent carbon next to nitrogen in the BT unit, indicating an increase of the BT content in the polymer backbone structure.

The powder X-ray diffraction (XRD) profile of CMP NPs shows a broad and low intensity pattern around 20° and 24° , which is an indication of amorphous nature (Figure 36).

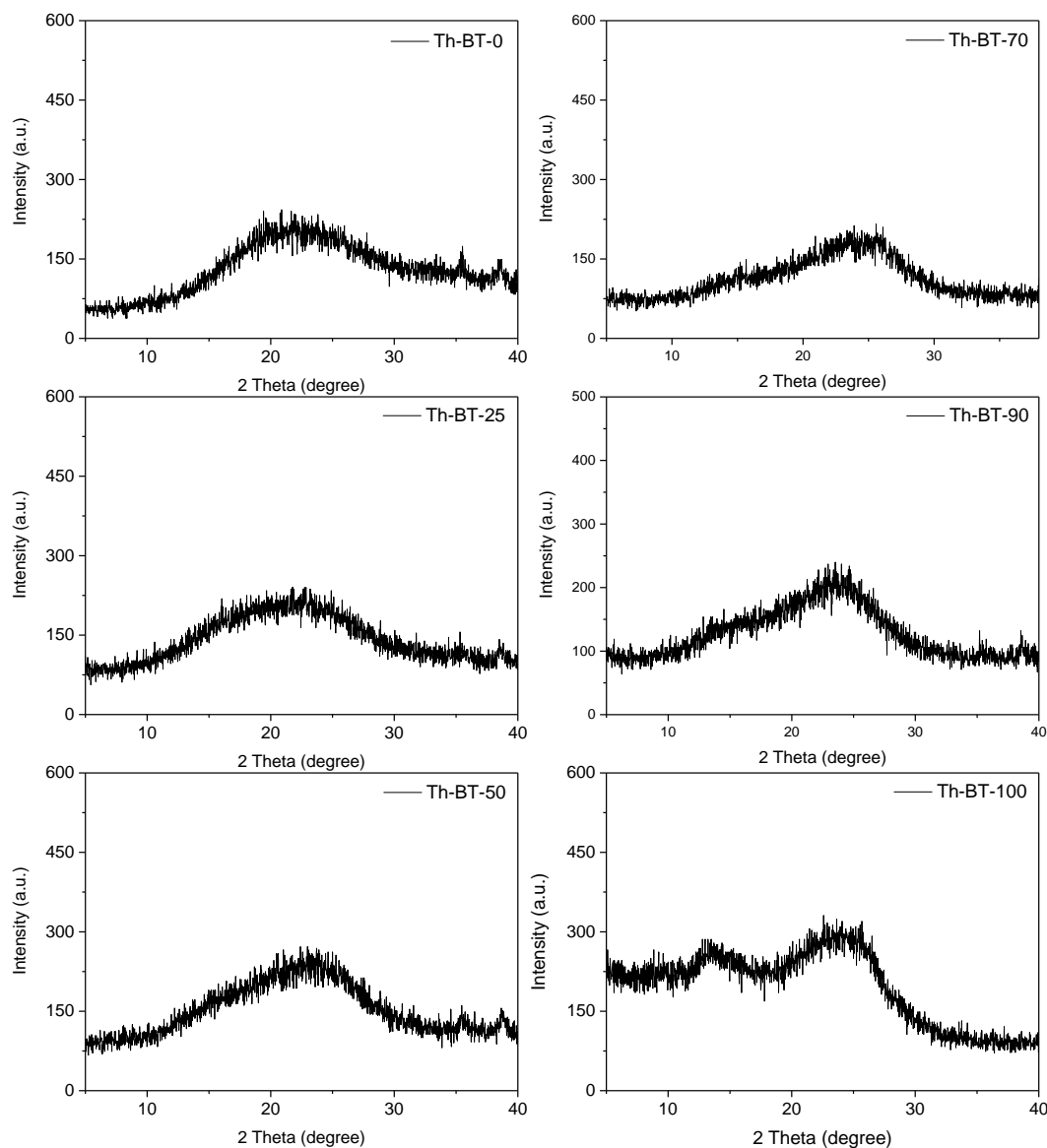


Figure 36. XRD patterns of CMP NPs.

The FTIR spectra of the polymers (Figure 37) showed characteristic vibrational peaks at about $2250\text{-}2100\text{ cm}^{-1}$, which corresponds to the alkyne triple bonds. A distinctive vibrational peak at about 840 cm^{-1} is assigned to the N-S deformation band of the BT unit on Th-BT-25, Th-BT-50, Th-BT-70, Th-BT-90 and Th-BT-100, and absent on Th-BT-0. At the same time, vibrational peaks at about 1196 cm^{-1} and 791 cm^{-1} are

attributed to thiophene units on Th-BT-0, Th-BT-25, Th-BT-50, Th-BT-70, Th-BT-90 and absent on Th-BT-100 (Figure 37).

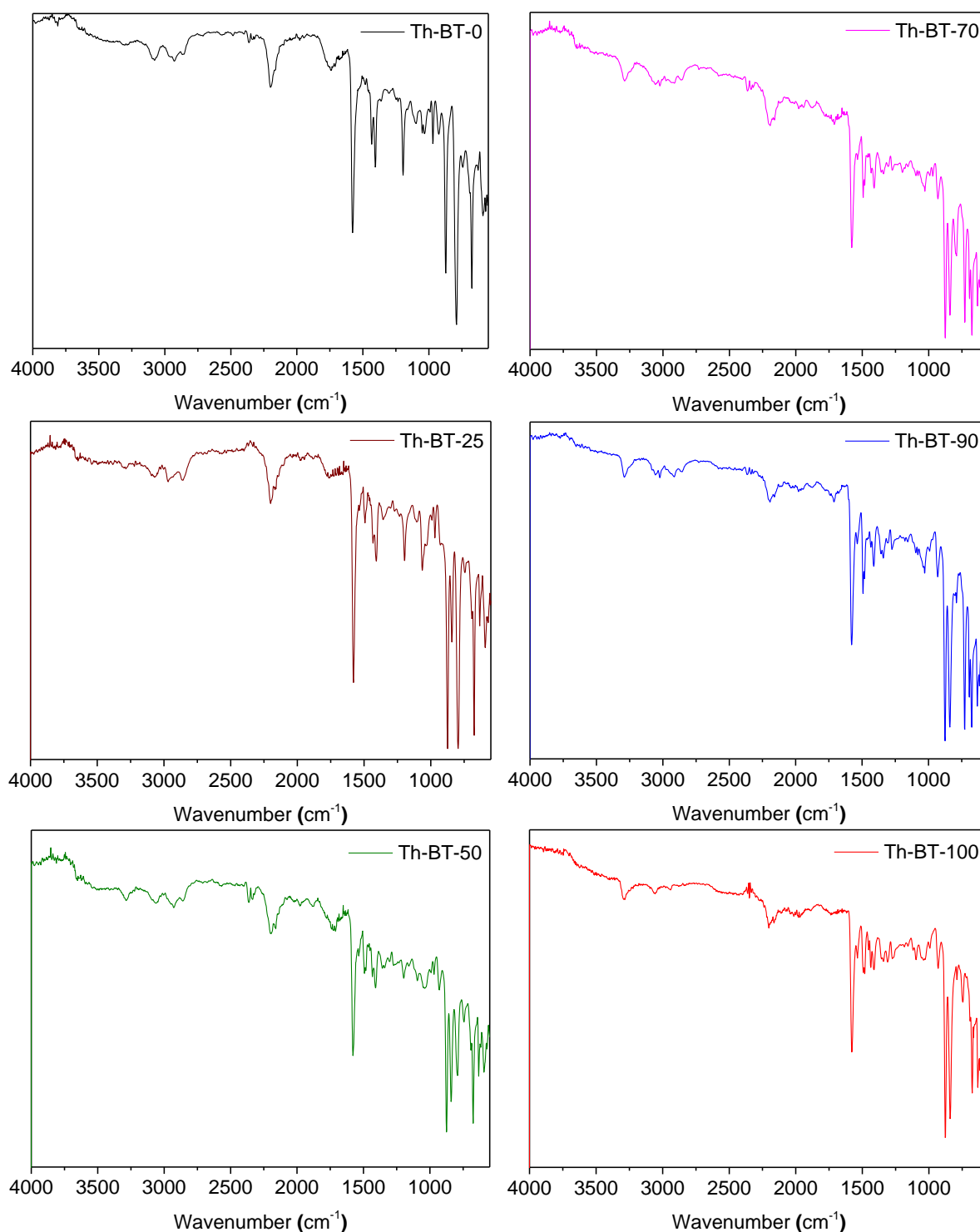


Figure 37. FTIR spectra of CMP NPs.

Thermogravimetric analysis (TGA) indicated that all CMP NPs are thermally stable up to 300°C, with Th-BT-0 which contains only thiophene units, exhibiting the

largest weight loss among all of CMP NPs (Figure 38). It is worth to note that the high weight content (about 75%) after heating the samples to 1000°C could indicate the formation of carbonized materials containing sulphur and nitrogen.

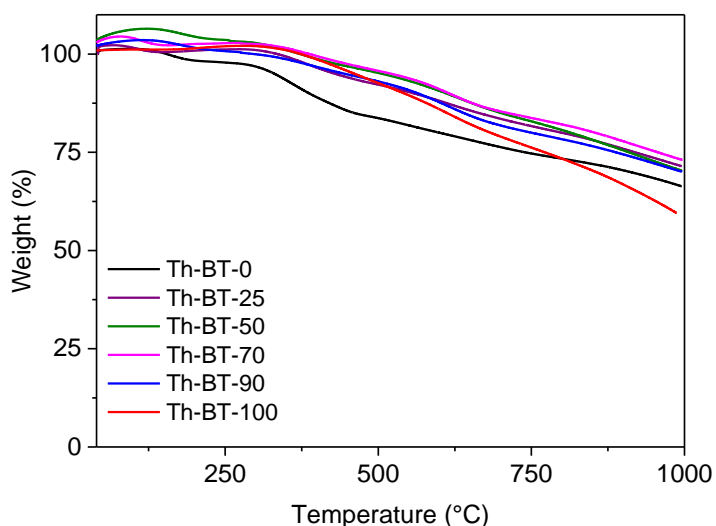


Figure 38. Thermogravimetric analysis of CMP NPs.

Table 3. Porosity data of CMP NPs.

CMP NPs	Surface area ^{a)} [m ² g ⁻¹]	Pore volume ^{b)} [cm ³ g ⁻¹]	Pore diameter [nm]
Th-BT-0	145	0.19	1.5
Th-BT-25	226	0.33	1.5
Th-BT-50	129	0.18	1.5
Th-BT-70	250	0.41	1.5
Th-BT-90	199	0.39	1.5
Th-BT-100	319	0.60	1.4

a) BET surface area calculated over the pressure range 0.05 – 0.35 P/P₀.

b) Pore volume calculated at P/P₀ = 0.99.

The porosity features of CMP NPs were investigated by nitrogen adsorption/desorption experiments at 77.3K. The pore size distribution data are listed in Table 3 and the N₂ sorption isotherms are shown in Figure 39 and Figure 40.

All CMP NPs showed a typical Type I adsorption isotherms (Figure 39 and Figure 40), which indicates a predominant microporous structure. The Brunauer-Emmett-Teller (BET) surface areas of the polymers varied from 129 to 319 $\text{m}^2 \text{g}^{-1}$, with Th-BT-100 exhibiting the highest BET surface area in the polymer series. A similar pore diameter (1.5 nm) was obtained for all CMP NPs (Table 3).

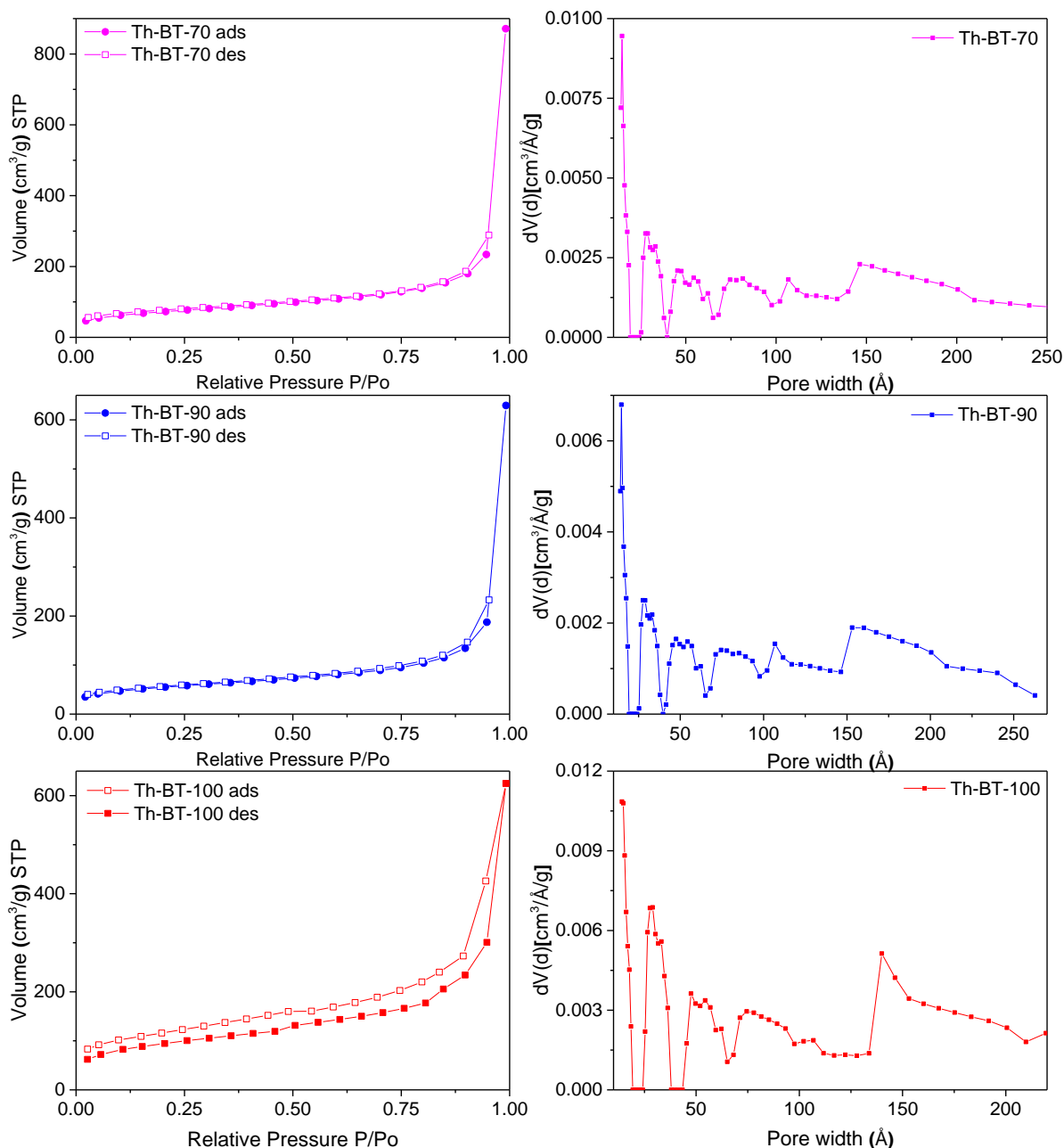


Figure 39. N_2 Sorption Isotherms and Pore Size Distributions of Th-BT-0, Th-BT-25 and Th-BT-50.

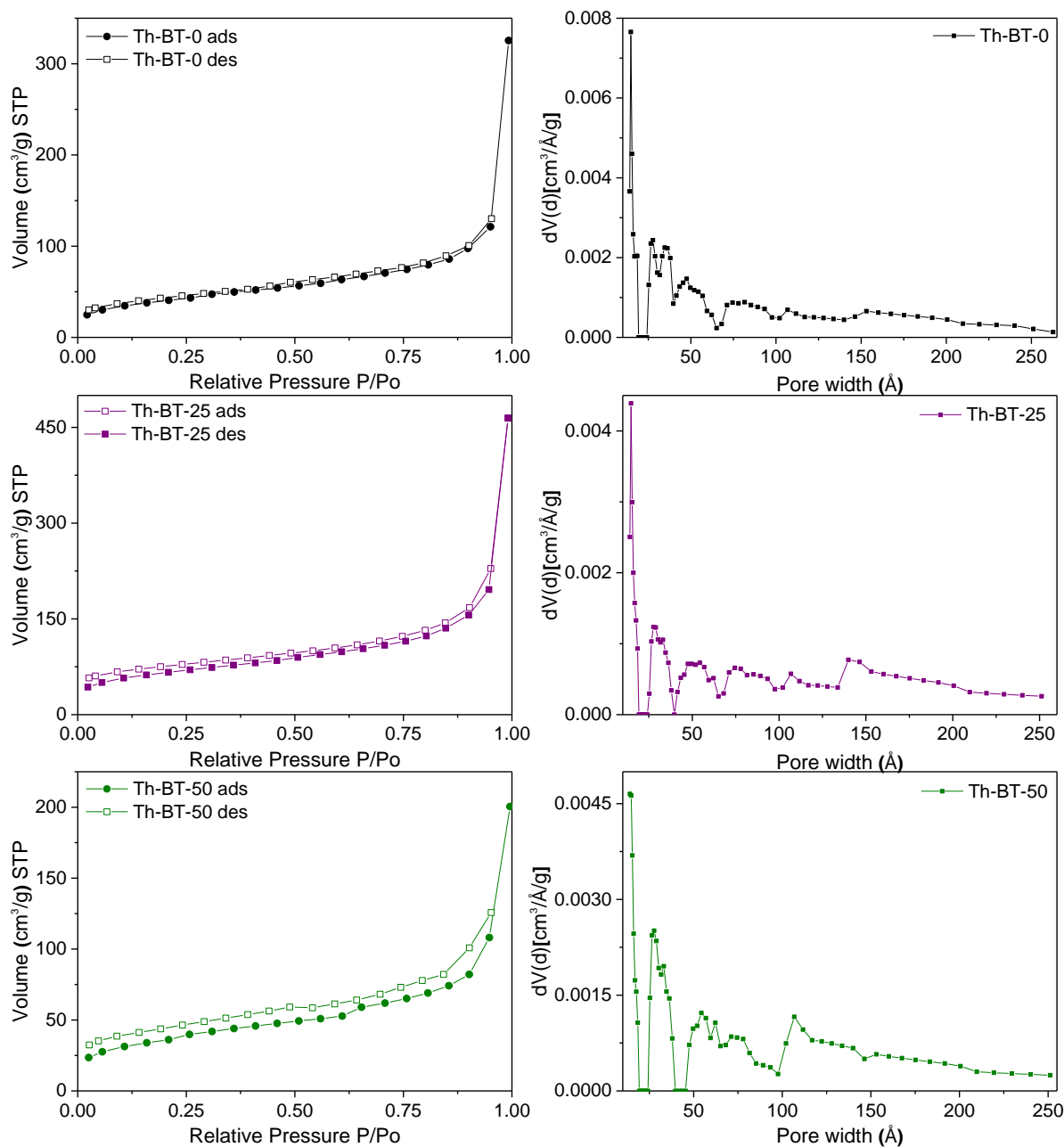


Figure 40. N_2 Sorption Isotherms and Pore Size Distributions of Th-BT-70, Th-BT-90 and Th-BT-100.

The UV/Vis absorption spectra of CMP NPs are displayed in Figure 41a clear trend in the absorption range among the polymers could be observed. The only donor-based Th-BT-0 showed the broadest absorption range in the visible light region. Via successive addition of increasing amounts of the BT unit into the polymer backbone the absorption range of the polymers became sharper towards the blue region of the spectrum. This indicates increasing HOMO-LUMO band gaps by adding more electron-withdrawing moieties into the polymer backbone. All polymers showed a similar

fluorescence emission range from 400 and 800 nm, with a peak at about 540 nm (Figure 41b). However, it can be seen that with the increase in the content of BT units, a progressive decrease in the fluorescence intensity was observed.

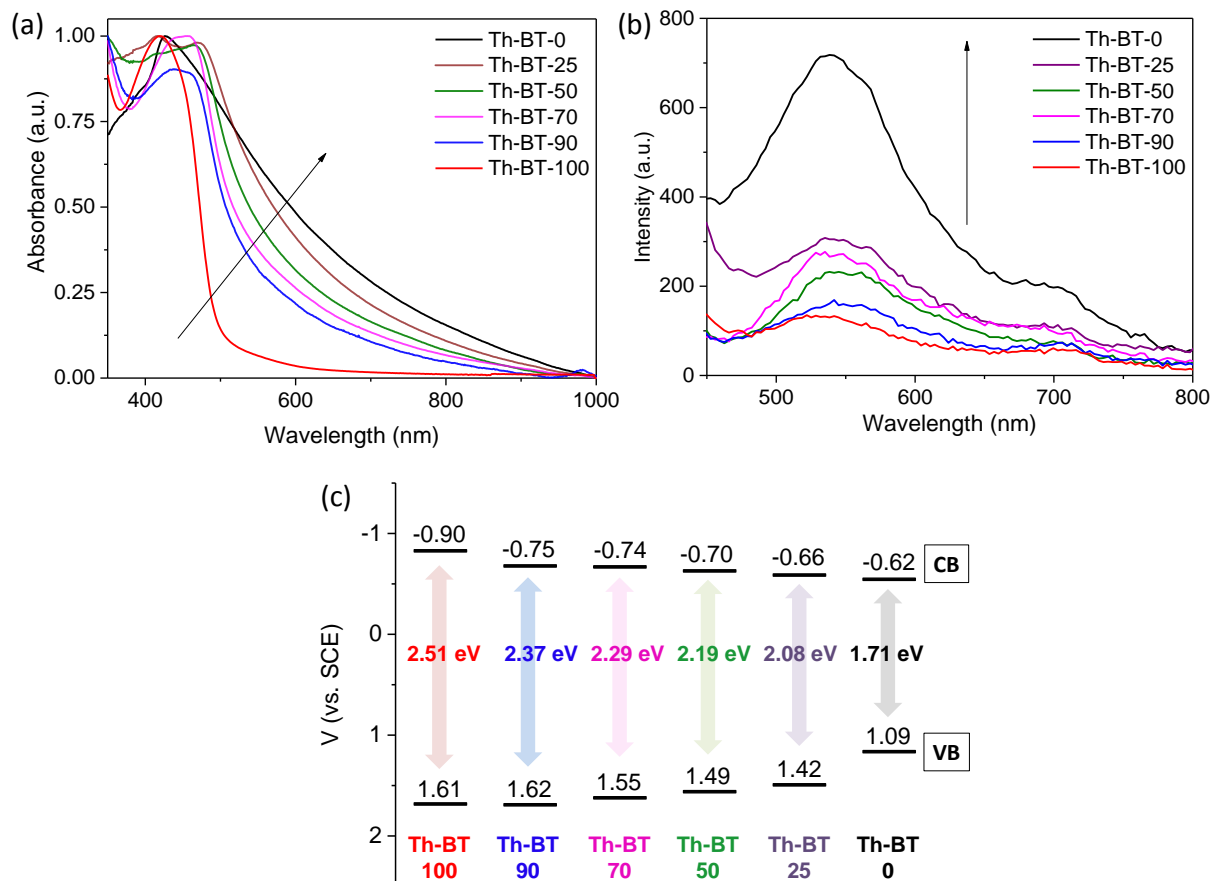


Figure 41. (a) UV/vis absorption spectra; (b) fluorescence emission spectra and (c) valence band (VB) and conduction band (CB) positions of the CMP NPs.

To further study the electronic properties of the polymers cyclic voltammetry (CV) measurements were conducted to determine the valence band (VB) and the conduction band (CB) positions. The CV data are displayed in Figure 41c. Significantly, a clear tendency for the expansion of the band gaps of the polymer series was observed by continuous addition of the electron-withdrawing BT units into the thiophene-based polymer network backbone. This result corresponds to the narrowing tendency observed in the UV/Vis absorption range of the polymers. Th-BT-100, which only contains BT, exhibited the broadest band gap of 2.51 eV with the VB and CB positions lying at +1.61 V and -0.90 V, indicating the highest redox potential of the material. In contrast, the only thiophene containing polymer Th-BT-0 exhibited the narrowest band gap of 1.71 eV with the VB and CB positions lying at +1.09 V and -0.62 V, respectively.

According to the aforementioned ability of conjugated microporous polymers in generating active oxygen species, electron paramagnetic resonance (EPR) spin trapping experiments were conducted using 2,2,6,6-tetramethylpiperidine (TEMP) and 5,5-dimethyl-1-pyrroline *N*-oxide (DMPO) as *singlet* oxygen ($^1\text{O}_2$) and superoxide ($\bullet\text{O}_2^-$) trapping agents, respectively.^[38, 231]

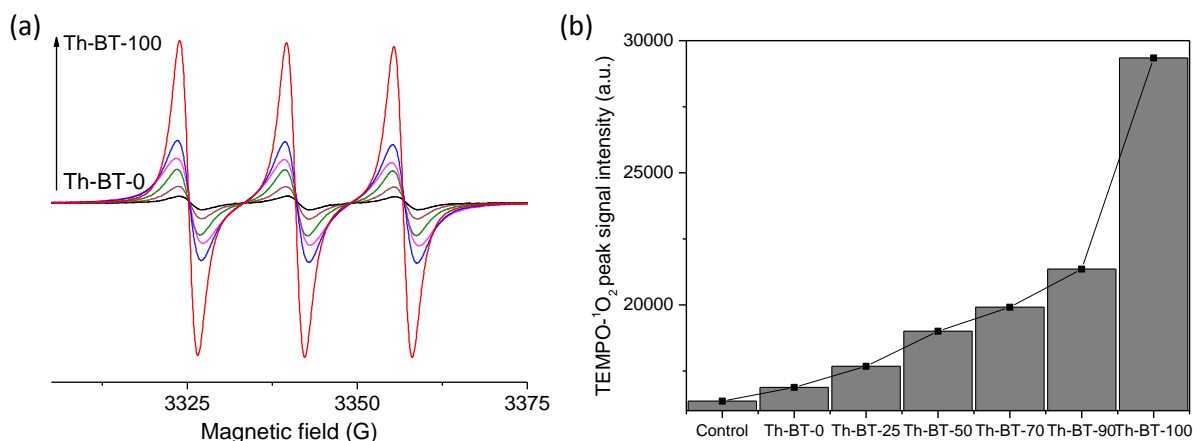


Figure 42. (a) Electron paramagnetic resonance (EPR) spin trapping spectra of TEMPO- $^1\text{O}_2$ adducts in acetonitrile generated by different CMP NPs under visible light irradiation. Conditions: CMP NPs (1 mg mL^{-1}), 2,2,6,6-tetramethylpiperidine (0.1 M), 2h white light irradiation, room temperature. (b) Difference between the TEMPO- $^1\text{O}_2$ adducts peak signal intensity for the CMP NPs after visible light exposure.

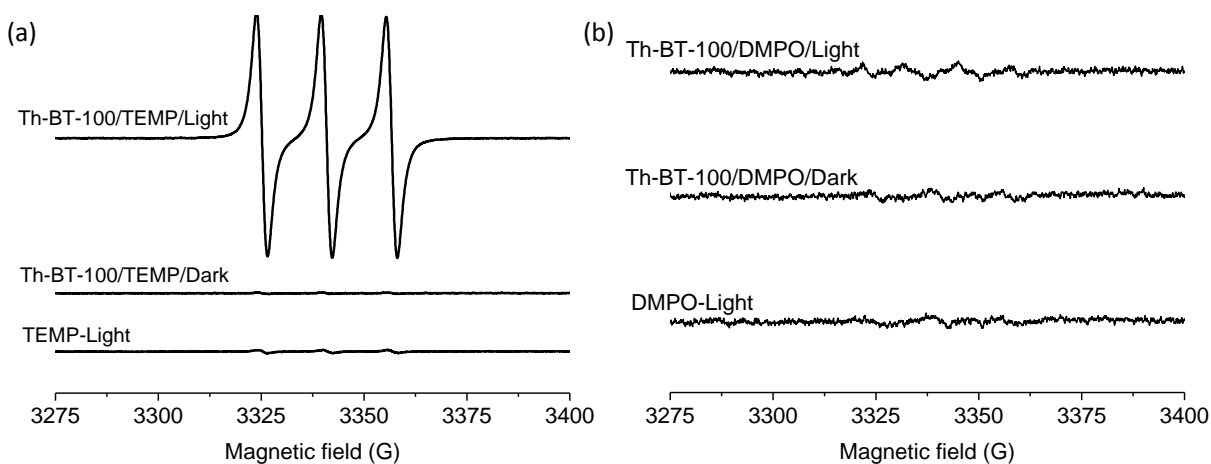


Figure 43. Comparison of the electron paramagnetic resonance (EPR) spectra of TEMPO- $^1\text{O}_2$ adducts (a) and DMPO- $\bullet\text{O}_2^-$ adducts (b) under visible light but in the absence of Th-BT-100, in the presence of Th-BT-100 but without light irradiation, and under visible light and in presence of Th-BT-100.

As displayed in Figure 42, 2,2,6,6-tetramethylpiperidinyloxy (TEMPO- $^1\text{O}_2$) adducts could be determined by using all the CMP nanoparticles under visible light

irradiation. A clear tendency can be seen for the increment of the TEMPO- $^1\text{O}_2$ signal intensity by using the CMP NPs containing increasing contents of BT units in the polymer backbone and Th-BT-100 was able to generate the most intense TEMPO- $^1\text{O}_2$ signals among all the polymer series. This result suggests its superior capacity to photogenerate $^1\text{O}_2$. It was also observed that weak DMPO- $\bullet\text{O}_2^-$ signals could be found in the experiments under light and darkness conditions, which indicates that only a minimal amount $\bullet\text{O}_2^-$ could be generated by the CMP NPs under visible light irradiation (Figure 43). Nevertheless, these results further demonstrate that Th-BT-100 with the highest redox potential was indeed the most efficient photocatalyst among all the series of polymers.

4.2.3 Photocatalytic antibacterial properties

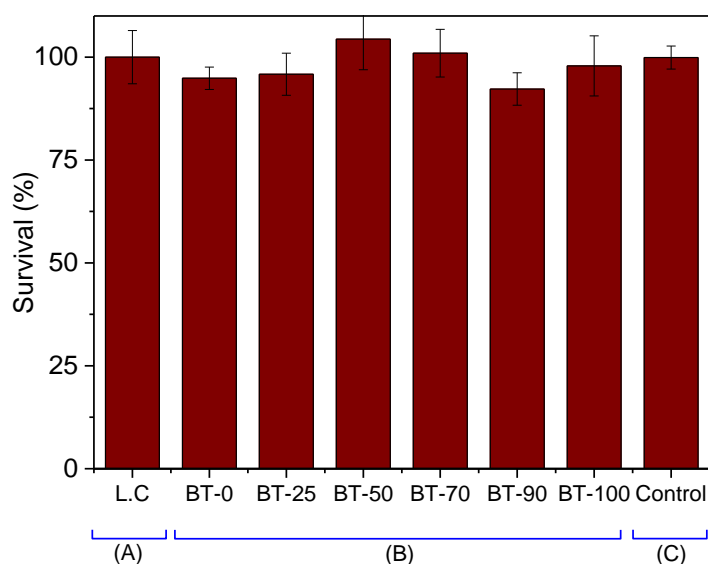


Figure 44. Control experiments of photocatalytic inactivation of *E.coli* K-12 (3×10^6 cfu mL $^{-1}$). (A) Absence of CMP NPs under visible light irradiation for 120 min. (B) In the presence of CMP NPs but without light irradiation for 120 min. (C) In the absence of CMP NPs and without light irradiation. Data represents the results of three independent experiments (mean \pm standard error of the mean).

The visible light promoted antibacterial ability of the CMP NPs were evaluated using *Escherichia coli* K-12 and *Bacillus subtilis* as Gram negative and Gram positive model systems respectively. In this study, a suspension of bacteria was incubated with CMP NPs and exposed to white light irradiation for different time intervals. The viability of the bacteria was assessed using the standard plating method (Experimental section

5.2). To note, all CMP NPs showed no toxic effects on bacteria cells in the absence of light irradiation as shown in the dark experiment (Figure 44).

Figure 45 summarizes the results of the antibacterial activity of all CMP NPs against *E. coli* K-12 and *Bacillus subtilis* under visible light irradiation. It could be clearly shown that the inactivation efficiency of the CMP NPs could be enhanced progressively by increasing the BT content in the polymer backbone, with Th-BT-100 as the most efficient antibacterial agent within the polymer series, achieving about 95% cell death after 120 min of visible light irradiation.

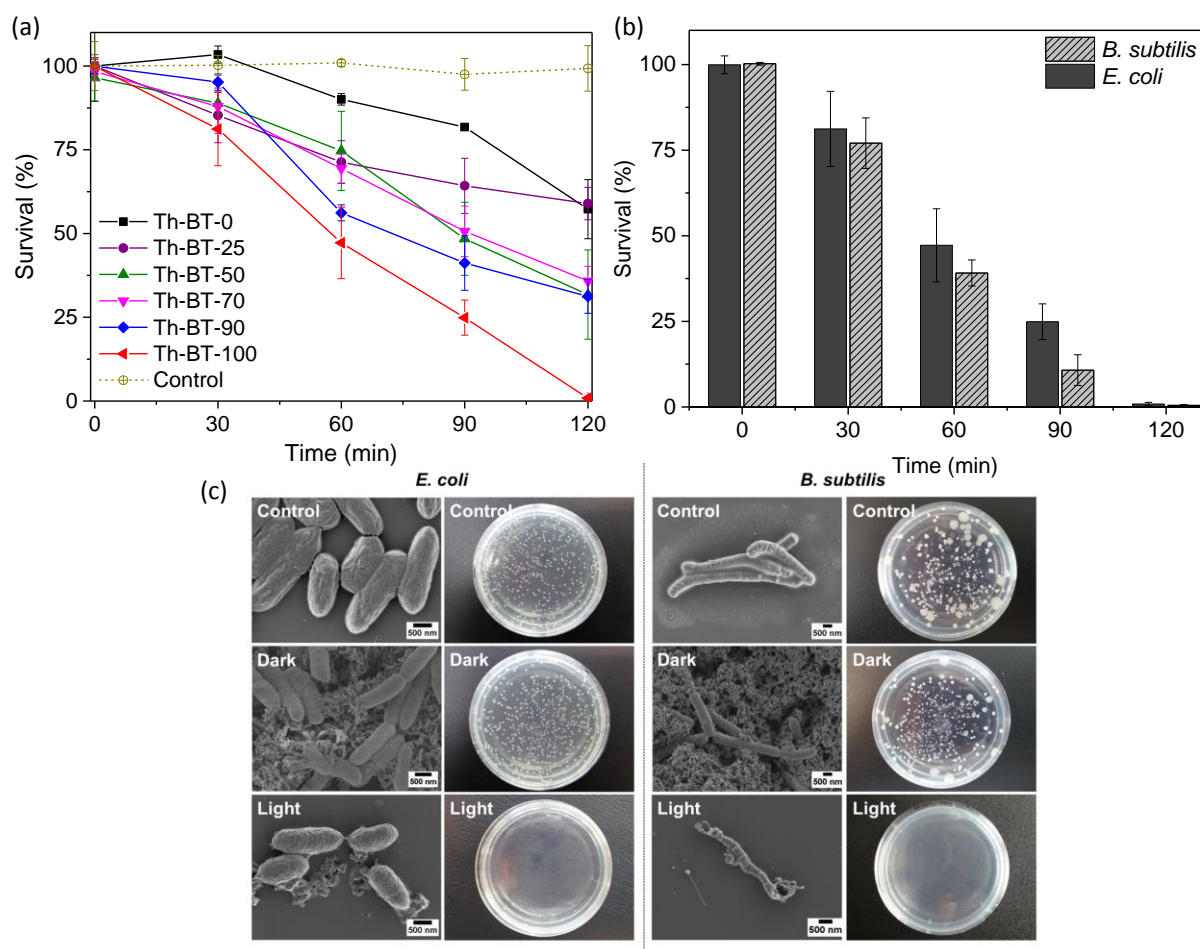


Figure 45. (a) Photocatalytic inactivation of *E. coli* K-12 in the presence of different CMP NPs (1 mg mL⁻¹) under visible light irradiation. Data represents the results of three independent experiments (mean \pm standard error of the mean); (b) Photocatalytic inactivation of *E. coli* K-12 and *B. subtilis* in the presence of Th-BT-100 (1 mg mL⁻¹) under visible light irradiation. Data represents the results of three independent experiments (mean \pm standard error of the mean); (c) SEM images and photographs of *E. coli* K-12 and *B. subtilis* colonies on agar plate as a control group in the absence of Th-BT-100 and light irradiation (top), treated with BT-100 in the dark (middle) and after 120 min of visible light irradiation (bottom).

Th-BT-100 also showed high disinfection efficiency against *B. subtilis* (Figure 45b), reaching about 97% of cell death after 120 min of visible light irradiation, which indicates that Th-BT-100 is highly effective in inactivating both Gram negative and Gram positive bacterium. The scanning electron microscopy (SEM) and photographs of *E. coli* K-12 and *B. subtilis* cells and colonies in the control, dark and light-induced antimicrobial experiments are shown in Figure 45c. It can be clearly seen that no microstructural changes of the bacteria cells can be observed either in the control experiment (Figure 45c top), without Th-BT-100 as antibacterial agent and absence of light irradiation, or in the presence of Th-BT-100 in dark (Figure 45c middle).

As a comparison, by using Th-BT-100 under visible light exposure as antibacterial agent, morphological changes with severe disruptions of the cell membrane of *E.coli* K-12 and *B. subtilis* were observed (Figure 45c bottom), which resulted into further release of cell content and cell death. These results indicate that the inactivation process of the bacteria is caused by the photocatalytic effect of the CMP NPs under light irradiation.

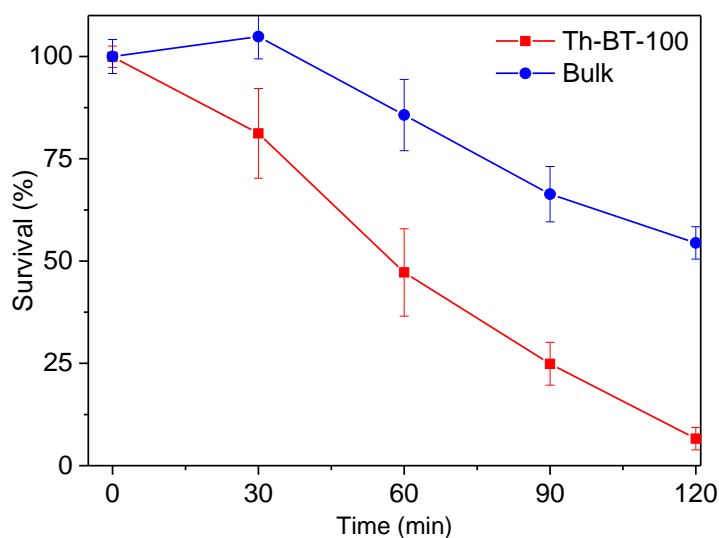


Figure 46. Photocatalytic inactivation of *E.coli* K-12 (3×10^6 cfu mL⁻¹) in the presence of Th-BT-100 and bulk-made Th-BT-100 (1 mg mL⁻¹) under visible light irradiation for different periods of time. Data represents the results of three independent experiments (mean \pm standard error of the mean).

These results are comparable with well-known non-metal based photocatalysts reported recently.^[38] Additionally, compared to its bulk-made form, Th-BT-100 as nanoparticles showed also significant higher antibacterial efficiency (Figure 46). This

result is in accordance to previous works in which nanoparticulate systems showed enhanced photocatalytic activity in contrast to the bulk material.^[7]

4.2.4 The role of reactive oxygen species

In chapter 4.1 it was already shown that CMP NPs could be used for photodegradation of organic dyes in water under visible light irradiation. A number of reactive species such as superoxide ($\bullet\text{O}_2^-$), *singlet* oxygen ($^1\text{O}_2$), electron (e^-), photo-generated hole (h^+) or hydrogen peroxide (H_2O_2) played important roles in the photocatalytic process.^[219, 232]

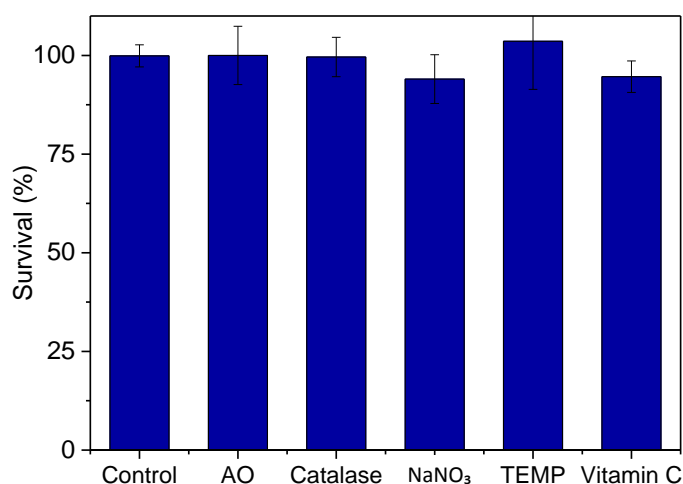


Figure 47. Toxicity test of different radical scavengers (ammonium oxalate – AO, catalase, NaNO_3 , TEMP and Vitamin C; 0.05 mmol L^{-1}) on *E.coli K-12* ($3 \times 10^6 \text{ cfu mL}^{-1}$) in the presence of Th-BT-100 (1 mg mL^{-1}) and in the darkness. Data represents the results of three independent experiments (mean \pm standard error of the mean).

In order to further understand the mechanism of the antimicrobial effect of the CMP NPs, a series of control experiments was conducted with the addition of different active species scavengers into the bacteria reaction system. In particular, ammonium oxalate (AO), catalase, NaNO_3 and TEMP were introduced as scavengers for h^+ , H_2O_2 , e^- and $^1\text{O}_2$ respectively. Vitamin C was also used as a general radical scavenger. It is important to mention that the concentration of each scavenger was adjusted to ensure the highest scavenging effect without presenting toxicity on *E.coli K-12* (Figure 47).^[220, 232]

The effects of different scavengers are illustrated in Figure 48. It can be seen that without the addition of any scavenger, nearly 95% of the *E.coli K-12* were inactivated after 120 min light irradiation. Via addition of TEMP, a *singlet* oxygen scavenger, the survival rate of *E.coli K-12* dropped only about 30%, which confirms the superior role of $^1\text{O}_2$ in the photo-inactivation process of the bacteria. The addition of NaNO_3 as a general electron scavenger showed a similar effect as TEMP, which suggests that once the electron is trapped it will no longer be able to transfer its energy to dioxygen, and therefore blocking the generation of $^1\text{O}_2$.

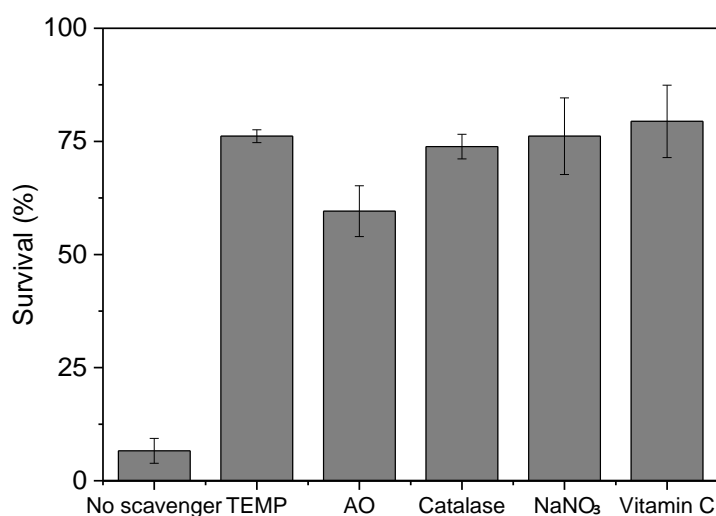


Figure 48. Photocatalytic inactivation of *E.coli K-12* using different scavengers (ammonium oxalate (AO), catalase, NaNO_3 , TEMP and Vitamin C) and Th-BT-100 as antibacterial agent. Conditions: 0.05 mmol L^{-1} concentration of scavengers, air, 120 min white light irradiation. Data represents the results of three independent experiments (mean \pm standard error of the mean).

Interestingly, the addition of AO as the hole scavenger led to about 60% of bacteria survival, which indicates that Th-BT-100 was not only able to promote photocatalytic bacterial disinfection via reduction of molecular oxygen, but also via a direct oxidative pathway from the photo-generated electron-hole species, which could likely oxidize the components of the cell membrane of *E.coli K-12* and subsequently leading to its direct inactivation and possible mineralization of its organic content.^[233, 234] As shown in Figure 45c, the bacteria cells were surrounded by the nanoparticles, this proximity was important for an enhanced diffusion of the active species from the nanoparticles onto the bacteria cells despite the short lifetime of $^1\text{O}_2$ in water.^[218, 235]

To further study the $^1\text{O}_2$ generation efficiency, an additional experiment was performed using α -terpinene as $^1\text{O}_2$ trapping agent.^[220, 232] Figure 49 shows the typical peaks assigned to the substrate α -terpinene before the reaction, mesitylene was used as an internal reference for the reaction.

A full conversion of ascaridole as product could be seen after 2 h under visible light using Th-BT-100 as photocatalyst (Figure 50), giving a $^1\text{O}_2$ generation rate of ca. $0.14 \text{ mmol g}^{-1} \text{ s}^{-1}$ for Th-BT-100. At the same time, no conversion was observed once the reaction was performed under the absence of oxygen (Figure 51).

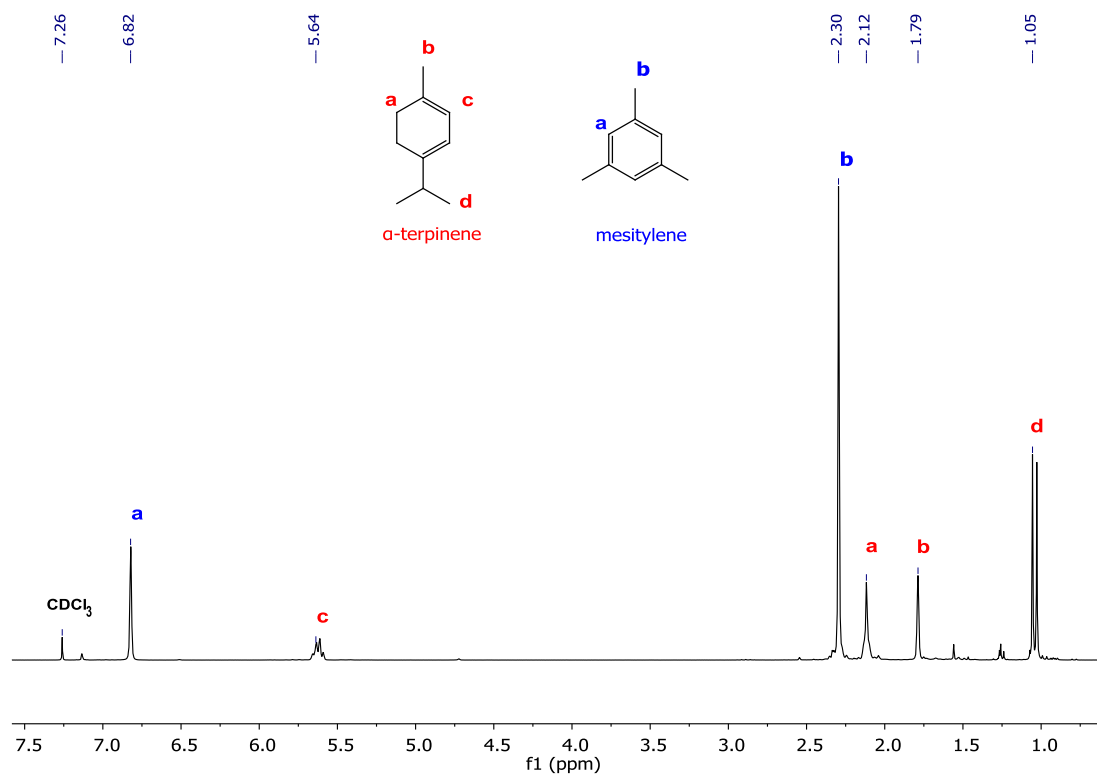


Figure 49. ^1H NMR spectra of mesitylene and the starting compound α -terpinene in CDCl_3 . ^1H NMR (250 MHz, CDCl_3): δ 6.82 (s, 3H, mesitylene), 5.65 – 5.61 (m, 1H, α -terpinene), 2.30 (s, 9H, mesitylene), 2.12 (m, 4H, α -terpinene), 1.79 (s, 3H, α -terpinene), 1.05 (d, 2H, α -terpinene).

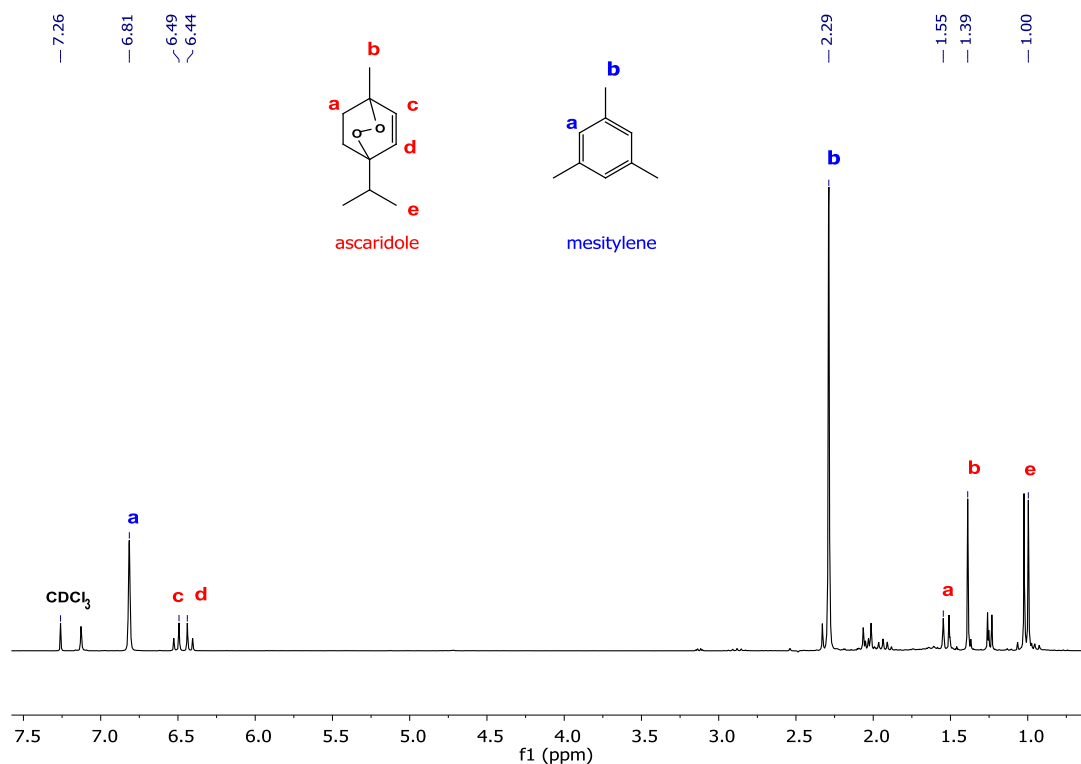


Figure 50. ^1H NMR spectra of mesitylene and the product ascaridole and in CDCl_3 . ^1H NMR (250 MHz, CDCl_3): δ 6.82 (s, 3H, mesitylene), 6.49 (d, 1H, ascaridole), 6.44 (d, 1H, ascaridole), 2.29 (s, 9H, mesitylene), 1.55 (m, 2H, ascaridole), 1.39 (s, 3H, ascaridole), 1.00 (d, 6H, ascaridole).

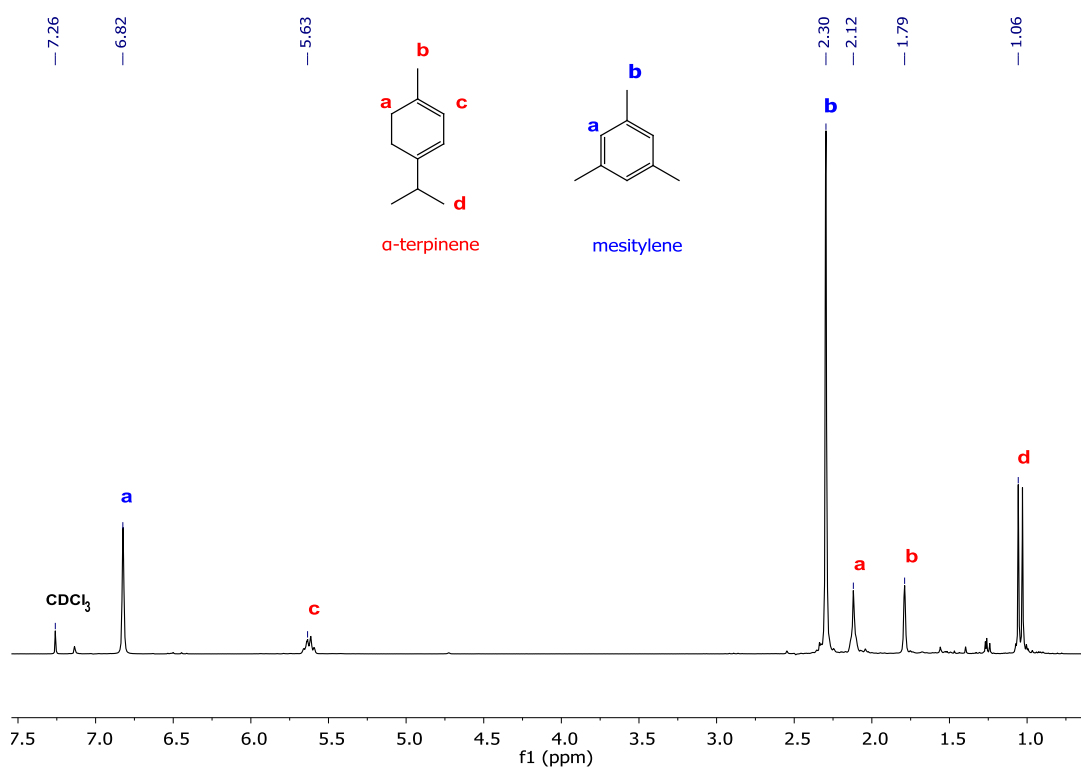


Figure 51. ^1H NMR spectra of mesitylene and α -terpinene in CDCl_3 under the absence of oxygen. ^1H NMR (250 MHz, CDCl_3): δ 6.82 (s, 3H, mesitylene), 5.65 – 5.61 (m, 1H, α -terpinene), 2.30 (s, 9H, mesitylene), 2.12 (m, 4H, α -terpinene), 1.79 (s, 3H, α -terpinene), 1.06 (d, 2H, α -terpinene).

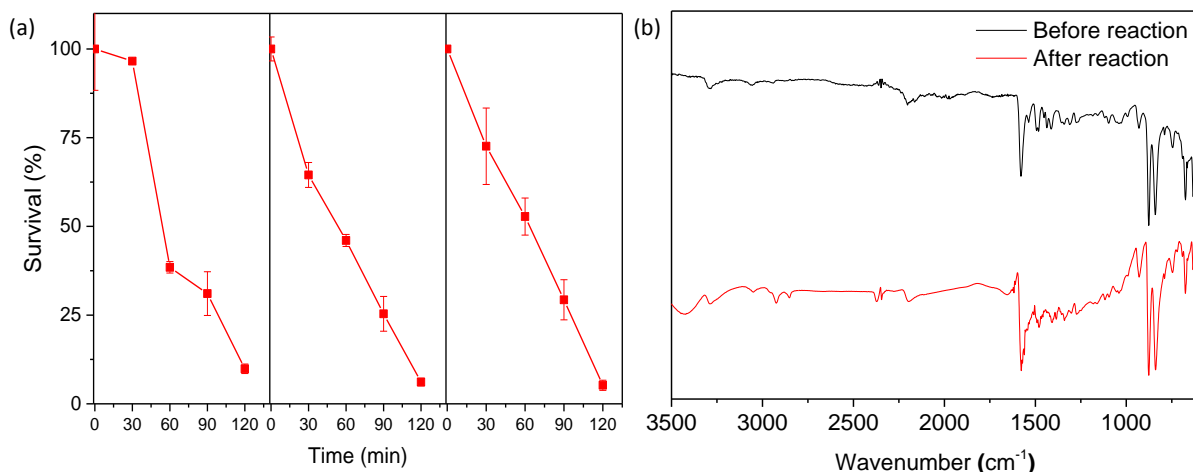


Figure 52. (a) Repeated experiments of photocatalytic inactivation of *E. coli* K-12 (3×10^6 cfu mL⁻¹) in the presence of Th-BT-100 (1 mg mL⁻¹) under visible light irradiation. Data represents the results of three independent experiments (mean \pm standard error of the mean); (b) FTIR spectra of Th-BT-100 before and after the third cycle of the repeating photocatalytic bacteria inactivation.

Furthermore, the stability and reusability of Th-BT-100 were investigated via repeating experiments under the same reaction conditions. As shown in Figure 52a, Th-BT-100 could be reused for another three additional cycles and nearly 95% of bacteria were inactivated in each cycle. No apparent changes were observed in the FTIR spectra of Th-BT-100 after the photocatalytic reaction, which indicates the high stability of the photocatalyst (Figure 52b).

4.2.5 Conclusions and outlook

As a conclusion from this chapter, a structural design principle of the conjugated microporous polymer nanoparticles was reported as a new class of highly effective photoactive agents for inactivation of bacteria in water under visible light irradiation. Via molecular doping method of electron-withdrawing moieties into the electron-donating polymer backbone, enhanced light-induced antimicrobial activity could be demonstrated in the photo-inactivation of *E. coli* K-12 and *B. subtilis*. Different photo-generated active species could be determined using the polymer nanoparticles, with *singlet* oxygen playing the main role during the photo-inactivation process. This study demonstrated a further application of conjugated microporous polymer nanoparticles as pure organic, non-toxic and active agents for the photodynamic inactivation of microorganisms.

4.3 Visible light induced photocatalytic recycling of NAD⁺ cofactor by Conjugated Microporous Polymer Nanoparticles[‡]

In this chapter a nicotinamide adenine dinucleotide (NAD⁺) cofactor regeneration module mediated by conjugated microporous polymer nanoparticles (CMP NPs) is presented. *Via* a simple visible light-induced photocatalytic oxidation process using CMP NPs as photocatalyst, high conversion rates of recycled NAD⁺ were obtained without the use of any additional mediators. Furthermore, the light-induced conversion of NADH to NAD⁺ coupled with the enzymatic oxidation of propylene glycol was successfully achieved in either one-pot or two steps enzymatic reactions.

4.3.1 Motivation

The recycling of nicotinamide nucleotide cofactors is an essential feature of the metabolism in living cells, which is necessary for the establishment of cytosolic redox homeostasis. In nature, this process is controlled by a complex and highly regulated network of enzymatic transformations responsible for the biosynthesis of important metabolites that support life.

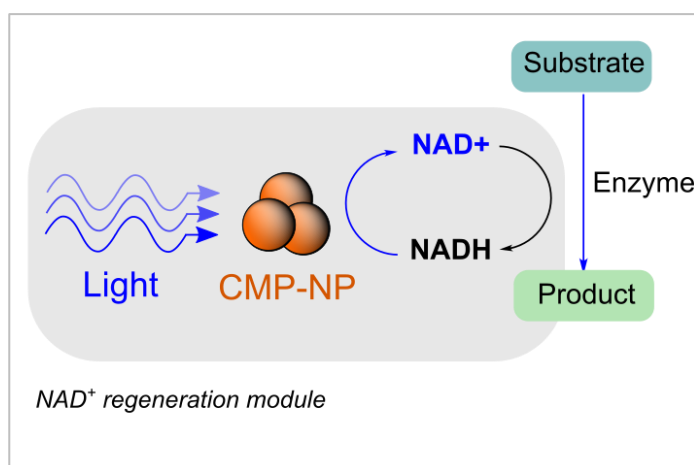
In the cell, nicotinamide cofactors, NAD(H) and NADP(H), are used by oxidoreductases responsible for the establishment of reduction/oxidation reactions of organic substrates. The high selectivity usually involved with such enzymatic reactions has been explored for large-scale production of high end-value compounds. Some examples include the production of enantiomerically pure amino acids, alcohols and steroids. [236, 237] However, the high costs of NAD(H) and NADP(H) significantly reduce the economic viability of redox biotransformations in large-scale. This limitation has prompted the development of cost-reducing cofactor regeneration strategies in which either the oxidized or reduced forms of the cofactor are selectively recycled after their transformations by oxidoreductases.[238]

While different systems have been investigated for the regeneration of reduced nicotinamide cofactors by non-enzymatic approaches, such as chemical and photochemical transformations, [238-241] the regeneration of bioactive oxidized cofactors is much less developed. [238, 242] Therefore, it is of great interest to further develop a new method for the regeneration of nicotinamide nucleotide cofactors with high efficiency.

[‡] This work was a cooperation project with Dr. Lucas Caire da Silva from Max Planck Institute for Polymer Research. *Manuscript in preparation.*

To develop a metal-free and more sustainable chemical process for the regeneration of NAD(H) and NAD⁺ cofactors without involving complex metal containing mediators, this chapter is aimed to explore the use of conjugated microporous polymers (CMPs), the new class of metal-free photocatalyst as described in previous chapters for this purpose. [7, 133, 150, 155, 197] Moreover, the use of light in the visible region offers a clean, abundant and environmental friendly alternative to perform countless of chemical reactions, and have the advantage of minimizing side reactions and are cost effective, which is more appealing for large-scale production since it does not require special costly settings. [18, 19]

In this work, a heterogeneous visible light-induced NAD⁺ regeneration module based on the photocatalytic oxidation of NADH mediated by conjugated microporous polymer nanoparticles is described. [118, 243] In Scheme 3, the principle of the regeneration module is displayed. The light-dependence offers an external control that triggers the regenerative response, producing bioactive NAD⁺ upon irradiation of visible light without the need for mediators or transfer agents between the cofactor and the photocatalyst. This approach allows a clean and efficient triggered-regeneration of NAD⁺ with facile removal of the nanoparticles.



Scheme 3. General scheme of NAD⁺ regeneration module. NADH can be selectively converted to NAD⁺ by nanoparticle mediated photocatalysis.

4.3.2 Synthesis and characterization

The nanoparticles of a conjugated microporous polymer B-BO₃ were prepared via palladium-catalysed Sonogashira-Hagihara cross-coupling polycondensation reaction of 4,7-dibromobenzooxadiazole (BO) with triethynylbenzene in an oil-in-water

mini-emulsion. The detailed synthesis and characterization of the polymers are described in the experimental section 5.3.

B-BO₃ was obtained as a dispersion of nanoparticles in aqueous medium. The SEM and TEM images displayed on Figure 53 showed the material as nanospheres with diameters between 50 - 80 nm.

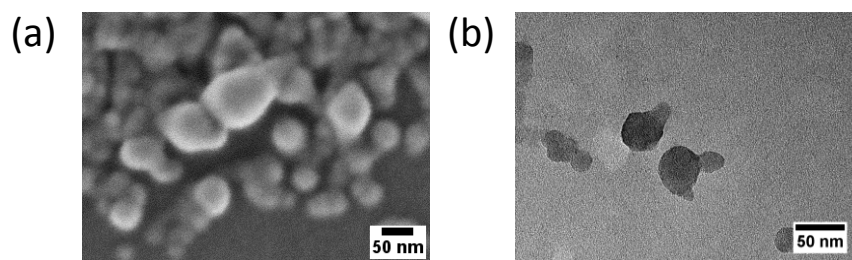


Figure 53. SEM (a) and TEM (b) images of B-BO₃.

Solid state ¹³C/MAS NMR spectra showed signals at 144 ppm, which can be assigned to the carbon adjacent to the nitrogen atom of the BO unit (Figure 54). The signals at 127 and 130 ppm can be assigned to the aromatic carbon atoms in the BO unit.

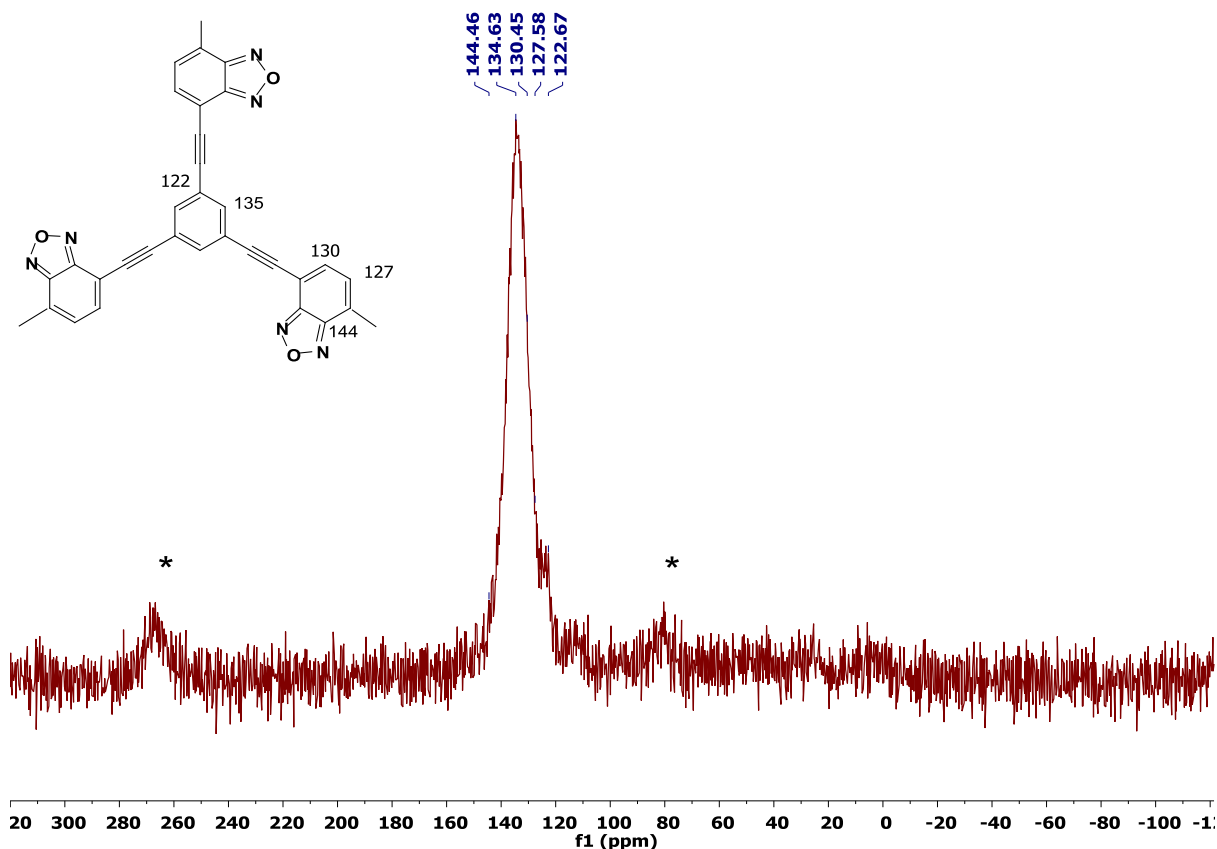


Figure 54. Solid state ¹³C CP/MAS NMR spectra of B-BO₃.

The FTIR spectra of B-BO₃ showed typical signals at 1400 and 1580 cm⁻¹, which can be assigned to the skeleton vibration of the aromatic rings and signals at 2204 cm⁻¹ can be assigned to C≡C bond vibration in the polymers. The signals at 1380 and 1520 - 1560 cm⁻¹ can be assigned to the N-O stretching modes of the BO unit (Figure 55).

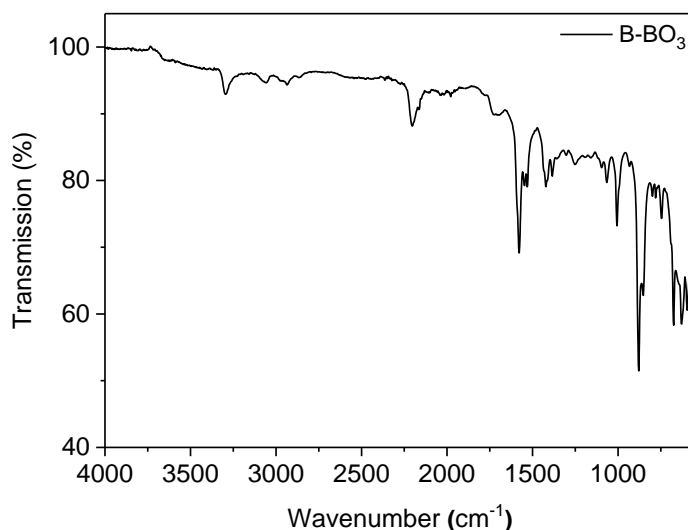


Figure 55. FTIR spectra of B-BO₃.

The powder X-ray diffraction (XRD) profile reveals a broad and low intensity pattern around 24°, which is an indication of amorphous nature of the CMP (Figure 56).

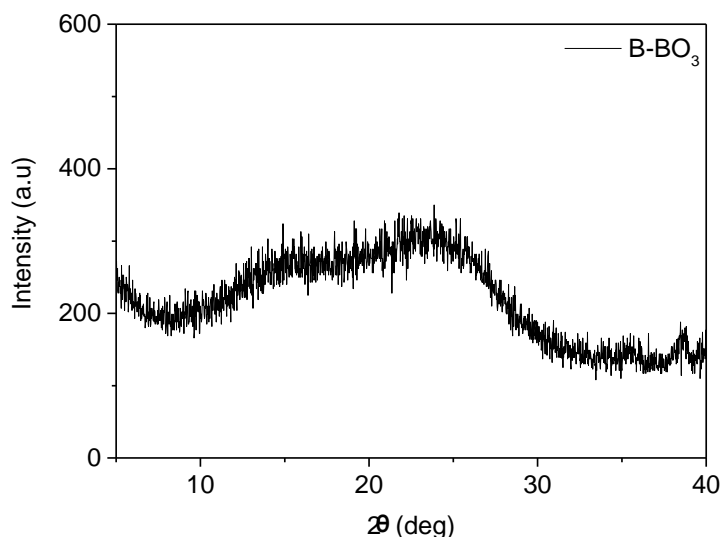


Figure 56. XRD patterns of B-BO₃.

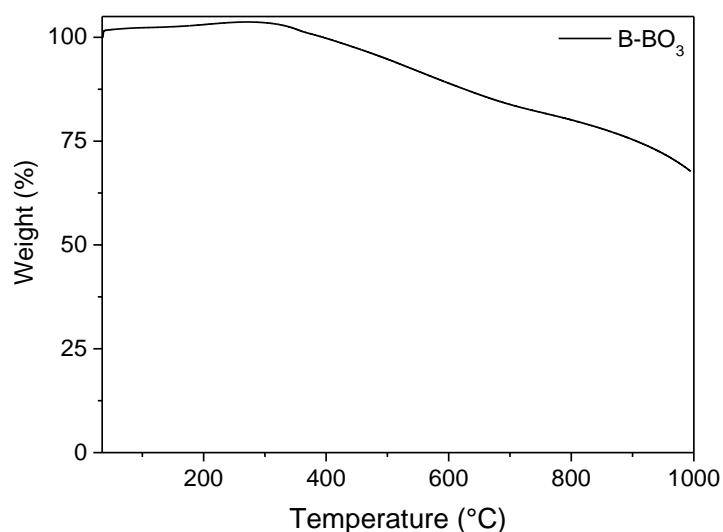


Figure 57. Thermogravimetric analysis of B-BO₃.

Thermogravimetric analysis (TGA) indicated that the polymer is thermally stable up to 300 °C (Figure 57). The high weight content (about 60%) after heating the sample to 1000 °C could indicate the formation of carbonized material.

The porosities of the B-BO₃ were investigated by nitrogen adsorption/desorption experiments at 77.3K. The B-BO₃ showed a typical Type I adsorption isotherms (Figure 58), which indicates a predominant microporous structure. The Brunauer-Emmett-Teller (BET) surface area was 412 m² g⁻¹ with a pore diameter of 1.4 nm.

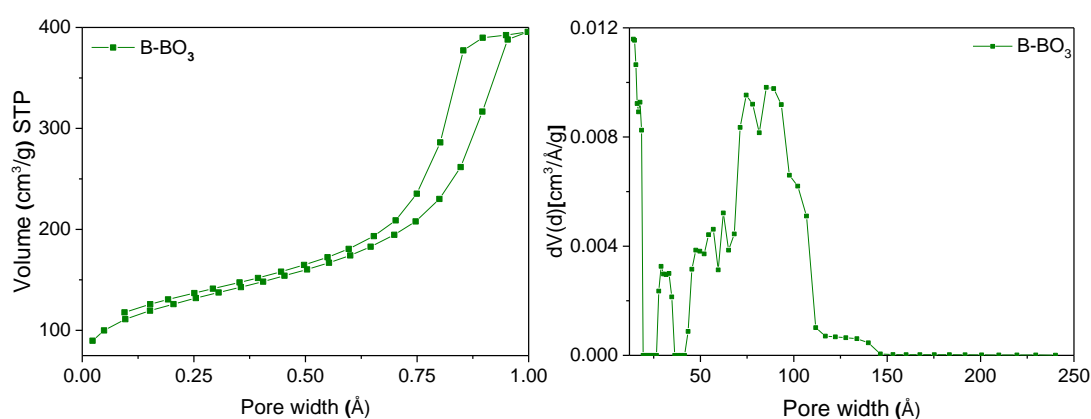


Figure 58. N₂ Sorption Isotherms and Pore Size Distributions of B-BO₃.

The UV/vis diffuse reflectance spectrum (DRS) of the polymer is displayed in Figure 59. B-BO₃ showed broad absorption range in the visible region. An optical gap of 2.48 eV could be estimated from the edge of the UV-vis spectra (Figure 59).

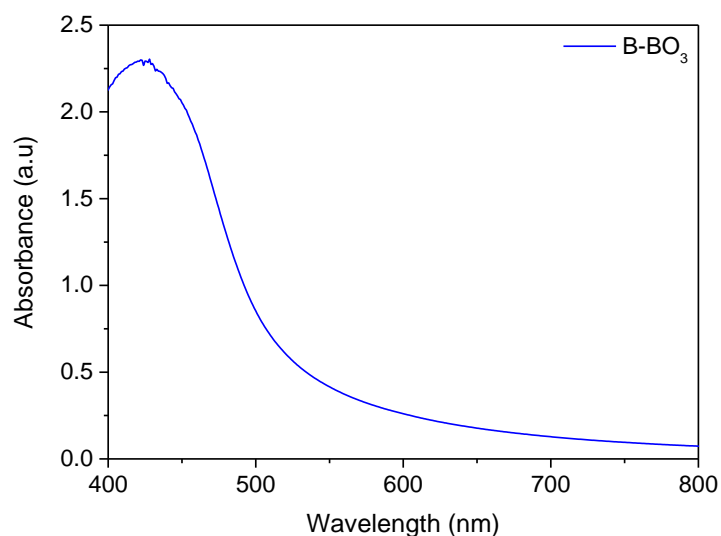


Figure 59. UV/vis absorption spectra of B-BO₃.

To further study the energy band structures of the polymers, cyclic voltammetry (CV) measurements were conducted (Figure 60a). The results showed that HOMO and LUMO positions laid at +1.69 V and -0.79 V vs. SCE, respectively (Figure 60b).

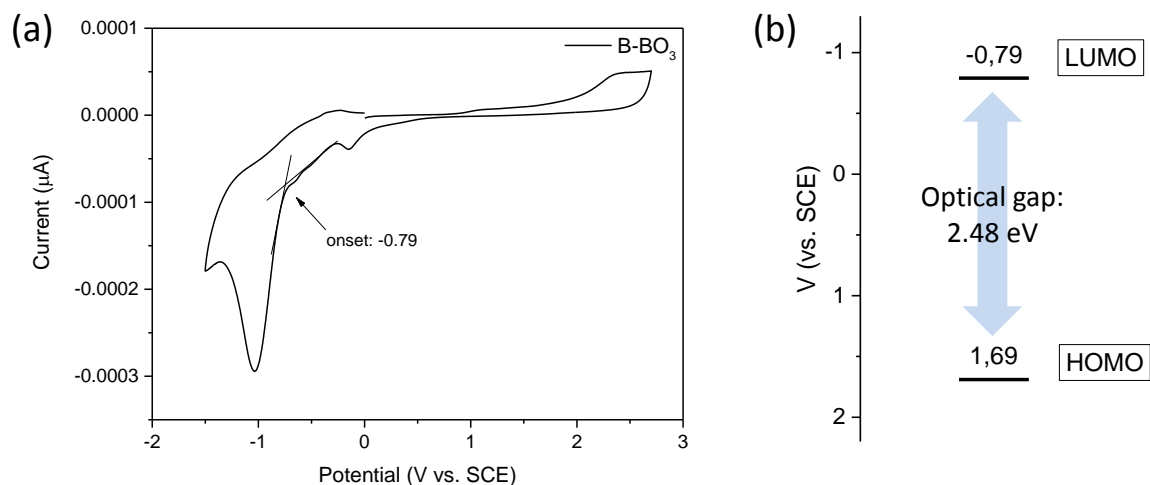


Figure 60. (a) Cyclic voltammetry measurement from B-BO₃; (b) HOMO and LUMO positions of B-BO₃.

4.3.3 Photocatalytic properties for regeneration of NAD⁺ cofactor

The conversion of NADH to NAD⁺ by B-BO₃ under visible light irradiation is shown in Figure 61. A clear chemical shift is observed where the aromatic protons of NAD⁺ are distinct from NADH (Figure 61a). The conversion of NADH was monitored by

integration of the corresponding peaks and shows that about 50% of the starting NADH (0.02 M) was oxidized after 1 h of light irradiation in the presence of B-BO₃ and O₂. Conversions up to 80% were observed in 2 h with longer reaction times leading to signs of degradation indicated by ¹H-NMR spectroscopy.

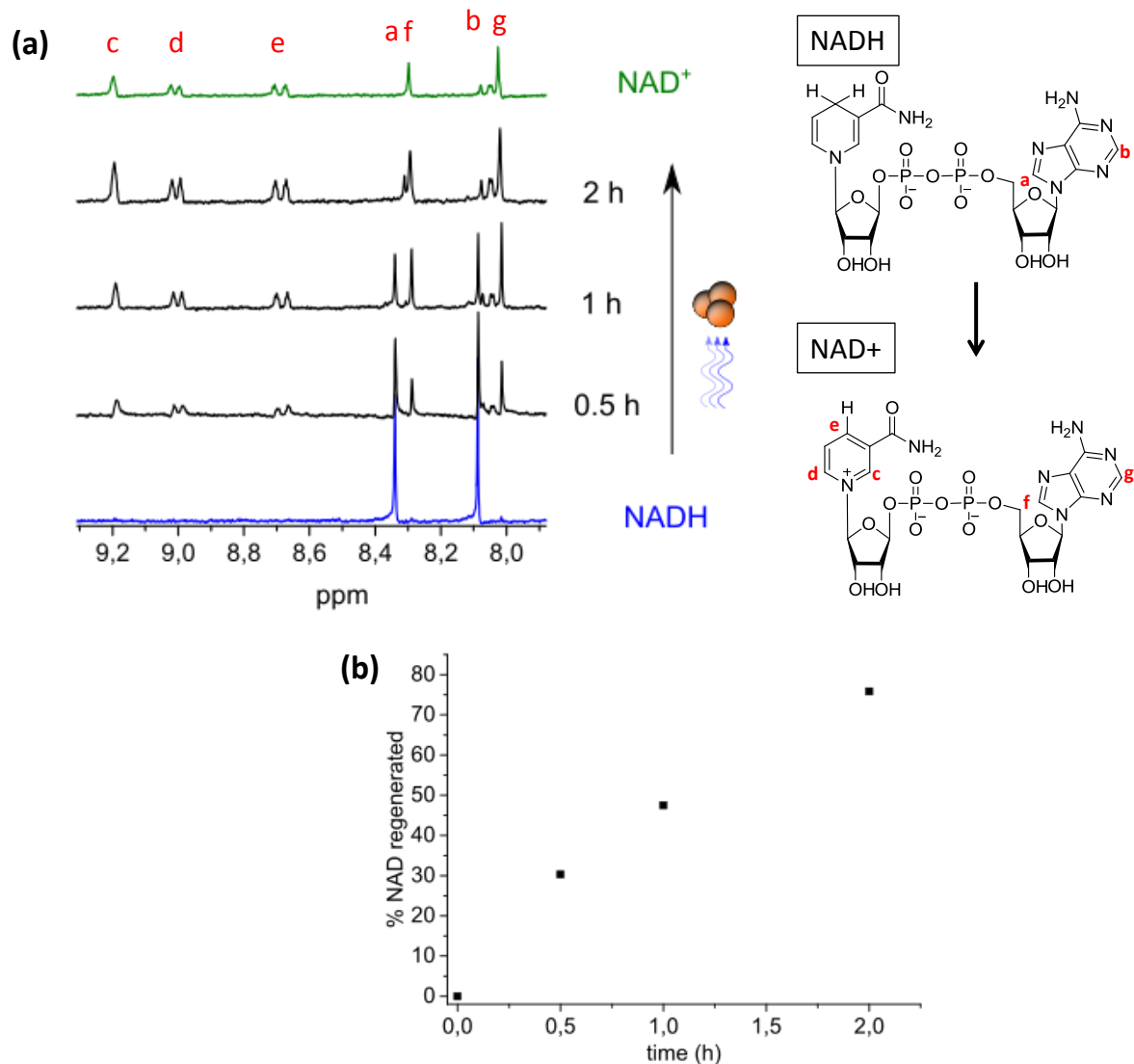


Figure 61. Regeneration of NAD⁺ from NADH with B-BO₃. a) ¹H-NMR spectra at different times during conversion under blue light irradiation in the presence of O₂. b) Conversion (%) of NAD⁺ over time.

The biocompatibility of the regenerated-NAD (rNAD) was tested with the NAD-dependent oxidation of propylene glycol (PG) to hydroxyacetone (HA) catalysed by glycerol dehydrogenase (GDH). Propylene glycol was chosen for its high affinity for GDH and the easy detection of the oxidation product (hydroxyacetone) by ¹H-NMR spectroscopy.^[244]

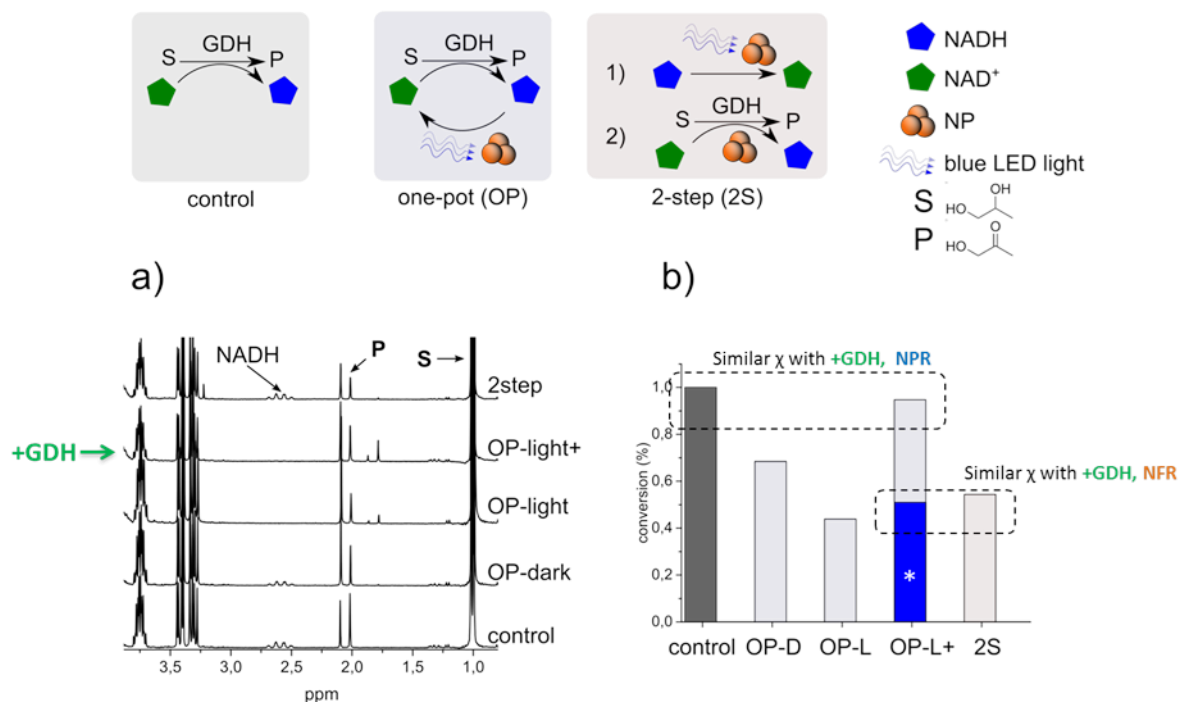


Figure 62. Oxidation of propylene glycol by NAD-dependent GDH given as % of converted substrate. a) Determination of reaction conversion by ^1H NMR at the equilibrium state. Values were obtained from the integration of the methyl protons in propylene glycol (P) relative to the equivalent signals from the substrate (S). b) Conversions of propylene glycol for the different experimental set-ups shown on top of diagram.

The enzymatic assays were carried out in both one- and two-steps reaction schemes depicted in Figure 62. The relative yield of the GDH assays was obtained by setting the equilibrium yield of the control reaction to one. A relative yield of 50% was obtained in the two-step reaction scheme in comparison to the control group. The lower yield is likely originated from the fact that only half of the original NADH could be converted to rNAD within the one hour allotted for the regeneration step, lowering the equilibrium amount of the product to a half in comparison to the control assay. B-BO_3 could be easily removed from the reaction media *via* filtration either before or after the enzymatic step, however, the final product yield with and without B-BO_3 filtration performed before the enzymatic step were similar.

The 2S scheme allows a physical separation between the regeneration module and the biocatalytic medium. This barrier can be removed if the biocatalysis is conducted in a one-pot reaction scheme (OP), offering a convenient design with all components being present in the same reaction vessel. The one-pot design allows shorter reaction times and minimization of the contact time between NAD(H) and the reaction media, which is an important aspect to be taken into account since many

oxidoreductases have ideal activities at pH ranges in which NAD⁺ or NADH becomes unstable. This is a common problem encountered with nicotinamide cofactors in general.^[238] In particular, about 4% of NAD⁺ is consumed in non-enzymatic secondary reactions after one hour in the presence of B-BO₃.

Figure 62 shows the results for OP reactions in different conditions. To assess the possible interaction between NP and other components in the reaction media, an additional control reaction was carried out containing B-BO₃ in the dark (OP-D), non-regenerated NAD⁺, buffer, PG and GDH. After one hour, a relative yield of 70% was obtained, lower than the yield obtained with the original control without B-BO₃. This result suggests a negative interaction between GDH and B-BO₃ that seems to deactivate the enzyme. Further deactivation, characterized by an even lower yield was observed when the same reaction was carried out under light irradiation for one hour (OP-L) which resulted in 40% relative yield. To test whether the enzyme was deactivated by interaction with B-BO₃, a buffered suspension containing only B-BO₃, O₂ and GDH was exposed to light irradiation with gentle stirring for two hours. The enzyme showed no detectable activity after treatment with B-BO₃, which confirms the deactivation role of the photocatalytic activity of the nanoparticles on the enzyme.

A significant improvement on the reaction yield was achieved by adding a second portion of fresh GDH after the first hour of OP-L under light irradiation (OP-L+). As shown in Figure 62, a 95% relative yield was obtained for OP-L+, confirming that the stability of GDH was the main reason behind the lower yields observed in one-pot approaches compared to the two-step reactions. OP-L+ was conducted with partially regenerated NAD⁺, i.e. the reaction was carried out with an initial amount of non-regenerated NAD⁺.

Fully regenerated NAD⁺ was used in OP-L+* (Figure 62), where the initial source of cofactors was pure NADH. Therefore, all the NAD⁺ species needed for the oxidation of PG by GDH were produced by light-induced photocatalysis with B-BO₃. Additional GDH was added to compensate for the enzyme deactivation after the first step of the photocatalysis followed by another one-hour period. The obtained yield was very close to that of the 2S design (about 50%). In this case, the lower yield resulted from the longer reaction times needed for the complete conversion of the initial NADH to NAD⁺. The deactivation of GDH overtime also contributes to lower reaction yields in this case.

4.3.4 Conclusions and outlook

In conclusion, a visible light-induced regeneration module for recycling of NAD⁺ from NADH was presented. By simple visible light induced photocatalysis using B-BO₃, high conversion rates of recycled NAD⁺ from NAD(H) were obtained. The pure organic heterogeneous photocatalyst B-BO₃ did not require any additional mediators and could be used in both one-pot and two steps enzymatic reactions. The designed two-step process offered the best results in terms of enzyme activity. The nanoparticles of B-BO₃ could be easily purified by filtration before the enzymatic step, an important feature in cases when the enzyme can be deactivated by surface-induced interaction with the nanoparticles. The light-induced conversion of NADH to NAD⁺ coupled with the enzymatic oxidation of PG was successfully demonstrated in a one-pot design in which NAD⁺ regeneration and NADH production were performed simultaneously. The use of light as a cheap energy source for the indirect regeneration of NAD⁺ without the need of additional mediators opens the way for the exploration of important synthetic applications such as the oxidation of relevant compounds such as glycerol. B-BO₃ can also be used as a module for the development of artificial cell while mimicking the regulation step of NAD⁺/NADH *via* visible light irradiation.

4.4 Molecular engineering of conjugated poly-benzothiadiazoles for enhanced hydrogen photosynthesis^{§**}

In this chapter a molecular structural design of pure organic photocatalysts derived from conjugated polybenzothiadiazoles is presented for photocatalytic hydrogen evolution under visible light. By alternating the substitution position of the electron-withdrawing benzothiadiazole unit on the phenyl unit as co-monomer, various polymers with either one or three dimensional structures were synthesized and the impact of their molecular structure on the catalytic activity was investigated. Highly efficient photocatalytic hydrogen evolution could be observed by employing the linear polymer based on the phenyl-benzothiadiazole-alternating main chain.

4.4.1 Motivation

The development of visible light photocatalysts for solar-energy conversion into chemical energy carriers remains a key target of modern material science, which is best guided by a fundamental understanding of the structural impact on functional properties.^[245-247] In recent years a great variety of photocatalytic systems have been intensely investigated, besides metal-based photocatalysts such as inorganic semiconductors or organometallic complexes, pure organic photocatalytic systems have gained much attention.^[248-251] Among those, binary carbon nitrides, a state-of-art example, have been greatly applied as metal-free photocatalysts due to their promising electronic and optical properties.^[76, 252, 253]

Another emerging class of metal-free photocatalysts, conjugated polymers are of particular interest because their semiconductor properties can be easily tuned by means of an appropriate choice of donor and acceptor in order to modify the band gap, band positions, and p/n characters.^[254, 255] Moreover, the processability of organic

[§] This chapter is based on the publication “Molecular engineering of conjugated polybenzothiadiazoles for enhanced hydrogen production by photosynthesis” by Can Yang*, Beatriz Chiyin Ma*, Linzhu Zhang, Sen Lin, Saman Ghasimi, Katharina Landfester, Kai A. I. Zhang and Xinchun Wang, published in 2016 in the *Angewandte Chemie International Edition*, volume 55, issue 32, pages 9202–9206. Reprinted with permission with copyright (2016) from Wiley-VCH Verlag GmbH & Co. KGaA, Weinheim. *Both authors contributed equally to this work.

^{**} This work was a cooperation project with Can Yang, Linzhu Zhang, Sen Lin and Xinchun Wang from Fuzhou University, China. The synthesis and characterization of the CMPs were prepared in this work (Experimental Sections 5.3.2 and 5.3.5) and the photocatalytic activity for hydrogen evolution, ICP-MS measurements and theoretical calculations (Experimental Sections 5.3.3 and 5.3.4) were performed by the group of Prof. Dr. Xinchun Wang.

photocatalysts allows for a device fabrication of photosynthetic units. Indeed, recent studies have shown several design strategies to enhance the photocatalytic properties of conjugated polymers for light-induced chemical transformation reactions.^[10, 256-259] Some approaches include a variation of chemical composition *via* copolymerization, band gap alignment by microstructural modification or nanostructured pathway with porosity control.^[102, 260] However, the number of examples on which conjugated polymers were employed for hydrogen production through photosynthesis from water or organic feedstocks under visible light, is very small.^[111, 156, 261]

Polyphenylenes and poly(azomethines) were reported for H₂ evolution, but the materials were mostly active under UV light with moderate activity.^[111, 261] Recently, Cooper's group developed a series of promising pyrene-based copolymers as photocatalysts for H₂ evolution with tunable optical gaps of 1.94-2.95 eV, and the best hydrogen evolution rate of 17.4 μmol h⁻¹.^[156] At the same time, a planarized fluorene-type polymers were very recently explored by the same group for enhanced H₂ evolution with visible light.^[110]

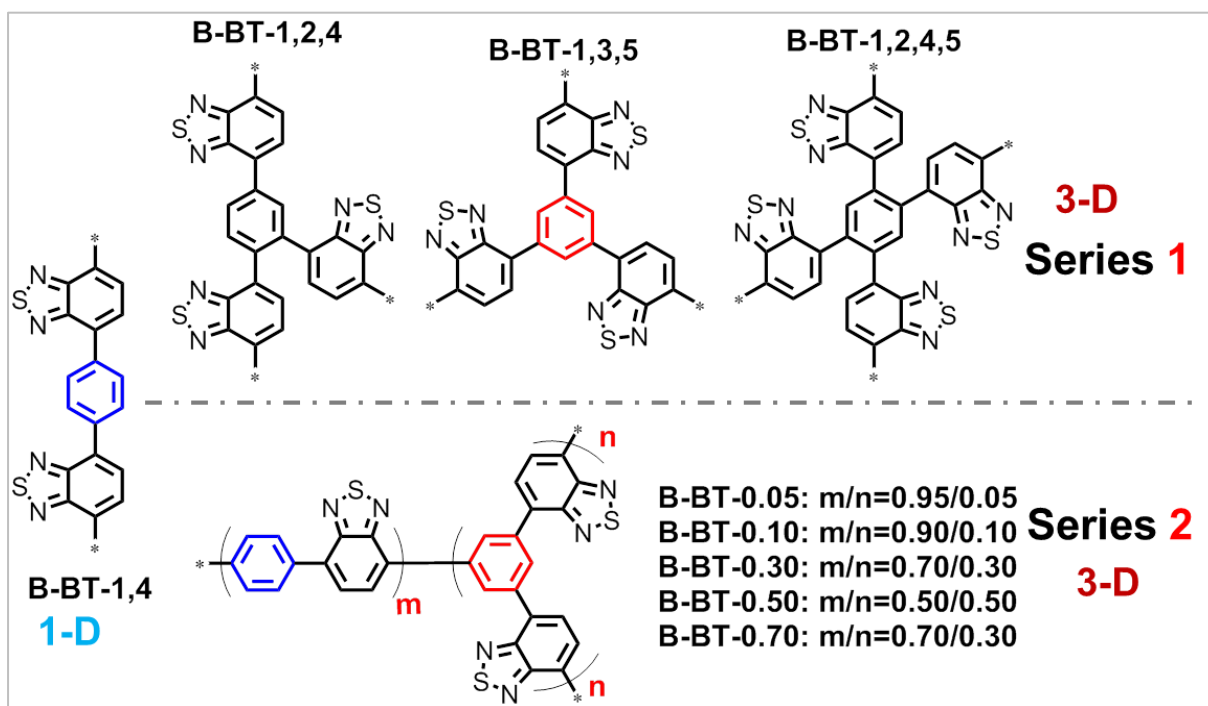
Taking into account the wide number of conjugated polymers and the diversity of structural variations which can be modified synthetically, further development of more efficient organic photocatalysts for enhanced H₂ generation by photosynthesis is envisaged. Therefore, in this chapter a molecular structural design strategy of electron donor-acceptor type conjugated polymers is investigated for the ability of this class of materials to be used as stable organic photocatalysts for visible light-promoted hydrogen evolution.

4.4.2 Synthesis and characterization

Taking a simple phenyl unit as a starting point, benzothiadiazole as an electron-withdrawing unit was incorporated into the polymer backbone at different positions on the phenyl ring, which resulted into polymers varying from one-dimensional (1D) linear polymers to three-dimensional (3D) networks (Scheme 4).

Two series of conjugated polybenzothiadiazoles were synthesized via Suzuki-Miyaura cross-coupling polycondensation reactions using 4,7-dibromobenzo[c][1,2,5]thiadiazole (BT) with either benzene-1,4-diboronic or 1,3,5-phenyltriboronic acid tris(pinacol) ester as co-monomer. In particular, the 1D linear

polymer B-BT-1,4 served as a starting material and the BT units were coupled at the 1,4-positions on the phenyl ring in the polymer main chain (Scheme 4 left).



Scheme 4. Structures of two series of poly-benzothiadiazoles with different molecular designs.

The polymers in series 1 (Scheme 4 top) were obtained by a variation of the substitution position on the phenyl ring, thus, resulting into the 3D polymer networks B-BT-1,2,4, B-BT-1,3,5 and B-BT-1,2,4,5. To precisely investigate the influence of the 3D network skeleton during the photocatalytic process of H₂ evolution, another series of polybenzothiadiazoles were synthesized by means of gradually increasing the number of 1,3,5-functionalized phenyl units, used as co-monomers, in the backbone of B-BT-1,4, which resulted in the polymer series 2 (Scheme 4 bottom). The detailed procedure and characterization data are described in the Experimental Section 5.3

The polymers in series 1 showed a variation of morphologies with fused particle-like shape for B-BT-1,2,4 and B-BT-1,2,4,5 and fused fiber-shape for B-BT-1,3,5, while the linear polymer B-BT-1,4 showed a non-specific fused flake-like shape (Figure 63 and Figure 64). The polymers in series 2 showed morphology similar to that of B-BT-1,4 except for B-BT-0.70 which presented a more fused particle-like shape.

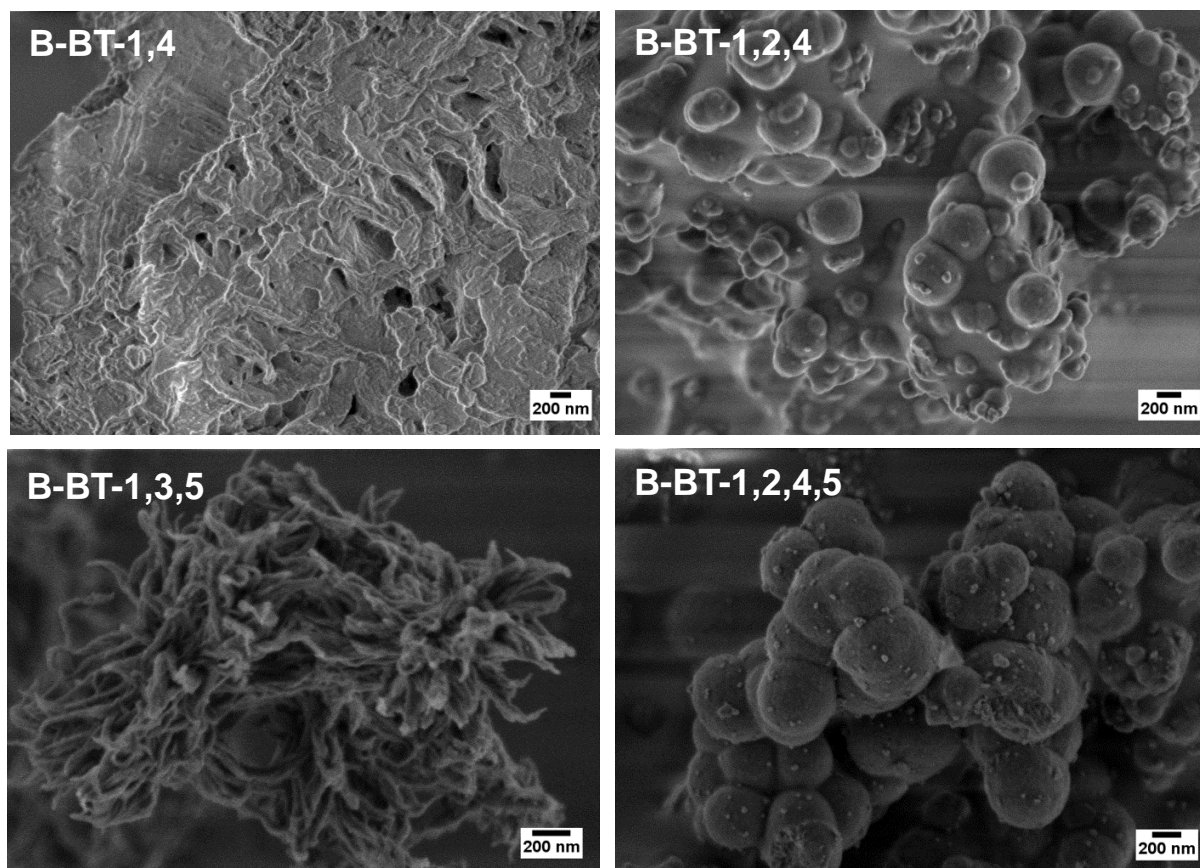


Figure 63. SEM images of the polymers from series 1.

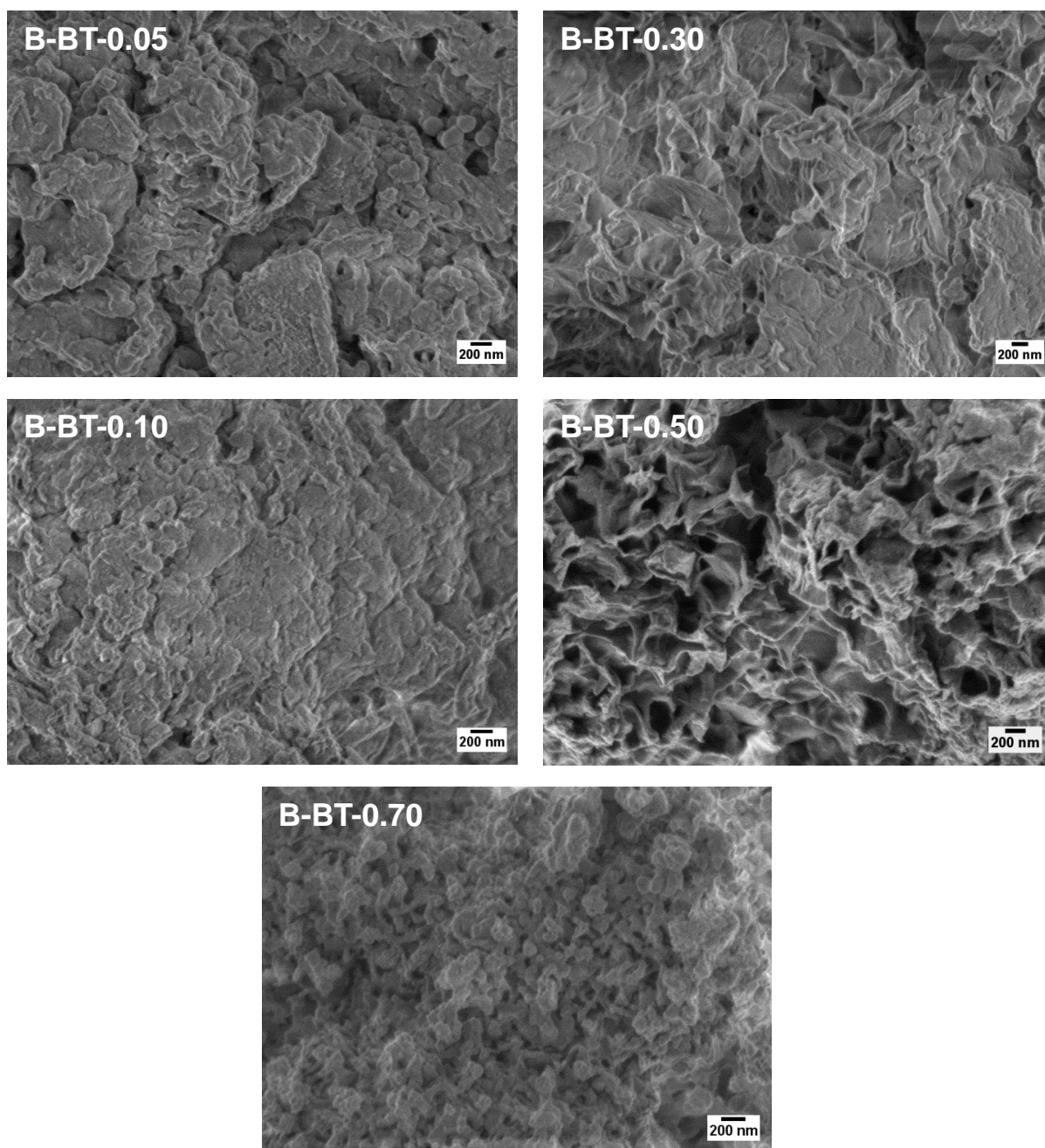


Figure 64. SEM images of the polymers from series 2.

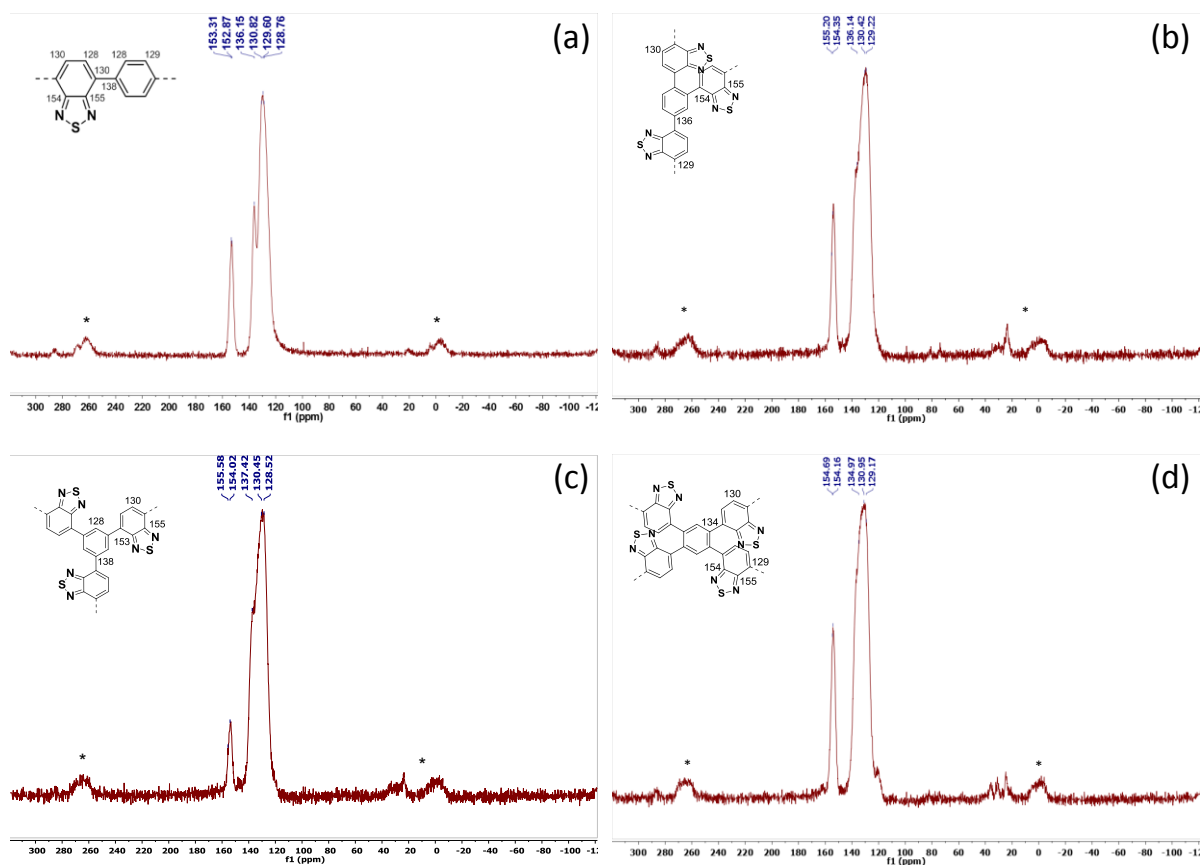


Figure 65. Solid state ^{13}C CP/MAS NMR spectra of the polymers from series 1. (a) B-BT-1,4; (b) B-BT-1,2,4; (c) B-BT-1,3,5 and (d) B-BT-1,2,4,5.

Solid state ^{13}C /MAS NMR spectra showed similar signals at 153 ppm, which can be assigned to the carbon adjacent to the nitrogen atom of the BT units for all polymers (Figure 65 and Figure 66). The signals between 115 and 146 ppm can be assigned to the aromatic carbon atoms in the BT unit.

To note, for the polymers in series 2, the chemical shift at 137 ppm, which can be assigned to the aromatic carbon atoms of the phenyl co-monomer, were gradually fused to the other carbon signals by introducing more 1,3,5-functionalized phenyl units as crosslinks in the polymer backbone (Figure 66). This result shows the extension of the cross-linked structure throughout the meta-position of the phenyl units in the polymer backbone structure.

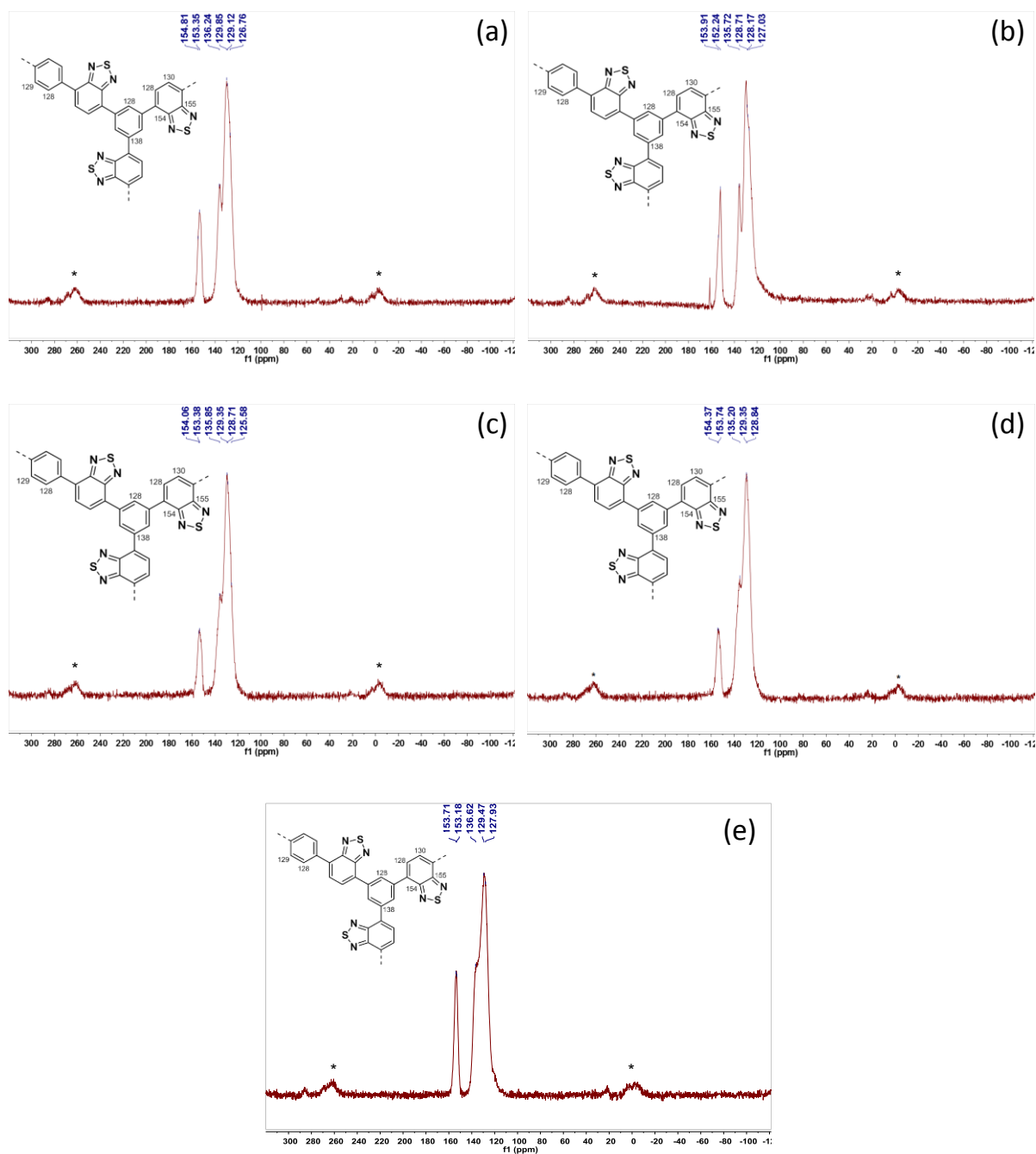


Figure 66. Solid state ^{13}C CP/MAS NMR spectra of the polymers from series 2. (a) B-BT-0.05; (b) B-BT-0.10; (c) B-BT-0.30; (d) B-BT-0.50 and (e) B-BT-0.70.

Transmission electron microscopy (TEM) and the fast Fourier transformation (FFT) measurements of the polymers showed no signs of crystallinity (Figure 67), and the powder X-ray diffraction (PXRD) profile reveals an amorphous character (Figure 68).

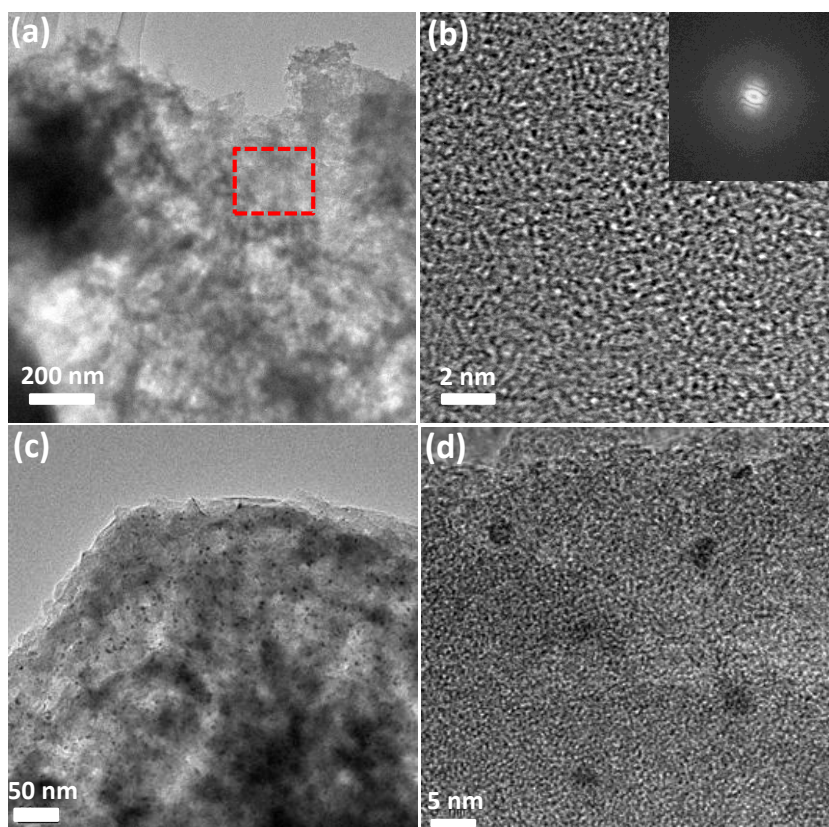


Figure 67. Transmission electron microscopy (TEM) and its fast Fourier transformation (FFT) measurements of the polymers (a) TEM image of B-BT-1,4 (b) HR-TEM of polymer B-BT-1,4. Insets: FFT. (c)(d), TEM of polymers after reaction.

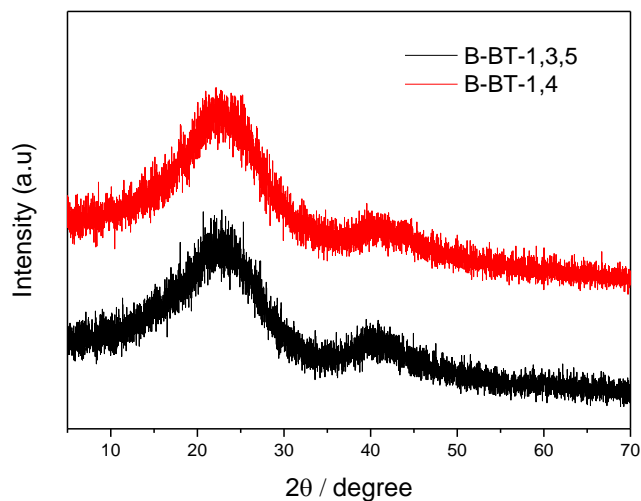


Figure 68. Powder X-ray diffraction (PXRD) of the polymers involving B-BT-1,3,5 and B-BT-1,4.

Interestingly, the nitrogen gas adsorption measurements revealed that the linear polymer B-BT-1,4 was slightly porous (Table 4, Figure 69) with a Brunauer–Emmett–

Teller (BET) surface area of about $39 \text{ m}^2 \text{ g}^{-1}$ and a pore diameter of 4.0 nm in the mesoporous range caused by a molecular twist combined with a π - π stacking effect, thus leading to a certain pore formation in the solid polymer. By comparison, B-BT-1,2,4, B-BT-1,3,5, and B-BT-1,2,4,5 in series 1 showed microporous properties with BET surface areas ranging from $40 \text{ m}^2 \text{ g}^{-1}$ to $280 \text{ m}^2 \text{ g}^{-1}$ and a similar pore diameter of about 1.5 nm.

The polymers in series 2 did not show a clear trend of porosity by gradually increasing the number of crosslinking units in the polymer backbone. The BET surface areas ranged from $40 \text{ m}^2 \text{ g}^{-1}$ to $129 \text{ m}^2 \text{ g}^{-1}$ with pore sizes ranging from about 3.8 to 10.7 nm (Table 4, Figure 70).

Table 4. Porosity data and electrochemical properties of the polymers.

Polymer	$S_{\text{BET}}^{\text{a}}$ [$\text{m}^2 \text{ g}^{-1}$]	PD ^b [nm]	PV ^c [$\text{m}^3 \text{ g}^{-1}$]	HOMO ^d / LUMO ^e [V vs. NHE]	OG ^f [eV]	HER ^g [$\mu\text{mol h}^{-1}$]
B-BT-1,4	39	0.14	4.0	1.28/-0.89	2.17	116
B-BT-1,2,4	17	0.03	4.5	1.27/-0.98	2.25	1.3
B-BT-1,3,5	280	0.37	1.5	1.41/-1.03	2.44	20
B-BT-1,2,4,5	40	0.06	1.5	1.23/-1.09	2.32	0.4
B-BT-0.05	58	0.10	3.8	1.25/-0.95	2.20	82
B-BT-0.10	93	0.24	3.8	1.24/-0.97	2.21	50
B-BT-0.30	129	0.51	4.5	1.23/-0.99	2.22	39
B-BT-0.50	40	0.20	10.7	1.23/-1.00	2.23	19
B-BT-0.70	84	0.20	3.8	1.27/-1.02	2.29	19

^a Specific surface area calculated from the N_2 adsorption isotherm

^b Pore diameter

^c Pore volume

^d Derived via extracting the LUMO level from the optical gap

^e Determined by cyclic voltammetry

^f Optical gap(OG) derived from the absorption edges

^g Reaction conditions: 50 mg polymer, 110 ml TEOA/ H_2O (10/100), 3 wt% Pt, 300W Xe lamp with cut-off filter $>420 \text{ nm}$.

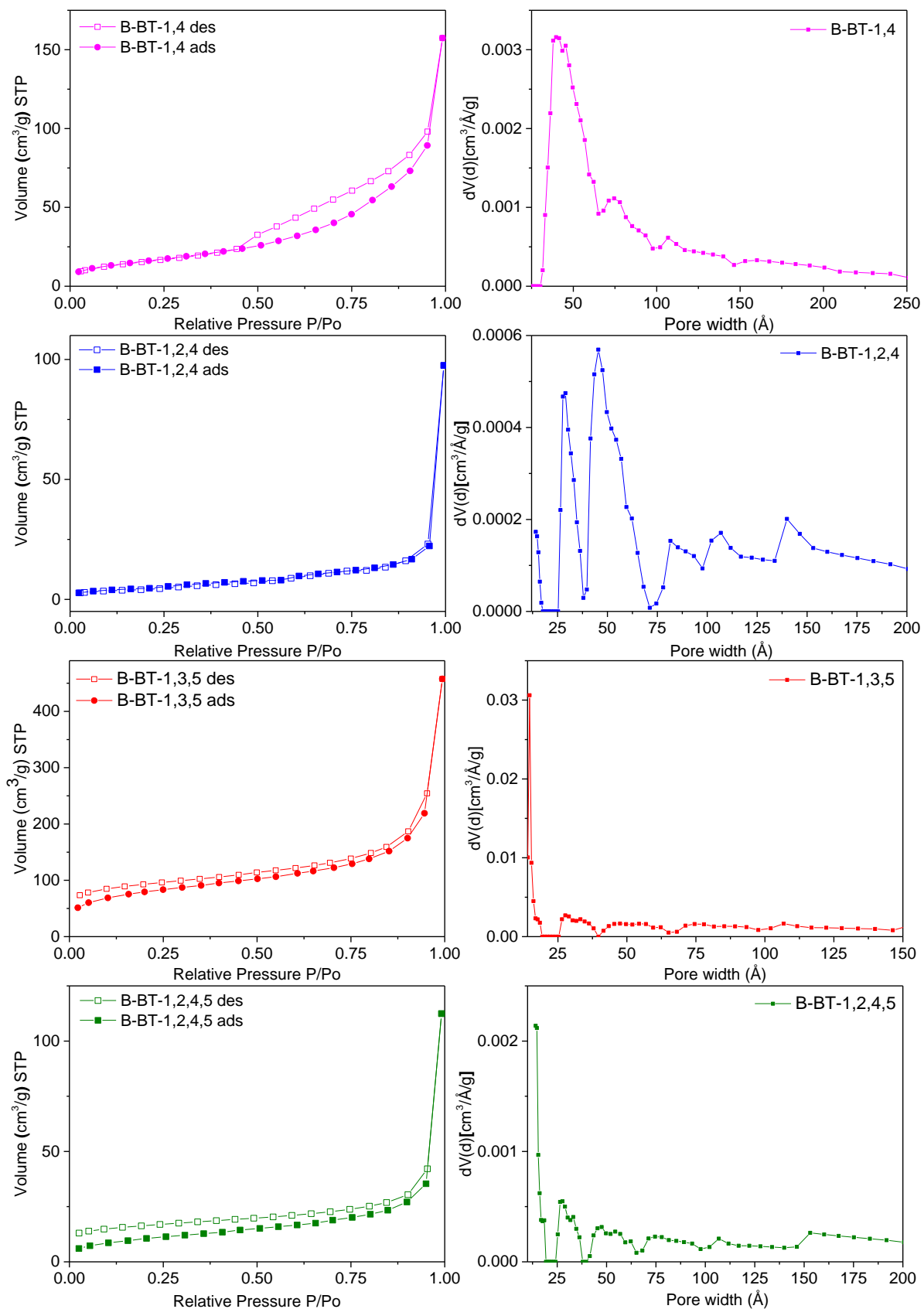
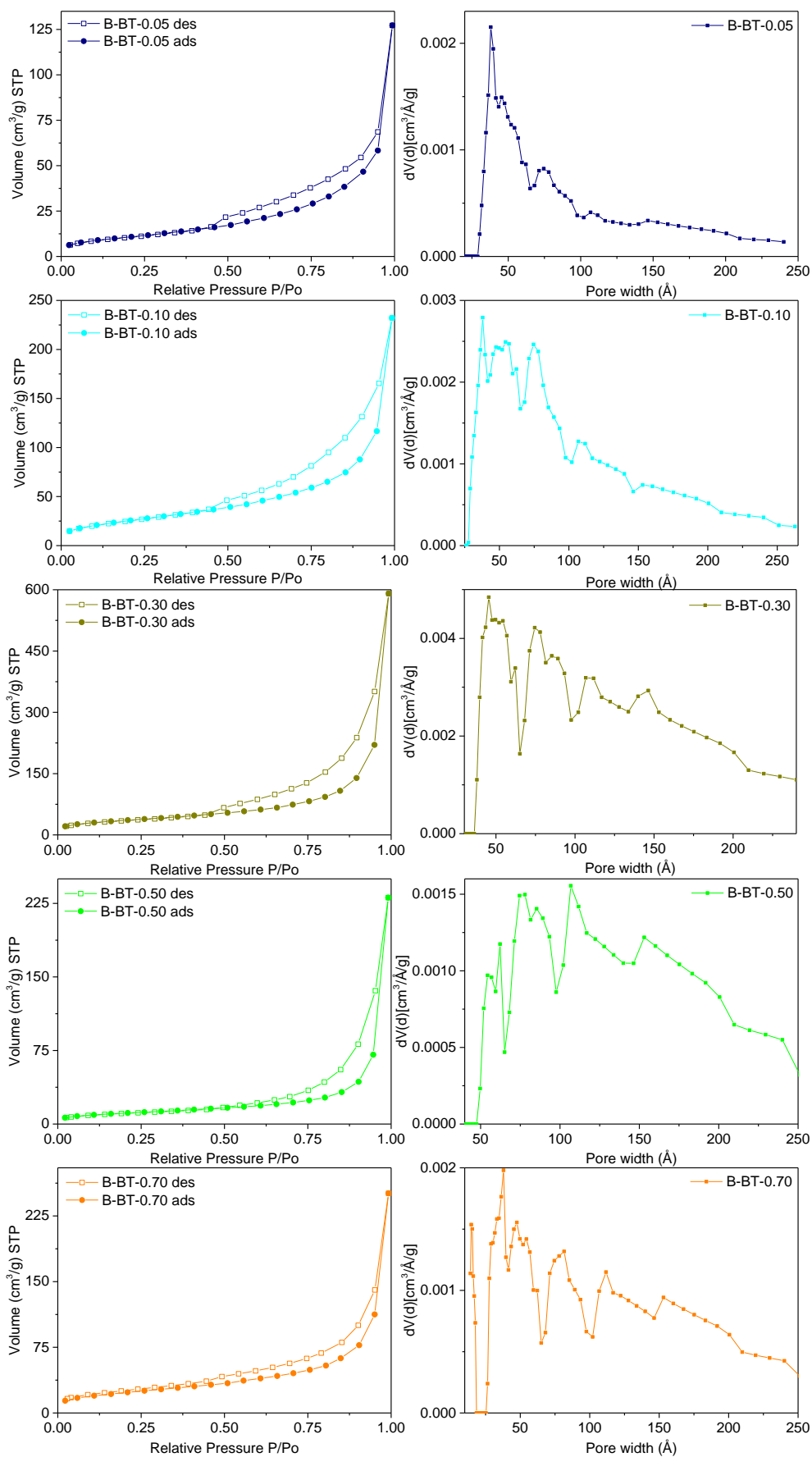


Figure 69. N₂ sorption isotherms and pore size distributions of the polymers from Series 1.

Figure 70. N_2 sorption isotherms and pore size distributions of the polymers from series 2.

Thermogravimetric analysis of the polymers revealed different thermal stabilities of the polymers with an overall tendency of higher stability for the linear polymer B-BT-1,4 and its 3D counterparts in series 2 (Figure 71).

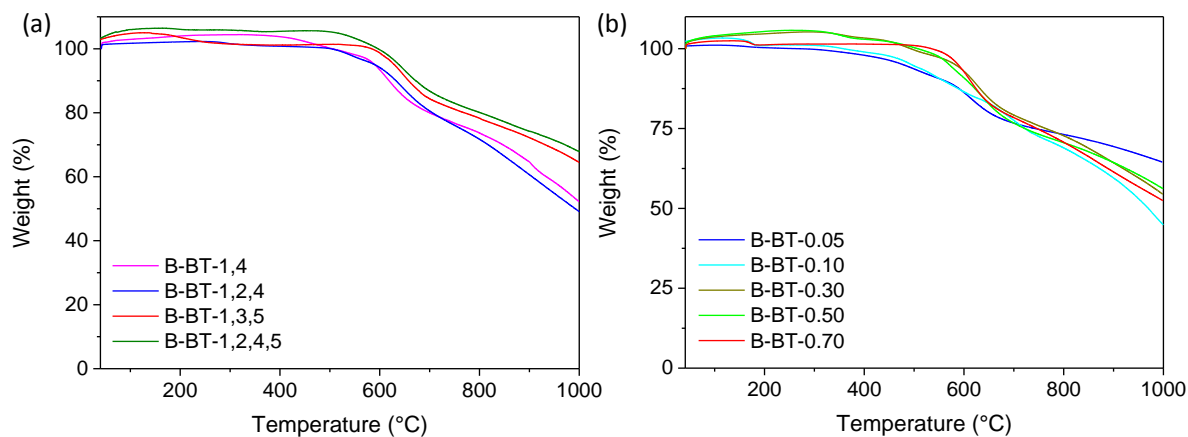


Figure 71. Thermogravimetric analysis of the polymers from (a) series 1 and (b) series 2.

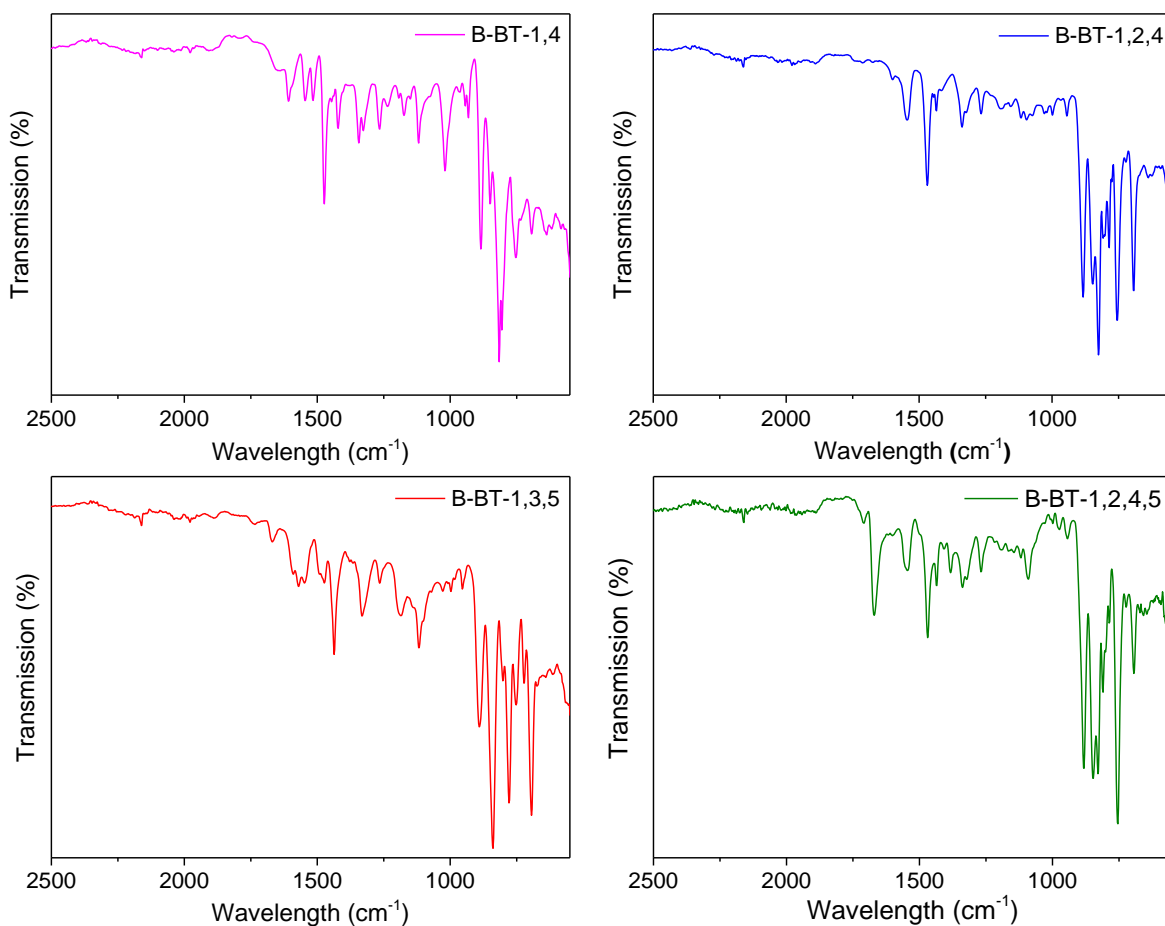


Figure 72. FTIR spectra of the poly-benzothiadiazoles from series 1.

The FTIR spectra showed typical signals at 1440 cm^{-1} and 1490 cm^{-1} , which can be assigned to the skeleton vibration of the aromatic rings in the polymers. The signals at 1340 cm^{-1} and 1570 cm^{-1} can be assigned to the C=N and N-S stretching modes, respectively, of the BT unit (Figure 72 and Figure 73).

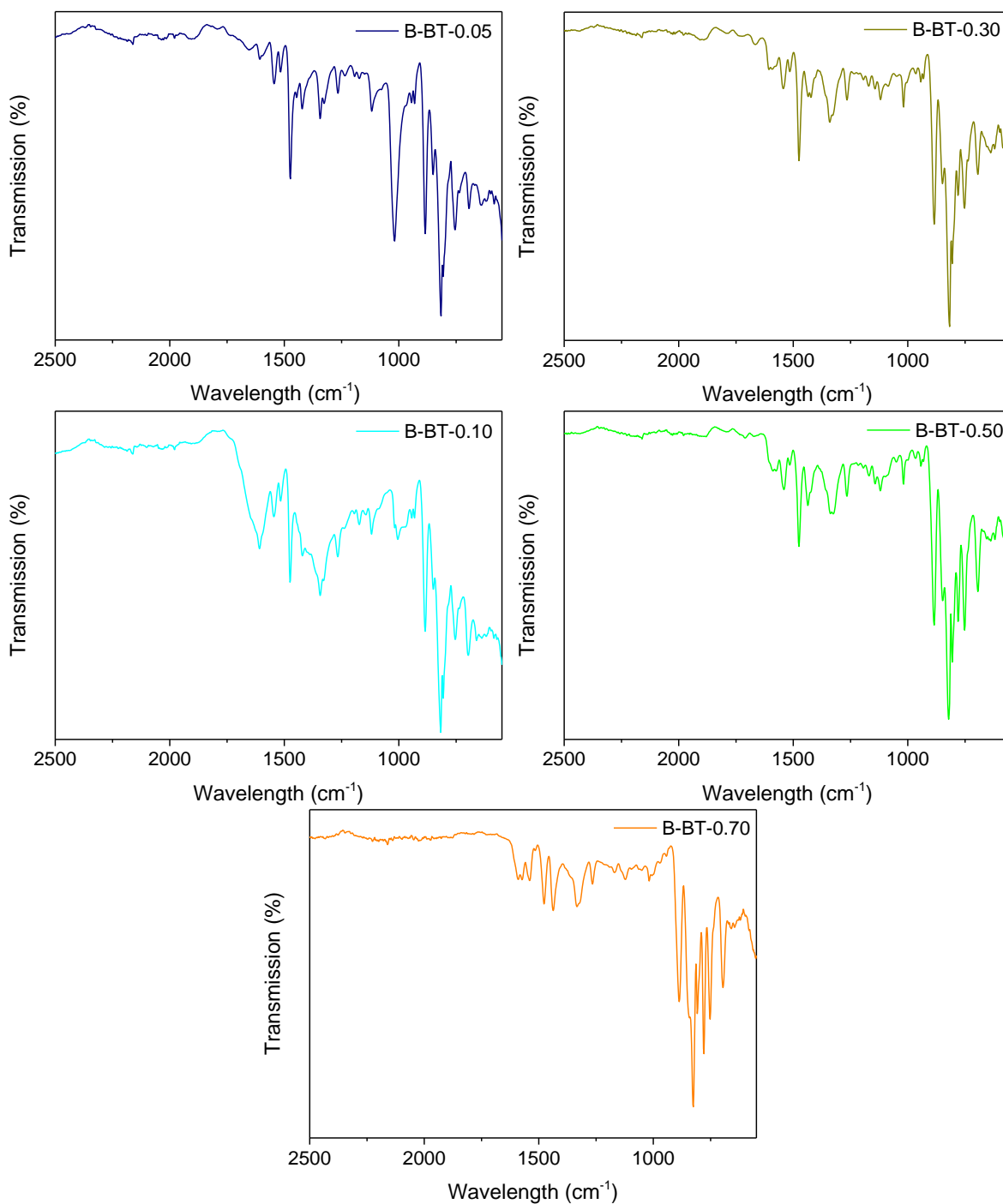


Figure 73. FTIR spectra of the poly-benzothiadiazoles from series 2.

The UV/vis diffuse reflectance spectra (DRS) of the polymers are displayed in Figure 74a and Figure 74b. Both series showed broad absorption range in the visible region. B-BT-1,4 exhibited the largest absorption area across both polymer series, whereas its 3D counterpart, B-BT-1,3,5, showed the narrowest absorption range. A clear tendency for optical absorption of the 3D structure could be observed for series 2.

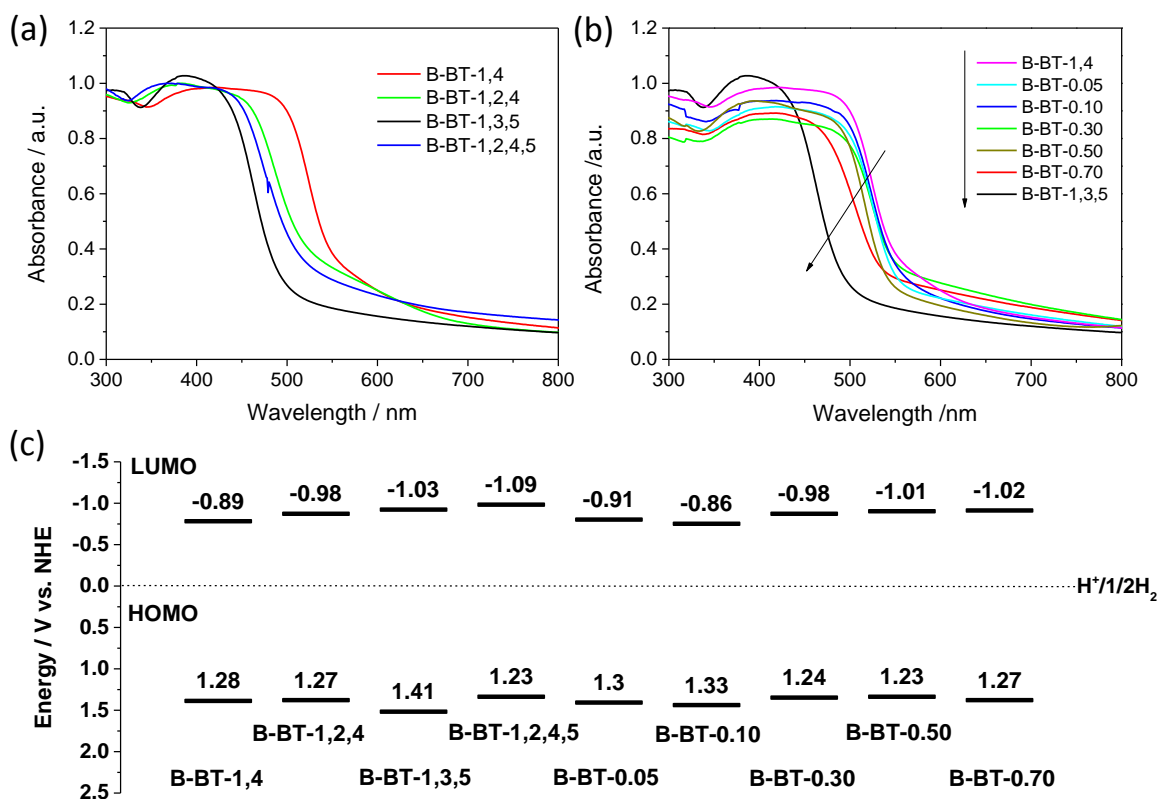


Figure 74. UV/Vis Diffuse Reflectance Spectra (DRS) of (a) polymer in series 1 and (b) Series 2, and (c) HOMO LUMO band position of the polymers.

The increase of the amount of cross-linkers in the polymer backbone, that is, the expansion of the 3D character of a polymer, led to a gradual decrease in the absorption range (Figure 74b). At the same time, optical gaps between about 2.1 and 2.5 eV could be derived from the absorption edges. The linear polymer B-BT-1,4 exhibited the narrowest band gap of 2.17 eV. In comparison, the 3D polymer networks in both series showed broader band gaps, with B-BT-1,3,5 possessing the broadest optical gap of 2.42 eV. The optical and electrochemical properties for both polymer series are also listed in Table 4.

To further study the energy band structure of the polymers, cyclic voltammetry (CV) measurements were conducted and revealed different energy levels within the polymer series (Figure 75 and Figure 76). The overall tendency showed that the 3D polymers in series 1 exhibited higher LUMO levels than the linear polymer B-BT-1,4 (-0.89 V vs. NHE, Figure 74c, Table 4). The lower-energy band of B-BT-1,4 is likely caused by the better extended conjugated system of the linear chain relative to its 3D counterpart, which has a rather twisted structure, and thus, a narrower band gap.

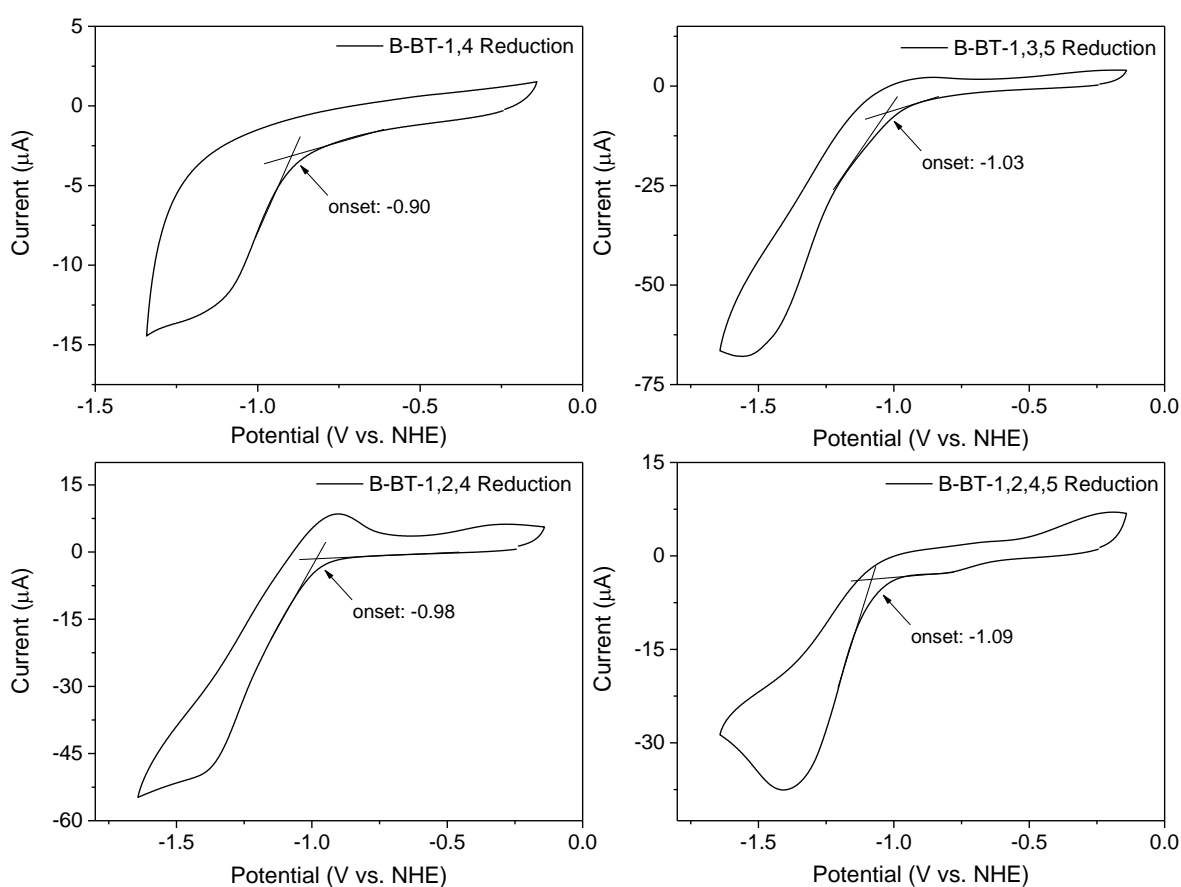


Figure 75. Cyclic voltammetry measurement from the polymers of Series 1.

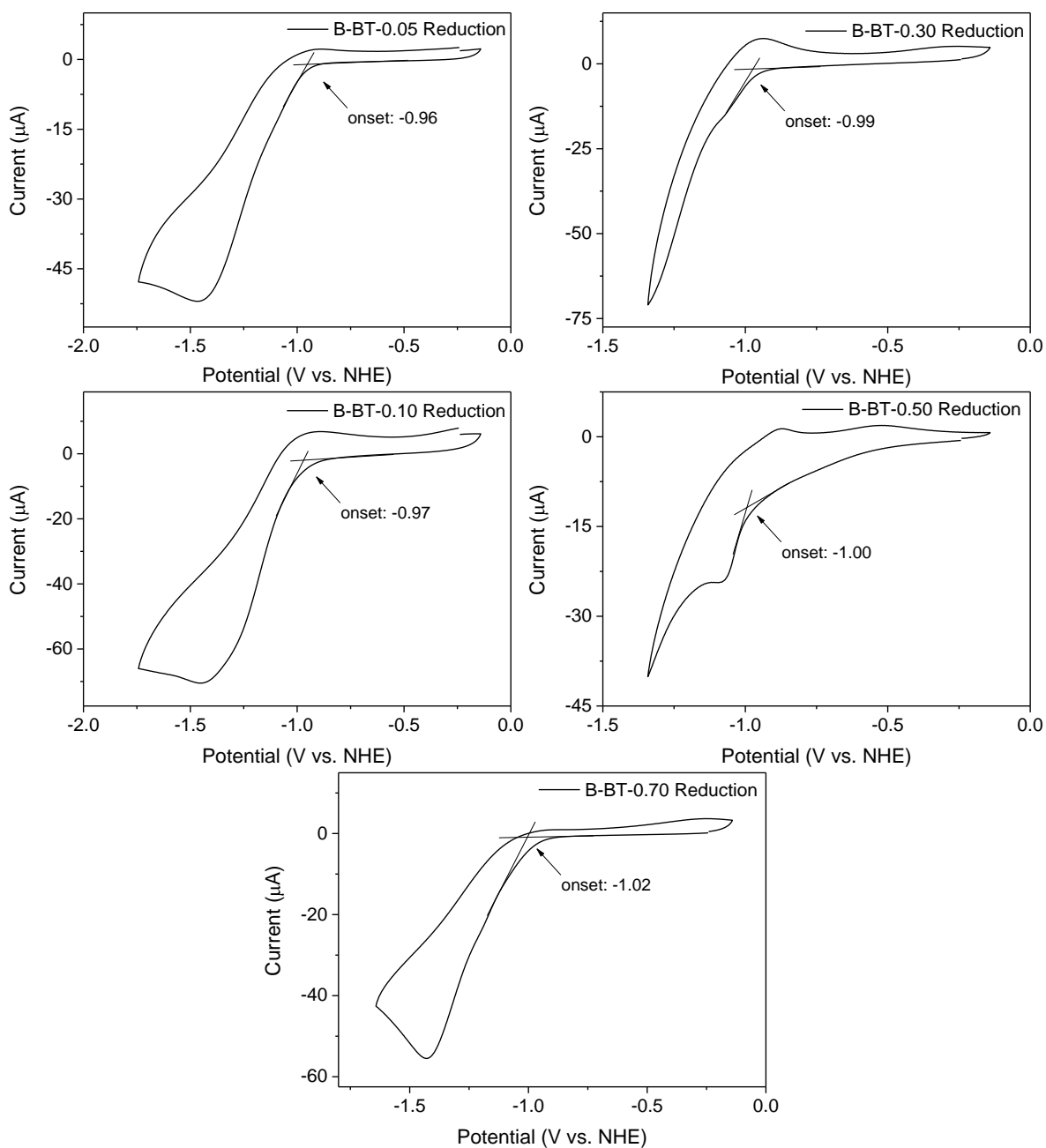


Figure 76. Cyclic voltammetry measurement from the polymers of series 2.

As a support, theoretical calculations of five possible 1D and 3D structures (Figure 77 - Figure 81) revealed that donor-acceptor features are more obvious in the charge density of the 1D B-BT-1,4 structure than those in the 3D B-BT-1,3,5 twisted structures, which can in principle decrease the π -conjugated system and reduce charge mobility. This data provides additional proof to explain the improved performance of B-BT-1,4 over B-BT-1,3,5.

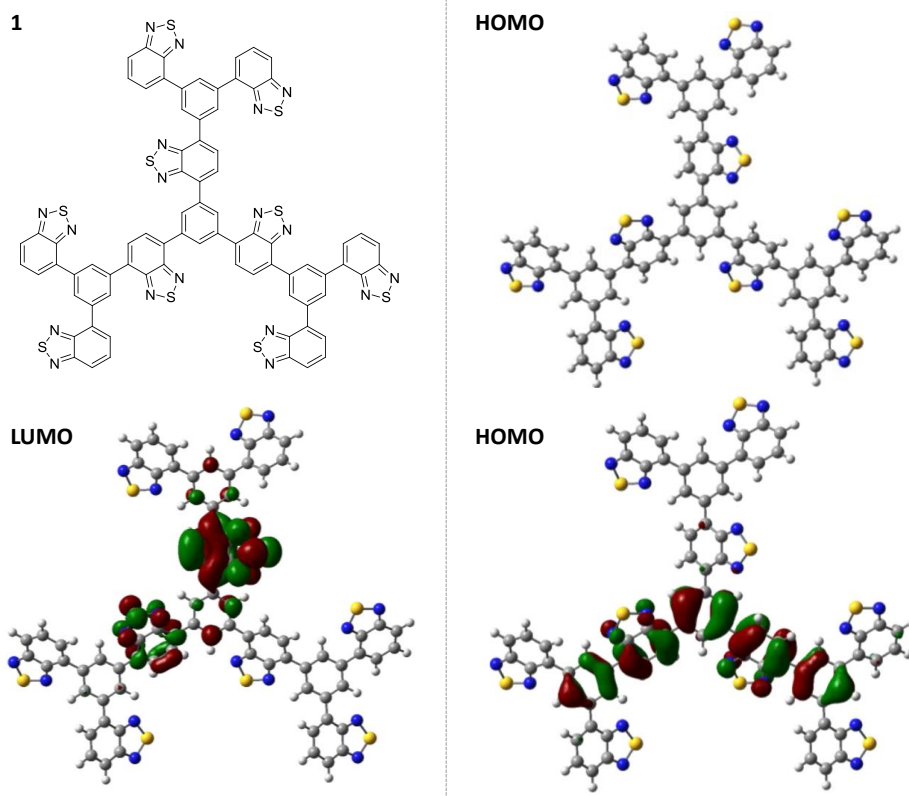


Figure 77. Molecular computing models for DFT calculation.

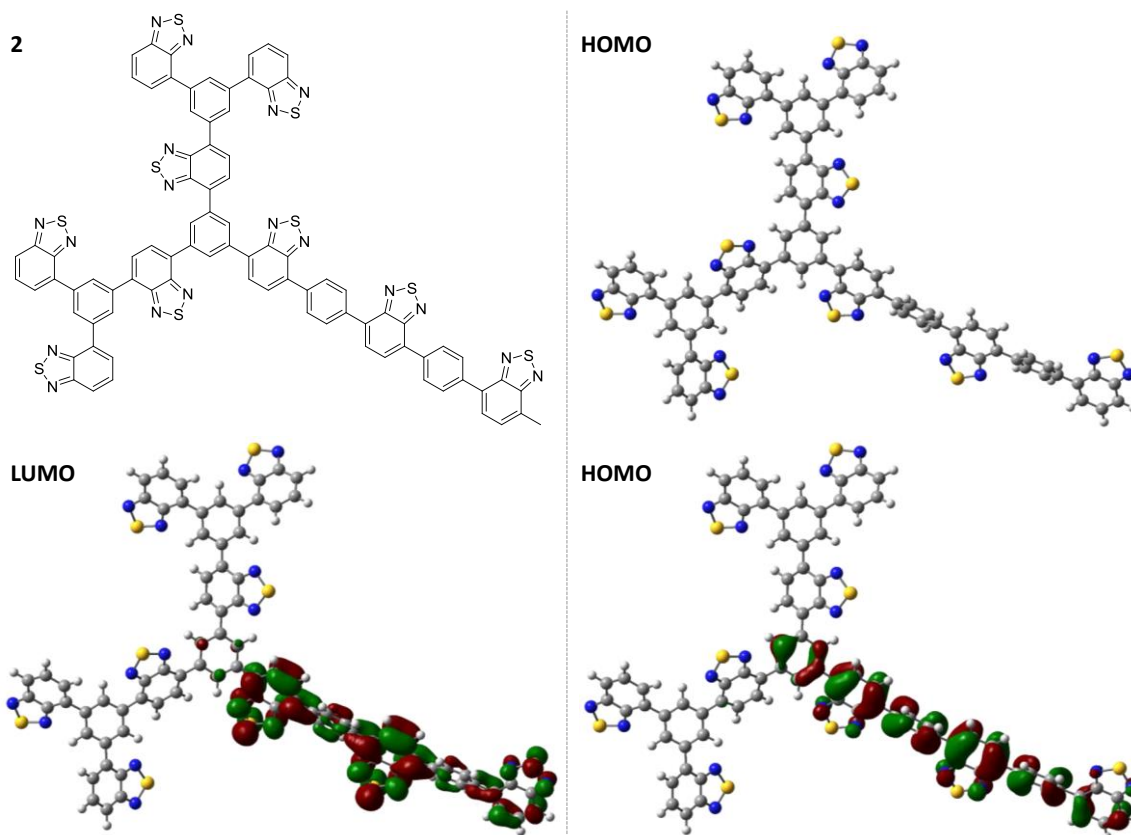


Figure 78. Molecular computing models for DFT calculation.

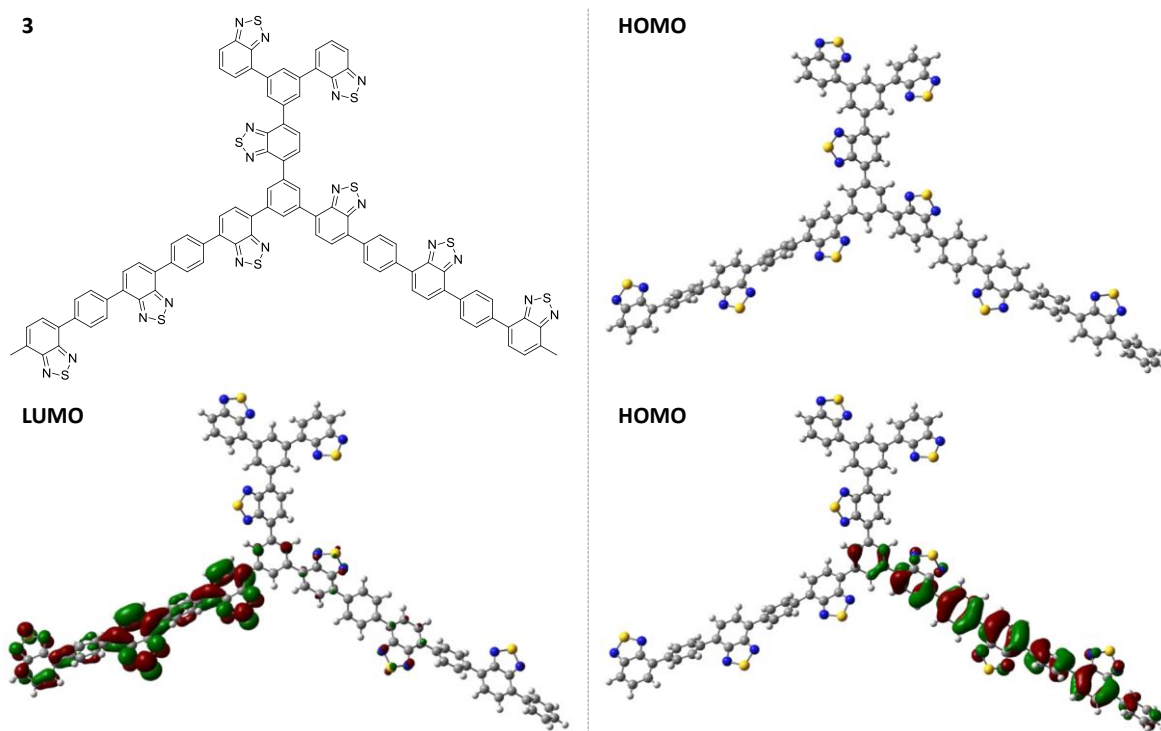


Figure 79. Molecular computing models for DFT calculation.

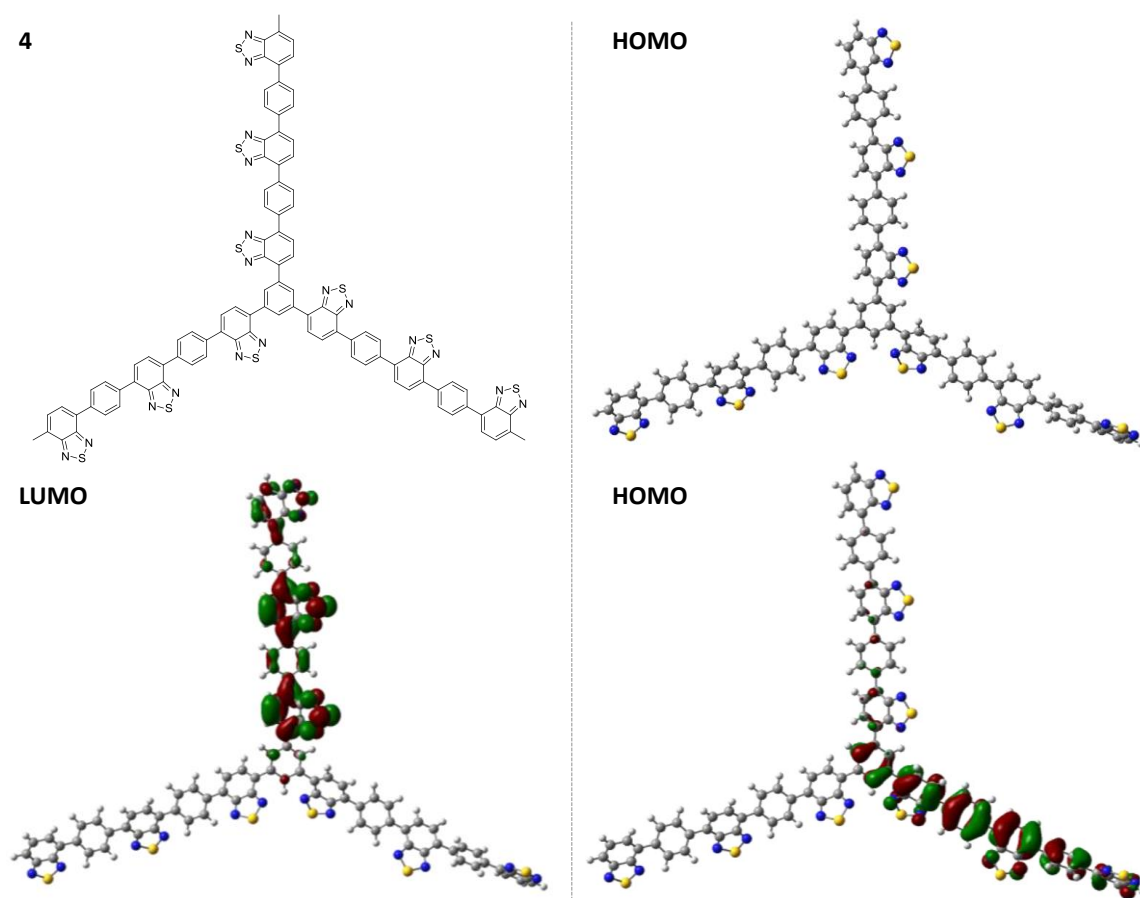


Figure 80. Molecular computing models for DFT calculation.

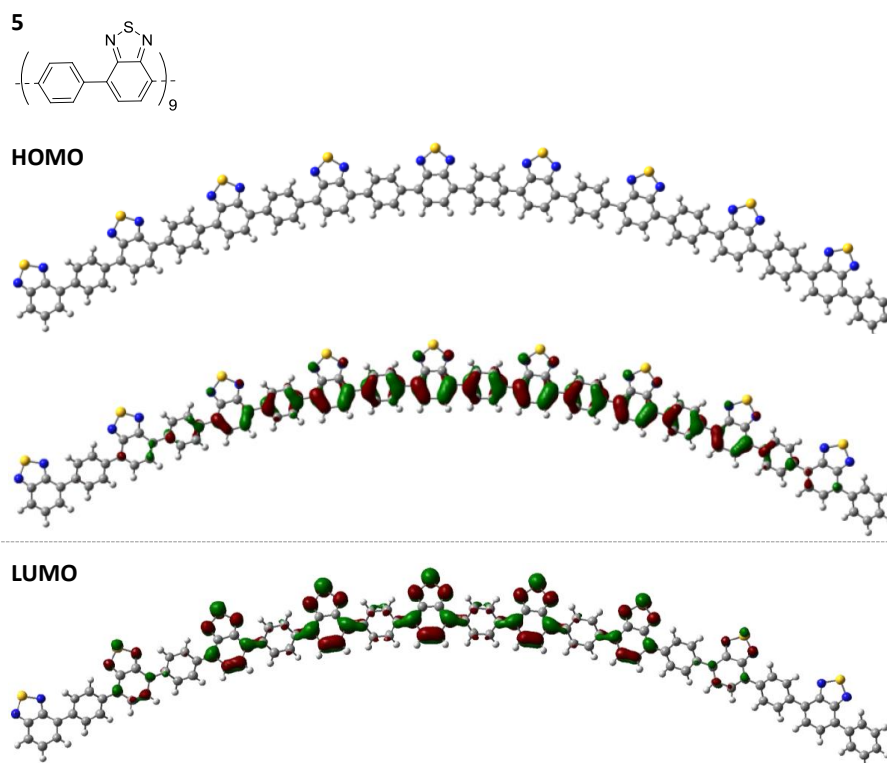


Figure 81. Molecular computing models for DFT calculation.

The photo-electrochemical properties of the polymers were further examined by photocurrent measurement (Figure 82). The linear B-BT-1,4 exhibited an enhanced photocurrent by a factor of four when compared to its 3D counterpart B-BT-1,3,5, thus indicating an improved light induced electronic conductivity, as well as charge transfer and charge separation in the linear polymer backbone structure B-BT-1,4 compared to the 3D structural variation.

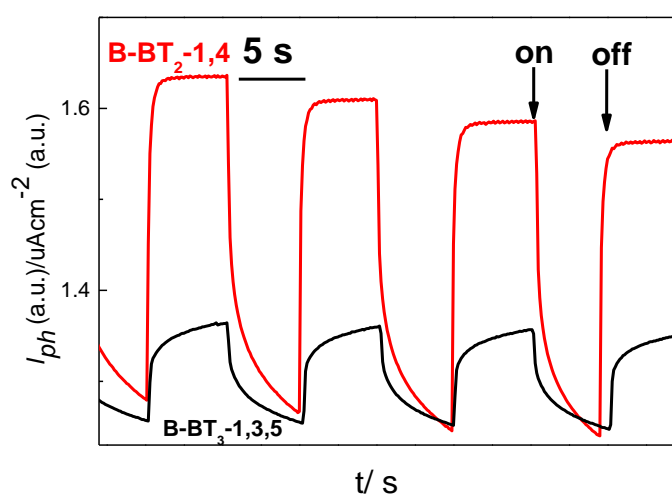


Figure 82. Photocurrent measurement comparison of B-BT-1,4 with its 3-D counterpart B-BT-1,3,5.

4.4.3 Photocatalytic properties for hydrogen photosynthesis

The photocatalytic activity of the polybenzothiadiazoles in H₂ evolution from water was then determined in the presence of the sacrificial electron donor (triethanolamine, TEOA). The hydrogen evolution rate (HER) of B-BT-1,4 was about 12 $\mu\text{mol h}^{-1}$ under visible-light irradiation ($\lambda > 420 \text{ nm}$, for experimental details see the Experimental Section 1.1).

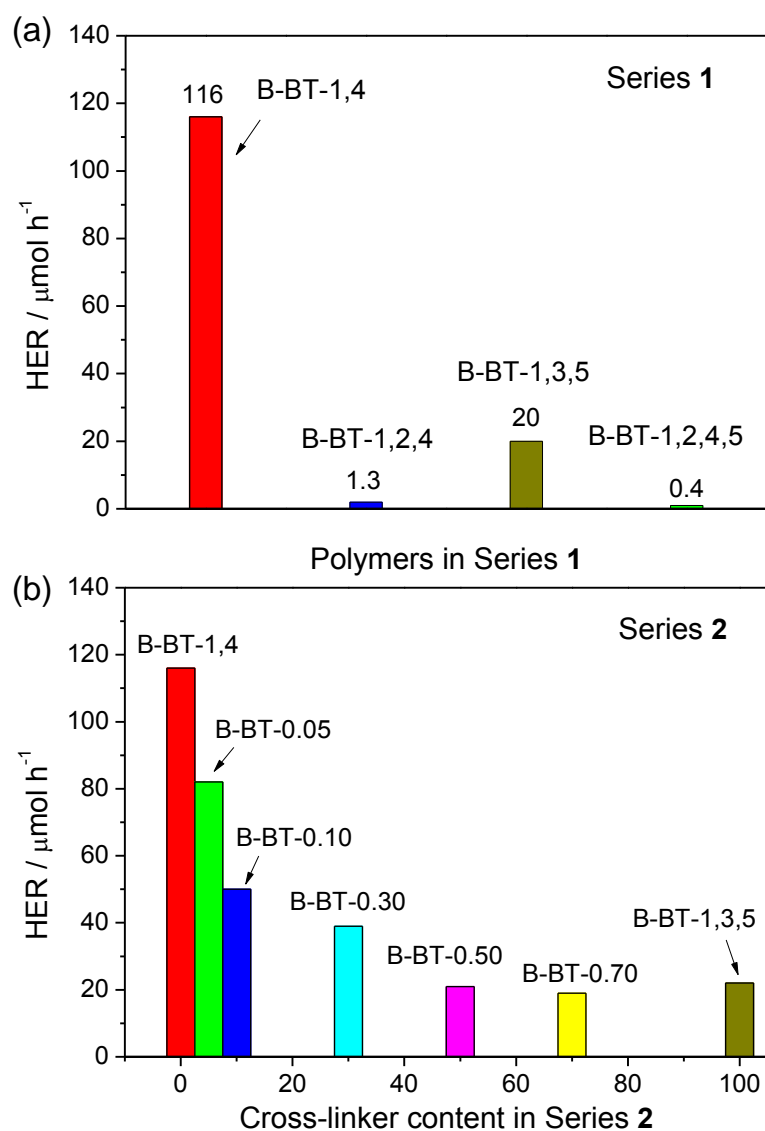


Figure 83. Hydrogen evolution rates using polymers in Series 1 (a) and Series 2 (b).

Under the optimized reaction conditions, employing about 3 wt.% Pt as the co-catalyst, a tenfold higher HER of 116 $\mu\text{mol h}^{-1}$ was achieved (Figure 83a). A direct comparison between B-BT-1,4 and fluorene-type polymers^[110] of high photocatalytic

activity was performed under same reaction conditions in the experimental set-up. Pt/B-BT-1,4 showed an apparent quantum yield (AQY) of 4.01% at 420 nm for H₂ evolution when using triethanolamine as the sacrificial agent, whereas P7(dibenzo[*b,d*]thiophene sulfone co-polymer) and Pt/P7 have shown an AQY of 2.62% and 2.48% respectively (Table 5; the P7 sample was kindly supplied by the authors of Ref. [110]). Once a triethylamine/methanol mixture was used as sacrificial agent, P7 showed the highest AQY of 6.61% and 5.38% for Pt/B-BT-1,4 (Table 6).

Table 5. The photocatalytic hydrogen evolution rate (HER) and apparent quantum yield (AQY) of the P7 and B-BT-1,4 samples using triethanolamine as sacrificial agent.

Entry	Sample*	HER [$\mu\text{mol h}^{-1}$]	AQY [%]
1	P7	21.3	2.62
2	Pt/P7	20.2	2.48
3	B-BT-1,4	11.6	1.43
4	Pt/B-BT-1,4	32.6	4.01

*Reaction conditions: photocatalyst (40 mg), triethanolamine (10 mL), water (100 mL). 420 nm LED lamp with a 420 nm band pass filter to provide monochromatic irradiation at 420 ± 4.6 nm, with light intensity of 14.3 mW cm^{-2} . Note that after the P7 sample was checked, H₂PtCl₆ was added into the reaction solution for 3 wt.% Pt nanoparticle photodeposition on the surface of P7 to yield Pt/P7.

Table 6. The photocatalytic hydrogen evolution rate (HER) and apparent quantum yield (AQY) of the P7 and B-BT-1,4 samples using TEA/MeOH as sacrificial agents.

Entry	Sample*	HER [$\mu\text{mol h}^{-1}$]	AQY [%]
1	P7	53.7	6.61
2	Pt/P7	49.5	6.09
3	B-BT-1,4	11.6	1.43
4	Pt/B-BT-1,4	43.7	5.38

*Reaction conditions: photocatalyst (40 mg), triethylamine (12 mL), methanol (12 mL), water (12 mL). 420 nm LED lamp with a 420 nm band pass filter to provide monochromatic irradiation at 420 ± 4.6 nm, with light intensity of 14.3 mW cm^{-2} . Note that after the P7 sample was checked, H₂PtCl₆ was added into the reaction solution for 3 wt.% Pt nanoparticle photodeposition on the surface of P7 to yield Pt/P7.

Clearly, the AQY depends on the type of sacrificial agent being used, and it is a remarkable observation that P7 and CP-CMP-10 can photocatalyse H₂ evolution without the Pt co-catalyst. A negative microstructural effect on the catalytic activity of the polymers was observed when employing the 3D polymers of series 1 as catalysts. In particular, the 3D polymer networks B-BT-1,2,4 and B-BT-1,2,4,5 only showed minimal HERs of 1.3 and 0.4 $\mu\text{mol h}^{-1}$, respectively, while B-BT-1,3,5 showed a moderate HER of 20 $\mu\text{mol h}^{-1}$.

To precisely study the 3D structural influence on the catalytic efficiency in H₂ production, the polymers in series 2 were investigated. It could be clearly observed that by gradually introducing the cross-linker into the polymer backbone based on B-BT-1,4, the HERs of the polymers decreased (Figure 83b), which is a further indication that the 3D character here could not effectively enhance the photocatalytic activity of the polymer series. This behaviour could be explained by the fact that the LUMO levels, that is, the reduction potentials for all polymers, were sufficient enough for reducing H⁺ to 1/2 H₂ with over-potentials between and 0.9 eV and 1.0 eV. These levels did not make a significant difference in their catalytic efficiencies. The main active factor should be the light induced electron mobility and electron transfer within the polymers, and the linear polymer B-BT-1,4 demonstrated its superior properties compared to the other polymers in both series. Another additional factor could be the absorption range of B-BT-1,4 in the visible region, which was broader than that for the other polymers.

Figure 84a shows the wavelength dependence of the AQY of B-BT-1,4 for H₂ production, thus indicating the correspondence of its photocatalytic activity in H₂ evolution with its maximal absorption at different wavelengths. Repeating experiments were conducted to demonstrate the stability and reusability of the polymers as photocatalysts. B-BT-1,4 could be reused for five additional cycles for 30 h without loss in its catalytic efficiency, by using a constant amount of the sacrificial agent (Figure 84b). No apparent changes could be observed on the FTIR spectra of B-BT-1,4 (Figure 85).

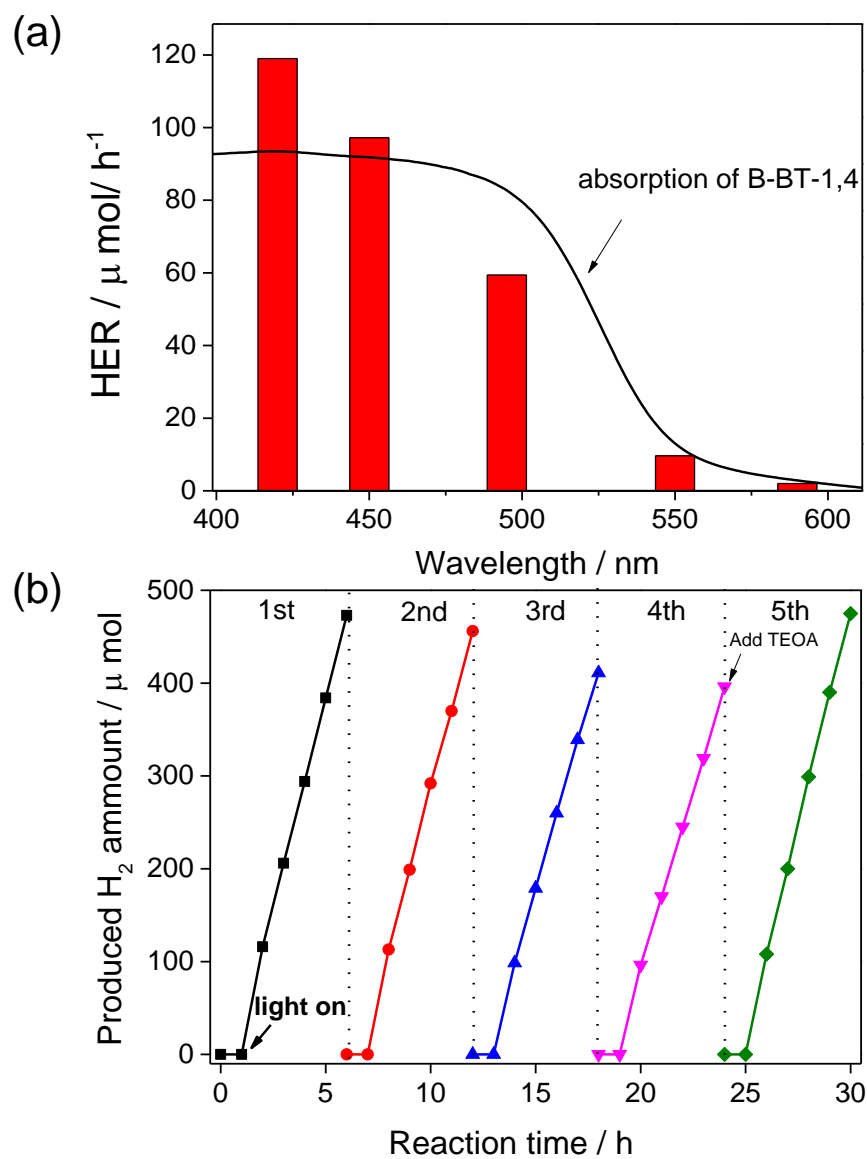


Figure 84. (a) Wavelength dependence of AQY on H₂ evolution using B-BT-1,4. (b) Stability and reusability test using B-BT-1,4 as a photocatalyst under visible-light irradiation ($\lambda > 420$ nm) for 30 h.

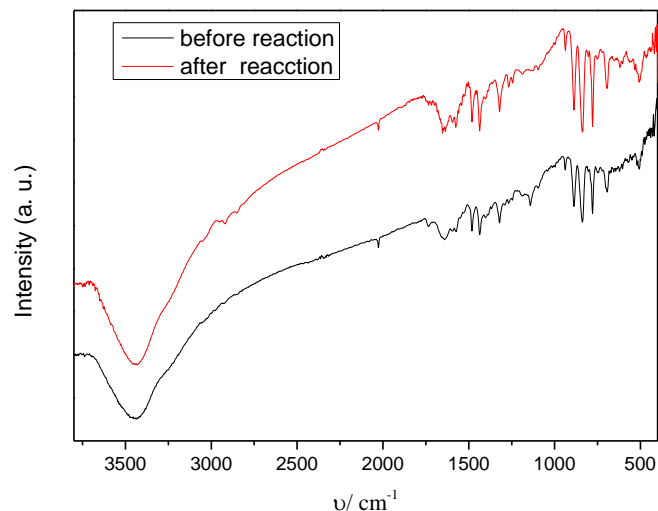


Figure 85. FTIR spectra of B-BT-1,4 before and after 5 repeating cycles of the hydrogen evolution process.

The polymers of both series were obtained as dark yellow powders with low content of Pd residue (Table 7). An additional study on the effect of metal co-catalysts confirmed the superior effect of Pt nanoparticles compared to those of Pd and Rh (Figure 86). TEM analysis of the used samples after the photocatalytic reaction revealed the formation of uniform Pt, Pd, and Rh nanoparticles on B-BT-1,4 (Figure 87 - Figure 90).

Table 7. Pd residue in the as-made polymers via ICP-MS measurements.

Polymer	Pd content (ppm)
B-BT-1,4	24.6
B-BT-1,3,5	31
B-BT-1,3,4	37.8
B-BT-1,2,4,5	29.8
B-BT-0.05	35.7
B-BT-0.1	24.5
B-BT-0.3	19.2
B-BT-0.5	23.1
B-BT-0.7	25.6
B-BT-1,4 (treated with thiourea)	5.1
B-BT-1,3,5 (treated with thiourea)	3.4

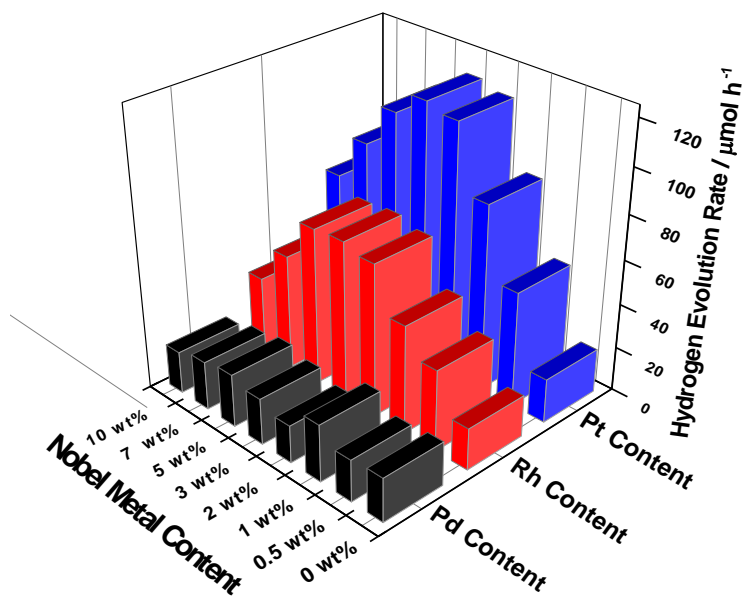


Figure 86. Co-catalysts study for hydrogen evolution from water using B-BT-1,4 as photocatalyst.

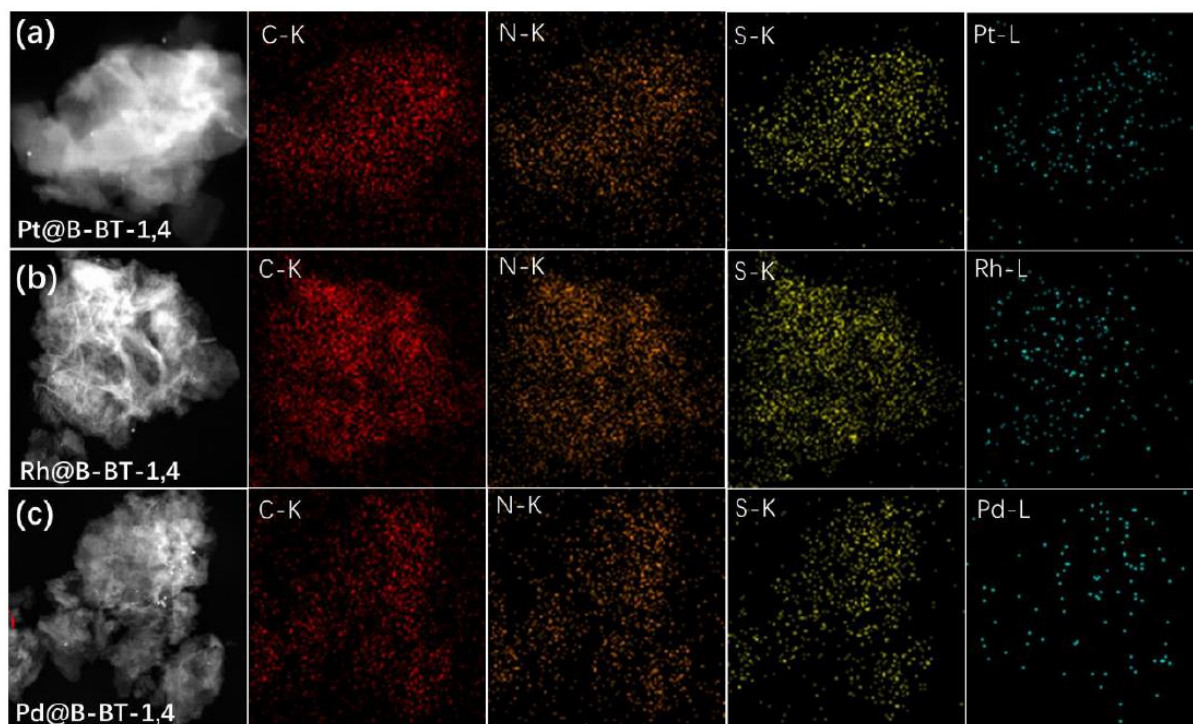


Figure 87. Elemental mapping of three metal nanoparticles (a) Pt, (b) Rh and (c) Pd on B-BT-1,4.

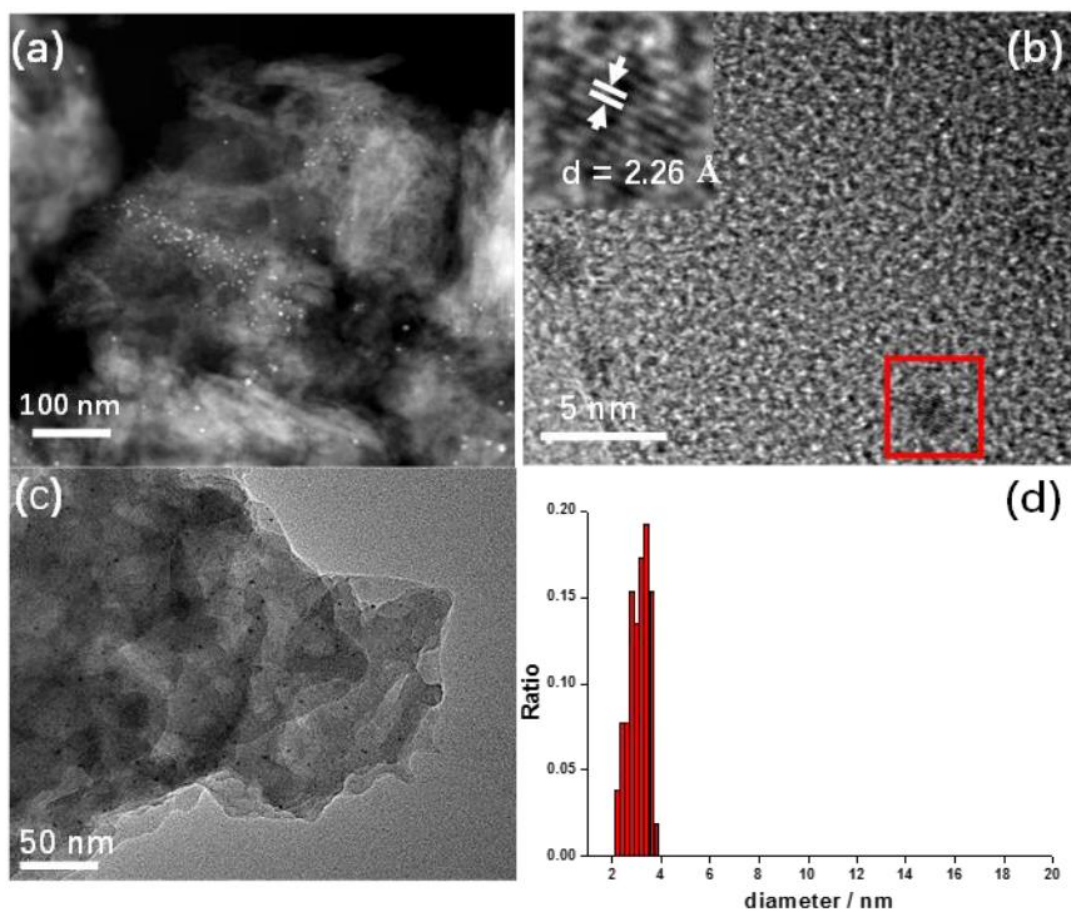


Figure 88. Characterization of Pt nanoparticles on B-BT-1,4.

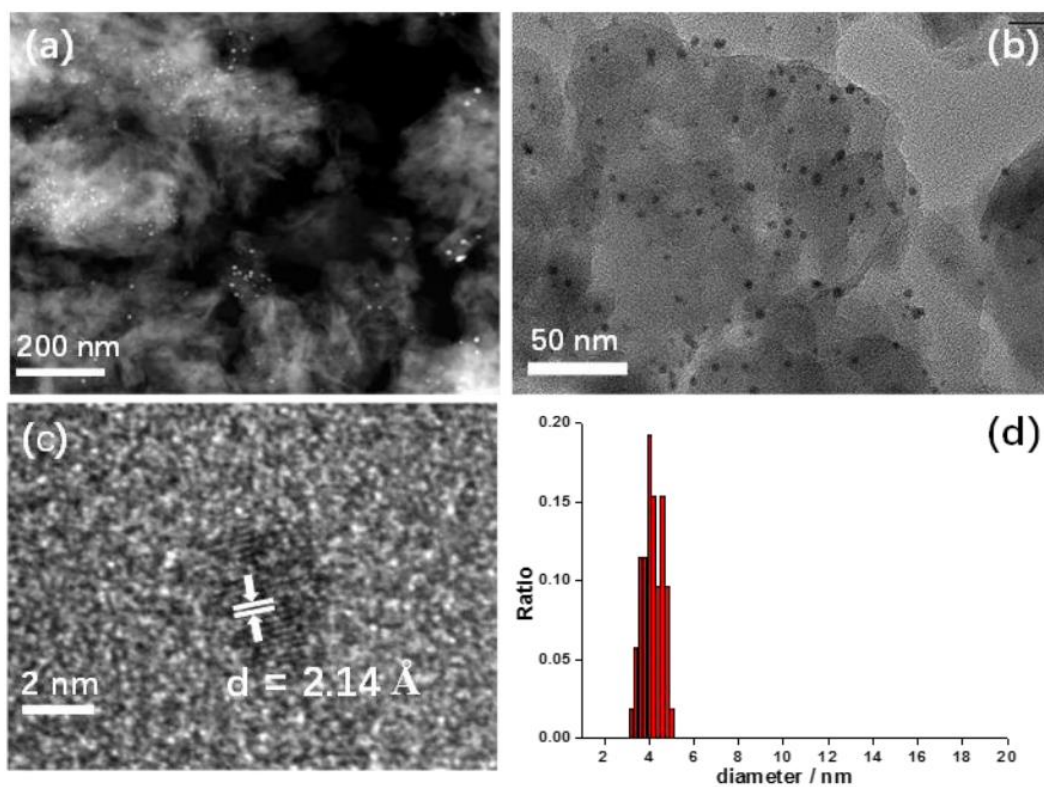


Figure 89. Characterization of Pd nanoparticles on B-BT-1,4.

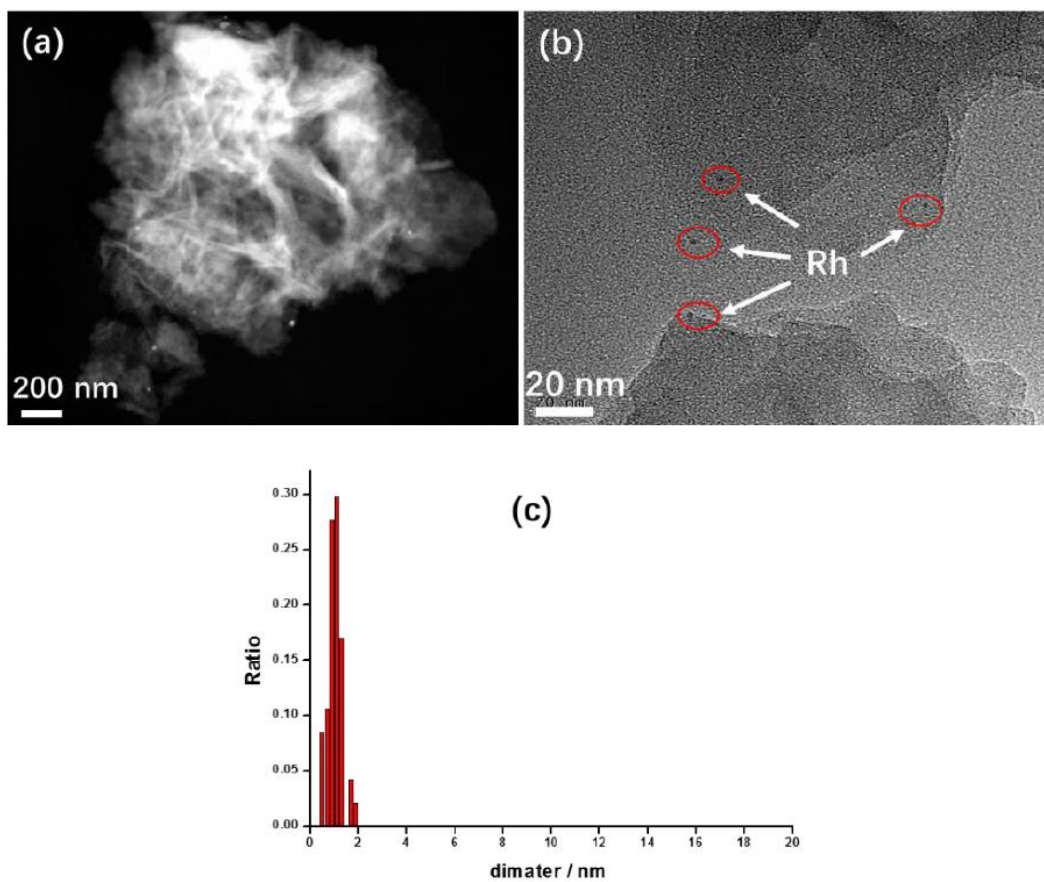


Figure 90. Characterization of Rh nanoparticles on B-BT-1,4.

4.4.4 Conclusions and outlook

In summary, a molecular structural design principle of conjugated polybenzothiadiazoles was presented as organic, heterogeneous photocatalytic systems for visible-light-promoted H₂ evolution. By simply copolymerizing the electron withdrawing benzothiadiazole units at different positions on phenyl rings, various polymers with defined energy-band structures and charge-transfer and charge-separation abilities could be obtained. Linear conjugated polymers based on a phenyl-benzothiadiazole alternating main chain exhibited superior photocatalytic activity, compared to its 3D polymer network counterparts, in H₂ evolution from water with a HER of 116 μmol h⁻¹. A negative effect on the H₂ evolution could be observed by introducing a 3D network character into the polymer backbone. The superior catalytic efficiency of the linear polybenzothiadiazole is likely attributed to the high efficiency of its light-induced charge-transfer, charge-separation, and electron-transfer ability. This design strategy could offer a promising platform of conjugated polymers as efficient and stable photocatalysts for H₂ evolution. There is a high potential for further optimization and molecular design possibilities, and it even allows the design of catalytic systems by coupling then with the oxidative photosynthetic units for water splitting and CO₂ fixation.

5 Experimental Section

5.1 Conjugated microporous polymer nanoparticles with enhanced photocatalytic applications in water

5.1.1 Materials

1,3,5-Triethynylbenzene (97%), copper (I) iodide (99%), tetrakis(triphenylphosphine) palladium(0) (99%), potassium carbonate (K_2CO_3) (99%), ammonium oxalate (99%), *p*-benzoquinone (98%), sodium azide (99%), *N,N,N',N'*-tetramethyl-*p*-phenylenediamine (TMPD) (97%), triethylamine (99%), rhodamine B (RhB) (99%) and all other solvents were purchased from Sigma Aldrich (Missouri, USA). Lutensol® AT50 (99%) was purchased from BASF (Ludwigshafen, Germany). Sodium *n*-dodecylsulfate (99%), 4,4'-dibromobiphenyl (98%), 9,9-dihexyl-2,7-dibromofluorene (98%), were obtained from Alfa Aesar (Massachusetts, USA). 4,7-dibromobenzo[*c*]-1,2,5-thiadiazole (97%) and 1,3,5-phenyltriboronic acid tris(pinacol) ester (97%) were purchased from Combi Blocks (California, USA). All chemicals and solvents were used as received unless otherwise specified.

5.1.2 Synthesis of B-FL₃-a, B-BPh₃-a and B-BT₃-a

B-FL₃-a, B-BPh₃-a and B-BT₃-a nanoparticles were synthesized using Suzuki-Miyaura cross coupling reaction via miniemulsion polymerization. First, 1,3,5-phenyltriboronic acid tris(pinacol) ester (2.5 mg mL⁻¹) and tetrakis(triphenylphosphine) palladium(0) (0.32 mg mL⁻¹) were dissolved in 2 mL of toluene (99%). Then, 9,9-dihexyl-2,7-dibromofluorene (4.06 mg mL⁻¹) was added to the mixture for B-FL₃-a, 4,4'-dibromobiphenyl (2.57 mg mL⁻¹) was added for B-BPh₃-a and 4,7-dibromobenzo[*c*]-1,2,5-thiadiazole (2.44 mg mL⁻¹) was added for B-BT₃-a. An aqueous solution (18 mL) of sodium *n*-dodecylsulfate (10 mg mL⁻¹) and K_2CO_3 (4.56 mg mL⁻¹) was added to the organic phase and vigorously stirred using a Branson W-450D digital Sonifier operating at 70% of amplitude for 2 min. Later, the homogeneous reaction mixture was stirred and heated at 80°C overnight. The resulted CMP nanoparticles were then transferred to a dialysis tube (MWCO 14.000 Da) with continuous water substitution to remove the surfactant.

5.1.3 Synthesis of B-FL₃-b, B-BPh₃-b and B-BT₃-b

The synthesis of B-FL₃-b, B-BPh₃-b and B-BT₃-b nanoparticles was performed using Sonogashira-Hagihara cross coupling reaction via miniemulsion polymerization. 1,3,5-Triethynylbenzene (2.5 mg mL⁻¹), tetrakis(triphenylphosphine) palladium(0) (0.98 mg mL⁻¹) and copper(I) iodide (0.16 mg mL⁻¹) were dissolved in 2 mL of toluene. Then, 9,9-dihexyl-2,7-dibromofluorene (12.29 mg mL⁻¹) was added to the mixture for B-FL₃-b, 4,4'-dibromobiphenyl (7.8 mg mL⁻¹) was added for B-BPh₃-b and 4,7-dibromobenzo[c]-1,2,5-thiadiazole (7.35 mg mL⁻¹) was added for B-BT₃-b. Triethylamine (2 mL) and an aqueous solution (17 mL) of sodium n-dodecylsulfate (10 mg mL⁻¹) were added to the organic phase and vigorously stirred using a Branson W-450D digital Sonifier operating at 70% of amplitude for 2 min. Later, the homogeneous reaction mixture was stirred and heated at 80°C overnight. The resulted CMP nanoparticles were transferred to a dialysis tube (MWCO 14.000 Da) with continuous water substitution to remove the surfactant.

5.1.4 Photodegradation of Rhodamine B

A mixture of CMP NPs dispersed in water (1 mg mL⁻¹) and RhB solution (10 mg L⁻¹) were stirred in the dark until reaching the adsorption/desorption equilibrium (60 min) between the nanoparticles and the solution. After that, the mixture was illuminated with a 23 W household energy saving light bulb (Osram) during different time intervals in air. Changes in RhB concentration were analysed using UV-vis spectroscopy. A control experiment with the reaction mixture under N₂, therefore, without oxygen in the reaction, was also performed. For the repeating experiments using B-BT₃-b as photocatalyst, the nanoparticles were separated via centrifugation after each photocatalytic reaction, and added to another RhB solution with the same concentration. The radical scavenger experiments were performed using ammonium oxalate (0.142 g mL⁻¹), *p*-benzoquinone (0.108 g mL⁻¹), sodium azide (65 mg mL⁻¹) and isopropanol (99%) (60 μL mL⁻¹). Each of the radical scavengers was added to a mixture of B-BT₃-b (1 mg mL⁻¹) and RhB solution (10 mg L⁻¹). After reaching the adsorption/desorption equilibrium the mixture was illuminated with a 23 W household energy saving light bulb (Osram) for 30 min and changes in RhB concentration were analysed using UV-vis spectroscopy.

5.1.5 Photooxidation of TMPD

A 10 mL glass vial containing Ar-saturated acetonitrile solutions (2 mL) of TMPD (32.85 mg mL⁻¹) with CMP NPs (4 mg mL⁻¹) was irradiated by a 23 W household energy saving light bulb for 5 h. After the irradiation, the CMP NPs were completely removed by centrifugation and filtration. The absorbance changes in UV-visible absorption spectra of the resulted solutions before and after irradiation were used to estimate the relative photocatalytic efficiency between the different CMP NPs.

5.1.6 Photooxidation of furoic acid into 5-hydroxy-2(5H)-furanone in aqueous solution

The heterogeneous singlet oxygen generation in aqueous solution was tested using a mixture of CMP nanoparticles dispersed in water (1 mg mL⁻¹) and furoic acid (22.42 mg mL⁻¹). The reaction mixture was irradiated at room temperature with a 23 W household energy saving light bulb (Osram) to initiate the photocatalytic reaction overnight. Later, the resulted mixture was then filtered with a 0.10 µm CME syringe filter and followed by lyophilisation. The full conversion of furoic acid into 5-hydroxy-2(5H)-furanone was analyzed by ¹H-NMR (250 MHz, D₂O).

5.1.7 Characterization

UV/vis absorption spectra were taken on a Perkin Elmer Lambda 25 UV-vis spectrometer. FT-IR spectra were recorded on a Nicolet 730 FT-IR spectrometer. TGA measurement was conducted on a Mettler Toledo TGA-851 system. Sample scans were carried out under nitrogen with temperature increase from 25°C to 1000°C using a heating rate of 10°C/min. SEM images were acquired on a LEO Gemini 1530 (Carl Zeiss AG, Germany) using an in lens SE detector. TEM images were performed on a JEM 1400 (JEOL, USA).

The polymer surface area and pore size distribution were measured by nitrogen adsorption and desorption at 77.3 K using Autosorb-1 (Quantachrome Instruments). Data were evaluated using QuadraWin software from Quantachrome Instruments. Pore size distributions and pore volumes were derived from the adsorption branches of the isotherms using Quenched Solid Density Functional Theory (QSDFT, N₂, assuming carbon adsorbent with slit pores). Samples were degassed at 100°C for 24 h under vacuum before analysis. The BET surface area calculation was based on data points

obtained from $0.05 < P/P_0 < 0.35$ and the nonlinear density functional theory (NLDFT) equilibrium model was used for the BET model fitting.

DLS measurements were carried out using a PSS Nicomp 380 Submicron Particle Sizer. Solid State ^{13}C CP/MAS NMR Spectroscopy was taken on a Bruker Avance solid state NMR spectrometer operating at 300 MHz Larmor frequency equipped with a standard 4 mm magic angle spinning (MAS) double resonance probe head. Electron paramagnetic resonance (EPR) was measured on a Magnettech Miniscope MS200 spectrometer.

5.2 Conjugated microporous polymer nanoparticles as visible light antibacterial photocatalysts via molecular doping

5.2.1 Materials

1,3,5-triethynylbenzene (97%), 2,5-dibromothiophene (96%), copper (I) iodide (99%), tetrakis(triphenylphosphine) palladium(0) (99%), potassium carbonate (K_2CO_3) (99%), ammonium oxalate (99%), catalase, sodium nitrate (99%), L-ascorbic acid (99%), triethylamine (99%), 5,5-dimethyl-1-pyrroline *N*-oxide (97%), 2,2,6,6-tetramethylpiperidine (98%), 5,5-dimethyl-1-pyrroline *N*-oxide (97%), α -terpinene (90%), mesitylene (98%) and all other solvents were purchased from Sigma Aldrich. Sodium *n*-dodecylsulfate (99%) was obtained from Alfa Aesar. 4,7-dibromobenzo[c]-1,2,5-thiadiazole (97%) was purchased from Combi Blocks. *Escherichia coli* K-12 and *Bacillus subtilis* were purchased from DSMZ Leibniz-Institute (Braunschweig, Germany). All chemicals and solvents were used as received unless otherwise specified.

5.2.2 Synthesis of CMP NPs

The synthesis of CMP nanoparticles was performed using Sonogashira-Hagihara cross coupling reaction via oil-in-water miniemulsion polymerization. 1,3,5-Triethynylbenzene (50 mg), tetrakis(triphenylphosphine) palladium(0) (19.24 mg), and copper(I) iodide (3.24 mg) were dissolved in 2 mL of toluene. Then, increasing amounts of 4,7-dibromobenzo[c]-1,2,5-thiadiazole and decreasing amounts of 2,5-dibromothiophene were added to the mixture on each reaction as following: Th-BT-0 (2,5-dibromothiophene: 120.96 mg), Th-BT-25 (2,5-dibromothiophene: 90.72 mg; 4,7-dibromobenzo[c]-1,2,5-thiadiazole: 36.75 mg), Th-BT-50 (2,5-dibromothiophene: 60.48 mg; 4,7-dibromobenzo[c]-1,2,5-thiadiazole: 73.50 mg), Th-BT-70 (2,5-dibromothiophene: 41.13 mg; 4,7-dibromobenzo[c]-1,2,5-thiadiazole: 97.89 mg), Th-BT-90 (2,5-dibromothiophene: 8.06 mg; 4,7-dibromobenzo[c]-1,2,5-thiadiazole: 138.17 mg) and Th-BT-100 (4,7-dibromobenzo[c]-1,2,5-thiadiazole: 146.99 mg). Triethylamine (2 mL) and an aqueous solution (17 mL) of sodium *n*-dodecylsulfate (200 mg) were added to the organic phase and vigorously stirred using a Branson W-450D digital Sonifier operating at 70% of amplitude for 2 min. The reaction mixture was then stirred and heated at 80°C overnight. The resulted CMP nanoparticles were transferred to a

dialysis tube (MWCO 14 000 Da) with continuous water substitution to remove the surfactant.

5.2.3 Photocatalytic disinfection test

The photocatalytic inactivation of bacteria was conducted using a White LED (0.25 W cm⁻², OSA Opto Lights) as light source. All glass apparatuses used in the experiments were autoclaved at 121°C for 20 min to ensure sterility. The bacterial cells were cultured in nutrient broth (Sigma Aldrich) and agitated at 300 rpm for 16h at 37°C and 30°C for *E. coli* K-12 and *B. subtilis* respectively. The cells were then washed with sterilized saline solution (0.9% NaCl) and the final cell density was adjusted to about 3.0×10^6 cfu (colony forming units) mL⁻¹. The CMP NP was then added to the cell suspension at a final concentration of 1 mg mL⁻¹ and kept in the dark for 60 min to ensure the establishment of an adsorption/desorption equilibrium between the photocatalyst and the bacterial cells. After this period, the reaction mixture was stirred at 25°C, bubbled with oxygen and irradiated with visible white light for different time intervals. At selected time intervals, aliquots of the sample were collected and serially diluted with sterilized saline solution. 0.1 mL of the diluted sample were then immediately spread on nutrient agar (Sigma Aldrich) plates and incubated at 37°C for 16 h to determine the number of viable cells (in cfu). For comparison, two extra control experiments were also conducted: the dark control was carried out with CMP NPs in absence of light and the light control was carried under visible light irradiation in the absence of CMP NPs. The survival fraction was determined by dividing the number of cfu of the samples incubated with CMP NPs by the number of the cfu of the control group in the absence of CMP NPs and light. The photocatalytic experiments using radical scavengers were performed similarly to the above photocatalytic disinfection test but with the addition of radical scavengers (ammonium oxalate, TEMP, catalase, NaNO₃ and Vitamin C), 0.05 mmol L⁻¹, to the reaction mixture. All treated and control experiments were performed in three independent studies.

5.2.4 Photooxidation of α -terpinene

The photooxidation of α -terpinene was performed using a mixture of α -terpinene (0.1 M), Th-BT-100 (1 mg mL⁻¹) and mesitylene (0.1 M) as internal standard in 10 ml water/acetonitrile (1:1). Under an oxygen flow of ca. 10 ml min⁻¹, the reaction mixture

was stirred at 25°C and irradiated with visible white light for 2h. After this, aliquots of the sample were collected and filtered with syringe filter and the solution was analyzed by $^1\text{H-NMR}$. The $^1\text{O}_2$ generation rate was defined as: $R(^1\text{O}_2) = (\text{obtained amount of ascaridole [mmol]})/(\text{weight of Th-BT-100[g]})/(\text{reaction time[s]})$. A dark control and a degassed sample were carried out in the absence of light and oxygen respectively.

5.2.5 Characterization

The UV/vis absorption spectra were recorded on a Perkin Elmer Lambda 25 UV-vis spectrometer. FT-IR spectra were recorded on a Nicolet 730 FT-IR spectrometer. Thermogravimetric analysis (TGA) was performed on a Mettler Toledo TGA-851 system. Sample scans were carried out under nitrogen using a heating rate of $10^\circ\text{C min}^{-1}$. Scanning electronic microscope (SEM) images were acquired on a LEO Gemini 1530 (Carl Zeiss AG, Germany) using an in lens SE detector. Transmission electronic microscope (TEM) images were performed on a JEM 1400 (JEOL, USA).

Polymer surface area and pore size distribution were measured by nitrogen adsorption and desorption at 77.3 K using Autosorb-1 (Quantachrome Instruments). Data were evaluated using QuadraWin software from Quantachrome Instruments. Pore size distributions and pore volumes were derived from the adsorption branches of the isotherms using Quenched Solid Density Functional Theory (QSDFT, N_2 , assuming carbon adsorbent with slit pores). Samples were degassed at 150°C for 24 h under vacuum before analysis. The BET surface area calculation was based on data points obtained from $0.05 < P/P_0 < 0.35$ and the nonlinear density functional theory (NLDFT) equilibrium model was used for the BET model fitting.

$^1\text{H-NMR}$ measurements were recorded on Bruker Avance 250 system. Solid State ^{13}C CP/MAS NMR spectroscopy was taken on a Bruker Avance solid state NMR spectrometer operating at 300 MHz Larmor frequency equipped with a standard 4 mm magic angle spinning (MAS) double resonance probe head. Electron paramagnetic resonance (EPR) was measured on a Magnettech Miniscope MS200 spectrometer.

Cyclic voltammetry (CV) measurements were carried out on a Metrohm Autolab PGSTAT204 potentiostat/galvanostat in a three-electrode-cell system: glassy carbon electrode as the working electrode, Hg/HgCl_2 electrode as the reference electrode, platinum wire as the counter electrode. The samples were prepared by first mixing ground polymer with 5 wt.% Nafion, the mixture was dropped cast on top of a glassy

carbon working electrode and let the solvent evaporate in a vacuum chamber for 60 min. The measurement was carried out in a 0.1 M solution of tetrabutylammonium hexafluorophosphate (0.1 M) as supporting electrolyte in acetonitrile with a scan rate of 100 mV s^{-1} in the range of -1.4 V to 0.1 V.

5.3 Visible light induced photocatalytic recycling of NAD⁺ cofactor by Conjugated Microporous Polymer Nanoparticles

5.3.1 Materials

1,3,5-Triethynylbenzene (97%), copper(I) iodide (99%), tetrakis(triphenylphosphine) palladium(0) (99%), potassium carbonate (K₂CO₃) (99%), triethylamine (99%) and all other solvents were purchased from Sigma Aldrich. Sodium n-dodecylsulfate (99%) was obtained from Alfa Aesar. 4,7-dibromobenzo[c][1,2,5]oxadiazole was synthesized according to literature [262]. All chemicals and solvents were used as received unless otherwise specified.

5.3.2 Synthesis of B-BO₃

The synthesis of CMP nanoparticles B-BO₃ was performed using the Sonogashira-Hagihara cross coupling reaction via oil-in-water miniemulsion polymerization. 1,3,5-triethynylbenzene (50 mg), 4,7-dibromobenzo[c][1,2,5]oxadiazole (138.95 mg) tetrakis(triphenylphosphine) palladium(0) (19.65 mg), and copper(I) iodide (6.48 mg) were dissolved in 2 mL of toluene. Then, triethylamine (1 mL) and an aqueous solution (17 mL) of sodium n-dodecylsulfate (200 mg) were added to the organic phase and vigorously stirred using a Branson W-450D digital Sonifier operating at 70% of amplitude for 2 min. The reaction mixture was then stirred and heated at 80 °C overnight. The resulting CMP nanoparticles were transferred to a dialysis tube (MWCO 14 000 Da) with continuous water substitution to remove the surfactant.

5.3.3 Photocatalytic test for regeneration of NAD⁺ cofactor

A mixture of an oxygen saturated water solution of NADH (0.02 M) with B-BO₃ (1 mg mL⁻¹) was illuminated with blue LED (460 nm, 0.25 W) during different time intervals. The production of NAD⁺ was followed over time by solution ¹H-NMR (300 MHz) and the product conversion was monitored by integration of the corresponding peaks. Control experiments with the reaction mixture in dark conditions were also performed.

5.3.4 Biocompatibility of regenerated-NAD (rNAD)

The enzymatic assays were carried out in one- and two-steps reactions For the two-step reactions (2S), first the regeneration of NAD⁺ (0.02 M) described in

experimental section 5.3.3 was conducted in a separate vessel for 2h. After this, B-BO₃ was removed using a syringe filter and the regenerated NAD⁺ solution was mixed with the reaction media containing glycerol dehydrogenase (1 unit mL⁻¹), propylene glycol (50 mM), ammonium sulphate (33 mM), phosphate (6 mM) and carbonate (0.10 M) buffers (pH 10.5), and kept at room temperature for 1h for the enzymatic assay. Longer reaction times were avoided to prevent degradation of NAD⁺ in the basic pH required for GDH.

For the one step reaction, a mixture of an oxygen saturated water solution of NADH (0.02 M) with B-BO₃ (1 mg mL⁻¹) together with all the enzymatic assay reagents were mixed in a single vessel and illuminated with blue LED (460 nm, 0.25 W) during different time intervals. The product conversion and relative yields were monitored over time by solution ¹H-NMR (300 MHz) by integration of the corresponding peaks. Control enzymatic assays with non-regenerated NAD⁺ were also performed.

5.3.5 Characterization

The UV/vis absorption spectra were recorded on a Perkin Elmer Lambda 25 UV-vis spectrometer. FTIR spectra were recorded on a Nicolet 730 FTIR spectrometer. ¹H-NMR measurements were recorded on Bruker Avance 250 system. Solid State ¹³C CP/MAS NMR spectroscopy was taken on a Bruker Avance solid state NMR spectrometer operating at 300 MHz Larmor frequency equipped with a standard 4 mm magic angle spinning (MAS) double resonance probe head.

Polymer surface area and pore size distribution were measured by nitrogen adsorption and desorption at 77.3 K using Autosorb-1 (Quantachrome Instruments). Data were evaluated using QuadraWin software from Quantachrome Instruments. Pore size distributions and pore volumes were derived from the adsorption branches of the isotherms using Quenched Solid Density Functional Theory (QSDFT, N₂, assuming carbon adsorbent with slit pores). Samples were degassed at 150 °C for 24 h under vacuum before analysis. The BET surface area calculation was based on data points obtained from 0.05 < P/P₀ < 0.35 and the nonlinear density functional theory (NLDFT) equilibrium model was used for the BET model fitting.

The powder X-ray diffraction (XRD) patterns were recorded on a Philips PW 1820 diffractometer with a CuK α radiation ($\lambda = 1.5418 \text{ \AA}$). Thermogravimetric analysis

(TGA) was performed on a Mettler Toledo TGA-851 system. Sample scans were carried out under nitrogen using a heating rate of $10^{\circ}\text{C min}^{-1}$.

Scanning electronic microscope (SEM) images were acquired on a LEO Gemini 1530 (Carl Zeiss AG, Germany) using an in lens SE detector. Transmission electronic microscope (TEM) images were performed on a JEM 1400 (JEOL, USA). Electron paramagnetic resonance (EPR) was measured on a Magnettech Miniscope MS200 spectrometer.

Cyclic voltammetry (CV) measurements were carried out on a Metrohm Autolab PGSTAT204 potentiostat/galvanostat in a three-electrode-cell system: glassy carbon electrode as the working electrode, Hg/HgCl₂ electrode as the reference electrode, platinum wire as the counter electrode. The samples were prepared by first mixing ground polymer with 5 wt.% Nafion, the mixture was dropped cast on top of a glassy carbon working electrode and let the solvent evaporate in a vacuum chamber for 60 min. The measurement was carried out in a 0.1 M solution of tetrabutylammonium hexafluorophosphate (0.1 M) as supporting electrolyte in acetonitrile with a scan rate of 100 mV s^{-1} in the range of -1.4 V to 0.1 V.

5.4 Molecular engineering of conjugated polybenzothiadiazoles for enhanced hydrogen production by photosynthesis

5.4.1 Materials

1,3,5-Phenyltriboronic acid tris(pinacol) ester (98%) and 4,7-dibromobenzo[c]-1,2,5-thiadiazole (97%) were purchased from Combi Blocks. 1,4-phenylenediboronic acid (95%), 1,2,4-tribromobenzene (95%), 1,2,4,5-tetrabromobenzene (94%), 2,1,3-benzothiadiazole-4,7-bis(boronic acid pinacol ester) (95%), tetrakis(triphenylphosphine) palladium(0) (99%), potassium carbonate (K_2CO_3) and all other solvents were purchased from Sigma-Aldrich. All chemicals and solvents were used as received unless otherwise specified.

5.4.2 Synthesis of polybenzothiadiazoles

The conjugated microporous polymer networks were synthesized using palladium catalysed Suzuki-Miyaura cross coupling condensation reaction. In the series 1 for B-BT-1,2,4 (yield: 82%), 1,2,4-tribromobenzene (300.00 mg), tetrakis(triphenylphosphine) palladium(0) (111.28 mg) were dissolved in 40 mL of DMF. Then, 2,1,3-benzothiadiazole-4,7-bis(boronic acid pinacol ester) (560.61 mg) was added to the mixture. The solution was degassed with nitrogen for 5 min. A degassed aqueous solution (5 mL) of K_2CO_3 (798.55 mg) was added to the organic phase. For B-BT-1,2,4,5 (yield: 79%), 1,2,4,5-tetrabromobenzene (300.00 mg), tetrakis(triphenylphosphine) palladium(0) (88.05 mg) were dissolved in 40 mL of DMF. Then, 2,1,3-benzothiadiazole-4,7-bis(boronic acid pinacol ester) (591.46 mg) was added to the mixture. The solution was degassed with nitrogen for 5 min. A degassed aqueous solution (5 mL) of K_2CO_3 (631.87 mg) was added to the organic phase. The reaction mixtures were stirred and heated at 130°C overnight. Later, the resulted precipitated solids were filtered off, washed with DCM and methanol in a Soxhlet overnight. The final products were dried at room temperature under vacuum. For the series 2, 4,7-dibromobenzo[c]-1,2,5-thiadiazole (500 mg), tetrakis(triphenylphosphine) palladium(0) (98.22 mg) were dissolved in 30 mL of DMF. Then, increasing amounts of 1,3,5 phenyltriboronic acid tris(pinacol) ester and decreasing amounts of 1,4-phenylenediboronic acid were added to the mixture on each reaction as following: B-BT₃-0% (1,4-phenylenediboronic acid: 282 mg; yield: 72%), B-BT₃-5% (1,4-

phenylenediboronic acid: 267.69 mg; 1,3,5 phenyltriboronic acid tris(pinacol) ester: 25.58 mg; yield: 69%), B-BT₃-10% (1,4-phenylenediboronic acid: 253.6 mg; 1,3,5 phenyltriboronic acid tris(pinacol) ester: 51.98 mg; yield: 73%), B-BT₃-30% (1,4-phenylenediboronic acid: 197.24 mg; 1,3,5 phenyltriboronic acid tris(pinacol) ester: 155.04 mg; yield: 75%), B-BT₃-50% (1,4-phenylenediboronic acid: 140.89 mg; 1,3,5 phenyltriboronic acid tris(pinacol) ester: 258.14 mg; yield: 69%), B-BT₃-70% (1,4-phenylenediboronic acid: 84.53 mg; 1,3,5 phenyltriboronic acid tris(pinacol) ester: 364.80 mg; yield: 74%) and B-BT₃-100% (1,3,5 phenyltriboronic acid tris(pinacol) ester: 516.28 mg; yield: 75%). The solution was degassed with nitrogen for 5 min. A degassed aqueous solution (5 mL) of K₂CO₃ (1409.69 mg) was added to the organic phase and the reaction mixture was stirred and heated at 130°C overnight. Later, the resulted precipitated solid was filtered off, washed with DCM and methanol in a Soxhlet overnight. The final product was dried at room temperature under vacuum.

5.4.3 Photocatalytic activity test for hydrogen evolution

Reactions were carried out in a Pyrex top-irradiation reaction vessel connected to a closed gas system. Hydrogen production was performed by dispersing 50 mg of catalyst powder in an aqueous solution (100 mL) containing 10 mL sacrificial agent (TEOA, 10 vol%) as electron donor. 3 wt.% noble metals (Pt, Rh and Pd) as co-catalysts were loaded on the surface of the polymer catalyst by *in situ* photodeposition method using H₂PtCl₆, RhCl₃ and PdCl₂. The reaction solution was evacuated several times assure complete removal of air prior to irradiation under a 300W Xe lamp. The wavelength of the excitation light was controlled by applying appropriate long-pass cut-off filters. The temperature of the reaction solution was maintained at room temperature by the flow of cooling water during the reaction. The evolved gases were analyzed by gas chromatography equipped with a thermal conductive detector (TCD) and 5A molecular sieve column, using argon as the carrier gas.

5.4.4 AQY measurement

The apparent quantum yield (AQY) for H₂ evolution was measured using monochromatic LED lamps with band pass filter of 405±3.9, 420±4.6, 470±4.4, 490±3.8, 520±4.0, 546±3.4 and 578±4.1 nm (errors of wavelength were dependent on Gauss Simulation of full width at half maximum), the intensities were 15.9, 14.3, 11.2, 7.6, 2.9,

5.8, 1.6 mW cm⁻¹ respectively (ILT 950 spectroradiometer). The irradiation area was controlled as 3×3 cm². Depending on the amount of hydrogen produced by the photocatalytic reaction in an average of one hour, and the AQY was calculated as follow:

$$\begin{aligned} \eta_{AQY} &= \frac{N_e}{N_p} \times 100\% = \frac{2 \times M \times N_A}{\frac{E_{total}}{E_{photon}}} \times 100\% \\ &= \frac{2M \times N_A}{S \times P \times t} \times 100\% = \frac{2 \times M \times N_A \times \hbar \times c}{S \times P \times t \times \lambda} \times 100\% \\ &\quad \hbar \times \frac{c}{\lambda} \end{aligned}$$

Where, M is the amount of H₂ molecules (mol), N_A is Avogadro constant (6.022×10²³/mol), h is the Planck constant (6.626×10⁻³⁴J·s), c is the speed of light (3×10⁸m/s), S is the irradiation area (cm²), P is the intensity of irradiation light (W/cm²), t is the photoreaction time (s), λ is the wavelength of the monochromatic light (m).

5.4.5 Characterization

DRS UV-Vis absorption spectra were recorded at room temperature on a Perkin Elmer Lambda 25 UV-vis spectrometer. FTIR spectra were recorded on a Nicolet 730 FT-IR spectrometer. Thermogravimetric analysis (TGA) was performed under nitrogen atmosphere on a Mettler Toledo TGA-851 system with temperature increase from 25°C to 1000°C at a heating rate of 10°C min⁻¹. Scanning electron microscope (SEM) images were acquired on a LEO Gemini 1530 (Carl Zeiss AG, Germany) using an in lens SE detector.

Polymer porous properties were measured by nitrogen adsorption and desorption at 77.3 K using Autosorb-1 (Quantachrome Instruments). Data were evaluated using QuadraWin software from Quantachrome Instruments. Pore size distributions and pore volumes were derived from the adsorption branches of the isotherms using Quenched Solid Density Functional Theory (QSDFT, N₂, assuming carbon adsorbent with slit pores). Samples were degassed at 100 °C for 24 h under vacuum before analysis. The BET surface area calculation was based on data points obtained from 0.05<P/P₀<0.35 and the nonlinear density functional theory (NLDFT) equilibrium model was used for the BET model fitting.

Solid State ^{13}C CP/MAS NMR spectroscopy was carried out using a Bruker Avance II solid state NMR spectrometer operating at 300 MHz Larmor frequency equipped with a standard 4 mm magic angle spinning (MAS) double resonance probe head.

Cyclic voltammetry (CV) measurements were carried out on a Metrohm Autolab PGSTAT204 potentiostat/galvanostat in a three-electrode-cell system: glassy carbon electrode as the working electrode, Hg/HgCl₂ electrode as the reference electrode, platinum wire as the counter electrode. The samples were prepared by first mixing ground polymer with 5 wt.% Nafion, the mixture was dropped cast on top of a glassy carbon working electrode and let the solvent evaporate in a vacuum chamber for 60 min. The measurement was carried out in a 0.1 M solution of tetrabutylammonium hexafluorophosphate (0.1 M) as supporting electrolyte in acetonitrile with a scan rate of 100 mV s⁻¹ in the range of -1.4 V to 0.1 V. For the conversion from Hg/HgCl₂ redox couple to the Normal Hydrogen Electrode (NHE), the equation $E_{\text{NHE}} = E_{\text{SCE}} - 0.24$ was applied.

Theoretical calculations were implemented in the Gaussian 03 program [2]. The B3LYP functions and the 6-31 G(d,p) basis set were used for all the atoms in the DFT calculations.

6 Summary and Outlook

This work highlights different designs and preparations of conjugated microporous polymers (CMPs) for heterogeneous visible light photocatalysis in aqueous media in order to overcome the two main limitations of the conventional CMPs: (i) solution processability due to their high hydrophobicity, and (ii) applications as heterogeneous visible light photocatalysts in aqueous media.

A nanostructured model of well dispersible conjugated microporous polymer nanoparticles was presented as synthetic strategy for the processability of CMPs. In particular, CMP NPs were prepared in direct miniemulsion polymerization method rendering highly stable dispersions. A range of different morphologies could be adjusted by simple introduction of different aromatic building block moieties into the polymer backbone. Superior photocatalytic activity of the CMP NPs was demonstrated in the degradation of rhodamine B and photooxidation of *N,N,N',N'*-tetramethyl-*p*-phenylenediamine under visible light irradiation of a household light bulb.

In the second part, a combination of miniemulsion method together with a molecular doping strategy of benzothiadiazole units into a polymer backbone containing thiophene units was employed for the synthesis of CMP NPs in order to investigate the impact of the structural design on a molecular level *via* electron donor and acceptor variations, which highly influenced the photocatalytic efficiency of the CMP NPs. From the obtained stable dispersions, it was demonstrated that CMP NPs with higher amounts of incorporated acceptor units resulted in higher photocatalytic efficiency for the generation of *singlet* oxygen with the best production rate of *ca.* 0.14 mmol g⁻¹ s⁻¹. Additionally, the CMP NPs demonstrated superior performance as visible light active agents for the photodynamic inactivation of the bacteria *E. coli K-12* and *B. subtilis*.

In the third part, CMP NPs were presented as a simple visible light-induced regeneration module for recycling of NAD⁺ from NADH. From the obtained dispersions of B-BO₃ it was demonstrated that high conversion rates of recycled NAD⁺ could be achieved and heterogeneous B-BO₃ photocatalyst did not require additional mediators for the photocatalytic performance. In addition, two-step reaction designs offered the best results in terms of enzyme activity and the light-induced conversion of NADH to NAD⁺ coupled with the enzymatic oxidation of PG was also demonstrated in a one-pot

design in which NAD^+ regeneration and NADH production could be performed simultaneously.

In the last part, a water processability of the conventional CMPs was achieved by using hydrophilic sacrificial agents both as phase transfer agent and electron donor in the photocatalytic process. Furthermore, a molecular structural design of conjugated polybenzothiadiazole based CMP series was presented as organic heterogeneous photocatalytic system for H_2 evolution under visible light irradiation. A variety of polymer architectures from 1D to 3D networks was obtained by co-polymerization of benzothiadiazole units at different positions on phenyl rings. It could be demonstrated that linear based conjugated polymers with the use of amine as a phase transfer agent exhibited exceptional photocatalytic activity for H_2 evolution from water in comparison to 3D polymer network counterparts.

In summary, the approaches explored in this work demonstrated promising perspectives for conjugated microporous polymers to be used as heterogeneous visible light photocatalyst in aqueous environment. The processability extended the range of applications to different fields and it offers a high potential for future optimization.

7 References

- [1] R. C. Evans, P. Douglas, H. D. Burrows, *Applied Photochemistry*, Springer Netherlands, 2013.
- [2] M. H. Abdel-Kader, *Photodynamic therapy. From theory to application*, Springer Berlin Heidelberg, 2014.
- [3] S. E. Braslavsky, *Pure Appl. Chem.* **2007**, 79, 293.
- [4] Y. H. Sang, H. Liu, A. Umar, *Chemcatchem* **2015**, 7, 559.
- [5] N. Corrigan, S. Shanmugam, J. Xu, C. Boyer, *Chem. Soc. Rev.* **2016**.
- [6] C. K. Prier, D. A. Rankic, D. W. C. MacMillan, *Chem. Rev.* **2013**, 113, 5322.
- [7] B. C. Ma, S. Ghasimi, K. Landfester, F. Vilela, K. A. I. Zhang, *Journal of Materials Chemistry A* **2015**, 3, 16064.
- [8] Q. Q. Liu, Z. Tang, M. D. Wu, Z. H. Zhou, *Polym. Int.* **2014**, 63, 381.
- [9] Y. H. Xu, S. B. Jin, H. Xu, A. Nagai, D. L. Jiang, *Chem. Soc. Rev.* **2013**, 42, 8012.
- [10] K. Zhang, D. Kopetzki, P. H. Seeberger, M. Antonietti, F. Vilela, *Angew. Chem. Int. Ed.* **2013**, 52, 1432.
- [11] G. Cheng, T. Hasell, A. Trewin, D. J. Adams, A. I. Cooper, *Angewandte Chemie-International Edition* **2012**, 51, 12727.
- [12] H. Urakami, K. Zhang, F. Vilela, *Chem. Commun.* **2013**, 49, 2353.
- [13] S. Ghasimi, K. Landfester, K. A. I. Zhang, *Chemcatchem* **2016**, 8, 694.
- [14] S. Deng, J. Zhi, X. Zhang, Q. Wu, Y. Ding, A. Hu, *Angewandte Chemie-International Edition* **2014**, 53, 14144.
- [15] P. Zhang, Z. H. Weng, J. Guo, C. C. Wang, *Chem. Mater.* **2011**, 23, 5243.
- [16] H. D. Roth, *Angewandte Chemie-International Edition in English* **1989**, 28, 1193.
- [17] A. Albini, *Photochemistry. Past, Present and Future*, Springer-Verlag Berlin Heidelberg, 2016.
- [18] T. P. Yoon, M. A. Ischay, J. N. Du, *Nat. Chem.* **2010**, 2, 527.
- [19] D. M. Schultz, T. P. Yoon, *Science* **2014**, 343, 985.
- [20] G. Ciamician, *Science* **1912**, 36, 385.
- [21] J. M. Coronado, F. Fresno, M. D. Hernández-Alonso, *Design of Advanced Photocatalytic Materials for Energy and Environmental Applications*, Springer London, 2013.

- [22] N. Serpone, A. V. Emeline, S. Horikoshi, V. N. Kuznetsov, V. K. Ryabchuk, *Photochemical & Photobiological Sciences* **2012**, 11, 1121.
- [23] A. J. B. Robertson, *Platinum Metals Reviews* **1975**, 19, 64.
- [24] A. Köhler, H. Bässler, *Electronic processes in organic semiconductors: an introduction*, Wiley-VCH Verlag GmbH & Co., 2015.
- [25] H. Kisch, *Angewandte Chemie-International Edition* **2013**, 52, 812.
- [26] X. J. Lang, X. D. Chen, J. C. Zhao, *Chem. Soc. Rev.* **2014**, 43, 473.
- [27] N. Li, X. Lang, W. Ma, H. Ji, C. Chen, J. Zhao, *Chem. Commun.* **2013**, 49, 5034.
- [28] S. Yurdakal, G. Palmisano, V. Loddo, V. Augugliaro, L. Palmisano, *J. Am. Chem. Soc.* **2008**, 130, 1568.
- [29] K. Sayama, H. Arakawa, *J. Phys. Chem.* **1993**, 97, 531.
- [30] Z. R. R. Tian, J. A. Voigt, J. Liu, B. McKenzie, M. J. McDermott, M. A. Rodriguez, H. Konishi, H. F. Xu, *Nature Materials* **2003**, 2, 821.
- [31] Y. Liu, L. Xie, Y. Li, R. Yang, J. L. Qu, Y. Q. Li, X. G. Li, *J. Power Sources* **2008**, 183, 701.
- [32] T. Ishihara, H. Nishiguchi, K. Fukamachi, Y. Takita, *J. Phys. Chem. B* **1999**, 103, 1.
- [33] A. International, Vol. 2016, ASTM International, 2012.
- [34] J. M. R. Narayanam, C. R. J. Stephenson, *Chem. Soc. Rev.* **2011**, 40, 102.
- [35] T. P. Nicholls, D. Leonori, A. C. Bissember, *Nat. Prod. Rep.* **2016**.
- [36] D. A. Nicewicz, T. M. Nguyen, *Acs Catalysis* **2014**, 4, 355.
- [37] N. A. Romero, D. A. Nicewicz, *Chem. Rev.* **2016**, 116, 10075.
- [38] Y. J. Cui, Z. X. Ding, P. Liu, M. Antonietti, X. Z. Fu, X. C. Wang, *Phys. Chem. Chem. Phys.* **2012**, 14, 1455.
- [39] X. C. Wang, K. Maeda, A. Thomas, K. Takanabe, G. Xin, J. M. Carlsson, K. Domen, M. Antonietti, *Nature Materials* **2009**, 8, 76.
- [40] X. B. Chen, S. H. Shen, L. J. Guo, S. S. Mao, *Chem. Rev.* **2010**, 110, 6503.
- [41] S. B. Wang, X. C. Wang, *Small* **2015**, 11, 3097.
- [42] D. Ravelli, M. Fagnoni, A. Albini, *Chem. Soc. Rev.* **2013**, 42, 97.
- [43] M. Neumann, S. Fuldner, B. Konig, K. Zeitler, *Angewandte Chemie-International Edition* **2011**, 50, 951.

- [44] C. Acar, I. Dincer, C. Zamfirescu, *International Journal of Energy Research* **2014**, 38, 1903.
- [45] J. Chen, J. Cen, X. L. Xu, X. N. Li, *Catalysis Science & Technology* **2016**, 6, 349.
- [46] W. W. Zhao, C. B. Liu, L. M. Cao, X. G. Yin, H. Xu, B. Zhang, *Rsc Advances* **2013**, 3, 22944.
- [47] X. J. Lang, W. Hao, W. R. Leow, S. Z. Li, J. C. Zhao, X. D. Chen, *Chemical Science* **2015**, 6, 5000.
- [48] C. L. Wang, D. Astruc, *Chem. Soc. Rev.* **2014**, 43, 7188.
- [49] S. M. Gupta, M. Tripathi, *High Energ. Chem.* **2012**, 46, 1.
- [50] T. Shishido, T. Miyatake, K. Teramura, Y. Hitomi, H. Yamashita, T. Tanaka, *Journal of Physical Chemistry C* **2009**, 113, 18713.
- [51] M. Rueping, J. Zoller, D. C. Fabry, K. Poscharny, R. M. Koenigs, T. E. Weirich, J. Mayer, *Chemistry-a European Journal* **2012**, 18, 3478.
- [52] W. C. Lin, Y. J. Lin, *Environ. Eng. Sci.* **2012**, 29, 447.
- [53] J. F. Zhu, W. Zheng, H. E. Bin, J. L. Zhang, M. Anpo, *Journal of Molecular Catalysis a-Chemical* **2004**, 216, 35.
- [54] H. Q. Zhuang, Q. Gu, J. L. Long, H. Lin, H. X. Lin, X. X. Wang, *Rsc Advances* **2014**, 4, 34315.
- [55] M. A. Zhang, C. C. Chen, W. H. Ma, J. C. Zhao, *Angewandte Chemie-International Edition* **2008**, 47, 9730.
- [56] V. Jeena, R. S. Robinson, *Chem. Commun.* **2012**, 48, 299.
- [57] G. Kim, W. Choi, *Applied Catalysis B-Environmental* **2010**, 100, 77.
- [58] F. Parrino, V. Augugliaro, G. Camera-Roda, V. Loddo, M. J. Lopez-Munoz, C. Marquez-Alvarez, G. Palmisano, L. Palmisano, M. A. Puma, *J. Catal.* **2012**, 295, 254.
- [59] Y. Park, N. J. Singh, K. S. Kim, T. Tachikawa, T. Majima, W. Choi, *Chemistry-a European Journal* **2009**, 15, 10843.
- [60] S. Higashimoto, N. Kitao, N. Yoshida, T. Sakura, M. Azuma, H. Ohue, Y. Sakata, *J. Catal.* **2009**, 266, 279.
- [61] S. Higashimoto, N. Suetsugu, M. Azuma, H. Ohue, Y. Sakata, *J. Catal.* **2010**, 274, 76.
- [62] X. F. Wang, S. F. Li, H. G. Yu, J. G. Yu, S. W. Liu, *Chemistry-a European Journal* **2011**, 17, 7777.
- [63] M. Saiful Islam, S. Lazure, R.-n. Vannier, G. Nowogrocki, G. Mairesse, *J. Mater. Chem.* **1998**, 8, 655.

- [64] G. Tian, Y. Chen, W. Zhou, K. Pan, Y. Dong, C. Tian, H. Fu, *J. Mater. Chem.* **2011**, 21, 887.
- [65] A. Kudo, K. Ueda, H. Kato, I. Mikami, *Catal. Lett.* **1998**, 53, 229.
- [66] S. Linic, P. Christopher, D. B. Ingram, *Nature Materials* **2011**, 10, 911.
- [67] P. Wang, B. B. Huang, Y. Dai, M. H. Whangbo, *Phys. Chem. Chem. Phys.* **2012**, 14, 9813.
- [68] H. Y. Zhu, X. B. Ke, X. Z. Yang, S. Sarina, H. W. Liu, *Angewandte Chemie-International Edition* **2010**, 49, 9657.
- [69] A. Pineda, L. Gomez, A. M. Balu, V. Sebastian, M. Ojeda, M. Arruebo, A. A. Romero, J. Santamaria, R. Luque, *Green Chem.* **2013**, 15, 2043.
- [70] A. Tanaka, K. Hashimoto, H. Kominami, *Chem. Commun.* **2011**, 47, 10446.
- [71] H. Y. Zhu, X. Chen, Z. F. Zheng, X. B. Ke, E. Jaatinen, J. C. Zhao, C. Guo, T. F. Xie, D. J. Wang, *Chem. Commun.* **2009**, 7524.
- [72] A. Maldotti, A. Molinari, R. Juarez, H. Garcia, *Chemical Science* **2011**, 2, 1831.
- [73] S. Sarina, H. Y. Zhu, E. Jaatinen, Q. Xiao, H. W. Liu, J. F. Jia, C. Chen, J. Zhao, *J. Am. Chem. Soc.* **2013**, 135, 5793.
- [74] X. Chen, H. Y. Zhu, J. C. Zhao, Z. T. Zheng, X. P. Gao, *Angewandte Chemie-International Edition* **2008**, 47, 5353.
- [75] M. Gonzalez-Bejar, K. Peters, G. L. Hallett-Tapley, M. Grenier, J. C. Scaiano, *Chem. Commun.* **2013**, 49, 1732.
- [76] X. Wang, K. Maeda, A. Thomas, K. Takanabe, G. Xin, J. M. Carlsson, K. Domen, M. Antonietti, *Nature Materials* **2009**, 8, 76.
- [77] F. Z. Su, S. C. Mathew, G. Lipner, X. Z. Fu, M. Antonietti, S. Blechert, X. C. Wang, *J. Am. Chem. Soc.* **2010**, 132, 16299.
- [78] V. T. Bhat, P. A. Duspara, S. Seo, N. S. B. Abu Bakar, M. F. Greaney, *Chem. Commun.* **2015**, 51, 4383.
- [79] Z. S. Zheng, X. S. Zhou, *Chin. J. Chem.* **2012**, 30, 1683.
- [80] D. M. O'Carroll, C. E. Petoukhoff, J. Kohl, B. X. Yu, C. M. Carter, S. Goodman, *Polymer Chemistry* **2013**, 4, 5181.
- [81] W. Barford, *Electronic and optical properties of conjugated polymers*, Oxford University Press, 2013.
- [82] S. C. Rasmussen, in *100+ Years of Plastics*, Vol. 1080 (Eds: E. T. Strom, S. C. Rasmussen), American Chemical Society, 2011, 147.

- [83] Nobelprize.org, Vol. 2016, Nobel Media AB 2016.
- [84] X. Wang, G. Zhang, Z.-A. Lan, *Angew. Chem. Int. Ed.* **2016**, n/a.
- [85] N. Stutzmann, R. H. Friend, H. Sirringhaus, *Science* **2003**, 299, 1881.
- [86] J. Veres, S. Ogier, G. Lloyd, D. de Leeuw, *Chem. Mater.* **2004**, 16, 4543.
- [87] G. Yu, J. Gao, J. C. Hummelen, F. Wudl, A. J. Heeger, *Science* **1995**, 270, 1789.
- [88] Y. J. Cheng, S. H. Yang, C. S. Hsu, *Chem. Rev.* **2009**, 109, 5868.
- [89] F. Dumur, D. Gigmes, J.-P. Fouassier, J. Lalevée, *Acc. Chem. Res.* **2016**, 49, 1980.
- [90] M. C. Chiappelli, R. C. Hayward, *Adv. Mater.* **2012**, 24, 6100.
- [91] V. Vohra, U. Giovanella, R. Tubino, H. Murata, C. Botta, *Acs Nano* **2011**, 5, 5572.
- [92] T. Piok, S. Gamerith, C. Gadermaier, H. Plank, F. P. Wenzl, S. Patil, R. Montenegro, T. Kietzke, D. Neher, U. Scherf, K. Landfester, E. J. W. List, *Adv. Mater.* **2003**, 15, 800.
- [93] M. Gross, D. C. Muller, H. G. Nothofer, U. Scherf, D. Neher, C. Brauchle, K. Meerholz, *Nature* **2000**, 405, 661.
- [94] L. H. Feng, C. L. Zhu, H. X. Yuan, L. B. Liu, F. T. Lv, S. Wang, *Chem. Soc. Rev.* **2013**, 42, 6620.
- [95] F. Y. Wang, M. Li, B. Wang, J. Y. Zhang, Y. Q. Cheng, L. B. Liu, F. T. Lv, S. Wang, *Sci. Rep.* **2015**, 5, 8.
- [96] H. Zhang, R. L. Zong, J. C. Zhao, Y. F. Zhu, *Environ. Sci. Technol.* **2008**, 42, 3803.
- [97] G. Z. Liao, S. Chen, X. Quan, H. Chen, Y. B. Zhang, *Environ. Sci. Technol.* **2010**, 44, 3481.
- [98] H. J. Yan, Y. Huang, *Chem. Commun.* **2011**, 47, 4168.
- [99] N. Sakai, G. K. Prasad, Y. Ebina, K. Takada, T. Sasaki, *Chem. Mater.* **2006**, 18, 3596.
- [100] T. Yang, H. Wang, X. M. Ou, C. S. Lee, X. H. Zhang, *Adv. Mater.* **2012**, 24, 6199.
- [101] Q. Z. Luo, X. Y. Li, D. S. Wang, Y. H. Wang, J. An, *Journal of Materials Science* **2011**, 46, 1646.
- [102] Z. Pei, L. Ding, M. Lu, Z. Fan, S. Weng, J. Hu, P. Liu, *The Journal of Physical Chemistry C* **2014**, 118, 9570.
- [103] Y. W. Su, W. H. Lin, Y. J. Hsu, K. H. Wei, *Small* **2014**, 10, 4427.
- [104] J. Wang, Y. Zhong, L. Wang, N. Zhang, R. Cao, K. Bian, L. Alarid, R. E. Haddad, F. Bai, H. Fan, *Nano Lett.* **2016**.

- [105] S. Kundu, A. Patra, *Chem. Rev.* **2016**.
- [106] M. Zhang, W. D. Rouch, R. D. McCulla, *Eur. J. Org. Chem.* **2012**, 2012, 6187.
- [107] T. Shibata, A. Kabumoto, T. Shiragami, O. Ishitani, C. Pac, S. Yanagida, *J. Phys. Chem.* **1990**, 94, 2068.
- [108] S. Yanagida, A. Kabumoto, K. Mizumoto, C. Pac, K. Yoshino, *Journal of the Chemical Society-Chemical Communications* **1985**, 474.
- [109] S. Ghosh, N. A. Kouame, L. Ramos, S. Remita, A. Dazzi, A. Deniset-Besseau, P. Beaunier, F. Goubard, P. H. Aubert, H. Remita, *Nature Materials* **2015**, 14, 505.
- [110] R. S. Sprick, B. Bonillo, R. Clowes, P. Guignon, N. J. Brownbill, B. J. Slater, F. Blanc, M. A. Zwijnenburg, D. J. Adams, A. I. Cooper, *Angewandte Chemie-International Edition* **2016**, 55, 1824.
- [111] L. Stegbauer, K. Schwinghammer, B. V. Lotsch, *Chemical Science* **2014**, 5, 2789.
- [112] V. S. Vyas, F. Haase, L. Stegbauer, G. Savasci, F. Podjaski, C. Ochsenfeld, B. V. Lotsch, *Nat Commun* **2015**, 6.
- [113] J. X. Jiang, F. Su, A. Trewin, C. D. Wood, N. L. Campbell, H. Niu, C. Dickinson, A. Y. Ganin, M. J. Rosseinsky, Y. Z. Khimiyak, A. I. Cooper, *Angewandte Chemie-International Edition* **2007**, 46, 8574.
- [114] A. I. Cooper, *Adv. Mater.* **2009**, 21, 1291.
- [115] Y. Li, Z. Y. Fu, B. L. Su, *Adv. Funct. Mater.* **2012**, 22, 4634.
- [116] D. C. Wu, F. Xu, B. Sun, R. W. Fu, H. K. He, K. Matyjaszewski, *Chem. Rev.* **2012**, 112, 3959.
- [117] T. P. I. Saragi, T. Spehr, A. Siebert, T. Fuhrmann-Lieker, J. Salbeck, *Chem. Rev.* **2007**, 107, 1011.
- [118] L. Chen, Y. Honsho, S. Seki, D. L. Jiang, *J. Am. Chem. Soc.* **2010**, 132, 6742.
- [119] U. Scherf, E. J. W. List, *Adv. Mater.* **2002**, 14, 477.
- [120] T. Yamamoto, A. Morita, Y. Miyazaki, T. Maruyama, H. Wakayama, Z. Zhou, Y. Nakamura, T. Kanbara, S. Sasaki, K. Kubota, *Macromolecules* **1992**, 25, 1214.
- [121] C. Liu, H. Zhang, W. Shi, A. W. Lei, *Chem. Rev.* **2011**, 111, 1780.
- [122] W. Shi, C. Liu, A. W. Lei, *Chem. Soc. Rev.* **2011**, 40, 2761.
- [123] H. Chen, C. Yu, C. M. Jiang, S. Zhang, B. H. Liu, J. L. Kong, *Chem. Commun.* **2009**, 5006.
- [124] E. H. Cordes, W. P. Jencks, *J. Am. Chem. Soc.* **1962**, 84, 832.

- [125] N. Miyaura, A. Suzuki, *J. Chem. Soc., Chem. Commun.* **1979**, 866.
- [126] N. Miyaura, K. Yamada, A. Suzuki, *Tetrahedron Lett.* **1979**, 20, 3437.
- [127] Y. Nishihara, *Applied Cross-Coupling Reactions*, Vol. 80, Springer-Verlag Berlin Heidelberg, 2013.
- [128] N. Miyaura, A. Suzuki, *Chem. Rev.* **1995**, 95, 2457.
- [129] A. J. J. Lennox, G. C. Lloyd-Jones, *Chem. Soc. Rev.* **2014**, 43, 412.
- [130] K. Sonogashira, Y. Tohda, N. Hagihara, *Tetrahedron Lett.* **1975**, 16, 4467.
- [131] R. Chinchilla, C. Najera, *Chem. Soc. Rev.* **2011**, 40, 5084.
- [132] K. Sonogashira, *J. Organomet. Chem.* **2002**, 653, 46.
- [133] Y. Xie, T. T. Wang, X. H. Liu, K. Zou, W. Q. Deng, *Nature Communications* **2013**, 4, 7.
- [134] J.-X. Jiang, F. Su, H. Niu, C. D. Wood, N. L. Campbell, Y. Z. Khimyak, A. I. Cooper, *Chem. Commun.* **2008**, 486.
- [135] A. Li, H. X. Sun, D. Z. Tan, W. J. Fan, S. H. Wen, X. J. Qing, G. X. Li, S. Y. Li, W. Q. Deng, *Energy Environ. Sci.* **2011**, 4, 2062.
- [136] X. S. Wang, J. Liu, J. M. Bonfont, D. Q. Yuan, P. K. Thallapally, S. Q. Ma, *Chem. Commun.* **2013**, 49, 1533.
- [137] Q. Chen, J. X. Wang, F. Yang, D. Zhou, N. Bian, X. J. Zhang, C. G. Yan, B. H. Han, *J. Mater. Chem.* **2011**, 21, 13554.
- [138] Y. H. Xu, A. Nagai, D. L. Jiang, *Chem. Commun.* **2013**, 49, 1591.
- [139] X. Liu, Y. Xu, D. Jiang, *J. Am. Chem. Soc.* **2012**, 134, 8738.
- [140] X. M. Liu, Y. W. Zhang, H. Li, A. Sigen, H. Xia, Y. Mu, *Rsc Advances* **2013**, 3, 21267.
- [141] Y. Kou, Y. Xu, Z. Guo, D. Jiang, *Angew. Chem. Int. Ed.* **2011**, 50, 8753.
- [142] R. Li, Z. J. Wang, L. Wang, B. C. Ma, S. Ghasimi, H. Lu, K. Landfester, K. A. I. Zhang, *Acs Catalysis* **2016**, 6, 1113.
- [143] L. Chen, Y. Yang, D. L. Jiang, *J. Am. Chem. Soc.* **2010**, 132, 9138.
- [144] L. Chen, Y. Yang, Z. Q. Guo, D. L. Jiang, *Adv. Mater.* **2011**, 23, 3149.
- [145] X. S. Ding, B. H. Han, *Angew. Chem. Int. Ed.* **2015**, 54, 6536.
- [146] J.-X. Jiang, C. Wang, A. Laybourn, T. Hasell, R. Clowes, Y. Z. Khimyak, J. Xiao, S. J. Higgins, D. J. Adams, A. I. Cooper, *Angew. Chem. Int. Ed.* **2011**, 50, 1072.

- [147] R. Palkovits, M. Antonietti, P. Kuhn, A. Thomas, F. Schüth, *Angew. Chem. Int. Ed.* **2009**, 48, 6909.
- [148] P. Zhang, Z. Weng, J. Guo, C. Wang, *Chem. Mater.* **2011**, 23, 5243.
- [149] L. Q. Ma, M. M. Wanderley, W. B. Lin, *Acs Catalysis* **2011**, 1, 691.
- [150] J. X. Jiang, Y. Y. Li, X. F. Wu, J. L. Xiao, D. J. Adams, A. I. Cooper, *Macromolecules* **2013**, 46, 8779.
- [151] X. M. Liu, A. Sigen, Y. W. Zhang, X. L. Luo, H. Xia, H. Li, Y. Mu, *Rsc Advances* **2014**, 4, 6447.
- [152] M. Liras, M. Iglesias, F. Sanchez, *Macromolecules* **2016**, 49, 1666.
- [153] Y. Zhang, Y. Zhang, Y. L. Sun, X. Du, J. Y. Shi, W. D. Wang, W. Wang, *Chemistry – A European Journal* **2012**, 18, 6328.
- [154] K. Zhang, Z. Vobecka, K. Tauer, M. Antonietti, F. Vilela, *Chem. Commun.* **2013**, 49, 11158.
- [155] N. Kang, J. H. Park, K. C. Ko, J. Chun, E. Kim, H. W. Shin, S. M. Lee, H. J. Kim, T. K. Ahn, J. Y. Lee, S. U. Son, *Angewandte Chemie-International Edition* **2013**, 52, 6228.
- [156] R. S. Sprick, J.-X. Jiang, B. Bonillo, S. Ren, T. Ratvijitvech, P. Guiglion, M. A. Zwijnenburg, D. J. Adams, A. I. Cooper, *J. Am. Chem. Soc.* **2015**, 137, 3265.
- [157] Z. J. Wang, S. Ghasimi, K. Landfester, K. A. I. Zhang, *Adv. Mater.* **2015**, 27, 6265.
- [158] C. L. Su, R. Tandiana, B. B. Tian, A. Sengupta, W. Tang, J. Su, K. P. Loh, *Acs Catalysis* **2016**, 6, 3594.
- [159] Z. J. Wang, S. Ghasimi, K. Landfester, K. A. I. Zhang, *J. Mater. Chem. A* **2014**, 2, 18720.
- [160] Z. J. Wang, S. Ghasimi, K. Landfester, K. A. I. Zhang, *Chem. Commun.* **2014**, 50, 8177.
- [161] L. L. Schramm, *Emulsions, Foams, and Suspensions: Fundamentals and Applications*, Wiley-VCH Verlag GmbH & Co. KGaA, 2005.
- [162] F. Leal-Calderon, V. Schmitt, J. Bibette, *Emulsion Science. Basic Principles*, Springer Science+Business Media, LLC, 2007.
- [163] K. Landfester, in *Annual Review of Materials Research*, Vol. 36, Annual Reviews, Palo Alto 2006, 231.
- [164] H.-J. Butt, K. Graf, M. Kappl, *Physics and Chemistry of Interfaces*, Wiley-VCH Verlag GmbH & Co. KGaA, 2003.
- [165] J. Bibette, F. Caruso, F. Currie, A. Elaissari, K. Esumi, F. Ganachaud, C. Gruber, M. Häger, K. Holmberg, I. Kräuter, K. Landfester, F. Leal-Calderon, C. M. Paleos, C. Pichot, V.

Schmitt, G. E. M. Tovar, D. Tsiourvas, *Colloid Chemistry II*, Springer-Verlag Berlin Heidelberg New York, 2003.

[166] S. Slomkowski, J. V. Alemán, R. G. Gilbert, M. Hess, K. Horie, R. G. Jones, P. Kubisa, I. Meisel, W. Mormann, S. Penczek, R. F. T. Stepto, *Pure Appl. Chem.* **2011**, 83, 2229.

[167] K. Landfester, *Angewandte Chemie, International Edition* **2009**, 48, 4488.

[168] K. Landfester, *Angewandte Chemie-International Edition* **2009**, 48, 4488.

[169] T. F. Tadros, *Colloid Stability: The Role of Surface Forces - Part I*, Vol. 1, Wiley-VCH Verlag GmbH & Co. KGaA, 2007.

[170] D. H. Napper, *Industrial & Engineering Chemistry Product Research and Development* **1970**, 9, 467.

[171] D. B. Williams, C. B. Carter, *Transmission Electron Microscopy: A Textbook for Materials Science*, Springer Science+Business Media, LLC 1996, 2009.

[172] J. I. Goldstein, D. E. Newbury, P. Echlin, D. C. Joy, C. E. Lyman, E. Lifshin, L. Sawyer, J. R. Michael, *Scanning Electron Microscopy and X-Ray Microanalysis*, Springer Science+Business Media, LLC, 2003.

[173] H.-H. Perkampus, *UV-VIS Spectroscopy and Its Applications*, Springer-Verlag Berlin Heidelberg, 1992.

[174] J. R. Lakowicz, *Principles of Fluorescence Spectroscopy*, Springer Science+Business Media, LLC, 2006.

[175] B. H. Stuart, *Infrared Spectroscopy: Fundamentals and Applications*, John Wiley & Sons, Ltd, 2004.

[176] E. Pretsch, P. Bühlmann, M. Badertscher, *Structure Determination of Organic Compounds: Tables of Spectral Data*, Springer-Verlag Berlin Heidelberg, 2009.

[177] M. J. N. Junk, *Assessing the Functional Structure of Molecular Transporters by EPR Spectroscopy*, Springer Berlin Heidelberg, 2012.

[178] R. G. Saifutdinov, L. I. Larina, T. I. i. Vakul'skaya, M. G. e. Voronkov, *Electron Paramagnetic Resonance in Biochemistry and Medicine*, Kluwer Academic Publishers, 2002.

[179] S. Lowell, J. E. Shields, M. A. Thomas, M. Thommes, *Characterization of Porous Solids and Powders: Surface Area, Pore Size and Density*, Springer Science+Business Media New York, 2004.

[180] K. S. W. Sing, D. H. Everett, R. A. W. Haul, L. Moscou, R. A. Pierotti, J. Rouquérol, T. Siemieniewska, *Pure Appl. Chem.* **1985**, 57, 603.

[181] H. Borchert, *Solar Cells Based on Colloidal Nanocrystals*, Springer International Publishing, 2014.

- [182] F. Scholz, *Electroanalytical Methods*, Springer-Verlag Berlin Heidelberg, 2010.
- [183] D. Gust, T. A. Moore, *Science* **1989**, 244, 35.
- [184] T. J. Meyer, *Acc. Chem. Res.* **1989**, 22, 163.
- [185] D. Gust, T. A. Moore, A. L. Moore, *Acc. Chem. Res.* **1993**, 26, 198.
- [186] M. Fagnoni, D. Dondi, D. Ravelli, A. Albini, *Chem. Rev.* **2007**, 107, 2725.
- [187] N. Hoffmann, *Chem. Rev.* **2008**, 108, 1052.
- [188] K. Kalyanasundaram, *Coord. Chem. Rev.* **1982**, 46, 159.
- [189] A. Juris, V. Balzani, F. Barigelletti, S. Campagna, P. Belser, A. von Zelewsky, *Coord. Chem. Rev.* **1988**, 84, 85.
- [190] M. L. Marin, L. Santos-Juanes, A. Arques, A. M. Amat, M. A. Miranda, *Chem. Rev.* **2012**, 112, 1710.
- [191] H. J. Liu, W. Feng, C. W. Kee, Y. J. Zhao, D. Leow, Y. H. Pan, C. H. Tan, *Green Chem.* **2010**, 12, 953.
- [192] M. Neumann, S. Földner, B. König, K. Zeitler, *Angew. Chem. Int. Ed.* **2011**, 50, 951.
- [193] R. J. White, R. Luque, V. L. Budarin, J. H. Clark, D. J. Macquarrie, *Chem. Soc. Rev.* **2009**, 38, 481.
- [194] B. Wu, N. Zheng, *Nano Today* **2013**, 8, 168.
- [195] L. Chen, Y. Honsho, S. Seki, D. Jiang, *J. Am. Chem. Soc.* **2010**, 132, 6742.
- [196] Y. Chen, J. Zhang, M. Zhang, X. Wang, *Chem Sci* **2013**, 4, 3244.
- [197] F. Vilela, K. Zhang, M. Antonietti, *Energy Environ. Sci.* **2012**, 5, 7819.
- [198] K. Zhang, D. Kopetzki, P. H. Seeberger, M. Antonietti, F. Vilela, *Angew. Chem. Int. Ed.* **2013**, 52, 1432.
- [199] K. Zhang, Z. Vobecka, K. Tauer, M. Antonietti, F. Vilela, *Chem. Commun.* **2013**, 49, 11158.
- [200] Z. J. Wang, S. Ghasimi, K. Landfester, K. A. I. Zhang, *Chem. Commun.* **2014**, 50, 8177.
- [201] J.-X. Jiang, Y. Li, X. Wu, J. Xiao, D. J. Adams, A. I. Cooper, *Macromolecules* **2013**, 46, 8779.
- [202] J. Luo, X. Zhang, J. Zhang, *Acs Catalysis* **2015**, 5, 2250.
- [203] Z. J. Wang, K. Landfester, K. A. I. Zhang, *Polym. Chem.* **2014**, 5, 3559.

- [204] S. Dadashi-Silab, H. Bildirir, R. Dawson, A. Thomas, Y. Yagci, *Macromolecules* **2014**, 47, 4607.
- [205] A. Patra, J.-M. Koenen, U. Scherf, *Chem. Commun.* **2011**, 47, 9612.
- [206] J. X. Jiang, F. Su, A. Trewin, C. D. Wood, H. Niu, J. T. A. Jones, Y. Z. Khimyak, A. I. Cooper, *J. Am. Chem. Soc.* **2008**, 130, 7710.
- [207] A. Laybourn, R. Dawson, R. Clowes, T. Hasell, A. I. Cooper, Y. Z. Khimyak, D. J. Adams, *Polym. Chem.* **2014**, 5, 6325.
- [208] J. D. White, J. P. Carter, H. S. Kezar, *J. Org. Chem.* **1982**, 47, 929.
- [209] M. I. Burguete, R. Gavara, F. Galindo, S. V. Luis, *Catal. Commun.* **2010**, 11, 1081.
- [210] H. Tokuyama, E. Nakamura, *J. Org. Chem.* **1994**, 59, 1135.
- [211] J. R. Choi, T. Tachikawa, M. Fujitsuka, T. Majima, *Langmuir* **2010**, 26, 10437.
- [212] C. R. Paula, V. L. J. Krebs, M. E. Auler, L. S. Ruiz, F. E. Matsumoto, E. H. Silva, E. M. A. Diniz, F. A. C. Vaz, *Med. Mycol.* **2006**, 44, 479.
- [213] P. E. Sudbery, *Nature Reviews Microbiology* **2011**, 9, 737.
- [214] Q. C. Zhang, G. Lambert, D. Liao, H. Kim, K. Robin, C. K. Tung, N. Pourmand, R. H. Austin, *Science* **2011**, 333, 1764.
- [215] P. A. Smith, F. E. Romesberg, *Nat. Chem. Biol.* **2007**, 3, 549.
- [216] R. Chait, A. Craney, R. Kishony, *Nature* **2007**, 446, 668.
- [217] M. Gao, Q. Hu, G. Feng, N. Tomczak, R. Liu, B. Xing, B. Z. Tang, B. Liu, *Advanced Healthcare Materials* **2015**, 4, 636.
- [218] M. C. DeRosa, R. J. Crutchley, *Coord. Chem. Rev.* **2002**, 233, 351.
- [219] J. Huang, W. Ho, X. Wang, *Chem. Commun.* **2014**, 50, 4338.
- [220] X. F. Jiang, L. Yang, P. Liu, X. Li, J. A. Shen, *Colloids and Surfaces B-Biointerfaces* **2010**, 79, 69.
- [221] S. Banerjee, S. C. Pillai, P. Falaras, K. E. O'Shea, J. A. Byrne, D. D. Dionysiou, *J. Phys. Chem. Lett.* **2014**, 5, 2543.
- [222] L. S. Zhang, K. H. Wong, H. Y. Yip, C. Hu, J. C. Yu, C. Y. Chan, P. K. Wong, *Environ. Sci. Technol.* **2010**, 44, 1392.
- [223] C. Xing, Q. Xu, H. Tang, L. Liu, S. Wang, *J. Am. Chem. Soc.* **2009**, 131, 13117.
- [224] H. X. Yuan, B. Wang, F. T. Lv, L. B. Liu, S. Wang, *Adv. Mater.* **2014**, 26, 6978.
- [225] C. Zhu, L. Liu, Q. Yang, F. Lv, S. Wang, *Chem. Rev.* **2012**, 112, 4687.

- [226] H. T. Bai, H. X. Yuan, C. Y. Nie, B. Wang, F. T. Lv, L. B. Liu, S. Wang, *Angewandte Chemie-International Edition* **2015**, 54, 13208.
- [227] S. Perni, P. Prokopovich, J. Pratten, I. P. Parkin, M. Wilson, *Photochemical & Photobiological Sciences* **2011**, 10, 712.
- [228] M. Gruner, L. Tuchscher, B. Loffler, D. Gonnissen, K. Riehemann, M. C. Staniford, U. Kynast, C. A. Strassert, *Acs Applied Materials & Interfaces* **2015**, 7, 20965.
- [229] A. P. Castano, P. Mroz, M. R. Hamblin, *Nature Reviews Cancer* **2006**, 6, 535.
- [230] F. Wang, J. H. Seo, Z. D. Li, A. V. Kvit, Z. Q. Ma, X. D. Wang, *Acs Applied Materials & Interfaces* **2014**, 6, 1288.
- [231] Y. Chen, J. S. Zhang, M. W. Zhang, X. C. Wang, *Chemical Science* **2013**, 4, 3244.
- [232] L.-S. Zhang, K.-H. Wong, H.-Y. Yip, C. Hu, J. C. Yu, C.-Y. Chan, P.-K. Wong, *Environ. Sci. Technol.* **2010**, 44, 1392.
- [233] M. N. Chong, B. Jin, C. W. K. Chow, C. Saint, *Water Res.* **2010**, 44, 2997.
- [234] A. Markowska-Szczupak, K. Ulfig, A. W. Morawski, *Catal. Today* **2011**, 169, 249.
- [235] D. R. Kearns, *Chem. Rev.* **1971**, 71, 395.
- [236] A. S. Bommarius, M. Schwarm, K. Drauz, *Journal of Molecular Catalysis B-Enzymatic* **1998**, 5, 1.
- [237] A. Galkin, L. Kulakova, T. Yoshimura, K. Soda, N. Esaki, *Appl. Environ. Microbiol.* **1997**, 63, 4651.
- [238] H. K. Chenault, G. M. Whitesides, *Appl. Biochem. Biotechnol.* **1987**, 14, 147.
- [239] H. Wu, C. Y. Tian, X. K. Song, C. Liu, D. Yang, Z. Y. Jiang, *Green Chem.* **2013**, 15, 1773.
- [240] F. Gao, X. Y. Guo, J. Yin, D. Zhao, M. G. Li, L. Wang, *Rsc Advances* **2011**, 1, 1301.
- [241] D. P. Summers, D. Rodoni, *Langmuir* **2015**, 31, 10633.
- [242] H. Z. Li, K. E. Worley, S. C. Barton, *Acs Catalysis* **2012**, 2, 2572.
- [243] K. V. Rao, R. Haldar, T. K. Maji, S. J. George, *Phys. Chem. Chem. Phys.* **2016**, 18, 156.
- [244] H. Yamada, A. Nagao, H. Nishise, Y. Tani, *Agric. Biol. Chem.* **1982**, 46, 2333.
- [245] N. S. Lewis, D. G. Nocera, *Proc. Natl. Acad. Sci. U. S. A.* **2006**, 103, 15729.
- [246] K. Maeda, K. Domen, *J. Phys. Chem. Lett.* **2010**, 1, 2655.
- [247] F. E. Osterloh, *Chem. Soc. Rev.* **2013**, 42, 2294.

- [248] I. Tsuji, H. Kato, H. Kobayashi, A. Kudo, *J. Am. Chem. Soc.* **2004**, 126, 13406.
- [249] K. Maeda, T. Takata, M. Hara, N. Saito, Y. Inoue, H. Kobayashi, K. Domen, *J. Am. Chem. Soc.* **2005**, 127, 8286.
- [250] K. Maeda, K. Teramura, D. L. Lu, T. Takata, N. Saito, Y. Inoue, K. Domen, *Nature* **2006**, 440, 295.
- [251] Q. Wang, T. Hisatomi, Q. X. Jia, H. Tokudome, M. Zhong, C. Z. Wang, Z. H. Pan, T. Takata, M. Nakabayashi, N. Shibata, Y. B. Li, I. D. Sharp, A. Kudo, T. Yamada, K. Domen, *Nature Materials* **2016**, 15, 611.
- [252] Y. Zheng, L. H. Lin, B. Wang, X. C. Wang, *Angewandte Chemie-International Edition* **2015**, 54, 12868.
- [253] D. J. Martin, P. J. T. Reardon, S. J. A. Moniz, J. W. Tang, *J. Am. Chem. Soc.* **2014**, 136, 12568.
- [254] A. G. Slater, A. I. Cooper, *Science* **2015**, 348, 11.
- [255] H. Xu, J. Gao, D. L. Jiang, *Nat. Chem.* **2015**, 7, 905.
- [256] C. Gu, N. Huang, Y. Chen, H. Zhang, S. Zhang, F. Li, Y. Ma, D. Jiang, *Angew. Chem. Int. Ed.* **2016**, 55, 3049.
- [257] S. Dalapati, M. Addicoat, S. B. Jin, T. Sakurai, J. Gao, H. Xu, S. Irle, S. Seki, D. L. Jiang, *Nature Communications* **2015**, 6, 8.
- [258] M. Shalom, S. Inal, C. Fettkenhauer, D. Neher, M. Antonietti, *J. Am. Chem. Soc.* **2013**, 135, 7118.
- [259] T. Simon, N. Bouchonville, M. J. Berr, A. Vaneski, A. Adrovic, D. Volbers, R. Wyrwich, M. Doblinger, A. S. Susha, A. L. Rogach, F. Jackel, J. K. Stolarczyk, J. Feldmann, *Nature Materials* **2014**, 13, 1013.
- [260] J. X. Jiang, A. Trewin, D. J. Adams, A. I. Cooper, *Chemical Science* **2011**, 2, 1777.
- [261] M. G. Schwab, M. Hamburger, X. L. Feng, J. Shu, H. W. Spiess, X. C. Wang, M. Antonietti, K. Mullen, *Chem. Commun.* **2010**, 46, 8932.
- [262] N. Blouin, A. Michaud, D. Gendron, S. Wakim, E. Blair, R. Neagu-Plesu, M. Belletete, G. Durocher, Y. Tao, M. Leclerc, *J. Am. Chem. Soc.* **2008**, 130, 732.

8 List of Acronyms

AO	Ammonium oxalate
AQY	Apparent quantum yield
BET	Brunauer Emmett Teller
BODIPY	Boron-dipyrromethene
BQ	Benzoquinone
BT	4,7-dibromobenzo[c][1,2,5]thiadiazole
CB	Conduction band
CMP	Conjugated microporous polymer
CMP NPs	Conjugated microporous polymer nanoparticles
CV	Cyclic voltammetry
DCM	Dichloromethane
DFT	Density functional theory
DLVO	Derjaguin-Landau and Verwey-Overbeek
DLS	Dynamic light scattering
DMAP	4-Dimethylaminopyridine
DMF	Dimethylformamide
DMPO	5,5-dimethyl-1-pyrroline <i>N</i> -oxide
DRS	Diffuse reflectance spectra
EPR	Electron paramagnetic resonance
FFF	Fast Fourier transformation

FL	Dihexylfluorene
FTIR	Fourier transform infrared spectroscopy
GDH	Glycerol dehydrogenase
HER	Hydrogen evolution rate
HIPES	High internal phase emulsions
HOMO	Highest occupied molecular orbital
IUPAC	International Union of Pure and Applied Chemistry
LED	Light emitting diode
LSPR	Localized surface plasmon resonance
LUMO	Lowest unoccupied molecular orbital
MLCT	Metal-to-ligand charge transfer transition
MWCO	Molecular weight cut-off
NAD ⁺	Nicotinamide adenine dinucleotide
NADH	Nicotinamide adenine dinucleotide (reduced form)
NHE	Normal hydrogen electrode
NLDFT	Nonlinear density functional theory
NMR	Nuclear magnetic resonance
OG	Optical gap
PANI	Polyaniline
P3HT	Poly(3-hexylthiophene-2,5-diyl)
PD	Pore diameter

PDT	Photodynamic therapy
PEDOT	Poly(3,4-ethylenedioxythiophene)
PV	Pore volume
PXRD	Powder X-ray diffraction
QD	Quantum dots
QSDFE	Quenched solid density functional theory
RhB	Rhodamine B
ROS	Reactive oxygen species
SCE	Saturated calomel electrode
SEM	Scanning electron microscopy
TCD	Thermal conductive detector
TEM	Transmission electron microscopy
TEMP	2,2,6,6-tetramethylpiperidine
TEMPO	2,2,6,6-Tetramethylpiperidine 1-oxyl
TEOA	Triethanolamine
TGA	Thermogravimetric analysis
TMPD	<i>N,N,N',N'</i> -tetramethyl- <i>p</i> -phenylenediamine
UV	Ultraviolet
VB	Valence band

9 List of Figures

Figure 1. Schematic illustration of the formation of photogenerated electron-hole pairs upon absorption of light.....	17
Figure 2. Solar spectrum adapted from ^[33]	18
Figure 3. Ruthenium and iridium complexes.....	19
Figure 4. Some of the organic dyes employed in visible light photocatalysis.....	20
Figure 5. Structure of cis- and trans-polyacetylene.....	23
Figure 6. Molecular structures of some conjugated polymer materials investigated in visible light photocatalysis. (a) poly(<i>p</i> -phenylene), (b) planarized fluorine-type analogue and (c) poly(diphenylbutadiyne).....	24
Figure 7. General scheme of the Suzuki-Miyaura cross-coupling reaction.....	25
Figure 8. Suzuki-Miyaura cross-coupling reaction mechanism. Adapted from ^[127, 129]	26
Figure 9. General scheme of the Sonogashira-Hagihara cross-coupling reaction.....	27
Figure 10. Sonogashira-Hagihara cross-coupling reaction mechanism. Adapted from ^[131]	28
Figure 11. Schematic illustration of the formation of nanoparticles by the miniemulsion process.....	32
Figure 12. Schematic illustration of (a) coalescence and (b) Oswald ripening.....	33
Figure 13. Illustration of the interaction potential between two particles as a function of distance according to the DLVO theory. Adapted from Napper ^[170]	34
Figure 14. Schematic illustration of the splitting of the energy levels of an electron spin under the influence of an applied magnetic field.....	37
Figure 15. Classification of adsorption isotherms. Adapted from ^[180]	38
Figure 16. Schematic illustration of a three-electrode configuration of an electrochemical cell for cyclic voltammetry.....	39
Figure 17. Solid state ¹³ C CP/MAS NMR spectra of (a) B-FL ₃ -a, (b) B-BPh ₃ -a, (c) B-BT ₃ -a, (d) B-FL ₃ -b, (e) B-BPh ₃ -b, (f) B-BT ₃ -b. *Asterisks denote spinning sidebands.....	43
Figure 18. Thermogravimetric analysis of CMP-NPs.....	44

Figure 19. FTIR spectra of (a) B-FL ₃ -a, (b) B-BPh ₃ -a, (c) B-BT ₃ -a, (d) B-FL ₃ -b, (e) B-BPh ₃ -b, (f) B-BT ₃ -b.	45
Figure 20. XRD patterns of CMP NPs.	46
Figure 21. N ₂ Sorption Isotherms and Pore Size Distributions of CMP nanoparticles using Suzuki-Miyaura cross-coupling condensation reaction via miniemulsion polymerization.	48
Figure 22. N ₂ Sorption isotherms and pore size distributions of CMP nanoparticles using Sonogashira-Hagihara cross-coupling condensation reaction via miniemulsion polymerization.	49
Figure 23. Photographs of the CMP NPs dispersed in water.	50
Figure 24. (a) SEM and (b) TEM images of the CMP NPs with different shapes.	50
Figure 25. Monitoring experiments of the nanoparticle formation of B-BT ₃ -b. SEM images of nanoparticles formed in different time intervals after ultrasonication and heating at 80 °C. (a) 1 min, (b) 3 min, (c) 5 min, (d) 10 min, (e) 30 min, (f) 60 min. (G) UV/vis spectra of the NPs formed after defined time intervals.	51
Figure 26. (a) Size distribution of B-BT ₃ -b measured by dynamic light scattering (DLS) and (b) SEM image of B-BT ₃ -b, using Lutensol as surfactant.	52
Figure 27. UV/vis absorption spectra of the CMP NPs in water dispersion.	53
Figure 28. (a) Photocatalytic degradation of RhB in the presence of the CMP NPs in water. <i>C</i> is the concentration of RhB after light irradiation for a certain period and <i>C</i> ₀ is the concentration of RhB after reaching adsorption/desorption equilibrium in dark. Concentration of CMP NPs: 1 mg mL ⁻¹ , concentration of RhB: 10 mg L ⁻¹ . (b) Photocatalytic set-up using a 23 W household energy saving light bulb.	54
Figure 29. UV-vis spectrum of RhB (10 mg L ⁻¹) after different illumination time intervals in the presence of CMP nanoparticles (1 mg mL ⁻¹). The black arrow indicates the decrease of RhB absorption (552 nm) as a function of irradiation time.	55
Figure 30. (a) Photocatalytic degradation of RhB in the presence of bulk CMP-BT ₃ and B-BT ₃ -b in water. <i>C</i> is the concentration of RhB after light irradiation for a certain period and <i>C</i> ₀ is the concentration of RhB after reaching adsorption/desorption equilibrium in dark. Concentration of CMP-BT ₃ and B-BT ₃ -b: 1 mg mL ⁻¹ , concentration of RhB: 10 mg L ⁻¹ . (b) UV/vis spectra of the reaction mixture of the photodegradation of RhB with B-BT ₃ -b before and after the 5 th repeating cycle of the experiment.	56
Figure 31. The effect of different scavengers, sodium azide (NaN ₃), ammonium oxalate (AO), benzoquinone (BQ), isopropanol (IP) and the absence of oxygen (under N ₂) on the	

degradation of Rhodamine B (RhB) over B-BT ₃ -b under 30 min of visible light irradiation.....	57
Figure 32. ¹ H NMR spectra of (a) furoic acid and (b) 5-hydroxy-2(5H)-furanone in D ₂ O. Peaks at 7.63, 7.22, 6.52 ppm are attributed to furoic acid, 7.40, 6.22 ppm are attributed to the 5-hydroxy-2(5H)-furanone.	58
Figure 33. Photooxidation of TMPD using different CMP NPs in acetonitrile. Concentration of CMP NPs: 1 mg mL ⁻¹ , concentration of TMPD: 32.85 mg mL ⁻¹ . The insert image shows: (left) pure TMPD solution after light irradiation and (right) TMPD solution mixed with B-BT ₃ -b after light irradiation.	59
Figure 34. (a) SEM and (b) TEM images of the CMP NPs.....	64
Figure 35. Solid state ¹³ C CP/MAS NMR spectra of (a)Th-BT-0, (b)Th-BT-25, (c)Th-BT-50, (d)Th-BT-70, (e)Th-BT-90 and (f)Th-BT-100. Asterisks denote spinning sidebands.	65
Figure 36. XRD patterns of CMP NPs.....	66
Figure 37. FTIR spectra of CMP NPs.....	67
Figure 38. Thermogravimetric analysis of CMP NPs.....	68
Figure 39. N ₂ Sorption Isotherms and Pore Size Distributions of Th-BT-0, Th-BT-25 and Th-BT-50.	69
Figure 40. N ₂ Sorption Isotherms and Pore Size Distributions of Th-BT-70, Th-BT-90 and Th-BT-100.....	70
Figure 41. (a) UV/vis absorption spectra; (b) fluorescence emission spectra and (c) valence band (VB) and conduction band (CB) positions of the CMP NPs.....	71
Figure 42. (a) Electron paramagnetic resonance (EPR) spin trapping spectra of TEMPO- ¹ O ₂ adducts in acetonitrile generated by different CMP NPs under visible light irradiation. Conditions: CMP NPs (1 mg mL ⁻¹), 2,2,6,6-tetramethylpiperidine (0.1 M), 2h white light irradiation, room temperature. (b) Difference between the TEMPO- ¹ O ₂ adducts peak signal intensity for the CMP NPs after visible light exposure.....	72
Figure 43. Comparison of the electron paramagnetic resonance (EPR) spectra of TEMPO- ¹ O ₂ adducts (a) and DMPO-•O ₂ ⁻ adducts (b) under visible light but in the absence of Th-BT-100, in the presence of Th-BT-100 but without light irradiation, and under visible light and in presence of Th-BT-100.....	72
Figure 44. Control experiments of photocatalytic inactivation of <i>E.coli</i> K-12 (3 x 10 ⁶ cfu mL ⁻¹). (A) Absence of CMP NPs under visible light irradiation for 120 min. (B) In the	

presence of CMP NPs but without light irradiation for 120 min. (C) In the absence of CMP NPs and without light irradiation. Data represents the results of three independent experiments (mean \pm standard error of the mean).....73

Figure 45. (a) Photocatalytic inactivation of *E.coli K-12* in the presence of different CMP NPs (1 mg mL^{-1}) under visible light irradiation. Data represents the results of three independent experiments (mean \pm standard error of the mean); (b) Photocatalytic inactivation of *E.coli K-12* and *B. subtilis* in the presence of Th-BT-100 (1 mg mL^{-1}) under visible light irradiation. Data represents the results of three independent experiments (mean \pm standard error of the mean); (c) SEM images and photographs of *E. coli K-12* and *B. subtilis* colonies on agar plate as a control group in the absence of Th-BT-100 and light irradiation (top), treated with BT-100 in the dark (middle) and after 120 min of visible light irradiation (bottom).....74

Figure 46. Photocatalytic inactivation of *E.coli K-12* ($3 \times 10^6 \text{ cfu mL}^{-1}$) in the presence of Th-BT-100 and bulk-made Th-BT-100 (1 mg mL^{-1}) under visible light irradiation for different periods of time. Data represents the results of three independent experiments (mean \pm standard error of the mean).75

Figure 47. Toxicity test of different radical scavengers (ammonium oxalate – AO, catalase, NaNO_3 , TEMP and Vitamin C; 0.05 mmol L^{-1}) on *E.coli K-12* ($3 \times 10^6 \text{ cfu mL}^{-1}$) in the presence of Th-BT-100 (1 mg mL^{-1}) and in the darkness. Data represents the results of three independent experiments (mean \pm standard error of the mean).....76

Figure 48. Photocatalytic inactivation of *E.coli K-12* using different scavengers (ammonium oxalate (AO), catalase, NaNO_3 , TEMP and Vitamin C) and Th-BT-100 as antibacterial agent. Conditions: 0.05 mmol L^{-1} concentration of scavengers, air, 120 min white light irradiation. Data represents the results of three independent experiments (mean \pm standard error of the mean).77

Figure 49. ^1H NMR spectra of mesitylene and the starting compound α -terpinene in CDCl_3 . ^1H NMR (250 MHz, CDCl_3): δ 6.82 (s, 3H, mesitylene), 5.65 – 5.61 (m, 1H, α -terpinene), 2.30 (s, 9H, mesitylene), 2.12 (m, 4H, α -terpinene), 1.79 (s, 3H, α -terpinene), 1.05 (d, 2H, α -terpinene).....78

Figure 50. ^1H NMR spectra of mesitylene and the product ascaridole and in CDCl_3 . ^1H NMR (250 MHz, CDCl_3): δ 6.82 (s, 3H, mesitylene), 6.49 (d, 1H, ascaridole), 6.44 (d, 1H, ascaridole), 2.29 (s, 9H, mesitylene), 1.55 (m, 2H, ascaridole), 1.39 (s, 3H, ascaridole), 1.00 (d, 6H, ascaridole).....79

Figure 51. ^1H NMR spectra of mesitylene and α -terpinene in CDCl_3 under the absence of oxygen. ^1H NMR (250 MHz, CDCl_3): δ 6.82 (s, 3H, mesitylene), 5.65 – 5.61 (m, 1H, α -terpinene), 2.30 (s, 9H, mesitylene), 2.12 (m, 4H, α -terpinene), 1.79 (s, 3H, α -terpinene), 1.06 (d, 2H, α -terpinene).....79

Figure 52. (a) Repeated experiments of photocatalytic inactivation of <i>E.coli K-12</i> (3×10^6 cfu mL ⁻¹) in the presence of Th-BT-100 (1 mg mL ⁻¹) under visible light irradiation. Data represents the results of three independent experiments (mean \pm standard error of the mean); (b) FTIR spectra of Th-BT-100 before and after the third cycle of the repeating photocatalytic bacteria inactivation.	80
Figure 53. SEM (a) and TEM (b) images of B-BO ₃	83
Figure 54. Solid state ¹³ C CP/MAS NMR spectra of B-BO ₃	83
Figure 55. FTIR spectra of B-BO ₃	84
Figure 56. XRD patterns of B-BO ₃	84
Figure 57. Thermogravimetric analysis of B-BO ₃	85
Figure 58. N ₂ Sorption Isotherms and Pore Size Distributions of B-BO ₃	85
Figure 59. UV/vis absorption spectra of B-BO ₃	86
Figure 60. (a) Cyclic voltammetry measurement from B-BO ₃ ; (b) HOMO and LUMO positions of B-BO ₃	86
Figure 61. Regeneration of NAD ⁺ from NADH with B-BO ₃ . a) ¹ H-NMR spectra at different times during conversion under blue light irradiation in the presence of O ₂ . b) Conversion (%) of NAD ⁺ over time.	87
Figure 62. Oxidation of propylene glycol by NAD-dependent GDH given as % of converted substrate. a) Determination of reaction conversion by ¹ H NMR at the equilibrium state. Values were obtained from the integration of the methyl protons in propylene glycol (P) relative to the equivalent signals from the substrate (S). b) Conversions of propylene glycol for the different experimental set-ups shown on top of diagram.	88
Figure 63. SEM images of the polymers from series 1.	94
Figure 64. SEM images of the polymers from series 2.	95
Figure 65. Solid state ¹³ C CP/MAS NMR spectra of the polymers from series 1. (a) B-BT-1,4; (b) B-BT-1,2,4; (c) B-BT-1,3,5 and (d) B-BT-1,2,4,5.	96
Figure 66. Solid state ¹³ C CP/MAS NMR spectra of the polymers from series 2. (a) B-BT-0.05; (b) B-BT-0.10; (c) B-BT-0.30; (d) B-BT-0.50 and (e) B-BT-0.70.	97
Figure 67. Transmission electron microscopy (TEM) and its fast Fourier transformation (FFT) measurements of the polymers (a) TEM image of B-BT-1,4 (b) HR-TEM of polymer B-BT-1,4. Insets: FFT. (c)(d), TEM of polymers after reaction.	98

Figure 68. Powder X-ray diffraction (PXRD) of the polymers involving B-BT-1,3,5 and B-BT-1,4.	98
Figure 69. N ₂ sorption isotherms and pore size distributions of the polymers from Series 1.	100
Figure 70. N ₂ sorption isotherms and pore size distributions of the polymers from series 2.	101
Figure 71. Thermogravimetric analysis of the polymers from (a) series 1 and (b) series 2.	102
Figure 72. FTIR spectra of the poly-benzothiadiazoles from series 1.	102
Figure 73. FTIR spectra of the poly-benzothiadiazoles from series 2.	103
Figure 74. UV/Vis Diffuse Reflectance Spectra (DRS) of (a) polymer in series 1 and (b) Series 2, and (c) HOMO LUMO band position of the polymers.	104
Figure 75. Cyclic voltammetry measurement from the polymers of Series 1.	105
Figure 76. Cyclic voltammetry measurement from the polymers of series 2.	106
Figure 77. Molecular computing models for DFT calculation.	107
Figure 78. Molecular computing models for DFT calculation.	107
Figure 79. Molecular computing models for DFT calculation.	108
Figure 80. Molecular computing models for DFT calculation.	108
Figure 81. Molecular computing models for DFT calculation.	109
Figure 82. Photocurrent measurement comparison of B-BT-1,4 with its 3-D counterpart B-BT-1,3,5.	109
Figure 83. Hydrogen evolution rates using polymers in Series 1 (a) and Series 2 (b). ..	110
Figure 84. (a) Wavelength dependence of AQY on H ₂ evolution using B-BT-1,4. (b) Stability and reusability test using B-BT-1,4 as a photocatalyst under visible-light irradiation ($\lambda > 420$ nm) for 30 h.	113
Figure 85. FTIR spectra of B-BT-1,4 before and after 5 repeating cycles of the hydrogen evolution process.	114
Figure 86. Co-catalysts study for hydrogen evolution from water using B-BT-1,4 as photocatalyst.	115

Figure 87. Elemental mapping of three metal nanoparticles (a) Pt, (b) Rh and (c) Pd on B-BT-1,4.....	115
Figure 88. Characterization of Pt nanoparticles on B-BT-1,4.....	116
Figure 89. Characterization of Pd nanoparticles on B-BT-1,4.....	117
Figure 90. Characterization of Rh nanoparticles on B-BT-1,4.....	117

10 List of Scientific Contributions

B. C. Ma*, S. Ghasimi, K. Landfester, F. Vilela and K. A. I. Zhang*. *Conjugated microporous polymer nanoparticles with enhanced dispersibility and water compatibility for photocatalytic applications*. J. Mater. Chem. A, **2015**, 3, 16064-16071. DOI: 10.1039/c5ta03820k

B. C. Ma*, S. Ghasimi, K. Landfester and K. A. I. Zhang*. *Enhanced visible light promoted antibacterial efficiency of conjugated microporous polymer nanoparticles via molecular doping*. J. Mater. Chem. B, **2016**, 4, 5112-5118. DOI: 10.1039/C6TB00943C

C. Yang*, B. C. Ma*, L. Zhang, S. Lin, S. Ghasimi, K. Landfester, K. A. I. Zhang* and X. Wang*. *Molecular engineering of conjugated polybenzothiadiazoles for enhanced hydrogen production by photosynthesis*. Angew. Chem. Int. Ed. **2016**, 55, 9202 – 9206. DOI: 10.1002/anie.201603532

S. Jiang*, B. C. Ma*, J. Reinholz, Q. Li, J. Wang, K. A. I. Zhang, K. Landfester and D. Crespy. *Efficient nanofibrous membranes for antibacterial wound dressing and UV protection*. ACS Appl. Mater. Interfaces, **2016**, DOI: 10.1021/acsami.6b09165.

R. Li, Z. J. Wang, L. Wang, B. C. Ma, S. Ghasimi, H. Lu, K. Landfester and K. A. I. Zhang. *Photocatalytic selective bromination of electron-rich aromatic compounds using microporous organic polymers with visible light*. ACS Catal., **2016**, 6 (2), pp 1113–1121. DOI: 10.1021/acscatal.5b02490

W. Huang, Z. J. Wang, B. C. Ma, S. Ghasimi, D. Gehrig, F. Laquai, K. Landfester and K. A. I. Zhang. *Hollow nanoporous covalent triazine frameworks via acid vapour-assisted solid phase synthesis for enhanced visible light photoactivity*. J. Mater. Chem. A, **2016**, 4, 7555-7559. DOI: 10.1039/C6TA01828A

B. C. Ma, L. C. Silva, K. A. I. Zhang, M. Bannwarth and K. Landfester. *Visible light induced photocatalytic recycling of NAD⁺ cofactor by Conjugated Microporous Polymer Nanoparticles*. In preparation.

R. Li, B. C. Ma, W. Huang, S. Ghasimi, L. Wang, H. Lu, K. Landfester and K. A. I. Zhang. *Regio- and stereo-selective [2+2] cycloaddition of styrene derivatives catalysed by photosensitive conjugated microporous polymer in visible light*. In preparation.

W. Huang, B. C. Ma, H. Lv, K. Landfester and K. A. I. Zhang. *Covalent Triazine Frameworks for Selective Oxidation of Alcohols and Hydrocarbons under Visible Light*. In preparation.

W. Huang, B. C. Ma, Z. J. Wang, K. Landfester and K. A. I. Zhang. *Fixed-Bed Photoreactor using Conjugated Nanoporous Polymer-Coated Glass Fibers for Visible Light-promoted Contentious Photoredox Reactions*. In preparation.

R. Li, D. Gehrig, L. Wang, W. Huang, Z. J. Wang, S. Ghasimi, B. C. Ma, M. Wagner, K. Landfester and K. A. I. Zhang. *4,7-diphenyl-2,1,3-benzothiadiazole as a novel efficient photosensitive organocatalyst for redox reactions*. In preparation.

11 Acknowledgement

This work could not be complete without expressing my sincere gratitude to all who have shone light on my path throughout this journey.

I would like to express my great appreciation to my advisor Prof. Dr. Katharina Landfester for giving me the great opportunity to be part of the group and also for providing me with all the support and advice.

Special thanks are dedicated to my project leader Dr. Kai Zhang for the priceless support, patience, guidance and advice which endowed me with broader research perspectives as a scientist.

I would like to thank the funding sources CAPES, DAAD, CNPq and the Max Planck Society for their financial support that made this work possible. I would also like to thank Prof. Dr. Michael Maskos and Prof. Dr. Thorsten Hoffmann for taking part as committee members and for their contributions to the evaluation of this work.

My sincere thanks also go to my collaboration partners Prof. Dr. Xinchun Wang, Can Yang, Dr. Shuai Jiang, Dr. Lucas Caire da Silva and colleagues Saman Ghasimi, Wei Huang, Run Li and Lei Wang who provided me with their scientific contributions and stimulating discussions. I would also like to thank Dr. Sapun Parekh for the research facilities support, the Polymer Analytics Group and all the technicians and administrative staff for their great help during my time at the Max Planck Institute for Polymer Research.

I would like to thank all my colleagues and friends from AK Landfester who have contributed to an enjoyable working atmosphere through all these years. In particular, I would like to thank Margherita, Matthew, Evandro, Diego, Alice, Cesare, Eli, Staffan, Claudia, Maria K. and Maria M. for your friendship and for all the great times together which will be memories that I will always treasure.

Of course I would like to express my special thanks to my beloved Otávio who was always my great support at all moments. My deepest thanks are dedicated to my family, without their unconditional love, support and encouragement throughout my life none of this would have been possible.

To all of you, my greatest and most sincere thank you.

